EFFICIENT SIGNAL PROCESSING TECHNIQUES FOR ISAC WITH MONO AND MULTISTATIC MIMO RADAR ARCHITECTURES

A THESIS SUBMITTED TO
THE GRADUATE SCHOOL OF NATURAL AND APPLIED SCIENCES
OF
MIDDLE EAST TECHNICAL UNIVERSITY

BY

UĞUR BERKAY SARAÇ

IN PARTIAL FULFILLMENT OF THE REQUIREMENTS
FOR
THE DEGREE OF DOCTOR OF PHILOSOPHY
IN
ELECTRICAL AND ELECTRONICS ENGINEERING

JULY 2025

Approval of the thesis:

EFFICIENT SIGNAL PROCESSING TECHNIQUES FOR ISAC WITH MONO AND MULTISTATIC MIMO RADAR ARCHITECTURES

submitted by **UĞUR BERKAY SARAÇ** in partial fulfillment of the requirements for the degree of **Doctor of Philosophy in Electrical and Electronics Engineering Department, Middle East Technical University** by,

Prof. Dr. Naci Emre Altun
Dean, Graduate School of **Natural and Applied Sciences** _____

Prof. Dr. Nevzat Güneri Gençer
Head of Department, **Electrical and Electronics Engineering** _____

Assist. Prof. Dr. Gökhan Muzaffer Güvensen
Supervisor, **Electrical and Electronics Engineering, METU** _____

Examining Committee Members:

Prof. Dr. Orhan Arıkan
Electrical and Electronics Engineering, Bilkent Uni. _____

Assist. Prof. Dr. Gökhan Muzaffer Güvensen
Electrical and Electronics Engineering, METU _____

Prof. Dr. Ali Özgür Yılmaz
Electrical and Electronics Engineering, METU _____

Prof. Dr. Umut Orguner
Electrical and Electronics Engineering, METU _____

Assist. Prof. Dr. Özlem Tuğfe Demir
Electrical and Electronics Engineering, TOBB ETU _____

Date:01.07.2025

I hereby declare that all information in this document has been obtained and presented in accordance with academic rules and ethical conduct. I also declare that, as required by these rules and conduct, I have fully cited and referenced all material and results that are not original to this work.

Name, Surname: Uğur Berkay Saraç

Signature :

ABSTRACT

EFFICIENT SIGNAL PROCESSING TECHNIQUES FOR ISAC WITH MONO AND MULTISTATIC MIMO RADAR ARCHITECTURES

Saraç, Uğur Berkay
Ph.D., Department of Electrical and Electronics Engineering
Supervisor: Assist. Prof. Dr. Gökhan Muzaffer Güvensen

July 2025, 160 pages

The huge increase in the quantity of telecommunication devices and the quality of communication made it necessary to use larger bandwidth and it also showed the importance of bandwidth efficiency. On the other hand, technological applications like automated vehicles or drones bring forward a significantly increasing need for high-resolution radars. Along with the use of millimeter waves, which may satisfy the need for high frequency and large bandwidth to a degree, coexistence of radar and communication in the same frequency band and utilization of multiple-input multiple-output (MIMO) architecture, which enables spatial diversity inside a frequency band, would increase bandwidth efficiency considerably. Despite numerous works in the literature about integrated sensing and communication (ISAC), there is not a consensus on the signal processing methods or the actual detectors that will be used on such systems. In this thesis, detailed system models for monostatic and multistatic ISAC systems using both single-input single-output (SISO) and MIMO architectures are developed and appropriate signal processing methods corresponding to these models, including knowledge-aided and adaptive clutter elimination, are proposed. The performances of the proposed methods are investigated through different performance metrics and

compared with their state-of-the-art counterparts in the literature.

Keywords: Integrated Sensing and Communications, OFDM Radar, MIMO Radar, Clutter Model, Multistatic Sensing

ÖZ

MONO VE MULTİSTATİK MIMO RADAR MİMARİLERİYLE ISAC İÇİN VERİMLİ SİNYAL İŞLEME TEKNİKLERİ

Saraç, Uğur Berkay
Doktora, Elektrik ve Elektronik Mühendisliği Bölümü
Tez Yöneticisi: Dr. Öğr. Üyesi. Gökhan Muzaffer Güvensen

Temmuz 2025 , 160 sayfa

İlerleyen teknolojiyle birlikte haberleşme yapan cihazların sayısında ve haberleşme kalitesinde meydana gelen büyük artış, hem daha fazla frekans bandı kullanılmasını zorunlu kılmış hem de kullanılan bantların verimli bir şekilde değerlendirilmesi konusunu gündeme getirmiştir. Öte yandan özellikle otonom taşıtlar ve insansız hava araçları gibi teknolojik uygulamalar, yüksek çözünürlüklü radarlara duyulan ihtiyacın da ciddi bir artış içinde olduğunu göstermektedir. Yüksek frekans ve geniş bant ihtiyacını bir ölçüde karşılayabilecek milimetre dalgalarının kullanımının yanı sıra, radar ve haberleşmenin aynı frekans bandında bir arada bulunması ve frekans bandı içinde uzamsal çeşitlilik sağlayan çoklu giriş çoklu çıkış (MIMO) mimarisinin kullanılması, bant genişliği verimliliğini önemli ölçüde artırabilir. Entegre algılama ve haberleşme (ISAC) konusunda literatürde çok sayıda çalışma bulunmasına rağmen, bu tür sistemlerde kullanılacak sinyal işleme yöntemleri veya detektörler konusunda ortak bir karar bulunmamaktadır. Bu tezde, hem tek giriş tek çıkış (SISO) hem de MIMO mimarileri kullanan monostatik ve multistatik ISAC sistemlerine yönelik ayrıntılı sistem modelleri geliştirilmiş ve bu modellere karşılık gelen, bilgi destekli ve

uyarlamalı kargaşa gidermeyi de içeren sinyal işleme yöntemleri önerilmiştir. Önerilen yöntemlerin performansları çeşitli performans ölçütleri üzerinden incelenmiş ve literatürdeki güncel yaklaşımlarla kıyaslanmıştır.

Anahtar Kelimeler: Ortak Radar-Haberleşme, OFDM Radar, MIMO Radar, Kargaşa Modeli, Multistatik Tespit

To my beloved ones...

ACKNOWLEDGMENTS

I would like to sincerely thank my advisor, Assist. Prof. Dr. Gökhan Muzaffer Güvensen, who was always there for me whenever I needed guidance, day or night. Our long whiteboard sessions and detailed discussions played a crucial role not only in shaping this thesis but also in my academic development. I truly appreciate the perfect balance of professionalism and friendship he offered throughout this journey. I feel incredibly fortunate to have had such a supportive and dedicated advisor.

I extend my sincere thanks to the members of my thesis monitoring committee, Prof. Dr. Orhan Arıkan and Prof. Dr. Ali Özgür Yılmaz, for their invaluable contributions to this work. Their shared experience, constructive criticism, and insightful suggestions have played a significant role in shaping this thesis. Throughout the process, they have always been supportive, and I am truly grateful for their guidance. I am also thankful to my Ph.D. defence jury members, Prof. Dr. Umut Orguner and Assist. Prof. Dr. Özlem Tuğfe Demir, for taking the time to participate in my thesis defense and for their valuable feedback, which helped strengthen the final version of this work. I would also like to express my gratitude to Prof. Dr. Mikko Valkama, with whom I had the opportunity to collaborate as a visiting researcher; his contributions to my academic development were both insightful and inspiring.

I would like to thank to the Scientific and Technological Research Council of Türkiye (TÜBİTAK) for supporting me through 2214-International Research Fellowship Programme (for Ph.D. students) 2023/2 with the application number 1059B142301233 when I was in Tampere, Finland as a visiting researcher.

I would like to express my appreciation to ASELSAN for the opportunity to be involved in several research projects during the course of my thesis work. Although these projects were not directly related to funding of this thesis, they significantly contributed to my knowledge, broadened my research skills, and greatly enriched my overall academic experience.

I would like to give special thanks to my friends, Hüseyin Aydın Seymen, Miray Kayhan Seymen, Mustafa Cihan Cinalioğlu, Sertap Ünlü Cinalioğlu, Gökçe Nihan Demirel and Fatih Demirel, who have stood by me not only during this thesis journey but throughout much of my life. Their constant support and presence have given me the strength and confidence to face any challenge, making me feel like I can never be defeated. I am truly grateful to have them by my side.

I sincerely acknowledge the support of my colleagues at work, especially my roommates Anıl Kurt, Murat Babek Salman and Safa Çelik, as well as my other friends, Berat Yüksel, Cemil Cömert, Hasan Aykut Şatana and Mehmet Çetinkaya. Throughout many years of my thesis and professional journey, they have always offered their full support whenever I needed it. During stressful times, they helped me get through and kept me going. I truly enjoyed the academic and educational discussions we had together, which made the challenging moments much more rewarding. I am also grateful to everyone in my work environment for their continuous encouragement and support.

I am deeply grateful to my family for their unwavering support throughout this journey. I feel proud to be part of such a loving and supportive family. Their presence in every possible way has given me great comfort and strength. I would like to especially remember my late father-in-law, whose encouragement and support during this challenging period meant a great deal to me. I cherish his memory deeply.

Finally, I would like to express my deepest gratitude to my spouse, Aniş Büşra Baran Saraç. She has always made an effort to support my research and constantly encouraged me to do better. She tolerated me even in my most stubborn and difficult moments. Her presence has filled my life with warmth, beauty, joy and happiness. Without her profound love, I could never have imagined completing this thesis.

TABLE OF CONTENTS

ABSTRACT v

ÖZ vii

ACKNOWLEDGMENTS x

TABLE OF CONTENTS xii

LIST OF TABLES xviii

LIST OF FIGURES xix

LIST OF ABBREVIATIONS xxii

NOMENCLATURE xxvi

CHAPTERS

1 INTRODUCTION 1

1.1 Literature Review 1

1.1.1 Motivation Behind ISAC Systems 2

1.1.2 Characterizations and Functional Variants of ISAC 3

1.1.3 MIMO Architectures in ISAC systems 4

1.1.4 Motivation and Usage of OFDM in ISAC systems 5

1.1.5 Multistatic ISAC in Distributed MIMO Architectures 7

1.2 Motivation and Contributions 9

1.2.1 Contributions of Chapter 3 10
1.2.2 Contributions of Chapter 4 10
1.2.3 Contributions of Chapter 5 11
1.3 Outline 12
1.4 Notation 12
2 PRELIMINARY SYSTEM MODEL AND PROBLEM SETTING FOR ISAC 15
2.1 Sensing Operation in OFDM-Based ISAC Systems 16
2.1.1 General System Model and Assumptions 16
2.1.2 Basics of OFDM Transmission and Reception 17
2.1.3 Channel Model for ISAC Targets and Interference 18
2.1.4 Two-Stage Signal Processing Scheme 19
2.1.5 Hypothesis Testing and Detection 20
2.2 Conclusion 23
3 ON THE EFFECTS OF RANGE-DOPPLER PROCESSING FOR TARGET DETECTION IN OFDM-BASED ISAC 25
3.1 Introduction and Literature Review 25
3.2 ISAC System with Multiple Scatterer Channel Model 26
3.3 Target Detection 29
3.3.1 Range-Doppler CCM Calculation 30
3.3.1.1 Before FT Processing 30
3.3.1.2 After FT Processing 30
3.3.2 Detector Structures 32
3.3.2.1 2D Periodogram Detector 32

3.3.2.2 Slow-Time Knowledge-Aided GLRT Detector 33
3.3.2.3 Burg-AMF Detector 34
3.4 Simulation Results 34
3.5 Conclusion 38
4 KNOWLEDGE-AIDED AND ADAPTIVE BEAM-SQUINT AWARE DETECTORS FOR MONOSTATIC MIMO-OFDM ISAC SYSTEMS 39
4.1 Introduction and Literature Review 40
4.2 System Model 42
4.2.1 MIMO Channel 42
4.2.2 Analog Beamformers 47
4.3 Proposed Signal Processing Methods and Detector Structure 49
4.3.1 Negative Effects of Channel Doppler 52
4.3.2 Doppler-Aware Code Bank (DACB) 53
4.3.3 Two-Variant Detector Scheme 55
4.3.3.1 The Need for Two-Variant Detector Scheme 56
4.3.3.2 $\mathcal{V}_1$ Detectors 60
4.3.3.3 $\mathcal{V}_2$ Detectors 60
4.3.4 Interference-Aware Sequential Angle-Range Processing 61
4.4 Alternative Filter Implementations in the Proposed Detector Structure 66
4.4.1 Alternative Filter Implementations 66
4.4.1.1 KA-SARP Given $\mathbf{X}_n$, $\mathcal{V}_1$ Detector 66
4.4.1.2 KA-SARP with Expected $\mathbf{X}_n$, $\mathcal{V}_1$ Detector 67
4.4.1.3 Fully Adaptive AMF-like SARP with SA, $\mathcal{V}_1$ Detector . 67

4.4.1.4 KA-SARP Given $\mathbf{X}_n$, $\mathcal{V}_2$ Detector 68
4.4.1.5 KA-SARP with Expected $\mathbf{X}_n$, $\mathcal{V}_2$ Detector 71
4.4.1.6 Fully Adaptive AMF-like SARP with SA, $\mathcal{V}_2$ Detector . 71
4.4.1.7 3D Periodogram Detector 72
4.4.2 The Effects of Beam-Squint on Different Filter Types 72
4.4.2.1 KA-SARP Given $\mathbf{X}_n$, $\mathcal{V}_1$ detector 73
4.4.2.2 Expected $\mathbf{X}_n$, $\mathcal{V}_1$ detector 73
4.4.2.3 Fully Adaptive AMF-like SARP with SA, $\mathcal{V}_1$ detector . 73
4.5 Numerical Evaluations 74
4.5.1 Simulation Parameters 74
4.5.2 Beamforming Scenarios 75
4.5.3 Simulation Results 77
4.5.3.1 Beam-squint effect is small 78
4.5.3.2 Beam-squint effect is severe 88
4.6 Conclusion 89
5 KNOWLEDGE-AIDED AND ADAPTIVE GLRT DETECTORS FOR MULTISTATIC MIMO-OFDM ISAC SYSTEMS 91
5.1 Introduction and Literature Review 92
5.2 System Model 93
5.2.1 Mapping to Physical Coordinates 93
5.2.2 Basic Assumptions 94
5.2.3 Beamforming and Distributed MIMO Channels 96
5.2.4 Cell Under Test and Hypothesis Testing 98

5.3 Signal Model and Radar Signal Processing 99
5.3.1 Signal Model in Matrix Notation 100
5.3.2 Processing along OFDM symbols and subcarriers 101
5.3.3 MIMO Processing and Detection 106
5.4 Processing Alternatives 110
5.4.1 Knowledge-Aided Processing Given X 110
5.4.2 Knowledge-Aided Processing with Expectation over X 110
5.4.3 AMF-like Processing with Sample Averaging After Preprocessing (AMF-SAAP) 111
5.4.4 AMF-like Processing with Sample Averaging Before Preprocessing (AMF-SABP) 113
5.4.5 3D Periodogram Processing 113
5.5 Numerical Evaluations 114
5.5.1 Beamformers 114
5.5.2 Performance Metrics 115
5.5.2.1 Bistatic Processing Gain / SINR Improvement Factor . . 115
5.5.2.2 Multistatic Probability of Detection (P_d) 116
5.5.3 Simulation Environment and Model Parameters 117
5.5.4 Numerical Results 117
5.5.4.1 Bistatic Processing Gain / SINR Improvement Factor . . 120
5.5.4.2 Multistatic Probability of Detection (P_d) 124
5.6 Conclusion 126
6 CONCLUSION 127
REFERENCES 131

APPENDICES 147

A Calculation of autocorrelation matrices in Chapter 4 147

A.1 Transmitted symbols are given 147

A.2 Transmitted symbols are not given 150

B Calculation of autocorrelation matrices in Chapter 5 154

B.1 Transmitted symbols are given 154

B.2 Transmitted symbols are not given 155

CURRICULUM VITAE 159

LIST OF TABLES

TABLES

Table 3.1 Simulation Parameters 35

Table 4.1 Alternative Filter Types for the Proposed Detector Structure 70

Table 4.2 Simulation Parameters 76

Table 5.1 Simulation Parameters 119

LIST OF FIGURES

FIGURES

Figure 2.1 Block diagram of the sparse frequency domain channel model, two-stage signal processing scheme, hypothesis testing and detection operations for a SISO ISAC system. 22

Figure 3.1 Overview of the OFDM-based ISAC system architecture. 27

Figure 3.2 Proposed OFDM frame processing structure: Frame index t is dropped in the rest of the chapter for simplicity, β is adjusted to set the false-alarm rate to P_{fa} when interference statistics ($\mathbf{R}_n$) are stationary along $\mathcal{L}$ frames. 32

Figure 3.3 SINR vs IT Velocity graphs for point (top) and realistic (bottom) clutter models. 36

Figure 3.4 P_d vs SNR per subcarrier graphs for both point (w/o markers) and realistic (w/ markers) clutter models, CUT is at 19^{th} range bin, 7^{th} (top) and 16^{th} (bottom) velocity bins. 38

Figure 4.1 Visualization of Tx-Rx sectors, DL and UL users, UITs and the IT in an example scenario of partially overlapping Tx-Rx sectors (top), and diagram of transmitted and received data matrices (bottom). 48

Figure 4.2 Block diagram of proposed frame, symbol and subcarrier structures and signal processing, including the two-variant detector scheme. . 51

Figure 4.3 SINR vs CUT angle graphs for a fully-overlapping toy-example scenario, CUT Range bin: 0, UIT Range bin: 10, UIT Angle: 0 degrees. 58

Figure 4.4 SINR vs CUT angle graphs for fully-overlapping scenarios, CUT Range bin: 0, CUT Doppler bin: 0 (0 m/s), UIT Range bin: 10, UIT Doppler bin: 0 (0 m/s), UIT Angle: 0 degrees. 59

Figure 4.5 Working principal and frame structure of the Fully-Adaptive (FA) Sample-Averaging detector, focusing on subband approach. 69

Figure 4.6 Tx, Rx and combined antenna gain patterns for fully overlapping (top) and no overlapping (bottom) schemes. 77

Figure 4.7 SINR vs CUT angle graphs for fully-overlapping (top) and non-overlapping (bottom) scenarios, CUT Range bin: 0 (top) and 10 (bottom), CUT Doppler bin: 0.32 (10 m/s). 79

Figure 4.8 SINR vs CUT range bin graphs for FO scenario, CUT Angle: 5 degrees (top) and 0 degrees (bottom), CUT Doppler bin: 0.32 (10 m/s). . 81

Figure 4.9 SINR vs CUT range bin graphs for NO scenario, CUT Angle: 12 degrees (top) and -12.5 degrees (bottom), CUT Doppler bin: 0.32 (10 m/s). 81

Figure 4.10 SINR vs CUT range bin graphs for $\mathcal{V}_1\&\mathcal{V}_2$ Given $\mathbf{X}_n$ (top) and $\mathcal{V}_1\&\mathcal{V}_2$ SA-AMF (bottom) detectors in a NO scenario, CUT Angle: -12.5 degrees, CUT Doppler bin: 0.32 (10 m/s). 83

Figure 4.11 SINR vs CUT Doppler bin graphs for FO scenario, CUT Angle: 5 degree (top) and 0 degree (bottom), CUT Range bin: 10. 83

Figure 4.12 SINR vs CUT Doppler bin graphs for FO (top) and NO (bottom) scenarios, CUT Angle: 0 degrees (top) and -12 degrees (bottom), CUT Range bin: 0 (top) and 10 (bottom). 85

Figure 4.13 P_d vs input SNR curves for NO scenarios, $P_{fa} = 10^{-3}$, number of Monte-Carlo trials: 300, CUT Range bin: 10, CUT Doppler bin: 0.32 (10 m/s), CUT Angle: -6 degree (top) and 16 degrees (bottom). 85

Figure 4.14 CDF values vs output SINR for different detector implementations with different numbers of Monte-Carlo trials. 87

Figure 4.15 SINR vs CUT angle graphs for NO scenarios when beam-squint effect is severe, CUT Range bin: 10, CUT Doppler bin: 0.32 (10 m/s). $f_c/W = 18.1274$. Number of subbands: 1 (top) and 8 (bottom). 89

Figure 5.1 Visualization of the UITs and the IT in an example scenario (top) and diagram of transmitted and received data matrices (bottom). 102

Figure 5.2 Block diagram of proposed signal processing for $(i,j)^{\text{th}}$ Rx-Tx pair. 105

Figure 5.3 Block diagram of ICM estimation processes for AMF-like detectors. 112

Figure 5.4 Locations of Tx and Rx antennas and UITs, illuminated Tx and Rx sectors, LOS paths, and CUT locations used in the simulations. . . . 118

Figure 5.5 SINR improvement factor maps for Given X (left) and Expected X (right) detectors. In top figures, the coordinates represent $\mathbf{p}_\star$ and $\dot{\mathbf{p}}_\star = [5,5]^{\mathrm{T}}$ m/s. In bottom figures, the coordinates represent $\dot{\mathbf{p}}$ and $\mathbf{p}_\star = [-15,12]^{\mathrm{T}}$ m. 121

Figure 5.6 SINR improvement factor CDFs for the CUTs in Area 1 (top) and Area 2(bottom). 122

Figure 5.7 SINR improvement factor vs $x_\star$ as CUT moves along Line 1 when $\dot{\mathbf{p}}_\star = [5,5]^{\mathrm{T}}$ m/s (top) and SINR improvement factor vs $\dot{x}_\star$ for different M values, $\mathbf{p}_\star = [-15,12]^{\mathrm{T}}$ m, $\dot{y}_\star = 0$ m/s (bottom). 123

Figure 5.8 Probability of detection vs IT RCS graphs for different thresholding schemes, $\mathbf{p}_\star = [-5,12]^{\mathrm{T}}$ m, $\dot{\mathbf{p}}_\star = [5,5]^{\mathrm{T}}$ m/s, $\mathrm{P_{fa}} = 10^{-3}$. 124

Figure 5.9 Probability of detection vs IT RCS graphs for different thresholding schemes, $\mathbf{p}_\star = [0,0]^{\mathrm{T}}$ m, $\dot{\mathbf{p}}_\star = [5,5]^{\mathrm{T}}$ m/s, $\mathrm{P_{fa}} = 10^{-3}$. 125

Figure 5.10 Probability of detection vs IT RCS graphs for different thresholding schemes, $\mathbf{p}_\star = [15,-11]^{\mathrm{T}}$ m, $\dot{\mathbf{p}}_\star = [5,5]^{\mathrm{T}}$ m/s, $\mathrm{P_{fa}} = 10^{-3}$. . . . 125

LIST OF ABBREVIATIONS

ABBREVIATIONS	
2D	2 Dimensional
3D	3 Dimensional
4D	4 Dimensional
5G	Fifth-Generation
6G	Sixth-Generation
ADC	Analog-to-Digital Converter
AFDM	Affine Frequency Division Multiplexing
AMF	Adaptive Matched Filter
BS	Beam-Squint
CCM	Clutter Covariance Matrix
CDF	Cumulative Distribution Function
CFAR	Constant False Alarm Ratio
CP	Cyclic Prefix
CPI	Coherent Processing Interval
CUT	Cell Under Test
DAC	Digital-to-Analog Converter
DACB	Doppler-Aware Code Bank
dB	Decibel
DFRC	Dual-Functional Radar-Communications
DFT	Discrete Fourier Transform
DL	Downlink
FA	Fully-Adaptive

FD	Full-Duplex
FO	Fully-Overlapping
FFT	Fast Fourier Transform
FT	Fast-Time
GLRT	Generalized Likelihood-Ratio Test
GLS	Generalized Least-Squares
ICI	Inter-Carrier Interference
IDFT	Inverse Discrete Fourier Transform
IF	Improvement Factor
IFFT	Inverse Fast Fourier Transform
iid	Independent and Identically Distributed
ISAC	Integrated Sensing and Communications
ISI	Inter-Symbol Interference
IT	Intended Target
JCAS	Joint Communications and Sensing
JSAC	Joint Sensing and Communications
KA	Knowledge-Aided
LOS	Line-of-Sight
LRT	Likelihood-Ratio Test
LS	Least Squares
MIMO	Multiple-Input Multiple-Output
ML	Maximum Likelihood
MSE	Mean-Square Error
MVDR	Minimum Variance Distortionless Response
NN	Neural Network
NO	No Overlapping
NR	New-Radio

OFDM	Orthogonal Frequency-Division Multiplexing
OTFS	Orthogonal Time-Frequency Space
P_d	Probability of Detection
P_{fa}	Probability of false alarm
PMN	Perceptive Mobile Networks
PRI	Pulse Repetition Interval
PSD	Power Spectral Density
PSK	Phase-Shift Keying
RadCom	Radar Communication
RCS	Radar Cross Section
RF	Radio Frequency
RIS	Reconfigurable Intelligent Surface
Rx	Receiver
SA	Sample Averaging
SARP	Sequential Angle-Range Processing
SCR	Signal-to-Clutter Ratio
SI	Self-Interference
SIC	Self-Interference Cancellation
SIMO	Single Input Multiple Output
SINR	Signal-to-Interference-plus-Noise Ratio
SISO	Single-Input-Single Output
SoI	Signal of Interest
SNR	Signal-to-Noise Ratio
ST	Slow-Time
THz	Terahertz
Tx	Transmitter
UE	User Equipment

UIT	Unintended Target
UL	Uplink

NOMENCLATURE

Common Variables

α	Random complex phase of the channel (in general)
$\bar{\mathcal{N}}$	Total # of subcarriers in each subband
$\bar{N}$	Total # of subcarriers
$\bar{n}$	Processed noise sample (in general)
$\Delta\bar{f}$	Subcarrier spacing
Δf	Subcarrier spacing between ISAC subcarriers
γ	Average power of the channel (in general)
$\hat{h}_{nm}$	Scalar channel estimate at n^{th} subcarrier in m^{th} OFDM symbol (in general)
λ	Wavelength (in general)
λ_c	Center wavelength
λ_n	Wavelength of n^{th} subcarrier
$\mathbf{I}_M$	$M \times M$ identity matrix
$\mathbf{I}_N$	$N \times N$ identity matrix
$\mathbf{I}_{\mathcal{J}D_t}$	$\mathcal{J}D_t \times \mathcal{J}D_t$ identity matrix
$\mathbf{I}_{D_rD_t}$	$D_rD_t \times D_rD_t$ identity matrix
$\mathbf{I}_{D_r}$	$D_r \times D_r$ identity matrix
$\mathbf{I}_{D_t}$	$D_t \times D_t$ identity matrix
$\mathbf{I}_{MD_r}$	$MD_r \times MD_r$ identity matrix
$\mathbf{X}$	Transmitted symbol matrix (in general)
$\mathbf{x}$	Transmitted symbol vector (in general)
$\mathbf{Y}$	Received symbol matrix (in general)
$\mathbf{y}$	Received symbol vector (in general)

$\mathcal{M}$	Alphabet size for the symbols
$\mathcal{N}$	# of ISAC subcarriers in each subband
π	The number *pi*
σ_n^2	Noise variance
τ	Round-trip time of channel (in general)
$\tilde{m}$	Doppler bin of the CUT
$\tilde{n}$	Range bin of the CUT
ξ	Scalar detection metric
c_0	Speed of light in vacuum
D_r	# of receive streams (in general)
D_t	# of transmit streams (in general)
e	Exponential function (Euler's number)
f_0	Carrier frequency of 0^{th} subcarrier
f_c	Center carrier frequency
f_D	Doppler frequency (in general)
f_n	Carrier frequency of n^{th} subcarrier
H_0	Null hypothesis
H_1	Detection hypothesis
h_{nm}	Scalar channel at n^{th} subcarrier in m^{th} OFDM symbol (in general)
j	Imaginary unit ($\sqrt{-1}$)
M	# of OFDM symbols
m	OFDM symbol index
N	# of ISAC subcarriers
n	Subcarrier index
N'	# of subbands
N_r	# of receive antennas (in general)
N_t	# of transmit antennas (in general)

n_{nm} Noise realization at n^{th} subcarrier in m^{th} OFDM symbol

T Symbol duration

T_{cp} CP duration

T_s Symbol duration with CP (PRI)

W Total transmission bandwidth

x Transmitted scalar symbol (in general)

x_{nm} Transmitted symbol at n^{th} subcarrier in m^{th} OFDM symbol

y Received scalar symbol (in general)

y_{nm} Received symbol at n^{th} subcarrier in m^{th} OFDM symbol

Chapter 3

α_m^{ik} Reflected complex gain of the k^{th} scatterer of i^{th} target

β Minus logarithm of false alarm probability

$\boldsymbol{\alpha}^{ik}$ $M \times 1$ reflected complex gain vector of the k^{th} scatterer of i^{th} target

$\boldsymbol{\omega}_{n,m}$ Slow-time max-SINR processing filter at n^{th} range bin and m^{th} Doppler bin

$\boldsymbol{\omega}_{n,m}^{(t)}$ $\boldsymbol{\omega}_{n,m}$ variable in $(t)^{\text{th}}$ frame

Δr Range resolution

Δr Velocity resolution

$\gamma_{(n,m)}$ Threshold at n^{th} subcarrier in m^{th} OFDM symbol

$\gamma_{(n,m)}^{(t)}$ $\gamma_{(n,m)}$ variable in $(t)^{\text{th}}$ frame

$\hat{\mathbf{R}}_n$ Estimate of $\hat{\mathbf{R}}_n$ matrix

$\hat{\mathbf{R}}_n^{(t)}$ $\hat{\mathbf{R}}_n$ matrix in $(t)^{\text{th}}$ frame

$\mathbf{d}^{(v)}$ $M \times 1$ slow-time steering vector towards velocity v

$\mathbf{H}$ $N \times M$ frequency domain received channel matrix estimate

$\mathbf{H}^{ik}$ $N \times M$ frequency domain channel matrix from k^{th} scatterer of i^{th} target

$\mathbf{h}^{ik}$ $NM \times 1$ vectorization of $\mathbf{H}^{ik}$

$\mathbf{N}'$ $N \times M$ noise matrix at the receiver

$\mathbf{N}$ $N \times M$ noise matrix after preprocessing

$\mathbf{Q}_N$ $N \times N$ DFT matrix

$\mathbf{q}_n$ n^{th} column of $N \times N$ DFT matrix

$\mathbf{r}^{ik}$ Fast-time return vector from k^{th} scatterer of i^{th} target

$\mathbf{R}_{\mathbf{h}}^{ik}$ $M \times M$ covariance matrix of $\mathbf{h}^{ik}$

$\mathbf{R}_{\text{fast}}^{ik}$ $M \times M$ covariance matrix of $\mathbf{r}^{ik}$

$\mathbf{R}_{\text{slow}}^{ik}$ $M \times M$ covariance matrix of $\mathbf{v}^{ik}$

$\mathbf{R}_{\boldsymbol{\alpha}}^{ik}$ $M \times M$ covariance matrix of $\boldsymbol{\alpha}^{ik}$

$\mathbf{R}_{\mathbf{y}}$ $M \times M$ slow-time covariance matrix of received symbols

$\mathbf{R}_n$ $M \times M$ slow-time covariance matrix of the fast-time processed samples

$\mathbf{R}_s$ $M \times M$ slow-time covariance matrix of the received SoI samples

$\mathbf{S}'$ $N \times M$ received UE data matrix

$\mathbf{S}$ $N \times M$ received UE data matrix after preprocessing

$\mathbf{s}'_n$ $M \times 1$ UE data vector at n^{th} subcarrier before OFDM demodulation

$\mathbf{u}_m$ m^{th} column of $M \times M$ windowed DFT matrix

$\mathbf{U}_N$ $N \times N$ Windowed DFT matrix

$\mathbf{u}_n$ n^{th} column of $N \times N$ windowed DFT matrix

$\mathbf{v}^{ik}$ $M \times 1$ slow-time return vector from k^{th} scatterer of i^{th} target

$\mathbf{W}_M$ $M \times M$ diagonal Hamming window matrix

$\mathbf{W}_N$ $N \times N$ diagonal Hamming window matrix

$\mathbf{X}$ $N \times M$ transmitted frequency domain symbol matrix

$\mathbf{x}_n$ $M \times 1$ transmitted symbol vector at n^{th} subcarrier after OFDM modulation

$\mathbf{Y}'$ $N \times M$ received frequency domain symbol matrix

$\mathbf{Y}$ $N \times M$ estimated frequency domain symbol matrix

$\mathbf{y}'_n$ $M \times 1$ received symbol vector at n^{th} subcarrier before OFDM demodulation

$\mathbf{Y}^{(t)}$ $\mathbf{Y}$ matrix in $(t)^{\text{th}}$ frame

$\mathbf{Z}$ $N \times M$ output of fast-time processing

$\mathbf{z}_n$ $M \times 1$ transpose of n^{th} row of $\mathbf{Z}$

$\mathcal{I}$ # of scattering targets

$\mathcal{K}^{(i)}$ # of scatterers of i^{th} target

$\mathcal{L}$ # of frames for sample averaging

$\phi_{(n,m)}$ Decision metric at n^{th} subcarrier in m^{th} OFDM symbol

$\phi^{(t)}_{(n,m)}$ $\phi_{(n,m)}$ variable in $(t)^{\text{th}}$ frame

$\psi^{\text{KA-GLRT}}_{(n,m)}$ $\psi_{(n,m)}$ variable for KA-GLRT method

$\psi^{\text{Perio}}_{(n,m)}$ $\psi_{(n,m)}$ variable for 2D Periodogram method

σ^{ik} Doppler spread of k^{th} scatterer of i^{th} target (in m/s)

σ_0^2 Average power of the returns from the IT

σ_i^2 Average power of the returns from i^{th} target

σ_s^2 SoI sample variance

i Index of scattering targets

k Index of scatterer points inside a target

l_i Length of i^{th} target

r_i Range of the center of i^{th} target

v_i Radial velocity of i^{th} target

$\mathbf{d}_m$ $M \times 1$ slow-time steering vector at m^{th} Doppler bin

r^{ik} Range of the k^{th} scatterer of i^{th} target

v^{ik} Radial velocity of the k^{th} scatterer of i^{th} target

Chapter 4

$\bar{\mathbf{x}}_{nm}$ $N_t \times 1$ transmitted symbol vector at n^{th} subcarrier and m^{th} OFDM symbol

$\bar{\mathbf{y}}_{nm}$ $N_r \times 1$ received symbol vector at n^{th} subcarrier and m^{th} OFDM symbol

$\boldsymbol{\eta}_n$ $D_r D_t \times 1$ vectorization of preprocessed interference matrix at n^{th} subcarrier

$\mathbf{\Lambda}_u^{\mathcal{S}}$ $M \times M$ diagonal Doppler spread matrix of the u^{th} UE

$\boldsymbol{\omega}_n$ $D_r D_t \times 1$ MIMO processing filter at n^{th} subcarrier

$\boldsymbol{\phi}_n$ $D_r D_t \times 1$ vectorization of preprocessed return matrix of the IT at n^{th} subcarrier

$\mathbf{\Sigma}^{\boldsymbol{\eta}}$ $N \times N$ temporal covariance matrix of the preprocessed interference

$\boldsymbol{\Sigma}^{\boldsymbol{\phi}}$ $N \times N$ temporal covariance matrix of the preprocessed IT signal

γ_{th} Detection threshold

$\gamma_{th}^{(t)}$ Detection threshold in $(t)^{\text{th}}$ frame

γ_{load} Diagonal loading factor

$\hat{\boldsymbol{\Sigma}}$ $N \times N$ SA estimate of $\boldsymbol{\Sigma}^{\boldsymbol{\eta}}$

$\hat{\mathbf{R}}_n^{\boldsymbol{\eta}}$ $D_r D_r \times D_r D_t$ SA estimate of $\mathbf{R}_n^{\boldsymbol{\eta}}$

$\hat{\mathbf{R}}_{n'}^{\boldsymbol{\eta}}$ $D_r D_r \times D_r D_t$ SA estimate of preprocessed interference covariance in the $(n')^{\text{th}}$ subband

$\mathbf{A}_k$ $N \times N$ temporal covariance matrix of k^{th} scatterer when range response is separated

$\mathbf{D}^{\boldsymbol{\eta}}$ $D_r D_r \times D_r D_t$ diagonal loading matrix for $\hat{\mathbf{R}}_n^{\boldsymbol{\eta}}$

$\mathbf{D}^{\mathbf{r}}$ $N \times N$ diagonal loading matrix for $\hat{\boldsymbol{\Sigma}}$

$\mathbf{p}_n$ $D_r D_t \times 1$ angular steering vector at n^{th} subcarrier

$\mathbf{q}$ $N \times 1$ temporal steering vector

$\mathbf{q}_k^{\mathcal{C}}$ $N \times 1$ temporal steering vector towards k^{th} scatterer

$\mathbf{r}$ $N \times 1$ fast-time vector of observations after MIMO processing

$\mathbf{r}^{(t)}$ $N \times 1$ fast-time vector of observations after MIMO processing in $(t)^{\text{th}}$ frame

$\mathbf{R}_k^{\boldsymbol{\alpha}}$ $M \times M$ covariance matrix of $\boldsymbol{\alpha}_k$

$\mathbf{R}_u^{\boldsymbol{\beta}}$ $M \times M$ covariance matrix of $\boldsymbol{\beta}_u$

$\mathbf{R}_n^{\boldsymbol{\eta}}$ $D_r D_t \times D_r D_t$ angular covariance matrix of the preprocessed interference at n^{th} subcarrier

$\mathbf{R}_{n_1 n_2}^{\boldsymbol{\eta}}$ $D_r D_t \times D_r D_t$ angular cross-covariance matrix of the preprocessed interference between n_1^{th} and n_2^{th} subcarriers

$\mathbf{R}_n^{\boldsymbol{\psi}}$ $D_r M \times D_r M$ angular covariance matrix of the raw interference at n^{th} subcarrier

$\mathbf{R}_{n_1 n_2}^{\boldsymbol{\psi}}$ $D_r M \times D_r M$ angular cross-covariance matrix of the raw interference between n_1^{th} and n_2^{th} subcarriers

$\mathbf{u}$ $N \times 1$ fast-time processing filter

$\mathbf{W}_r$ $N_r \times D_r$ receive beamforming matrix

$\mathbf{W}_t$ $N_t \times D_t$ transmit beamforming matrix

$\mathcal{K}$ # of total scatterers in the scenario

$\mathcal{T}$ # of frames in the simulations

$\mathcal{U}$ # of total UEs in the scenario

$\mathcal{V}_1$ Variant-1 detector

$\mathcal{V}_2$ Variant-2 detector

$\overline{\mathbf{\Sigma}^{\boldsymbol{\eta}}}$ Expectation of $\mathbf{\Sigma}^{\boldsymbol{\eta}}$ over all $\mathbf{X}_n$s

$\overline{\mathbf{R}_n^{\boldsymbol{\eta}}}$ Expectation of $\mathbf{R}_n^{\boldsymbol{\eta}}$ over $\mathbf{X}_n$

$\overline{\mathbf{R}_{n_1 n_2}^{\boldsymbol{\eta}}}$ Expectation of $\mathbf{R}_{n_1 n_2}^{\boldsymbol{\eta}}$ over $\mathbf{X}_{n_1}$ and $\mathbf{X}_{n_2}$

$\rho_k^{\mathcal{C}}$ Doppler frequency of k^{th} scatterer

$\rho_u^{\mathcal{S}}$ Doppler frequency of u^{th} UE

τ_k Round-trip time for k^{th} scatterer

$\tilde{\theta}$ Angle bin index

$\tilde{m}$ Doppler bin index

$\tilde{n}$ Range bin index

$\xi^{(t)}$ Scalar detection metric in $(t)^{\text{th}}$ frame

d Inter-element spacing in the antenna arrays

j_{unm} Transmitted SoI data from u^{th} UE at n^{th} subcarrier and m^{th} OFDM symbol

n' Subband index

r_k Range of k^{th} scatterer

u UE index

v_k Radial velocity of k^{th} scatterer

$\boldsymbol{\alpha}_k$ $M \times 1$ reflected complex gain vector from k^{th} scatterer

$\boldsymbol{\beta}_u$ $M \times 1$ reflected complex gain vector from u^{th} UE

$\mathbf{\Lambda}_0^{\mathcal{C}}$ $M \times M$ diagonal Doppler spread matrix of the IT

$\mathbf{\Lambda}_k^{\mathcal{C}}$ $M \times M$ diagonal Doppler spread matrix of the k^{th} scatterer

$\boldsymbol{\psi}_{nm}$ $D_r \times 1$ received stream vector from the total interference at n^{th} subcarrier and m^{th} OFDM symbol

$\boldsymbol{\Psi}_n$ $D_r \times M$ received stream matrix from the total interference at n^{th} subcarrier

$\hat{\mathbf{H}}_n$ $D_r \times D_t$ output of DACB at n^{th} subcarrier

$\mathbf{a}_{kn}$ $N_r \times 1$ receive steering vector towards k^{th} scatterer at n^{th} subcarrier

$\mathbf{a}_n(\theta)$ $N_r \times 1$ arbitrary steering vector towards angle θ

$\mathbf{a}_{un}$ $N_r \times 1$ receive steering vector towards u^{th} UE at n^{th} subcarrier

$\mathbf{b}_{kn}$ $N_t \times 1$ transmit steering vector towards k^{th} scatterer at n^{th} subcarrier

$\mathbf{C}_{kn}$ $D_r \times M$ received stream matrix from the k^{th} scatterer at n^{th} subcarrier

$\mathbf{c}_{nm}$ $D_r \times 1$ received stream vector from the clutter at n^{th} subcarrier and m^{th} OFDM symbol

$\mathbf{C}_n$ $D_r \times M$ received stream matrix from the clutter at n^{th} subcarrier

$\mathbf{D}_{\tilde{m}}$ $M \times M$ diagonal Doppler filter at the $\tilde{m}^{\text{th}}$ Doppler bin

$\mathbf{D}_k^{\mathcal{C}}$ $M \times M$ diagonal Doppler phase matrix of the k^{th} scatterer

$\mathbf{D}_u^{\mathcal{S}}$ $M \times M$ diagonal Doppler phase matrix of the u^{th} UE

$\mathbf{g}_{unm}$ $D_r \times 1$ angle-range-Doppler channel vector from u^{th} UE at n^{th} subcarrier and m^{th} OFDM symbol

$\mathbf{g}_{un}$ $D_r \times 1$ angle-range channel matrix from u^{th} UE at n^{th} subcarrier

$\mathbf{H}_{0nm}$ $D_r \times D_t$ angle-range-Doppler channel matrix from the IT at n^{th} subcarrier and m^{th} OFDM symbol

$\mathbf{H}_{knm}$ $D_r \times D_t$ angle-range-Doppler channel matrix from k^{th} scatterer at n^{th} subcarrier and m^{th} OFDM symbol

$\mathbf{H}_{kn}$ $D_r \times D_t$ angle-range channel matrix from k^{th} scatterer at n^{th} subcarrier

$\mathbf{J}_n$ $\mathcal{U} \times M$ transmit stream matrix of the UEs at n^{th} subcarrier

$\mathbf{j}_{un}$ $M \times 1$ transmit stream vector of the u^{th} UE at n^{th} subcarrier

$\mathbf{n}_{nm}$ $D_r \times 1$ noise vector at the receiver at n^{th} subcarrier and m^{th} OFDM symbol

$\mathbf{N}_n$ $D_r \times M$ noise matrix at the receiver at n^{th} subcarrier

$\mathbf{s}_{nm}$ $D_r \times 1$ received stream vector from the UEs at n^{th} subcarrier and m^{th} OFDM symbol

$\mathbf{S}_n$ $D_r \times M$ received stream matrix from the UEs at n^{th} subcarrier

$\mathbf{S}_{un}$ $D_r \times M$ received stream matrix from the u^{th} UE at n^{th} subcarrier

$\mathbf{t}_{nm}$ $D_r \times 1$ received stream vector from the IT at n^{th} subcarrier and m^{th} OFDM symbol

$\mathbf{T}_n$ $D_r \times M$ received stream matrix from the IT at n^{th} subcarrier

$\mathbf{V}_n$ $M \times D_t$ DACB matrix at n^{th} subcarrier

$\mathbf{x}_{nm}$ $D_t \times 1$ transmitted stream vector at n^{th} subcarrier and m^{th} OFDM symbol

$\mathbf{X}_n$ $D_r \times M$ transmit stream matrix at n^{th} subcarrier

$\mathbf{Y}^{(t)}$ $D_r \times M \times N$ received stream cube in $(t)^{\text{th}}$ frame

$\mathbf{y}_{nm}$ $D_r \times 1$ received stream vector at n^{th} subcarrier and m^{th} OFDM symbol

$\mathbf{Y}_n$ $D_r \times M$ received stream matrix at n^{th} subcarrier

$\mathbf{Y}_n^{(t)}$ $D_r \times M$ received stream matrix at n^{th} subcarrier in $(t)^{\text{th}}$ frame

$\mathbf{Z}_n$ $D_r \times D_t$ output of DACB at n^{th} subcarrier

$\mathbf{z}_n$ $D_r D_t \times 1$ vectorized output of DACB at n^{th} subcarrier

$\mathbf{z}_n^{(t)}$ $D_r D_t \times 1$ vectorized output of DACB at n^{th} subcarrier in $(t)^{\text{th}}$ frame

$\overline{\mathbf{V}}_n$ $MD_r \times D_t D_r$ effective DACB matrix at n^{th} subcarrier

k Scatterer index

T_f Frame duration

α_{km} Reflected complex gain from k^{th} scatterer at m^{th} OFDM symbol

β_{um} Received complex gain from u^{th} UE at m^{th} OFDM symbol

$\gamma_k^{\mathcal{C}}$ Average power of the echoes of k^{th} scatterer

$\gamma_u^{\mathcal{S}}$ Average power of the received signal from u^{th} UE

Chapter 5

$\alpha_{\star m}^{(i,j)}$ Mean Doppler shift and random complex phase of the echoes of the IT in the m^{th} OFDM symbol between $(i,j)^{\text{th}}$ Rx-Tx pair

$\alpha_{km}^{(i,j)}$ Mean Doppler shift and random complex phase of the echoes of k^{th} scatterer in the m^{th} OFDM symbol between $(i,j)^{\text{th}}$ Rx-Tx pair

$\bar{\alpha}_{\star m}^{(i,j)}$ Deterministic mean Doppler shift part in $\alpha_{\star m}^{(i,j)}$

$\bar{\alpha}_{km}^{(i,j)}$ Deterministic mean Doppler shift part in $\alpha_{km}^{(i,j)}$

$\boldsymbol{\alpha}_{\star}^{(i,j)}$ $M \times 1$ vector of $\alpha_{\star m}^{(i,j)}$ variables

$\boldsymbol{\alpha}_{k}^{(i,j)}$ $M \times 1$ vector of $\alpha_{km}^{(i,j)}$ variables

$\boldsymbol{\eta}^{(i,j)}$ $D_r D_t \times 1$ vectorization of $\boldsymbol{\Gamma}^{(i,j)}$ matrix

$\boldsymbol{\Gamma}^{(i,j)}$ $D_r \times D_t$ preprocessed interference matrix between $(i,j)^{\text{th}}$ Rx-Tx pair

$\boldsymbol{\omega}^{(i,j)}$ $D_r D_t \times 1$ max-SINR MIMO processing filter between $(i,j)^{\text{th}}$ Rx-Tx pair

$\boldsymbol{\Psi}^{(i)}$ $D_r \times MN$ Rx interference matrix at the i^{th} Rx array

$\boldsymbol{\psi}_{nm}^{(i)}$ $D_r \times 1$ received interference vector at i^{th} receiver at n^{th} subcarrier and m^{th} symbol

$\boldsymbol{\Psi}_{n}^{(i)}$ $D_r \times M$ Rx interference matrix at the i^{th} Rx array at n^{th} subcarrier

$\boldsymbol{\rho}_{\star}^{(i,j)}$ $N \times 1$ vector of $\rho_{\star n}^{(i,j)}$ variables

$\boldsymbol{\rho}_{k}^{(i,j)}$ $N \times 1$ vector of $\rho_{kn}^{(i,j)}$ variables

$\tilde{\boldsymbol{\alpha}}_{k}^{(i,j)}$ $M \times 1$ random complex phase vector of the k^{th} scatterer between $(i,j)^{\text{th}}$ Rx-Tx pair

δ Kronecker delta function

$\Delta\gamma^{(i,j)}$ Power difference parameter between $(i,j)^{\text{th}}$ Rx-Tx pair

$\dot{\boldsymbol{\omega}}^{(i,j)}$ $D_r D_t \times 1$ MIMO processing filter of 3D Periodogram detector between $(i,j)^{\text{th}}$ Rx-Tx pair

$\dot{\mathbf{p}}$ 2×1 cartesian velocity vector

$\dot{\mathbf{p}}_{\star}$ 2×1 velocity vector of the IT

$\dot{\mathbf{R}}_{\boldsymbol{\eta}}^{(i,j)}$ $D_r D_t \times D_r D_t$ matrix equal to $\mathbf{I}_{D_r D_t}$

$\dot{\mathbf{z}}_{\star}^{(i,j)}$ $D_r D_t \times 1$ windowed angular steering vector of the IT for 3D Periodogram detector

$\dot{\xi}^{(i,j)}$ Scalar detection metric of 3D Periodogram detector between $(i,j)^{\text{th}}$ Rx-Tx pair

$\dot{x}$ Rate of change of x-coordinate value

$\dot{x}_{\star}$ Rate of change of x-coordinate value of the IT

$\dot{x}_{k}$ Rate of change of x-coordinate value of k^{th} scatterer

$\dot{y}$ Rate of change of y-coordinate value

$\dot{y}_\star$ Rate of change of y-coordinate value of the IT

$\dot{y}_k$ Rate of change of y-coordinate value of k^{th} scatterer

γ_{RCS} RCS of a scatterer (in general)

γ_{ref} Reference power for multistatic scenario

$\gamma_0^{(i,j)}$ Average power of the LOS path between $(i,j)^{\text{th}}$ Rx-Tx pair

$\gamma_\star^{(i,j)}$ Average power of the echoes from the IT between $(i,j)^{\text{th}}$ Rx-Tx pair

$\gamma_k^{(i,j)}$ Average power of the echoes from the k^{th} scatterer between $(i,j)^{\text{th}}$ Rx-Tx pair

$\hat{\boldsymbol{\omega}}^{(i,j)}$ $D_rD_t \times 1$ MIMO processing filter of AMF-SAAP detector between $(i,j)^{\text{th}}$ Rx-Tx pair

$\hat{\hat{\boldsymbol{\omega}}}^{(i,j)}$ $D_rD_t \times 1$ MIMO processing filter of AMF-SABP detector between $(i,j)^{\text{th}}$ Rx-Tx pair

$\hat{\hat{\mathbf{D}}}^{(i,j)}$ $D_rD_t \times D_rD_t$ diagonal loading matrix for the estimation in AMF-SABP detector

$\hat{\hat{\mathbf{R}}}_{\boldsymbol{\eta}}^{(i,j)}$ $D_rD_t \times D_rD_t$ estimate of $\mathbf{R}_{\boldsymbol{\eta}}^{(i,j)}$ for AMF-SABP detector

$\hat{\hat{\xi}}^{(i,j)}$ Scalar detection metric of AMF-SABP detector between $(i,j)^{\text{th}}$ Rx-Tx pair

$\hat{\mathbf{D}}^{(i,j)}$ $D_rD_t \times D_rD_t$ diagonal loading matrix for the estimation in AMF-SAAP detector

$\hat{\mathbf{H}}^{(i)}$ $D_r \times \mathcal{J}D_t$ block matrix of $\hat{\mathbf{H}}^{(i,j)}$ matrices

$\hat{\mathbf{H}}^{(i,j)}$ $D_r \times D_t$ angular channel estimate between $(i,j)^{\text{th}}$ Rx-Tx pair

$\hat{\mathbf{h}}^{(i,j)}$ $D_rD_t \times 1$ vectorization of $\hat{\mathbf{H}}^{(i,j)}$

$\hat{\mathbf{H}}_\star^{(i,j)}$ $D_r \times D_t$ angular channel estimate of the IT between $(i,j)^{\text{th}}$ Rx-Tx pair

$\hat{\mathbf{R}}_{\boldsymbol{\eta}}^{(i,j)}$ $D_rD_t \times D_rD_t$ estimate of $\mathbf{R}_{\boldsymbol{\eta}}^{(i,j)}$ for AMF-SAAP detector

$\hat{\xi}^{(i,j)}$ Scalar detection metric of AMF-SAAP detector between $(i,j)^{\text{th}}$ Rx-Tx pair

$\hat{\zeta}_\star^{(i,j)}$ ML estimate of $\zeta_\star^{(i,j)}$

$\jmath$ Imaginary unit

$\mathbf{a}_0^{(i)}$ $N_r \times 1$ receive steering vector from the i^{th} Rx array to the LOS tx array

$\mathbf{a}_k^{(i)}$ $N_r \times 1$ receive steering vector from the i^{th} Rx array to the k^{th} scatterer

$\mathbf{B}$ $\mathcal{J}D_t \times \mathcal{J}D_t$ intermediate matrix for cross-transmitter effects

$\mathbf{B}_{j_1}^{(j_2)}$ $D_t \times D_t$ block inside $\mathbf{B}$ indexed with j_1 and j_2

$\mathbf{b}_0^{(j)}$ $N_t \times 1$ transmit steering vector from the j^{th} Tx array to the LOS Rx array

$\mathbf{b}_k^{(j)}$ $N_t \times 1$ transmit steering vector from the j^{th} Tx array to the k^{th} scatterer

$\mathbf{D}_{\bar{\alpha}_\star}^{(i,j)}$ $M \times M$ diagonal matrix of $\bar{\alpha}_{\star m}^{(i,j)}$ variables

$\mathbf{D}_{\rho\alpha_\star}^{(i)}$ $\mathcal{J}MN \times MN$ block matrix of $\mathbf{D}_{\rho\alpha_\star}^{(i,j)}$ matrices

$\mathbf{D}_{\rho\alpha_\star}^{(i,j)}$ $MN \times MN$ diagonal matrix of $\rho_{kn}^{(i,j)}$ and $\alpha_{\star m}^{(i,j)}$ variables

$\mathbf{D}_{\rho\alpha_k}^{(i)}$ $\mathcal{J}MN \times MN$ block matrix of $\mathbf{D}_{\rho\alpha_k}^{(i,j)}$ matrices

$\mathbf{D}_{\rho\alpha_k}^{(i,j)}$ $MN \times MN$ diagonal matrix of $\rho_{kn}^{(i,j)}$ and $\alpha_{km}^{(i,j)}$ variables

$\mathbf{D}_{\rho\bar{\alpha}_\star}^{(i)}$ $\mathcal{J}MN \times MN$ block matrix of $\mathbf{D}_{\rho\bar{\alpha}_\star}^{(i,j)}$ matrices

$\mathbf{D}_{\rho\bar{\alpha}_\star}^{(i,j)}$ $MN \times MN$ diagonal matrix of $\rho_{kn}^{(i,j)}$ and $\bar{\alpha}_{\star m}^{(i,j)}$ variables

$\mathbf{D}_{\rho_\star}^{(i,j)}$ $N \times N$ diagonal matrix of $\rho_{\star n}^{(i,j)}$ variables

$\mathbf{D}_{\rho_k}^{(i,j)}$ $N \times N$ diagonal matrix of $\rho_{kn}^{(i,j)}$ variables

$\mathbf{D}_{w_r}$ $N_r \times N_r$ diagonal window matrix for receive beamformer

$\mathbf{D}_{w_t}$ $N_t \times N_t$ diagonal window matrix for transmit beamformer

$\mathbf{D}_{\alpha_\star}^{(i,j)}$ $M \times M$ diagonal matrix of $\alpha_{\star m}^{(i,j)}$ variables

$\mathbf{D}_{\alpha_k}^{(i,j)}$ $M \times M$ diagonal matrix of $\alpha_{km}^{(i,j)}$ variables

$\mathbf{N}^{(i)}$ $D_r \times MN$ noise matrix at the i^{th} Rx array

$\mathbf{n}_{nm}^{(i)}$ $D_r \times 1$ noise vector at i^{th} receiver at n^{th} subcarrier and m^{th} symbol

$\mathbf{N}_n^{(i)}$ $D_r \times M$ noise matrix at the i^{th} Rx array at n^{th} subcarrier

$\mathbf{p}$ 2×1 cartesian position vector

$\mathbf{p}_\star$ 2×1 position vector of the IT

$\mathbf{p}_{\text{ref}}$ 2×1 position vector of the reference point for multistatic scenario

$\mathbf{p}_k$ 2×1 cartesian position vector of k^{th} scatterer

$\mathbf{p}_r^{(i_u)}$ 2×1 position vector of u^{th} antenna in the i^{th} Rx array

$\mathbf{p}_r^{(i_u)}$ 2×1 position vector of the center of the i^{th} Rx array

$\mathbf{p}_t^{(j_v)}$ 2×1 position vector of v^{th} antenna in the j^{th} Tx array

$\mathbf{p}_t^{(j_v)}$ 2×1 position vector of the center of the j^{th} Tx array

$\mathbf{R}_{\boldsymbol{\psi} n}^{(i)}$ $D_r M \times D_r M$ angular covariance matrix of the raw interference at i^{th} Rx array at n^{th} subcarrier

$\mathbf{R}_{\eta}^{(i,j)}$ $D_r D_t \times D_r D_t$ covariance matrix of $\boldsymbol{\eta}^{(i,j)}$

$\mathbf{R}_{\psi n_1 n_2}^{(i)}$ $D_r M \times D_r M$ angular cross-covariance matrix of the raw interference at i^{th} Rx array between n_1^{th} and n_2^{th} subcarriers

$\mathbf{V}_{nj'}^{(i,j)}$ $M \times D_t$ preprocessing matrix between $(i,j)^{\text{th}}$ Rx-Tx pair stemming from $(j')^{\text{th}}$ Tx array at n^{th} subcarrier

$\mathbf{W}_r^{(i)}$ $N_r \times D_r$ receive beamforming matrix of the i^{th} Rx array

$\mathbf{W}_t^{(j)}$ $N_t \times D_t$ transmit beamforming matrix of the j^{th} Tx array

$\mathbf{X}$ $\mathcal{J} D_t \times \mathcal{J} M N$ Tx stream matrix from all Tx arrays

$\mathbf{X}^{(j)}$ $D_t \times MN$ Tx stream matrix from the j^{th} Tx array

$\mathbf{x}_{nm}^{(j)}$ $D_t \times 1$ Tx stream vector from the j^{th} transmitter at n^{th} subcarrier and m^{th} symbol

$\mathbf{X}_n^{(j)}$ $D_t \times M$ Tx stream matrix from the j^{th} Tx array at n^{th} subcarrier

$\mathbf{Y}^{(i)}$ $D_r \times MN$ Rx stream matrix at the i^{th} Rx array

$\mathbf{Y}_{\star}^{(i)}$ $D_r \times MN$ Rx stream matrix from the IT at the i^{th} Rx array

$\mathbf{Y}_{n\star}^{(i)}$ $D_r \times M$ Rx stream matrix from the IT at the i^{th} Rx array at n^{th} subcarrier

$\mathbf{y}_{nm\star}^{(i)}$ $D_r \times 1$ Rx stream vector of the i^{th} receiver from the IT at n^{th} subcarrier and m^{th} symbol

$\mathbf{y}_{nm}^{(i)}$ $D_r \times 1$ Rx stream vector of the i^{th} receiver at n^{th} subcarrier and m^{th} symbol

$\mathbf{Y}_n^{(i)}$ $D_r \times M$ Rx stream matrix at the i^{th} Rx array at n^{th} subcarrier

$\mathbf{z}_{\star}^{(i,j)}$ $D_r D_t \times 1$ vectorization of $\hat{\mathbf{H}}_{\star}^{(i,j)}$

$\mathcal{I}$ # of receive antenna arrays

$\mathcal{J}$ # of transmit antenna arrays

$\mathcal{K}$ # of UIT scatterers

$\overline{\boldsymbol{\omega}}^{(i,j)}$ $D_r D_t \times 1$ MIMO processing filter of Expected X detector between $(i,j)^{\text{th}}$ Rx-Tx pair

$\overline{\mathbf{R}}_{\boldsymbol{\eta}}^{(i,j)}$ $D_rD_t \times D_rD_t$ expectation of $\mathbf{R}_{\boldsymbol{\eta}}^{(i,j)}$ over $\mathbf{X}$

$\overline{\mathbf{R}}_{\boldsymbol{\psi} n_1 n_2}^{(i)}$ $D_rM \times D_rM$ expectation of $\mathbf{R}_{\psi n_1 n_2}^{(i)}$

$\overline{\mathbf{V}}_{nj'}^{(i,j)}$ $D_rM \times D_rD_t$ intermediate matrix for preprocessing operation

$\overline{\xi}^{(i,j)}$ Scalar detection metric of Expected X detector between $(i,j)^{\text{th}}$ Rx-Tx pair

$\rho_{0n}^{(i,j)}$ Phase shift due to the LOS path between $(i,j)^{\text{th}}$ Rx-Tx pair at n^{th} subcarrier

$\rho_{\star n}^{(i,j)}$ The deterministic complex phase at the n^{th} subcarrier from the j^{th} Tx array to the IT to the i^{th} Rx array

$\rho_{kn}^{(i,j)}$ The deterministic complex phase at the n^{th} subcarrier from the j^{th} Tx array to the k^{th} scatterer to the i^{th} Rx array

$\tau_{r,k}^{(i_u)}$ Trip-time from the k^{th} scatterer to the u^{th} antenna of the i^{th} Rx array

$\tau_{t,k}^{(j_v)}$ Trip-time from the v^{th} antenna of the j^{th} Tx array to the k^{th} scatterer

$\tau_{\star}^{(i_u,j_v)}$ Total trip-time from the v^{th} antenna of the j^{th} Tx array to the IT to the u^{th} antenna of the i^{th} Rx array

$\tau_{k}^{(i_u,j_v)}$ Total trip-time from the v^{th} antenna of the j^{th} Tx array to the k^{th} scatterer to the u^{th} antenna of the i^{th} Rx array

$\tilde{\alpha}_{\star m}^{(i,j)}$ Random complex phase part in $\alpha_{\star m}^{(i,j)}$

$\tilde{\alpha}_{\star}^{(i,j)}$ A variable equal to $\tilde{\alpha}_{\star m}^{(i,j)}$

$\tilde{\alpha}_{km}^{(i,j)}$ Random complex phase part in $\alpha_{km}^{(i,j)}$

ξ Joint GLRT statictic

$\xi^{(i,j)}$ Scalar detection metric of max-SINR detector between $(i,j)^{\text{th}}$ Rx-Tx pair

d Custom distance function

i Receiver index

j Transmitter index

k Scatterer index

L CUT window length for AMF-SAAP detector

u Receive antenna index in a receive antenna array

v Transmit antenna index in a transmit antenna array

x x-coordinate value

$x_\star$ x-coordinate value of the IT

x_k x-coordinate value of k^{th} scatterer

$x_r^{(i_u)}$ x-coordinate value of u^{th} antenna in the i^{th} Rx array

$x_r^{(i_u)}$ x-coordinate value of the center of the i^{th} Rx array

$x_t^{(j_v)}$ x-coordinate value of v^{th} antenna in the j^{th} Tx array

$x_t^{(j_v)}$ x-coordinate value of the center of the j^{th} Tx array

y y-coordinate value

$y_\star$ y-coordinate value of the IT

y_k y-coordinate value of k^{th} scatterer

$y_r^{(i_u)}$ y-coordinate value of u^{th} antenna in the i^{th} Rx array

$y_r^{(i_u)}$ y-coordinate value of the center of the i^{th} Rx array

$y_t^{(j_v)}$ y-coordinate value of v^{th} antenna in the j^{th} Tx array

$y_t^{(j_v)}$ y-coordinate value of the center of the j^{th} Tx array

$\dot{p}_k^{(i_u,j_v)}$ Rate of increase of the total distance from the v^{th} antenna of the j^{th} Tx array to the k^{th} scatterer to the u^{th} antenna of the i^{th} Rx array

$\dot{p}_{r,k}^{(i_u)}$ Rate of increase of the distance between the u^{th} antenna of the i^{th} Rx array and k^{th} scatterer

$\dot{p}_{t,k}^{(j_v)}$ Rate of increase of the distance between the v^{th} antenna of the j^{th} Tx array and k^{th} scatterer

$\mathbf{H}_{\star nm}^{(i,j)}$ $D_r \times D_t$ angle-range-Doppler channel matrix from the IT at n^{th} subcarrier and m^{th} OFDM symbol between $(i,j)^{\text{th}}$ Rx-Tx pair

$\mathbf{H}_\star^{(i,j)}$ $D_r \times D_t$ angular channel matrix from the IT between $(i,j)^{\text{th}}$ Rx-Tx pair

$\mathbf{H}_{knm}^{(i,j)}$ $D_r \times D_t$ angle-range-Doppler channel matrix from k^{th} scatterer at n^{th} subcarrier and m^{th} OFDM symbol between $(i,j)^{\text{th}}$ Rx-Tx pair

$\mathbf{H}_k^{(i,j)}$ $D_r \times D_t$ angular channel matrix from k^{th} scatterer between $(i,j)^{\text{th}}$ Rx-Tx pair

$\mathbf{R}_k^{\tilde{\boldsymbol{\alpha}}^{(i,j)}}$ $M \times M$ covariance matrix of $\tilde{\boldsymbol{\alpha}}_k^{(i,j)}$

$\zeta_\star^{(i,j)}$ Unknown nonrandom complex gain parameter of the IT

CHAPTER 1

INTRODUCTION

Integrated sensing and communication (ISAC) systems have emerged as a promising paradigm that enables the joint use of hardware, spectrum, and signal resources for both communication and sensing functionalities. Among various waveform and system design alternatives, monostatic and multistatic multiple-input multiple-output (MIMO) radar architectures have gained increasing attention due to their flexibility and high spatial resolution. This thesis investigates the development of efficient signal processing techniques and detectors tailored for such ISAC systems, aiming to improve sensing performance under realistic interference models and system parameters. The study places particular emphasis on overcoming the limitations of conventional processing methods when applied to practical MIMO ISAC scenarios.

The rest of this chapter starts with a review of the relevant literature, especially focusing on the motivation of ISAC, different variants of ISAC usage, orthogonal frequency-division multiplexing (OFDM)-based ISAC systems, MIMO ISAC architectures, and multistatic ISAC applications. This is followed by a discussion of the motivation behind this study and a summary of the contributions made in this thesis. The chapter concludes with an outline of the overall thesis structure and a description of the notation and conventions used throughout the document.

1.1 Literature Review

In this section, the scientific literature on ISAC systems will be reviewed from various points of view under different subsections.

1.1.1 Motivation Behind ISAC Systems

The ever-increasing demand for high data rates, ultra-reliable low-latency communication, and massive device connectivity has resulted in a significant increase in the need for larger bandwidths in modern wireless networks [1–3]. With the rise of fifth-generation (5G) communication standards, millimeter-wave (mm-wave) systems have been used commonly to meet these demands [4, 5], and looking ahead to sixth-generation (6G) communications, solutions like massively distributed antenna systems, reconfigurable intelligent surfaces (RIS) and terahertz (THz) communication is being actively explored [6–14]. However, even with these technological advancements in available bandwidth, the radio frequency (RF) spectrum remains a scarce and valuable resource. Traditionally, radar and communication systems have operated in separate frequency bands using independent hardware platforms. This separation, while functional up to the present, results in inefficient spectrum usage and increased hardware complexity.

In recent years, ISAC has emerged as a promising phenomenon to address these challenges by enabling the joint use of spectral and hardware resources for both radar sensing and data communication. ISAC proposes the use of the same waveform, frequency band, and device architecture for both communication and radar purposes simultaneously, instead of allocating distinct frequency bands and devices for each function. This approach improves spectral efficiency, reduces system costs, and facilitates coordination between sensing and communication tasks in several applications [15–24].

The potential applications of ISAC systems span a wide range of areas, especially where both reliable communication and environmental awareness are important. Autonomous driving is one of such domains [25–27], as the vehicles should both communicate with road-side units and at the same time sense their environments for potential risks. Similarly, the road-side units can warn the vehicles about potential hazards or update their information about the traffic by utilizing sensing and communication with the same infrastructure [28, 29]. ISAC systems can also be useful in drone applications where the drones are controlled by the operators or communicate between each other with high-reliability communication and sense any kind of ground

or flying objects simultaneously [30–36]. In urban areas, ISAC systems can sense the presence of humans or animals or track their movement patterns to enable energy-efficient lighting or enhance environmental security, while providing uninterrupted communication service. Integrating sensing capabilities into indoor communication systems may be useful in emergency situations like fire or earthquake, as the ISAC systems can detect both the movement of people or animals inside the building and the blocked or unblocked escape routes, and send these information to individuals' mobile devices to dynamically manage their evacuation. These example scenarios show the wide range of potential applications of ISAC systems, which can be extended further to adapt to the needs of any real-life situation.

1.1.2 Characterizations and Functional Variants of ISAC

Based on the diverse application areas of ISAC systems, it is not surprising that there are several works on this topic in the literature using different names for the phenomenon. The most commonly used names are *Integrated Sensing and Communications (ISAC)*, *Joint Sensing and Communications (JSAC)*, *Joint Communications and Sensing (JCAS)*, Dual-Functional Radar-Communications (DFRC), and simply *RadCom*. Besides these systems that deliberately integrate radar and communication operations on the same device, there are other types of systems that use the already existing signals on the air to sense their environments while maintaining communication. Systems that utilize *Perceptive Mobile Networks (PMN)* are examples of such systems [37–43] and they can be considered to be integrating sensing and communication, in a different way than others. Other than the distinction in the names and sensing methods, there are *communication-centric* and *radar-centric* ISAC systems in the literature [16, 17, 44, 45]. Communication-centric systems' main focus is to sustain the communication while adding sensing capability with no or minimal effects to the communication performance. Conversely, radar-centric systems try to add communication utility to radar systems without disturbing the sensing operation. The focus of this work is on the systems that utilize communication-centric approach by using the transmitted communication waveform without any changes.

Given that the literature on ISAC is already crowded and continues to rapidly grow,

providing a comprehensive overview is beyond the scope of this thesis. Nevertheless, recent studies alone reflect the diversity and richness of the research in this area. In [46], ISAC using light signals is investigated through a wavelength-division duplexing scheme. In [47], the interference received by an ISAC system due to another noncooperative downlink (DL) base-station is mitigated and exploited to improve localization performance. In [48], the existing 5G New-Radio (NR) synchronization signal burst is used in a network-side ISAC system to achieve multiple target detection. Similarly in [49], positioning reference signals are used to detect high-speed trains near a 5G NR receiver. In [50], a deep neural network based processing scheme is proposed to enhance sensing performance in a cell-free MIMO system. [51] is a comprehensive work that suggests six different unique integration strategies to improve ISAC performance. In [52], a phase-configured reflecting plane is used with a communicating BS to construct a near-field image of an area using successive far-field acquisitions. Similarly in [53], extremely large-scale MIMO antennas and RIS are used for holographic sensing and imaging of an area with already existing communication waveforms. In [54], a neural network (NN)-based framework is utilized in a cell-free ISAC system to achieve maximum likelihood (ML) estimation performance for the angular parameters of possible targets in the sector of interest. In [55], ISAC schemes for both base-stations and user-equipments (UE) are proposed covering the features of different waveforms such as OFDM, orthogonal time-frequency-space (OTFS) and affine frequency-division multiplexing (AFDM). [56,57] tackle the problem of self-interference cancellation (SIC) in far-field and near-field full-duplex (FD) ISAC systems. [58] investigates the ISAC systems from the wireless security and privacy points of view. It should be noted that these studies are only a few examples of different functionalities of ISAC systems.

1.1.3 MIMO Architectures in ISAC systems

As can be seen from the numerous studies in the literature, ISAC is a key phenomenon for 5G and 6G networks. On the other hand, in the literature for 5G and 6G systems, mm-wave MIMO communications are also commonly focused due to the large communication band and high processing gain it provides. Therefore, the alignment of ISAC with MIMO technology is an important task to achieve. MIMO communication

systems basically supports simultaneous multi-user transmission-reception through multiple data streams, utilizing antenna arrays and orthogonality of waveforms to discriminate between different users [59]. MIMO systems are crucial for the present and future communication systems as they greatly increase spectral efficiency. On the other hand, MIMO radars are also a promising alternative for classical phased-array radar systems as they enable scanning a large angular sector of interest without losing antenna array gain, and enhance interference suppression by effectively utilizing transmit beamforming [60]. The relation between MIMO technology and both communication and radar areas makes the integration of MIMO architectures into ISAC systems a critical research direction [61–67].

As expected, there are several MIMO ISAC studies investigating sensing operation integrated into MIMO communication systems. In [67], separate two antennas are utilized for radar signal transmission while a large antenna array continues MIMO communication and sensing. In [68], a portion of the transmit (Tx) power is allocated for beam-scanning for radar detection. In [69], both transmit and receive (Rx) beamformers are optimized for sensing performance at a known target inside the cell under test. In [70], hybrid beamformers and compressive sensing are utilized for ISAC signal processing. In [71], radar detection is performed using the angle-sidelobes of the communication beams. These are only a few examples showing how different the MIMO ISAC approaches can be, mainly due to the large number of parameters, e.g. antenna and waveform structures, Tx and Rx beamformers, signal processing methods, etc. [72–79] are also valuable works about MIMO ISAC systems using OFDM waveforms, which will be investigated in the following subsection.

1.1.4 Motivation and Usage of OFDM in ISAC systems

In this thesis, efficient signal processing techniques are proposed for ISAC systems with MIMO architectures to enhance interference suppression and improve the probability of detecting a weak target around strong interfering sources. To ensure that the techniques are broadly applicable, the system models are intentionally constructed to be as generic as possible. In other words, the framework in this thesis can be adapted to various system configurations via slight modifications. In this context, it is not of

utmost importance that which specific communication waveform is selected, because the models remain compatible with a wide range of different waveforms.

OFDM is a commonly used method in wireless communication systems because it easily solves the multipath channel equalization problem. OFDM waveforms are also commonly studied for radar systems; however, the intrinsic power inefficiency makes OFDM signals not the best radar waveform in most cases. Nonetheless, a communication-centric approach is adopted and OFDM is selected as the ISAC waveform in this thesis, due to its extensive adoption in the literature and foreseen continued dominance over the other waveforms in future communication systems [80]. Both OFDM communications and OFDM radar systems are well-known and widely investigated research areas, making OFDM a common choice of waveforms for ISAC systems in the literature [72–93]. As a consequence, given that the focus of this thesis is not on the waveform design and OFDM has already been extensively studied in the literature, it will not be thoroughly investigated in this work. Instead, the necessary details will be provided as brief summaries, with only the essential aspects included to clarify the signal models and processing methods.

In most OFDM radar studies, the radar targets are assumed to be point scatterers, and receiver processing is done via the computationally easy periodogram method [80,88]. Some studies mention the high-sidelobe problem of the periodogram method and use superresolution methods like MUSIC, compressed sensing, etc. to identify targets [94], use artificial intelligence to learn clutter environment [40], use subspace-based algorithms like ESPRIT and linear least squares to cope with the computational burden of other methods [95]. However, these studies mostly approximate the targets and clutter as point scatterers. In Chapter 3 of this thesis, the point scatterer assumption is replaced with a more realistic multiple-scatterer channel model, and the resulting performance degradation of classical methods under this model is thoroughly examined. To mitigate these losses, novel knowledge-aided and adaptive detection algorithms are proposed.

1.1.5 Multistatic ISAC in Distributed MIMO Architectures

This thesis provides a comprehensive study on ISAC system models and detector structures, including systems using Distributed MIMO (D-MIMO) architectures. By their nature, D-MIMO communication systems enable multistatic sensing through ISAC operation. Although multistatic radar systems were well-known for many years, D-MIMO ISAC systems have received significant interest in recent years, possibly due to the advances in signal processing capabilities. There are several survey-like articles in the literature about this area. [96] explores D-MIMO ISAC systems across various design architectures and deployments, highlighting conflicts, synergies, and the practical challenges and opportunities for implementation. [19] presents a vision for 6G ISAC networks, detailing how signal processing, optimization, and machine-learning techniques can enable them, with a separate section allocated for D-MIMO ISAC systems.

Along with the D-MIMO ISAC articles, there are several works focusing more on D-MIMO radar operation, which are relevant here to express as this thesis also focuses on increasing the radar detection performance while keeping the communication performance unharmed. [97] is a detailed report which analyzes simulation models for future 6G radio systems, including advantages and challenges like non-idealities and waveform impairments of D-MIMO systems. [98] examines the shift from far-field to near-field channel models in 6G, driven by technology enablers including D-MIMO systems. [99] is a thesis and [100] is an article which present the development and testing of a novel coherent multistatic radar system, demonstrating performance improvements over monostatic systems in spatial diversity and target resolution, with evaluations of centralized and decentralized detection algorithms and practical data fusion challenges. [101] examines the advantages of bistatic and multistatic radar, including enhanced detection and resilience against jamming, highlighting synchronization needs and geometry-dependent processing for range and Doppler. [102] examines target localization accuracy in D-MIMO systems, analyzing optimal antenna placement for coherent and noncoherent processing.

One of the biggest challenges of D-MIMO systems is synchronization between spatially separated transmit and receive nodes. There are several articles in the literature

that touch on this issue. [103] explores synchronization methods for a cooperative coherent imaging system utilizing D-MIMO ISAC operation for vehicular radar networks, where radar-equipped vehicles collaborate to enhance sensing accuracy and distinguish weak targets near strong ones. [104] investigates efficient device positioning and tracking in 5G networks, providing solutions to different kind of synchronization problems faced in D-MIMO systems. [105] investigates the detection capabilities of D-MIMO radar systems by developing a comprehensive model that incorporates various system errors such as synchronization errors in time, frequency, and phase, uncertainties in site position and beam pointing, and mismatch errors between the test-cell center and the target, along with non-orthogonal waveforms and spatially correlated target echoes. [106] examines the impact of synchronization errors in D-MIMO radar systems, where orthogonal waveforms may lose their orthogonality due to distinct delays and Doppler frequency offsets in spatially separated transmit and receive antennas. [107] explores radar sensing using large antenna arrays and OFDM waveforms, demonstrating that massive MIMO systems can achieve accurate near-field localization even at low carrier frequencies and narrow bandwidths, with experimental validation from a massive MIMO testbed proposing solutions to different synchronization challenges.

Another challenge in D-MIMO ISAC systems is to create a useful target and channel model. There are some articles in the literature that focus on this issue by putting forward some models. [108] introduces the concept of statistical MIMO radar, which differs from traditional radar systems by leveraging the diversity of target scattering rather than maximizing coherent processing gain. It puts forward the conditions for the signals at the receivers in a D-MIMO system architecture to be uncorrelated. In this chapter of the thesis, these uncorrelation assumptions are also used wherever needed, to efficiently utilize GLRT detectors. [109] uses a similar target model and presents an ML-based parameter estimation framework for a millimeter wave D-MIMO ISAC system.

Clutter suppression is another challenge in D-MIMO systems. [110] introduces a novel nonhomogeneous clutter model and builds a CFAR GLRT detector for moving target detection in D-MIMO radar systems. [111] addresses the challenges of joint target detection and clutter mitigation in D-MIMO radar, where nonorthogonality of

the waveforms are taken into consideration.

Other than the literature that focus on the main challenges of D-MIMO radar and ISAC systems, there are some articles in the literature that focus on different issues in D-MIMO systems. [112] investigates the distributed radar multi-frame detection method for detecting dim targets with a GLRT detector while addressing the high computation and communication costs of processing numerous measurements. [113] explores the potential of using terahertz (THz) frequencies in OFDM-based bistatic multiple antenna ISAC systems, to enhance the sensing capabilities while overcoming the range ambiguity problem due to increased subcarrier spacing.

1.2 Motivation and Contributions

One of the biggest differences between radar detection in ISAC systems and classical radar systems is the modulation on the transmitted communication waveform. In classical radar systems, the transmitted waveform can be designed to meet the requirements such as range or Doppler resolutions. However in communication-centric ISAC systems, the transmitted waveform is dictated by the communication functionality, leaving limited flexibility for waveform design considering radar signal processing. Specifically for OFDM waveforms, the channel between the transmitter (Tx) and the receiver (Rx), which is supposed to carry valuable information about the possible targets in the area, is different for each subcarrier and OFDM symbol due to the changing transmitted symbol. Consequently, knowing or correctly learning the transmitted symbols is of paramount importance in ISAC systems in order to accurately extract the position or velocity information from the *symbol-dependent* channel. If the effects of transmitted symbols on the channel can be eliminated and the channel can be established without errors with appropriate signal processing, then, at the detector side, the interference-suppression algorithms can work well and targets can be detected with high-precision. If the elimination of transmitted symbols from the channel is not successful, then, the strong interferences contaminate all subcarriers and symbols due to the ever-changing random transmitted symbols, deteriorating the detection performance at the detector side.

In light of the preceding challenges, this thesis aims to create a comprehensive framework for ISAC operation. It proposes efficient signal processing algorithms for ISAC systems that effectively suppress strong interferences by eliminating the symbol-dependent channel effects, and introduces detectors that utilizes these algorithms to achieve better detection performance than benchmark Periodogram-based methods.

In the following subsection, the contributions of the works done in each chapter to the literature will be summarized in separate lists.

1.2.1 Contributions of Chapter 3

- A signal model is developed for monostatic ISAC systems with Single-Input Single-Output (SISO) antenna architecture using OFDM waveforms.
- In accordance with the high range and angle resolution of the proposed system, a sparse clutter model is constructed in which large objects are modeled as combinations of multiple point-like scatterers.
- The failure of classical radar signal processing methods, like periodogram, under the multiple-scatterer interference model is explicitly shown both theoretically and with simulation results.
- To improve detection of weak targets under strong interference, an efficient knowledge-based range-Doppler processing and generalized likelihood-ratio test (GLRT) are presented.
- To overcome the computational burden of GLRT, a practical single-snapshot adaptive detector is also proposed and shown to have superior detection performance than classical methods.

1.2.2 Contributions of Chapter 4

- A detailed system model for the monostatic MIMO-OFDM channel under the disruptive effects of multiple-scatterer clutter, uplink (UL) users, beam-squint effect and Doppler mismatch is constructed.

- The signal dependent disturbance on angle and range covariances due to the Doppler mismatch is explained in detail. A novel least-squares (LS) based approach is proposed to simultaneously apply classical Doppler processing and get rid of the signal dependency while preserving the dimensions required to apply further MIMO signal processing. The residual signal dependencies are also calculated and exploited for performance increase.
- A suboptimal knowledge-aided sequential angle-range processing (SARP) is proposed. Within SARP, theoretical SINR expressions and SINR maximizing filters are provided.
- A novel detector scheme is proposed to overcome the performance losses arising due to suboptimality. Its performance is evaluated in terms of SINR and probability of detection (P_d) metrics, including the comparison with benchmark Periodogram-like detectors in the literature.
- To reduce the complexity of the proposed detector, computationally softer detectors are also proposed and their mathematical backgrounds are provided. A novel, adaptive matched filter (AMF)-like [114] fully adaptive detector is also provided, which uses symbol-independent filters that do not require recalculation for multiple frames.

1.2.3 Contributions of Chapter 5

- A detailed system model for the OFDM-based multistatic D-MIMO channel under the disruptive effects of multiple-scatterer clutter and range-Doppler mismatch is constructed.
- A novel knowledge-aided two-stage signal processing method and max-SINR detector is proposed to suppress the strong interference and increase the probability of detecting a weak target.
- A novel knowledge-aided approximate detector is proposed to reduce the computational requirements of the max-SINR detector.
- Two different fully adaptive detectors are proposed in order to compensate for the knowledge requirements of the previously proposed detectors.

- All proposed detectors are compared to the benchmark 3 dimensional (3D) Periodogram method and are shown to perform significantly better especially at detecting weak targets near strong interferences.

- Advantages of multistatic systems on resolving position and Doppler ambiguities are explicitly shown.

1.3 Outline

The rest of this thesis will be organized as follows:

In Chapter 3, a SISO ISAC system model using OFDM waveforms is constructed and novel radar signal processing methods are proposed and compared with benchmark methods in the literature.

In Chapter 4, the OFDM-based ISAC model is extended to MIMO architectures. The inevitable signal-dependent interference problem of MIMO ISAC systems is characterized and novel radar signal processing methods and detector schemes are proposed to overcome this inherent challenge.

In Chapter 5, the OFDM-based MIMO ISAC model is extended to multistatic system geometries. Unique challenges and advantages of multistatic D-MIMO ISAC systems are clarified. Under this circumstances, the multistatic GLRT detector is proposed, as well as an approximate-GLRT detector and two fully-adaptive detectors for trading-off some performance for computational ease.

In Chapter 6, concluding remarks about the thesis are provided.

1.4 Notation

Throughout the thesis, if otherwise explicitly stated, regular letters (like a), bold lowercase letters (like $\mathbf{a}$) and bold uppercase letters (like $\mathbf{A}$) denote scalars, vectors and matrices, respectively. $[\cdot]^{\mathrm{T}}$, $[\cdot]^{\mathrm{H}}$, $(\cdot)^*$, $[\cdot]^{\#}$, $|\cdot|$, $||\cdot||$, $\mathrm{tr}\{\cdot\}$, $\mathrm{vec}\{\cdot\}$, $\mathbb{E}\{\cdot\}$, $\mathrm{Var}\{\cdot\}$, $\odot$, $\oslash$, $\otimes$ and $\circledcirc$ denote transpose, Hermitian transpose, conjugate, pseudo-inverse, abso-

lute value, Euclidean norm, trace, vectorization, expectation, variance, element-wise (Hadamard) multiplication, element-wise (Hadamard) division, Kronecker product and Khatri-Rao (column-wise Kronecker) product operations, respectively. $\mathrm{diag}\{\mathbf{A}\}$ represents a vector including diagonal elements of $\mathbf{A}$ and $\mathrm{diag}\{\mathbf{a}\}$ represents a diagonal matrix $\mathbf{A}$ whose diagonal elements are $\mathbf{a}$. $\mathrm{bdiag}\{(\mathbf{A}_n)_{n=1}^{N}\}$ represents a block diagonal matrix whose n^{th} diagonal block is $\mathbf{A}_n$. $[\mathbf{a}]_{(n)}$, $[\mathbf{A}]_{(n,m)}$ and $[\mathbf{A}]_{[n,m]}$ represents n^{th} element of vector $\mathbf{a}$, $(n,m)^{\text{th}}$ element of matrix $\mathbf{A}$ and $(n,m)^{\text{th}}$ block matrix inside matrix $\mathbf{A}$, respectively. Throughout the thesis, $\exp\{\cdot\}$ and $e^{(\cdot)}$ are used interchangeably to denote the exponential function.

CHAPTER 2

PRELIMINARY SYSTEM MODEL AND PROBLEM SETTING FOR ISAC

This thesis provides a comprehensive detector framework for ISAC systems, including both SISO and MIMO antenna architectures, monostatic and multistatic system configurations, and several disruptive effects such as beam-squint, multiple-scatterer sparse clutter, computational power limitations, etc. In this chapter, the preliminary background and mathematical foundations necessary for understanding the ISAC system models considered throughout this thesis will be provided. Specifically, this chapter introduces the general ISAC system architecture, waveform and signal processing models, and fundamental detector structures, serving as a common basis for the subsequent chapters. Unless otherwise stated, the assumptions and formulations presented in this chapter apply to all later system configurations. In chapters that involve additional components, modified assumptions, or extended parameters such as MIMO architectures, beam squint effects, or multistatic scenarios, these modifications will be explicitly described in the introduction parts of the corresponding chapters.

In this thesis, a communication-centric ISAC approach is adopted, namely the sensing utility of the system works with minimal or no harm to the communication utility of the system. Within this approach, any kind of modeling, designing or optimization of the communication system, communication waveforms or signal processing methods that increase communication performance is out of the focus. To this end, OFDM modulation is used in ISAC systems throughout the thesis as it is the most commonly used communication waveform and its performance has been accepted as a benchmark in the vast majority of the literature. In the following section, preliminary information on using OFDM waveforms for sensing purposes will be provided.

2.1 Sensing Operation in OFDM-Based ISAC Systems

This section introduces the overall framework for sensing in OFDM-based ISAC systems, upon which the proposed detection strategies are built. It begins by outlining the general system model and underlying assumptions, followed by a brief overview of the basic principles of OFDM transmission and reception. The subsequent subsections detail the modeling of ISAC-specific target and interference channels, and describe the two-stage signal processing scheme, including channel estimation and parameter extraction stages, designed to enable effective detection of sensing targets. Finally, the formulation of the detection problem is presented through a hypothesis testing approach, which lays the foundation for the development of the proposed detection methods.

2.1.1 General System Model and Assumptions

In this thesis, the transmitted communication symbols are denoted with the letter x, $\mathbf{x}$ or $\mathbf{X}$, depending on the dimensions as described in Section 1.4. These symbols are randomly drawn complex numbers, selected from an $\mathcal{M}$-sized alphabet, specifically either from phase-shift keying ($\mathcal{M}$-PSK) or quadrature amplitude modulation ($\mathcal{M}$-QAM) alphabets.

In each transmitted OFDM symbol, $\bar{N}$ different subcarriers with subcarrier spacing $\Delta\bar{f}$ are used. Among these subcarriers, some of them is left blank and some of them are selected to be pilots conventionally. The number of residual subcarriers that can be used for ISAC signal processing purposes is denoted as N. The carrier frequency of the n^{th} subcarrier is denoted as $f_n = f_0 + n\Delta f$ for $n = 1, 2, \cdots, N$. Selection of these N ISAC subcarriers among $\bar{N}$ ones is not an issue this thesis focuses on, but some possible effects of this selection will be discussed in Section 4.5. In this thesis, it is assumed that the whole subcarriers are separated into $\bar{N}/N$-subcarrier groups and first subcarrier of each group is selected as an ISAC subcarrier. In other words, the subcarrier spacing between the chosen N subcarriers are assumed to be the same and denoted as Δf, where $\Delta f = \Delta\bar{f}\bar{N}/N$. As a consequence, the total transmission bandwidth, which is denoted as W, can be written as $W = \bar{N}\Delta\bar{f} = N\Delta f$. Specific to

the Chapter 4 of this thesis, the total transmission bandwidth may be divided into N' equal and consecutive subbands. In this case, the bandwidth of each subband becomes W/N', the number of total subcarriers in each subband becomes $\bar{\mathcal{N}} \triangleq \bar{N}/N'$, and the number of ISAC subcarriers in each subband becomes $\mathcal{N} \triangleq N/N'$.

In each coherent processing interval (CPI), M OFDM symbols are transmitted and received consecutively. Each of these symbols lasts for the duration T_s, making the duration of a CPI MT_s. In classical radar signal processing notation, T_s would be referred to as the pulse repetition interval (PRI). In general, $T_s = T + T_{\text{cp}}$, where T is the symbol duration dictated by the subcarrier spacing through $T = 1/\Delta\bar{f}$, and T_{cp} is the cyclic prefix (CP) duration, required in OFDM systems to be guarded from inter-symbol interference (ISI) due to the multipath components in the communication channel. In this thesis, the CP is assumed to be sufficiently long to ensure that the round-trip delays from all scatterers within the area of interest fall within the CP duration, which is a standard assumption in OFDM radar systems [87].

2.1.2 Basics of OFDM Transmission and Reception

The transmitted symbol at n^{th} subcarrier in m^{th} OFDM symbol is denoted as x_{nm}. In OFDM systems, x_{nm} are considered as frequency domain symbols and they are transformed into time domain by Inverse Discrete Fourier Transform (IDFT) operation among the subcarriers for each of the M OFDM symbols. In the next step, CP is added to each OFDM symbol. Digital-to-analog conversion (DAC) and RF operations are conducted before the signal is transmitted through the antenna. The signal propagates in the channel and possibly reflected by the scatterers in the environment. At the receiver side, the incoming signal is processed by RF signal processing and analog-to-digital conversion (ADC) steps, followed by the removal of the CP in each OFDM symbol. Finally, the time-domain received symbols are transformed back into frequency domain by Discrete Fourier Transform (DFT) operation to get the received symbols y_{nm}.

Unless otherwise stated, the transmission and the reception of the OFDM symbols are assumed to be conducted perfectly in this thesis. In other words, x_{nm} and y_{nm} are assumed to be known at the transmitter and the receiver sides, respectively, with-

out focusing on the intermediate steps required for OFDM signal transmission and reception.

2.1.3 Channel Model for ISAC Targets and Interference

In this thesis, two types of radar targets are assumed to coexist. The first target group is assumed to have been existing in the frames, namely CPIs, for a while and behaves like clutter. These targets are called *"unintended"* targets (UITs) as the detectors do not intend to detect these targets; because they have already been detected in the previous CPIs, and they are in the scope of the tracker in the current CPI. The other target group is assumed to be new in the current frame and their characteristics are unknown to the detector. These targets are called *"intended"* targets (ITs), as the detectors intend to identify these targets' characteristics in the current frame. If the intended targets are successfully detected in a CPI, they are passed to the tracker and become unintended targets of the subsequent CPI.

Assuming that a SISO architecture is used in a monostatic ISAC system and there is a single point-like Swerling-1 type IT scatterer in the environment, the received echo signal from that scatterer at n^{th} subcarrier in m^{th} OFDM symbol can be written as [87]:

$$y_{nm} = \alpha\sqrt{\gamma}e^{j2\pi m f_D T_s}e^{-j2\pi n\Delta f\tau}x_{nm} + n_{nm} \triangleq h_{nm}(f_D,\tau)x_{nm} + n_{nm}, \tag{2.1}$$

where α corresponds to the random phase in the received signal, γ corresponds to the deterministic received signal power which is related to the propagation loss and scatterer radar cross-section (RCS), f_D is the Doppler frequency due to the relative velocity between the radar system and the scatterer, τ is the time between the signal transmission and reception, $h_{nm}(f_D,\tau)$ is the overall channel between the Tx and Rx due to the target, and n_{nm} is the circularly symmetric additive white Gaussian noise component inside the received signal. The exact calculations of these parameters and the mappings from f_D and τ to target velocity and range are fairly straightforward and can be easily found in the classical radar literature [115, 116]. However, the formulations slightly change depending on whether the scenario is mono or multistatic, therefore they are explained in detail in the introduction parts of the corresponding

chapters, while this section's focus is kept on the general understanding of sensing operation in OFDM-based ISAC systems.

2.1.4 Two-Stage Signal Processing Scheme

In (2.1), it can be seen that target velocity and range affects the channel $h_{nm}(f_D, \tau)$, and thus the received echo signal y_{nm}, through two different complex exponentials. In order to be safe from inter-carrier interference (ICI), the subcarrier spacing Δf must be larger than the Doppler frequency f_D of the target with maximum radial velocity [87], and the parameters are chosen accordingly in this thesis. Related to this fact, the processing along the subcarriers indexed with n is called *fast-time (FT) processing* and the processing along the OFDM symbols indexed with m is called *slow-time (ST) processing* conventionally, and in the rest of this thesis.

In a broad perspective, the aim of the sensing utility of ISAC systems is either to estimate f_D, τ and γ to find the estimates of target parameters (velocity, range and RCS) or to make a decision about whether there is a target or not with specific predetermined parameters. This thesis focuses on the latter aim, namely it proposes *detectors* that hypothesize that there is a target with specific parameters and test this hypothesis via clever signal processing methods. To this end, it can be seen in (2.1) that the transmitted symbols are not related to any of the parameters. In fact, the whole information on the parameters of interest lie in the channel $h_{nm}(f_D, \tau)$, and x_{nm} acts as an interfering source that complicates the extraction of this information.

Based on the above discussion, the signal processing methods for ISAC systems can be separated into two main parts. The first step is to remove the effects of transmitted symbols from the received ones to find (or estimate) the sensing channel. The second step is then extracting the information related to the parameters of interest from the estimated channel by fast and slow-time processings. In conventional OFDM-based SISO ISAC systems, the first step is done by simple division as:

$$\hat{h}_{nm}(f_D, \tau) = \frac{y_{nm}}{x_{nm}} = h_{nm}(f_D, \tau) + \frac{n_{nm}}{x_{nm}} \tag{2.2}$$

where $\hat{h}_{nm}(f_D, \tau)$ is the channel estimate. The second step usually involves DFT in slow-time and IDFT in fast-time to combine the energy in the OFDM symbols and

subcarriers, respectively, and a magnitude square operation to compensate for the random phase term. DFT and IDFT can be taken with large numbers of samples by zero-padding but using the minimal requirements and taking M-point DFT and N-point IDFT is a convention for the sake of simplicity. Then, the $\tilde{m}^{\text{th}}$ DFT bin and $\tilde{n}^{\text{th}}$ IDFT bin of the resultant metric becomes:

$$\xi(\tilde{m},\tilde{n}) = \frac{1}{MN}\left|\sum_{n=0}^{N-1}\sum_{m=0}^{M-1}\hat{h}_{nm}(f_D,\tau)e^{-j2\pi m\tilde{m}/M}e^{j2\pi n\tilde{n}/N}\right|^2. \tag{2.3}$$

It can be seen from (2.1), (2.2) and (2.3) that if x_{nm} is chosen from a constant-modulus alphabet like PSK, and the DFT/IDFT processings are matched to the single point target in the scenario, namely $\tilde{m}/M = f_D T_s$ and $\tilde{n}/N = \Delta f \tau$, then

$$\xi(\tilde{m},\tilde{n}) = \gamma MN + \bar{n} \tag{2.4}$$

where $\bar{n}$ is the processed white noise. If the received noise power is denoted as σ_n^2, then the output signal-to-noise ratio (SNR) becomes $\gamma MN/\sigma_n^2$, which is the largest SNR that can be achieved within this configuration. This classical method is usually denoted as *2 dimensional (2D) Periodogram* method, as it resembles the periodogram spectral estimation method. As it can be seen, in this specific scenario with several strong assumptions, 2D Periodogram method is in fact an optimal method in terms of SNR.

2.1.5 Hypothesis Testing and Detection

After the signal processing is done and the scalar metric is extracted, the remaining step is making the decision of whether there is a target with the corresponding parameters or not. In the simplified model of single point scatterer in a monostatic SISO environment, the binary hypothesis testing on the received signal can be written as:

$$y_{nm} = \begin{cases} n_{nm}, & \text{under } H_0 \\ h_{nm}(f_D,\tau)x_{nm} + n_{nm}, & \text{under } H_1 \end{cases} \tag{2.5}$$

where H_0 represents the null hypothesis of there is no target component in the received signal, and H_1 represents the detection hypothesis of there is a target component in the received signal. After the signal processing operations, the binary hypoth-

esis testing on the $\tilde{m}^{\text{th}}$ DFT bin and $\tilde{n}^{\text{th}}$ IDFT bin can be written as:

$$\xi(\tilde{m},\tilde{n}) = \begin{cases} \bar{n}, & \text{under } H_0 \\ \gamma MN + \bar{n}, & \text{under } H_1 \end{cases} \tag{2.6}$$

where H_0 represents the null hypothesis of there is no target component in the corresponding DFT/IDFT bin, and H_1 represents the detection hypothesis of there is a target component in the corresponding DFT/IDFT bin. It should be noted that the signal processing is done with the assumption of there is a target with specified Doppler and range, therefore the hypothesis testing is done in the corresponding DFT/IDFT bin. In conventional radar systems, the range-Doppler space is considered to be divided into *cells*, and each cell is tested for a detection after being processed with the suitable signal processing method for that cell. The cell which is currently being tested is conventionally called as *cell under test (CUT)*, and this abbreviation will be used in the rest of this thesis.

Binary hypothesis testing for each CUT is typically performed using likelihood ratio tests (LRT), with thresholds set theoretically or adaptively to meet a desired false-alarm rate. Since the LRTs vary across the chapters of this thesis, they will be specified in the relevant sections of each chapter.

To provide an overview of the preliminary system model and problem setting discussed in this chapter, the sparse frequency domain channel model, two-stage signal processing scheme, and hypothesis testing operations are illustrated in the block diagram in Figure 2.1. This figure focuses on a SISO ISAC system and omits the angular domain for simplicity, but the overall aspects like scatterers in fractional bins, Tx symbol effects on the channel, and two-stage signal processing scheme is common in all chapters of this thesis. In Figure 2.1, the range-Doppler space is discretized into grids, where colored objects represent targets with possibly multiple scatterers located at fractional bins. The received signal is randomly distorted by the transmitted symbols, as previously discussed. Hence, in the first stage, the channel is estimated with minimal contamination from the transmitted signals. Subsequently, signal processing operations such as interference suppression or energy compression are applied on each CUT to extract meaningful information and derive a decision metric. Finally, detection is performed for each CUT via thresholding.

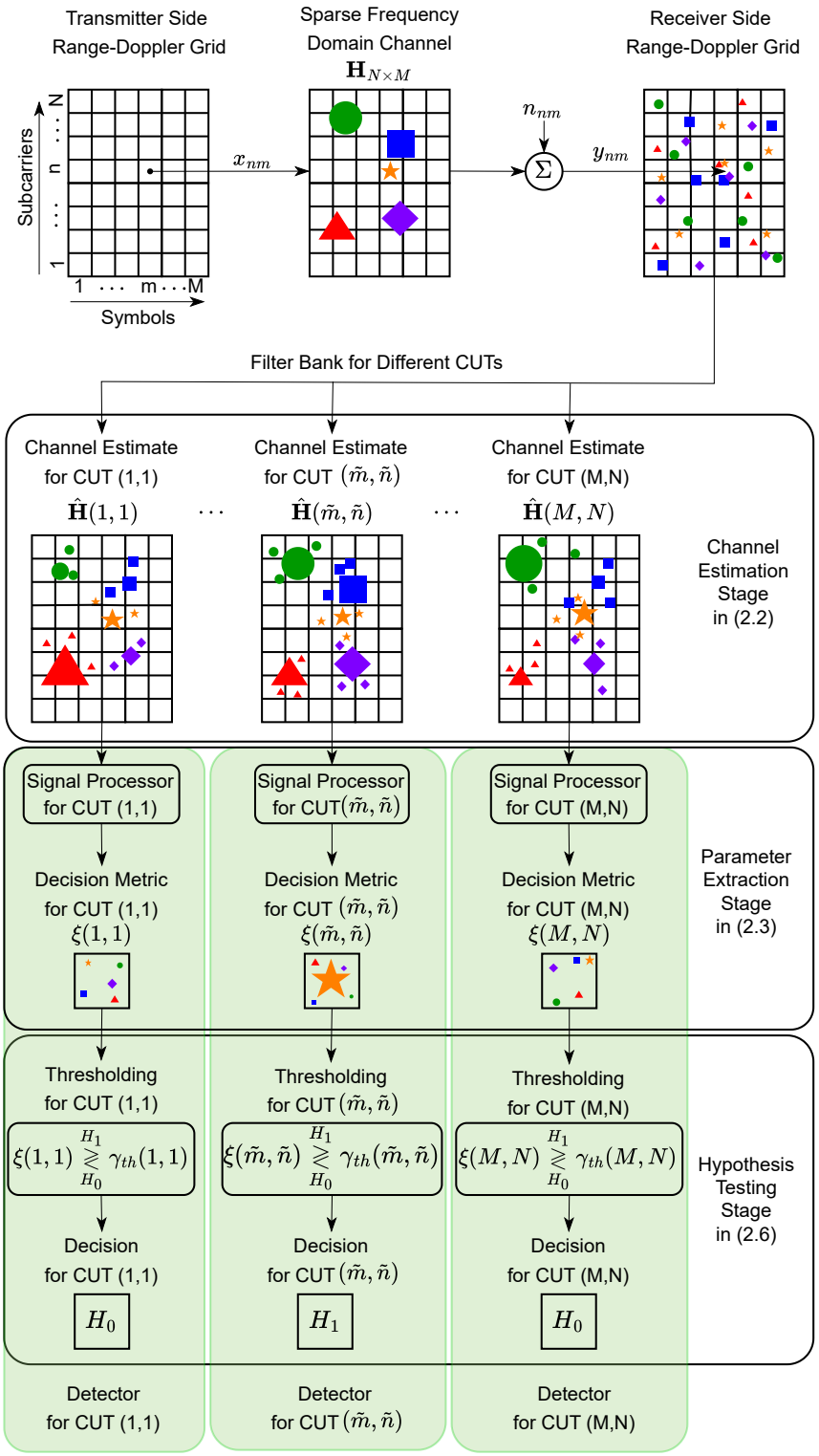


Figure 2.1: Block diagram of the sparse frequency domain channel model, two-stage signal processing scheme, hypothesis testing and detection operations for a SISO ISAC system.

2.2 Conclusion

In this chapter, a simplified channel model with single point target is investigated under a monostatic SISO ISAC system using OFDM waveforms. The detection problem is defined and the conventional benchmark 2D Periodogram method is briefly explained. The rest of this thesis extends the simplified signal and channel model by replacing it with more realistic representations in several aspects, and provides a detailed mathematical analysis of the resulting effects. As expected, these analyses reveal performance losses associated with conventional signal processing methods. After identifying the fundamental reasons for these losses through the developed mathematical models, potential solutions are proposed and their performance is compared against the classical approaches. Due to the diversity of the more sophisticated models and the proposed signal processing techniques, further details of the extended signal models will be presented in the introduction sections of the corresponding chapters. Nonetheless, the two-staged signal processing method involving channel estimation and parameter extraction, along with the hypothesis testing and detection operations discussed in this chapter, serves as a foundational framework for the remainder of the thesis.

CHAPTER 3

ON THE EFFECTS OF RANGE-DOPPLER PROCESSING FOR TARGET DETECTION IN OFDM-BASED ISAC

In Chapter 2, a general framework for OFDM-based ISAC systems is provided for a simple scenario in which there is only a single point scatterer in the area of interest. While 2D Periodogram method in OFDM-based ISAC systems is shown to be simple and effective in this proper circumstances, its detection performance under scenarios including multiple scatterers is expected to be negatively affected, which is an issue which has not yet been investigated thoroughly in the literature. This chapter focuses on this scenario, indicating that the commonly used 2D Periodogram method performs poorly when the targets in the area of interest consist of multiple scattering centers. Then, a knowledge-aided GLRT detector and an interference-aware adaptive detector are proposed and shown to be robust against such realistic target scenarios. Both analytical calculations and simulation results are provided at the end of the chapter to support the idea.

The following section briefly outlines the assumptions of the scenario and reviews additional relevant literature.

3.1 Introduction and Literature Review

This thesis works on a practical scenario in which there are multiple targets whose reflection coefficients significantly vary in power. Besides, strong and weak targets happen to be close in range and Doppler dimensions. The high range resolution of wideband OFDM radar is also taken into account, which results in long targets that cover multiple range bins and include multiple scattering centers in each range bin.

Under these circumstances, the effects of range-Doppler processing on target detection performance are investigated by using the signal model developed for OFDM-based ISAC systems, and significant losses on detection performance for standard methods are exhibited. Moreover, to improve the detection performance of weak targets which are close to strong ones, an efficient clutter covariance matrix (CCM) knowledge-based range-Doppler processing and interference-aware knowledge-aided (KA) GLRT are presented. In addition, a more practical AMF [117] type detector based on clutter Doppler power spectrum estimation, which works with only a single fast-slow-time CPI, is proposed and shown to have considerable performance improvement with respect to standard methods when multiple scatterer model is used. A detailed investigation of the multiple scatterer channel model and its effects on detection performance can be found in [118], which forms the basis of the works done in this chapter of the thesis.

In this chapter, general notation rules described in Section 1.4 will be followed and no other notation will be introduced.

The rest of this chapter is organized as follows. In Section 3.2, the extended sparse scatterer model for OFDM-based ISAC is introduced. In Section 3.3, the hypothesis test for detection is put forward, and a theoretical model for the clutter Doppler power spectrum is developed. In Section 3.4, the simulation parameters are given, performance metrics are explained, and simulation results are provided. The chapter is concluded with some future suggestions and remarks in Section 3.5.

3.2 ISAC System with Multiple Scatterer Channel Model

The signal model in this chapter mostly follows the general system model description explained in Chapter 2, but the most important aspects will be repeated here for the sake of ease in readability. The transmit waveform of the ISAC system is chosen to be an OFDM waveform since it is the most commonly used waveform model in modern communications. Let N denote the number of subcarriers in an OFDM symbol, and M denote the number of symbols in an OFDM frame. Then, the transmitted (and received) OFDM waveform can be represented by an $N \times M$ matrix [80, 87] whose

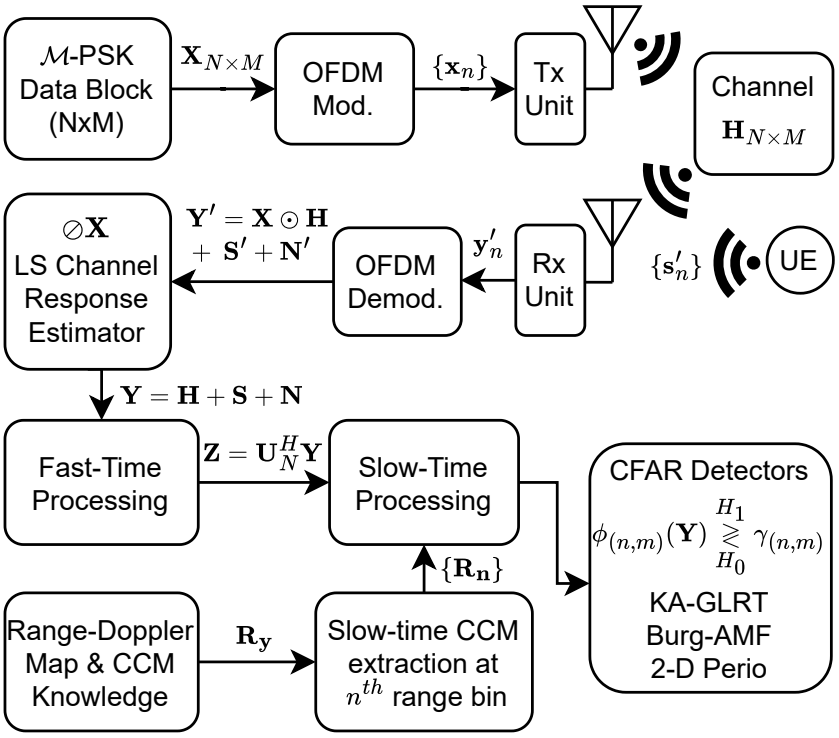


Figure 3.1: Overview of the OFDM-based ISAC system architecture.

n, m^{th} element represents the symbol, chosen from an $\mathcal{M}$-PSK alphabet, transmitted in m^{th} OFDM symbol at n^{th} subcarrier. In other words, each column represents an OFDM symbol, and each row represents a subcarrier. In the transmitter side, CP is added and Inverse Fast Fourier Transform (IFFT) is applied (to convert frequency-domain symbols into time-domain) before OFDM-modulation. It is assumed that upsampling and DAC operations in the transmitter side and ADC and downsampling operations in the receiver side are done perfectly, so they are not in the scope of this thesis. After OFDM demodulation, the sequence is passed through Fast Fourier Transform (FFT) in order to return the time-domain symbols into frequency-domain, and CP is removed. The resultant received vector can be put into the same matrix form as in the transmitter side and element-wise divided to the transmitted symbols to acquire the $N \times M$ received matrix $\mathbf{Y}$. The general overview of the system architecture is shown in Figure 3.1. The detailed description of each sub-block will be explained in the subsequent sections.

The channel between the radar Tx and Rx is modeled as a combination of several targets, each consisting of several point scatterers. Each scatterer reflects the trans-

mitted signal back to the receiver, and the total received signal matrix is the combination of received matrices of all scatterers. Let the received channel matrix from the k^{th} point scatterer of i^{th} target be denoted as $\mathbf{H}^{ik}$. Assume that the $N \times M$ matrix $\mathbf{H}^{ik}$ is acquired after element-wise division of the received symbols by the transmitted symbols, like in [80, 87], so that the frequency response of each scatterer point is effectively estimated in least-square sense, and is independent of the randomly generated transmitted symbols. It should be noted that the channel between each scatterer and the radar transceiver is assumed to be a scalar number, therefore the division operation effectively estimates the channel. Since OFDM is used, FFT is applied to the received signal before the division, making $\mathbf{H}^{ik}$ a frequency-domain matrix. The matrix $\mathbf{H}^{ik}$ can be written as:

$$\mathbf{H}^{ik} = \mathbf{r}^{ik}(\mathbf{v}^{ik} \odot \boldsymbol{\alpha}^{ik})^{\mathrm{T}}, \tag{3.1}$$

where

$$\begin{aligned} [\mathbf{r}^{ik}]_{(n)} &\triangleq \exp(-j2\pi n(2r^{ik}/c_0)\Delta f), \\ [\mathbf{v}^{ik}]_{(m)} &\triangleq \exp(j2\pi m(2v^{ik}/\lambda)T), \\ [\boldsymbol{\alpha}^{ik}]_{(m)} &\triangleq \alpha_m^{ik} \end{aligned} \tag{3.2}$$

for $n = 0, 1, \ldots, N-1$ and $m = 0, 1, \ldots, M-1$, where c_0 is the speed of light in free space, Δf is the subcarrier spacing, λ is the wavelength of the carrier signal and T is the OFDM symbol duration. In (3.2), $\mathbf{r}^{ik}$ is the *fast-time* (range) return vector of an OFDM symbol from k^{th} scatterer of i^{th} target, r^{ik} being the range of this scatterer; and similarly, $\mathbf{v}^{ik}$ is the *slow-time* (Doppler) return vector of a subcarrier from k^{th} scatterer of i^{th} target, v^{ik} being the relative radial velocity of this scatterer. On the other hand, the random scalar α_m^{ik} is the reflected complex gain of the k^{th} scatterer of i^{th} target seen by the receiver, which accounts for the random fluctuations around the mean Doppler frequency $2v^{ik}/\lambda$ and is assumed to be independent from other scatterer points.

In real-world radar applications, targets consist of many scatterers. In this chapter, the targets are modeled as the combination of $\mathcal{K}^{(i)}$ scatterer points uniformly placed along the radial axis of the radar antenna, where i is the index of different targets. Let the total number of targets inside the region that the radar illuminates be $\mathcal{I}+1$. Then,

the total radar return matrix $\mathbf{Y}$ in frequency domain becomes

$$\mathbf{Y} \triangleq \sum_{i=0}^{\mathcal{I}} \sum_{k=1}^{\mathcal{K}^{(i)}} \mathbf{H}^{ik} + \mathbf{S} + \mathbf{N} \triangleq \mathbf{H} + \mathbf{S} + \mathbf{N} \tag{3.3}$$

where $\mathbf{N}$ is the noise matrix, $\mathbf{S}$ is the SoI matrix, and $\mathbf{H}$ is the total channel response matrix after element-wise division operation. The SoI is considered to be another $\mathcal{M}$-PSK modulated uplink OFDM signal of user equipments, independent from the transmitted signal. The noise samples are assumed to be drawn from a white Gaussian process. It can be shown that element-wise division operation does not affect the whiteness of noise or SoI [95].

In the rest of this chapter, it is assumed that there is only one IT, and there are several UITs in the region that radar illuminates. In (3.3), $i = 0$ denotes the intended target, and $i = 1, 2, \ldots, \mathcal{I}$ denote unintended targets.

3.3 Target Detection

In this chapter and the following chapters of this thesis, a single IT is tried to be detected when multiple UITs (clutter signal) exist in the region. The H_0 hypothesis states that there are only UITs in the received signal, while H_1 hypothesis states that the received signal includes both intended and unintended targets. Then, the hypotheses at the received signal matrix can be written as:

$$\begin{aligned} H_0 : \mathbf{Y} &= \sum_{i=1}^{\mathcal{I}} \sum_{k=1}^{\mathcal{K}^{(i)}} \mathbf{H}^{ik} + \mathbf{N} + \mathbf{S}, \\ H_1 : \mathbf{Y} &= \sum_{i=0}^{\mathcal{I}} \sum_{k=1}^{\mathcal{K}^{(i)}} \mathbf{H}^{ik} + \mathbf{N} + \mathbf{S}. \end{aligned} \tag{3.4}$$

For each range-Doppler CUT, there is a pre-determined constant false-alarm ratio (CFAR) threshold $\gamma_{(n,m)}$ to set the false-alarm rate to a desired value. The calculation of the thresholds is depicted in the flowchart given in Figure 3.2. On the receiver side, the return matrix $\mathbf{Y}$ is processed and a metric $\phi(\mathbf{Y})$ is acquired so that the below hypothesis test on decision metric can be done:

$$\phi_{(n,m)}(\mathbf{Y}) \underset{H_0}{\overset{H_1}{\gtrless}} \gamma_{(n,m)}. \tag{3.5}$$

3.3.1 Range-Doppler CCM Calculation

In this part, the range-Doppler clutter covariance matrices (CCMs) are calculated before and after fast-time (FT) processing.

3.3.1.1 Before FT Processing

In this section, the range-Doppler CCM derivation is provided for a point scatterer's return matrix $\mathbf{H}^{ik}$. Since the return matrices of different scatterers are assumed to be independent from each other, the total slow-time CCM can be found by simple addition. Following the definition in (3.1), let's define the vectorization of $\mathbf{H}^{ik}$ as [119]:

$$\mathbf{h}^{ik} \triangleq \text{vec}\{\mathbf{H}^{ik}\} = (\mathbf{v}^{ik} \odot \boldsymbol{\alpha}^{ik}) \otimes \mathbf{r}^{ik}, \tag{3.6}$$

and

$$\mathbf{R}_{\mathbf{h}}^{ik} \triangleq \mathbb{E}\{\mathbf{h}^{ik}(\mathbf{h}^{ik})^{\text{H}}\}. \tag{3.7}$$

Then, by some manipulations, it can be written as

$$\begin{aligned}\mathbf{R}_{\mathbf{h}}^{ik} &= \mathbb{E}\{((\mathbf{v}^{ik} \odot \boldsymbol{\alpha}^{ik}) \otimes \mathbf{r}^{ik})((\mathbf{v}^{ik} \odot \boldsymbol{\alpha}^{ik})^{\text{H}} \otimes (\mathbf{r}^{ik})^{\text{H}})\} \\ &= \left(\mathbf{v}^{ik}(\mathbf{v}^{ik})^{\text{H}} \odot \mathbf{R}_{\boldsymbol{\alpha}}^{ik}\right) \otimes \left(\mathbf{r}^{ik}(\mathbf{r}^{ik})^{\text{H}}\right) \\ &= \mathbf{R}_{\text{slow}}^{ik} \otimes \mathbf{R}_{\text{fast}}^{ik}\end{aligned} \tag{3.8}$$

where $\mathbf{R}_{\text{slow}}^{ik} \triangleq \mathbf{v}^{ik}(\mathbf{v}^{ik})^{\text{H}} \odot \mathbf{R}_{\boldsymbol{\alpha}}^{ik}$, $\mathbf{R}_{\text{fast}}^{ik} \triangleq \mathbf{r}^{ik}(\mathbf{r}^{ik})^{\text{H}}$ and

$$\mathbf{R}_{\boldsymbol{\alpha}}^{ik} \triangleq \mathbb{E}\{\boldsymbol{\alpha}^{ik}(\boldsymbol{\alpha}^{ik})^{\text{H}}\} \tag{3.9}$$

is the autocorrelation matrix of the slow-time radar cross-section vector $\boldsymbol{\alpha}^{ik}$ in (3.2).[1]

3.3.1.2 After FT Processing

In order to compress the energy in range dimension, windowed IDFT is applied to $\mathbf{Y}$ in (3.4). Let $\mathbf{Q}_N$ be the $N \times N$ normalized DFT matrix and $\mathbf{q}_n$ be the n^{th} column of $\mathbf{Q}_N$, N and n being arbitrary numbers. Let $\mathbf{W}_N$ be $N \times N$ diagonal matrix whose

[1] In (3.8), α_m^{ik} is chosen to be a realization of a zero-mean complex Gaussian process whose Power Spectral Density is Gaussian shaped with a variance of $(\sigma^{ik})^2$ and mean of zero. Such a process can be easily shown to have its autocorrelation matrix entries as $[\mathbf{R}_{\boldsymbol{\alpha}}^{ik}]_{(m_1,m_2)} = \exp(-2\pi^2(\sigma^{ik})^2(m_1 - m_2)^2T^2)$.

diagonal elements constitute a finite-length window. Let's define $\mathbf{U}_N \triangleq \mathbf{W}_N\mathbf{Q}_N$, which is $N \times N$ windowed DFT matrix, and $\mathbf{u}_n$ is the n^{th} column of $\mathbf{U}_N$. Let $\mathbf{Z}$ be the resultant matrix of the windowed IDFT operation, which means $\mathbf{Z} \triangleq \mathbf{U}_N^{\text{H}}\mathbf{Y}$. Let the n^{th} row of $\mathbf{Z}$ be $(\mathbf{z}_n)^{\text{T}}$. In other words, $\mathbf{z}_n = \text{vec}\{\mathbf{u}_n^{\text{H}}\mathbf{Y}\}$, which can be rewritten as $\mathbf{z}_n = (\mathbf{I}_M \otimes \mathbf{u}_n^{\text{H}})\,\text{vec}\{\mathbf{Y}\}$. The correlation matrix of $\mathbf{z}_n$ is the slow-time correlation matrix at the n^{th} range bin after the FT processing, and it is denoted shortly as $\mathbf{R}_n$, which can be found as

$$\mathbf{R}_n \triangleq \mathbb{E}\{\mathbf{z}_n\mathbf{z}_n^{\text{H}}|H_0\} = (\mathbf{I}_M \otimes \mathbf{u}_n^{\text{H}})\mathbf{R}_{\mathbf{y}}(\mathbf{I}_M \otimes \mathbf{u}_n) \tag{3.10}$$

where $\mathbf{R}_{\mathbf{y}} \triangleq \mathbb{E}\{\text{vec}\{\mathbf{Y}\}(\text{vec}\{\mathbf{Y}\})^{\text{H}}|H_0\}$. Using the definition in (3.4), and (3.8), $\mathbf{R}_{\mathbf{y}}$ can be written as

$$\mathbf{R}_{\mathbf{y}} = \sum_{i=1}^{\mathcal{I}}\sum_{k=1}^{\mathcal{K}^{(i)}}\mathbf{R}_{\mathbf{h}}^{ik} + \mathbf{R}_{\mathbf{n}} \otimes \mathbf{I}_N + \mathbf{R}_{\mathbf{s}} \otimes \mathbf{I}_N \tag{3.11}$$

where $\mathbf{R}_{\mathbf{n}} \triangleq \sigma_n^2\mathbf{I}_M$ is the slow-time autocorrelation matrix of the noise, and $\mathbf{R}_{\mathbf{s}} \triangleq \sigma_s^2\mathbf{I}_M$ is the slow-time autocorrelation matrix of the SoI before FT processing, σ_n^2 and σ_s^2 being the average powers of noise and the SoI, respectively.[2]

Using the decomposition in (3.8) and the calculation in (3.11), slow-time CCM for n^{th} range bin, namely $\mathbf{R}_n$ in (3.10), can be obtained as

$$\begin{aligned}\mathbf{R}_n &= \sum_{i=1}^{\mathcal{I}}\sum_{k=1}^{\mathcal{K}^{(i)}}(\mathbf{I}_M \otimes \mathbf{u}_n^{\text{H}})(\mathbf{R}_{\text{slow}}^{ik} \otimes \mathbf{R}_{\text{fast}}^{ik})(\mathbf{I}_M \otimes \mathbf{u}_n) + (\mathbf{R}_{\mathbf{s}} + \mathbf{R}_{\mathbf{n}}) \otimes (\mathbf{u}_n^{\text{H}}\mathbf{u}_n) \\ &= \sum_{i=1}^{\mathcal{I}}\sum_{k=1}^{\mathcal{K}^{(i)}}\mathbf{R}_{\text{slow}}^{ik}(\mathbf{u}_n^{\text{H}}\mathbf{R}_{\text{fast}}^{ik}\mathbf{u}_n) + ||\mathbf{u}_n||^2(\mathbf{R}_{\mathbf{s}} + \mathbf{R}_{\mathbf{n}})\end{aligned} \tag{3.12}$$

It can be seen from (3.12) that each scatterer affects the slow-time CCM at n^{th} range bin. The structure of $\mathbf{R}_n$ depends on $\mathbf{R}_{\text{slow}}^{ik}$ and the scaling coefficients $(\mathbf{u}_n^{\text{H}}\mathbf{R}_{\text{fast}}^{ik}\mathbf{u}_n)$ in (3.12), which depend on $\mathbf{R}_{\text{fast}}^{ik}$ and FT processing filter $\mathbf{u}_n$. It should be noted that the effect of a UIT on $\mathbf{R}_n$ after FT processing depends on not only the power of the returns from it, $\mathbb{E}\{|\alpha_m^{ik}|^2\}$, but also whether or not it lies at exactly the center of a range bin.

[2] It can be shown that the frequency selectivity or Doppler effects on the SoI channels does not affect the whiteness due to frequency domain processing. Morover, any kind of FT operations applied to $\mathbf{N}$ or $\mathbf{S}$ in (3.4) would not affect the slow-time whiteness.

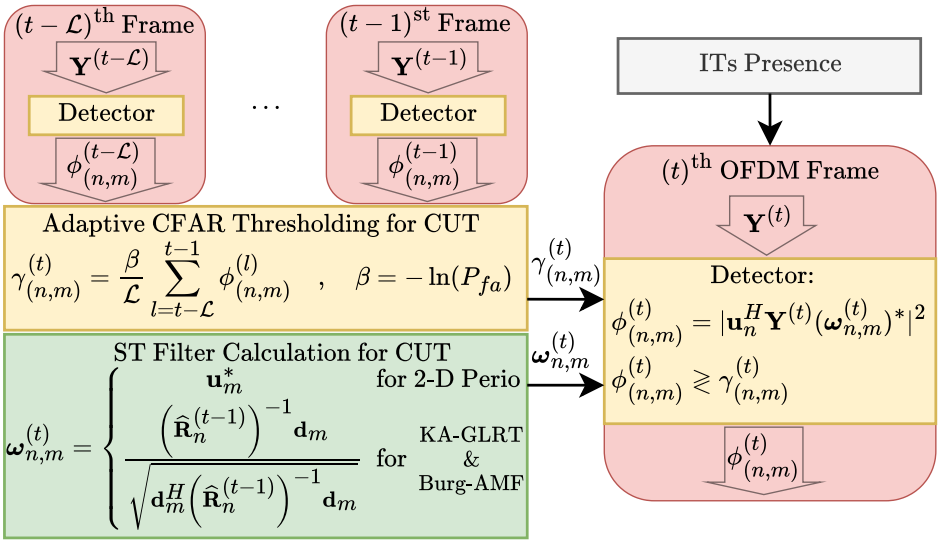


Figure 3.2: Proposed OFDM frame processing structure: Frame index t is dropped in the rest of the chapter for simplicity, β is adjusted to set the false-alarm rate to $\mathrm{P_{fa}}$ when interference statistics ($\mathbf{R}_n$) are stationary along $\mathcal{L}$ frames.

3.3.2 Detector Structures

The proposed OFDM frame processing structure, on which three different detectors are examined with CFAR thresholding, is provided in Figure 3.2. In Figure 3.2, the detector at current frame for $(n,m)^{\text{th}}$ CUT is shown in the right-hand side. ST filter is updated in the current $(t)^{\text{th}}$ frame by using $\widehat{\mathbf{R}}_n^{(t-1)}$ which can be obtained from the tracker unit or direct estimation from $\mathbf{Y}^{(t-1)}$, depending on the detector type. The threshold is provided to the detector from the processors of previous frames. At the initial frame ($t=1$), all targets are assumed to be ITs with $\widehat{\mathbf{R}}_n^{(0)} = (\sigma_n^2 + \sigma_s^2)\mathbf{I}_N$ and $\gamma_{(n,m)}^{(1)} = \beta(\boldsymbol{\omega}_{n,m}^{(1)\mathrm{H}} \widehat{\mathbf{R}}_n^{(0)} \boldsymbol{\omega}_{n,m}^{(1)})$.

3.3.2.1 2D Periodogram Detector

This detector is commonly used in OFDM radar literature due to its simplicity. Revisiting (3.2) and (3.3), the purpose of the radar signal processing is to find the frequencies of different complex exponentials when a combination of these complex exponentials are received. A simple solution is using DFT in the Doppler axis and IDFT in the range axis. This method can be implemented computationally efficiently

using FFT and IFFT and works well when the scatterer range and velocities match the IDFT and DFT bins. The metric for the 2D Periodogram method [80, 88], which will be called "2-D Perio" in this chapter, can be written for $(n, m)^{\text{th}}$ CUT as:

$$\phi^{\text{Perio}}_{(n,m)}(\mathbf{Y}) = \left|[\mathbf{U}_N^{\text{H}}\mathbf{Y}\mathbf{U}_M]_{(n,m)}\right|^2. \tag{3.13}$$

3.3.2.2 Slow-Time Knowledge-Aided GLRT Detector

This detector is interference-aware in the sense that it utilizes the pre-calculated slow-time CCM for each range bin to eliminate the effects of interference on the intended target. The true ST CCM at the n^{th} range bin is $\mathbf{R}_n$ as found in (3.12). Define $\mathbf{d}_m$ to be the steering vector which is adjusted to m^{th} Doppler bin, meaning that $(m')^{\text{th}}$ element of $\mathbf{d}_m$ is $[\mathbf{d}_m]_{(m')} = \exp(j(2\pi/M)mm')$ for $m' = 0, 1, \ldots, M-1$. If the CUT is at n^{th} range bin and m^{th} Doppler bin, the Knowledge-Aided GLRT detector metric becomes

$$\begin{aligned}
\phi^{\text{KA-GLRT}}_{(n,m)}(\mathbf{Y}) &= |\boldsymbol{\omega}_{n,m}^{\text{H}}\mathbf{z}_n|^2 \\
&= |\boldsymbol{\omega}_{n,m}^{\text{H}}\,\text{vec}\{\mathbf{u}_n^{\text{H}}\mathbf{Y}\}|^2 \\
&= |(\boldsymbol{\omega}_{n,m} \otimes \mathbf{u}_n)^{\text{H}}\,\text{vec}\{\mathbf{Y}\}|^2 \\
&= |\mathbf{u}_n^{\text{H}}\mathbf{Y}\boldsymbol{\omega}_{n,m}^*|^2
\end{aligned} \tag{3.14}$$

where $\boldsymbol{\omega}_{n,m}$ is the $M \times 1$ vector representing the ST processing, i.e. filtering operation, on the CUT and is given by

$$\boldsymbol{\omega}_{n,m} = \frac{\mathbf{R}_n^{-1}\mathbf{d}_m}{\sqrt{\mathbf{d}_m^{\text{H}}\mathbf{R}_n^{-1}\mathbf{d}_m}}. \tag{3.15}$$

It should be noted that the filter in (3.15) maximizes the signal-to-interference-plus-noise ratio (SINR) expression given in (3.16), and the detector in (3.14) is actually the *max-SINR detector* if the CCM is perfectly known and the intended point target velocity v matches the m^{th} velocity bin, i.e. $v = m(\lambda/2TM)$. [3]

[3] It is assumed that this radar detector, "KA-GLRT", is working alongside a tracker, which continuously provides precise range-Doppler estimates of the previously detected targets (UITs) in order to construct ST CCM via (3.12).

3.3.2.3 Burg-AMF Detector

This detector has the same structure as the *max-SINR* detector in (3.14) and (3.15), where the ST CCM $\mathbf{R}_n$ is not known but is estimated. Since the ST characteristics of the clutter environment are estimated, this detector resembles the AMF. There are lots of spectral estimation techniques in the literature for estimating $\mathbf{R}_n$, but these techniques are not in the scope of this thesis. In this thesis, Burg's spectral estimation method is used to get the estimation of ST CCM matrix, which is denoted as $\widehat{\mathbf{R}}_n$, by using a *single* previous ST snaphot: $\mathbf{z}_n = \mathrm{vec}\{\mathbf{u}_n^{\mathrm{H}}\mathbf{Y}\}$ [120]. Burg's method is known to work well with a small number of snapshots [120]. In summary, this detector is the same as the one in (3.14) and (3.15), with $\mathbf{R}_n$ replaced with $\widehat{\mathbf{R}}_n$, which results in lower SINR value than KA-GLRT.

It can be noted that 2-D Perio detector does not use any kind of information about the CCM, while KA-GLRT and Burg-AMF are interference-aware detectors such that they use perfect and estimated CCM knowledge in (3.10), respectively.

3.4 Simulation Results

In the scenario under consideration, there is only a single intended target (the IT) to be detected and 3 unintended targets (UITs) acting as clutter, one of them being so close to the transmitter that it can be considered as the self-interference (SI). In this scenario, two different UIT models are used and compared. One model approximates the UITs as point targets, which is commonly used in the literature due to its simplicity. The second UIT model proposed here approximates the UITs as a combination of several point targets lying across the radial axis of the radar transceiver. Since the bandwidth of the system limits the range resolution, it cannot be improved indefinitely to resolve each point scatterer along the radial axis. This means that multiple scatterer points may exist in one range resolution cell. The number of scatterer points per resolution cell is 10. The average power of each UIT is adjusted to be the same for both models. On the other hand, the average powers of scatterers in a UIT are assumed to be equal for simplicity, yet a more realistic model could assume otherwise. In both models, the Doppler spread of each scatterer is equated to 0.01 times the ve-

Table 3.1: Simulation Parameters

Parameter	Symbol	Value
# of subcarriers	N	1024
# of OFDM symbols	M	256
Subcar. spacing, symbol duration	$\Delta f, T$	90.9 kHz, 12.375 μs
Speed of light, wavelength	c_0, λ	$3e8$ n/s, 12.5 mm
Range & Velocity Resolutions	$\Delta r, \Delta v$	1.61 n, 1.97 n/s
PSK Const. Size, # of UITs	$\mathcal{M}, \mathcal{I}$	16, 3
Avg. powers of UITs	σ_i^2	50, 30, 10 dB
Avg. powers of IT, noise, SoI	$\sigma_0^2, \sigma_n^2, \sigma_s^2$	10, 0, 10 dB
Lengths of UITs	l_i	0.1, 10, 5 n
Ranges of centers of UITs	r_i	1, 24.17, 14.50 n
Velocities of UITs	v_i	0.001, 10, 15 n/s
Velocity/Doppler spread ratio	v^{ik}/σ^{ik}	100
Range and velocity of the IT	r, v	29 n, 11.05, 30 n/s
# of scatterers of UITs	$\mathcal{K}^{(i)}$	1, 64, 32
Probability of false alarm	$\mathrm{P_{fa}}$	10^{-3}

locity of the corresponding UIT. The velocities of different scatterers in a UIT are taken to be the same, as expected. The simulation parameters are given in Table 3.1.

It should be noted that the IT is taken to be a point target, i.e. $\mathcal{K}^{(0)} = 1$, even if the multiple scatterer extended UIT model is used. This means that the problem in this scenario is not extended target detection but point target detection under an extended clutter model, which is more realistic such that point target assumption for UITs is avoided, and UITs include multiple scatterers which lie on, in general, fractional range bins.

The detectors examined in Section 3.3.2 are used with both models discussed above and they are compared with respect to probability of detection ($\mathrm{P_d}$) vs SNR per subcarrier, and SINR vs target velocity (v) curves.

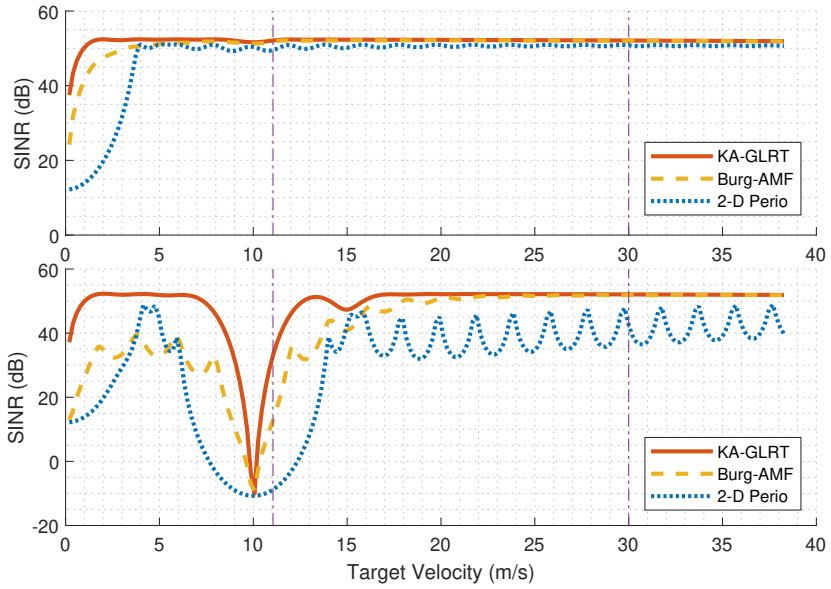


Figure 3.3: SINR vs IT Velocity graphs for point (top) and realistic (bottom) clutter models.

SINR vs IT velocity curves are drawn at 19^{th} range cell. The slow-time CCM at this range cell is calculated for each UIT scatterer using (3.12). Let the IT's CCM at n^{th} range cell be defined as $\mathbf{R}_n^0 \triangleq \sum_{k=1}^{\mathcal{K}^{(0)}} \mathbf{R}_{\text{slow}}^{0k} (\mathbf{u}_n^{\text{H}} \mathbf{R}_{\text{fast}}^{0k} \mathbf{u}_n)$. Then, the SINR at n^{th} range cell and m^{th} Doppler cell can be found by:

$$\text{SINR}_{n,m} \triangleq \frac{\boldsymbol{\omega}_{n,m}^{\text{H}} \mathbf{R}_n^0 \boldsymbol{\omega}_{n,m}}{\boldsymbol{\omega}_{n,m}^{\text{H}} \mathbf{R}_n \boldsymbol{\omega}_{n,m}}. \tag{3.16}$$

In (3.16), the steering vector inside $\boldsymbol{\omega}_{n,m}$ in (3.15) is taken to be perfectly matched to the actual intended target velocity so that the effects of straddle loss are not visible. For the "2-D Perio" detector, $\boldsymbol{\omega}_{n,m}$ is equal to $\mathbf{W}_M \mathbf{d}^{(v)}$ where

$$[\mathbf{d}^{(v)}]_{(m')} \triangleq \exp(j2\pi m'(2v/\lambda)T) \tag{3.17}$$

and $\mathbf{W}_M$ represents a Hamming window. The resultant SINR vs v graphs are provided for both models in Figure 3.3. The vertical dashed-dotted lines in Figure 3.3 represent the velocities of the IT (CUT) at which P_d vs SNR curves will be drawn. As can be seen in the top figure in Figure 3.3, when the targets are considered point scatterers and their location is close to the center of a range bin, all three detectors have similar SINR values. However, when the realistic model is used, the "2-D Perio" method brings more SINR loss than the other methods, especially when the IT is

close to a powerful UIT along the Doppler axis. After FT processing with windowed IDFT, strong UITs at fractional range bins may yield significant interference for IT detection in CUT. This phenomenon can be eliminated by signal processing methods that consider these effects, like in the "Burg-AMF" detector. The critical point being argued is that the "2-D Perio" method is severely affected in case of realistic clutter models.

P_d vs SNR per subcarrier curves of all three detectors are found with 10^5 Monte-Carlo simulations for both models at 19^{th} range cell and 7^{th} and 16^{th} velocity cells, which are the closest cells to the IT. The results are provided in Figure 3.4. As seen in Figure 3.4, the P_d vs SNR curves are in correspondence with the SINR vs target velocity curves, indicating that the "2-D Perio" method performs poorly when a realistic clutter model is adapted. In the top graph in Figure 3.4, the CUT is close to a strong UIT in both range and Doppler dimensions. The performances of all detectors are similar when point scatterer model is used, as seen in the top-left corner of the graph. When the multiple scatterer model is used, all detectors lose some SNR but the loss of "2-D Perio" is more severe than the other detectors. In the bottom graph in Figure 3.4, the CUT is at the same range bin but it is far away from the UITs in the Doppler dimension. It can be seen that all detectors perform much better than the first case, and the effects of the target scatterer model are reduced. However, it can still be said that "2-D Perio" loses more SNR than the other detectors when the point scatterer model is switched to multiple scatterer model.

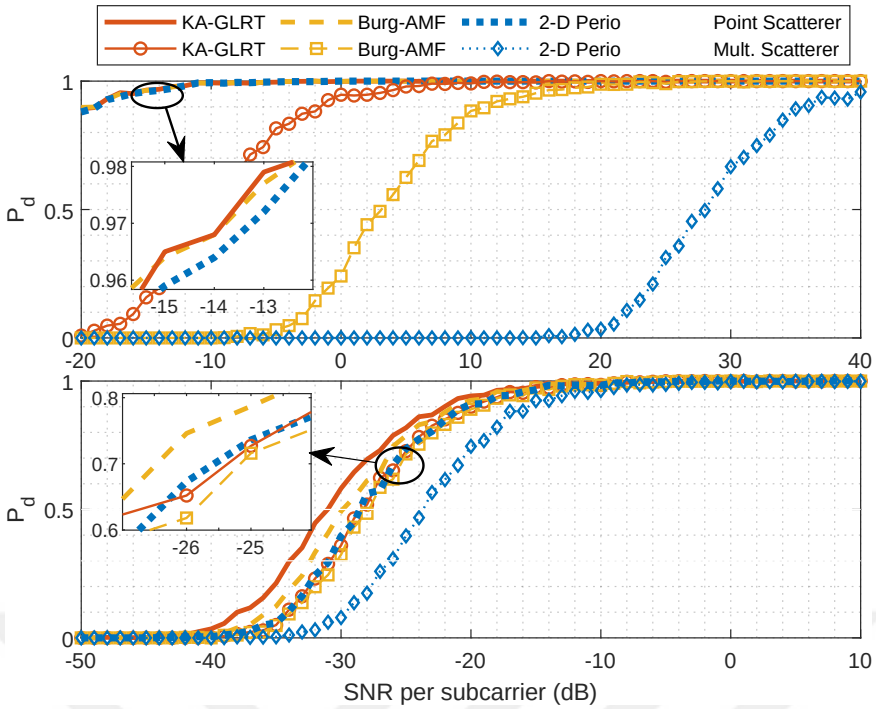


Figure 3.4: P_d vs SNR per subcarrier graphs for both point (w/o markers) and realistic (w/ markers) clutter models, CUT is at 19^{th} range bin, 7^{th} (top) and 16^{th} (bottom) velocity bins.

3.5 Conclusion

This chapter demonstrates that classical 2D Periodogram detector for OFDM radar detection suffers from target shadowing when a realistic clutter model is used, as opposed to other detectors. As the ISAC applications gain more and more attention, it will be a necessity to focus more on selecting the correct detector type to keep radar detection performances at high levels. Moreover in this chapter, SoI signal is considered pure interference. In future works, iterative decoding and cancellation of SoI [121] in OFDM-based ISAC scenarios may be considered to improve target detection performances further.

The next chapter will include an extension of the work of the current chapter to MIMO case in which more assumptions that are used in OFDM-based SISO ISAC systems would be eliminated.

CHAPTER 4

KNOWLEDGE-AIDED AND ADAPTIVE BEAM-SQUINT AWARE DETECTORS FOR MONOSTATIC MIMO-OFDM ISAC SYSTEMS

In Chapter 3, an OFDM-based SISO ISAC system model with multiple scatterer interference channel is constructed and two different detectors have been proposed to overcome the contamination of strong interference at the CUT. In this chapter, the same interference channel model is extended to be used in an OFDM-based monostatic MIMO ISAC system where the transceiver has the ability to transmit and receive multiple streams of data simultaneously. The system is utilized to communicate with DL users while receiving echoes from possible targets and multiple clutters, in addition to separate OFDM-modulated UL communication waveforms. The Tx and Rx employ hybrid beamformers, with analog beamformers precisely designed to cover flat angular sectors. Tx and Rx beams are directed towards DL and UL users, respectively, with the possibility of overlapping or separate angular sectors. For the signal processing stage, a Doppler-Aware Code Bank (DACB) is proposed, thoroughly investigating the effects of the inevitable mismatch between the Doppler frequencies of CUT and the interference sources. Following DACB, a sub-optimal SARP method is proposed to maximize the output SINR while maintaining feasible processing. A two-variant detector scheme is proposed to address the suboptimality of SARP method. Four different detectors with varying complexities, including a fully adaptive detector, are introduced. The potential beam-squint (BS) effect due to increased bandwidth is also considered, and a subband approach is proposed to mitigate these effects. Simulation results for all four detectors, as well as a conventional 3D Periodogram detector commonly used as a benchmark in the literature, are provided. The results demonstrate that the proposed detectors can significantly enhance SINR and the probability of detection, particularly when accounting for the coupling between the transmitted

symbols and interference covariances.

In the following section, the assumptions specific to the new scenario will be outlined, accompanied by a review of related literature and a discussion of the distinctive phenomena that arise within the proposed model.

4.1 Introduction and Literature Review

In this chapter, the main focus is the radar detection performance of an OFDM-based MIMO-ISAC system under a realistic multiple scatterer clutter model and the disruptive effects of BS and UL communication users. The effects of UL users are straightforwardly similar to jammers in classical radar systems as the UL communication data is independent from DL ISAC data, and contaminates the whole band (all subcarriers) and whole time (all OFDM symbols). On the other hand, beam-squint is dependent on one of the important aspects of OFDM-based MIMO-ISAC systems, which is the effective bandwidth (W). In general, using as large W as possible is beneficial for both communication and sensing purposes; however, significantly increasing the W of the system can reduce the range resolution of the system so much that different antennas in the array can see different range responses coming from the same scatterer. In another perspective, a single scatterer can be seen at different angles in different subcarriers in a MIMO-OFDM detector. This effect is investigated in [122] and has been shown to be effective for low carrier frequency over bandwidth (f_c/W) ratios[1]. In [65], this effect is mentioned and ignored as the W is selected to be relatively small. In [123], the beam-squint effect is intentionally used for searching purposes.

In the scenario of this chapter, there are multiple scatterers in the sector of interest, similar to Chapter 3. The receiver gets the echoes of the transmitted signal from all of these scatterers but is interested in detecting only one of them. The scatterer that the receiver is trying to detect, mostly because it is a newcomer to the sector of interest, is called the intended target (IT). All other scatterers are also targets for the radar system but they are unwanted, this is why they are called unintended targets (UITs).

[1] As a rule of thumb, $f_c/W < 50$ can be considered as low enough to be affected from beam-squint.

UITs act like clutter, and they may be more powerful than the IT itself. The UITs also consist of multiple scattering centers, making sure that some part of them lies on fractional range and angle bins, making it harder to suppress them. As explained in Chapter 2 the detector focuses on a CUT, but the cells are determined as range-Doppler-angle cells due to the MIMO capability introduced in this chapter. Since the UITs in the area can have different range-Doppler-angle values which are possibly spread over fractional bins, the CUT will be inevitably separated from some of the UITs in all of these three domains. This separation is called as a *mismatch* between the CUT and the UITs. Regarding the signal model that will be introduced in this chapter, Doppler mismatch will be of utmost importance as it results in a transmitted symbol-dependent interference and undermines both angle and range processing if not handled correctly.

The moving targets are usually related to the ICI problem in the literature. In [73], ICI is allowed and cleverly utilized to gain an advantage against range ambiguity problem. In [124], ICI problem is explained and mitigated by imposing a constraint on the linear dependency of modulation symbols. In [125], the same effect is mitigated by designing a special beamformer. In [126] and [127], ICI problem is challenged by utilizing modulations like OTFS and AFDM, which are shown to be more robust then OFDM to high mobility scenarios. As can be seen from all these examples, ICI can be a problem when there are moving targets with high velocities, which is a well-known and investigated problem. However, Doppler mismatch in OFDM-based MIMO-ISAC systems poses another problem, signal-dependent interference, which undermines interference suppression even if the target velocities are small. In [81], this effect is mentioned and a modified element-wise division method is suggested to remove the negative effects of signal-dependent interference, losing the ability to apply further MIMO processing. A more detailed investigation into this often overlooked effect's underlying causes and potential mitigation strategies is presented in [128], which also forms the basis for the work presented in this chapter.

In this chapter, general notation rules described in Section 1.4 will be followed and no other notation will be introduced.

The rest of this chapter is organized as follows. The system model including the

MIMO channel and well-defined beamformers are explained in Section 4.2. The proposed Doppler-Aware Code Bank, two-variant detector scheme, and SARP method are explained in detail in Section 4.3. An explicit interpretation of the Doppler mismatch effect is also included in this section. In Section 4.4, the alternative filter implementations used in this chapter, arising in the two-variant detector scheme, are investigated. The simulation results and discussions are provided in Section 4.5, followed by the concluding remarks in Section 4.6.

4.2 System Model

In this section, the mathematical model used in this chapter will be explained. In the first part, the MIMO channel is constructed and the necessary assumptions are made. In the second part, the analog beamformers are constructed and the different scenarios investigated in this chapter are explained.

4.2.1 MIMO Channel

In this chapter, following the general system model introduced in Chapter 2, there are M OFDM symbols with duration T_s in a CPI, among which the reflected complex gain from any scatterer is highly correlated, enabling Doppler processing operations. On the other hand, the reflected complex gains from the scatterers are independent and identically distributed (iid) from CPI to CPI (Swerling-1 model). The parameters of the scatterers (range, angle, velocity) are assumed to be the same through $\mathcal{T}$ CPIs, which are called frames, with duration T_f, in this chapter. The subcarrier selection strategy is similar to the one explained in Chapter 2. Since this thesis focuses on radar signal processing, the word 'subcarriers' will always mean the N ISAC subcarriers used for radar purposes, unless otherwise is clearly stated. The subcarrier spacing is Δf and the carrier frequency of n^{th} subcarrier is $f_n = f_1 + (n-1)\Delta f$, for $n = 1, 2, \cdots, N$. This means that total RF bandwidth is $W = N\Delta f$ and the center carrier frequency is $f_c = (f_1 + f_N)/2$. Corresponding to these subcarrier frequencies, the wavelength of n^{th} subcarrier is $\lambda_n = c_0/f_n$, where c_0 is the speed of light in free space.

In this chapter, MIMO capability enables the system to resolve the scatterers in angle domain. In this regard, the UITs are considered to be large objects, possibly covering multiple range and angle resolution cells. For the sake of simplicity, the targets are approximated as collections of several point scattering centers. There are multiple UITs in the section of interest, each having a specific number of scatterers, which depends on the size of the corresponding UIT. A total of $\mathcal{K}$ scatterers exist in the scenario and in the rest of the chapter, k is the index used for counting the scatterers. The k^{th} scatterer is assumed to be at range r_k, corresponding to a round-trip time of $\tau_k = 2r_k/c_0$, and has a radial velocity of v_k, corresponding to a normalized Doppler frequency of $\rho_k^{\mathcal{C}} = (2v_k/\lambda_c){T_s}^2$, where $\lambda_c = c_0/f_c$ is the wavelength corresponding to the center carrier frequency. The superscript $\{\cdot\}^{\mathcal{C}}$ indicates that the variable is related to the clutters, and the superscript $\{\cdot\}^{\mathcal{S}}$ will indicate that the variable is related to the SoI from UL users in the rest of this chapter.

It is assumed that there are N_t Tx antennas, N_r Rx antennas, D_t Tx RF chains and D_r Rx RF chains in the system. The Tx and Rx analog beamformers are denoted as $\mathbf{W}_t$ and $\mathbf{W}_r$, respectively. Therefore, for the n^{th} subcarrier and m^{th} OFDM symbol, if the full-dimension transmitted symbols from the antennas are represented with a $N_t \times 1$ vector $\overline{\mathbf{x}}_{nm}$, then the transmitted symbol stream can be represented with a $D_t \times 1$ vector $\mathbf{x}_{nm}$, where $\overline{\mathbf{x}}_{nm} = \mathbf{W}_t^* \mathbf{x}_{nm}$. Similarly, if the full-dimension received symbols at the antennas are represented with a $N_r \times 1$ vector $\overline{\mathbf{y}}_{nm}$, then the received symbol stream can be represented with a $D_r \times 1$ vector $\mathbf{y}_{nm} = \mathbf{W}_r^{\text{H}} \overline{\mathbf{y}}_{nm}$. Using these variables, the frequency-domain MIMO channel matrix of the k^{th} scatterer for n^{th} subcarrier and m^{th} OFDM symbol can be written as:

$$\begin{aligned} \mathbf{H}_{knm} &= \alpha_{km} e^{j2\pi\rho_k^{\mathcal{C}} m} \mathbf{H}_{kn} \\ &= \alpha_{km} e^{j2\pi\rho_k^{\mathcal{C}} m} [\mathbf{W}_r^{\text{H}} \mathbf{a}_{kn} \mathbf{b}_{kn}^{\text{T}} \mathbf{W}_t^* e^{-j2\pi\tau_k \Delta f n}] \end{aligned} \tag{4.1}$$

where $\mathbf{a}_{kn}$ and $\mathbf{b}_{kn}$ are the receive and transmit steering vectors towards k^{th} scatterer at n^{th} subcarrier. The difference between $\mathbf{H}_{knm}$ and $\mathbf{H}_{kn}$ is that the m-dependent random and deterministic phases are separated from $\mathbf{H}_{kn}$, making it the $D_r \times D_t$ effective

[2] The Doppler shift is clearly dependent on the carrier frequency, and this results in different Doppler shifts occur in different subcarriers. However, when the center frequency f_c and bandwidth W of the system satisfies $f_c/W > M/2$, the maximum amount of Doppler shift across subcarriers becomes insignificant with respect to the Doppler resolution of the system. In this thesis, this inequality is assumed to be satisfied so that the normalized Doppler frequency is not dependent on subcarrier index.

MIMO channel, including only range and angle information of the scatterer after dimensions are reduced via analog beamforming. The range and angle parameters of scatterers are assumed to be stationary during M symbols as explained before; therefore, $\mathbf{H}_{kn}$ has no m index inside it. This separation is indeed beneficial because the phases in the received signal due to the range or angle of the scatterers are assumed to be deterministic, but the phases across OFDM symbols are assumed to be realizations of a random process as the scatterers are assumed to have Doppler spreads.

The gain of the echo signals from the k^{th} UIT is denoted as $\gamma_k^{\mathcal{C}}$ and it is included in the random phase parameter for the sake of notational simplicity. Then, the random variable α_{km} can be described as the reflected complex gain, depicting the complex amplitude and Doppler spread information of the scatterer, and $e^{j2\pi\rho_k^{\mathcal{C}}m}$ is for the mean Doppler shift of the scatterer. It should be noted that α_{km} is a realization of a stationary slow-time random process with a given power spectral density (PSD) along the Doppler axis. Let's define

$$\boldsymbol{\alpha}_k \triangleq [\alpha_{k1}\ \alpha_{k2}\ \cdots\ \alpha_{kM}]^{\mathrm{T}}, \mathbf{R}_k^{\boldsymbol{\alpha}} \triangleq \mathbb{E}\left\{\boldsymbol{\alpha}_k \boldsymbol{\alpha}_k^{\mathrm{H}}\right\}, \tag{4.2}$$

where all of the diagonal elements of $\mathbf{R}_k^{\boldsymbol{\alpha}}$ are assumed to be equal to $\gamma_k^{\mathcal{C}} \triangleq \mathbb{E}\{|\alpha_{km}|^2\}$ because the average power of the returns from the scatterer is assumed to be the same for all M symbols. The off-diagonal elements of $\mathbf{R}_k^{\boldsymbol{\alpha}}$ determines the slow-time correlation properties of the k^{th} UIT[3].

The receive and transmit digital steering vectors towards a scatterer at angle θ from the boresight of ISAC antenna array at the n^{th} subcarrier are denoted as $\mathbf{a}_n(\theta)$ and $\mathbf{b}_n(\theta)$, which are $N_r \times 1$ and $N_t \times 1$ vectors, respectively. When the steering vectors are for k^{th} UIT or u^{th} user, the angle is not explicitly shown and simply $\mathbf{a}_{kn}$ or $\mathbf{b}_{un}$ are used for notational simplicity. The reader should understand that $\mathbf{a}_{kn}$ is the steering vector for k^{th} UIT, which is at angle θ_k. For example, if the inter-antenna spacing in the antenna array is denoted as d, the receive steering vector can be written as:

$$\mathbf{a}_n(\theta) = \left[1 \quad e^{j\frac{2\pi}{\lambda_c}\frac{f_n}{f_c}d\sin\theta}\ \cdots\ e^{j\frac{2\pi}{\lambda_c}\frac{f_n}{f_c}N_r d\sin\theta}\right]^{\mathrm{T}} \tag{4.3}$$

which depends on n due to the beam-squint effect. The (f_n/f_c) ratio determines how much the wave number shifts from its center value $(2\pi/\lambda_c)$, and its value is assumed

[3] The random variable α_{km} is chosen to be a realization of a zero-mean complex Gaussian process, whose PSD function is Gaussian shaped with a variance of $(\sigma_k^{\mathcal{C}})^2$ and mean of zero. Such processes can be easily shown to have their autocorrelation matrix entries as $[\mathbf{R}_k^{\boldsymbol{\alpha}}]_{(i,j)} = \gamma_k^{\mathcal{C}} \exp(-2\pi^2(\sigma_k^{\mathcal{C}})^2(i-j)^2 T_s^2)$.

to be unity in most scenarios. However, when W is comparable with f_c, it can be seen that $1-(W/2f_c) \leq (f_n/f_c) \leq 1+(W/2f_c)$. Namely, as the (f_c/W) ratio decreases, even a single point scatterer can produce echoes spread over a wide angular sector, meaning that beam-squint can negatively affect angular processing and impair sensing performance if not handled correctly, as will be shown in Sections 4.4 and 4.5.

Along with the UITs, a total of $\mathcal{U}$ single antenna communication users are assumed to be present in the section of interest. The u^{th} user sends the frequency domain communication symbol j_{unm} at n^{th} subcarrier in m^{th} symbol duration. Similar to the definition in (4.1), the effective channel vector for the u^{th} user at n^{th} subcarrier for m^{th} symbol is defined as:

$$\mathbf{g}_{unm} \triangleq \beta_{um} e^{j2\pi\rho_k^{\mathcal{S}} m} \mathbf{g}_{un} = \beta_{um} e^{j2\pi\rho_k^{\mathcal{S}} m} [\mathbf{W}_r^{\text{H}} \mathbf{a}_{un}] \tag{4.4}$$

where $\mathbf{g}_{un}$ is the $D_r \times 1$ effective single-input multiple-output (SIMO) channel including complex channel and angle information of the user after dimensions are reduced via analog beamforming. Note that this channel is also assumed to be stationary during M symbols, therefore it has no m index inside it. The random variable β_{um} is the received complex gain including the received power and Doppler spread information of the user channel and $e^{j2\pi\rho_k^{\mathcal{S}} m}$ is for the mean Doppler shift of the user[4]. Similar to (4.2),

$$\boldsymbol{\beta}_u \triangleq [\beta_{u1}\ \beta_{u2}\ \cdots\ \beta_{uM}]^{\text{T}}, \mathbf{R}_u^{\boldsymbol{\beta}} \triangleq \mathbb{E}\left\{\boldsymbol{\beta}_u \boldsymbol{\beta}_u^{\text{H}}\right\}, \tag{4.5}$$

where all of the the diagonal elements of $\mathbf{R}_u^{\boldsymbol{\beta}}$ are assumed to be equal to $\gamma_u^{\mathcal{S}} \triangleq \mathbb{E}\{|\beta_{um}|^2\}$[5].

Based on the previous definitions, the $D_r \times 1$ received signal vector $\mathbf{y}_{nm}$ at the radar transceiver can be written as:

$$\mathbf{y}_{nm} = \underbrace{\mathbf{H}_{0nm}\mathbf{x}_{nm}}_{\mathbf{t}_{nm}} + \underbrace{\underbrace{\sum_{k=1}^{\mathcal{K}} \mathbf{H}_{knm}\mathbf{x}_{nm}}_{\mathbf{c}_{nm}} + \underbrace{\sum_{u=1}^{\mathcal{U}} \mathbf{g}_{unm} j_{unm}}_{\mathbf{s}_{nm}}}_{\boldsymbol{\psi}_{nm}} + \mathbf{n}_{nm} \tag{4.6}$$

[4] Since it is assumed that the synchronization is done for the SoI channel, the complex phase coming from propagation delay is not included in $\mathbf{g}_{unm}$. On the other hand, angular coherence time is assumed to be much larger than the CPI so that $\mathbf{g}_{un}$ and $\mathbf{H}_{kn}$ stay the same for M symbol durations.

[5] The random variable β_{um} is chosen to be a realization of a zero-mean complex Gaussian process, whose PSD function is Gaussian shaped with a variance of $(\sigma_u^{\mathcal{S}})^2$ and mean of zero, whose autocorrelation matrix becomes $[\mathbf{R}_u^{\boldsymbol{\beta}}]_{(i,j)} = \gamma_u^{\mathcal{S}} \exp(-2\pi^2(\sigma_u^{\mathcal{S}})^2(i-j)^2 T_s^2)$.

where $\mathbf{x}_{nm}$ is the $D_t \times 1$ vector of Tx streams to DL users, and j_{unm} is the Rx symbol received from u^{th} UL user, at n^{th} subcarrier in m^{th} OFDM symbol. $\mathbf{t}_{nm}$, $\mathbf{c}_{nm}$, $\mathbf{s}_{nm}$ and $\mathbf{n}_{nm}$ are $D_r \times 1$ vectors who represent the received signal vector from the IT, total received signal vector from the UITs, total received signal vectors from UL user signals, and noise, respectively. $\mathbf{H}_{0nm}$ is the effective MIMO channel for the IT, whose expression is the same as the channels for UITs, given in (4.1). $\boldsymbol{\psi}_{nm}$ is the total additive interference on the IT's response, namely the clutter, noise and the communication SoI. The noise vector $\mathbf{n}_{nm}$ is also defined after beamforming operation, namely it consists of D_r circularly symmetric zero-mean Gaussian random variables with covariance $\sigma_n^2 \mathbf{W}_r^{\text{H}} \mathbf{W}_r$. For notational simplicity, let's define:

$$\begin{aligned}
&\mathbf{X}_n \triangleq [\mathbf{x}_{n1}\ \mathbf{x}_{n2}\ \cdots\ \mathbf{x}_{nM}], && \mathbf{T}_n \triangleq [\mathbf{t}_{n1}\ \mathbf{t}_{n2}\ \cdots\ \mathbf{t}_{nM}],\\
&\mathbf{C}_n \triangleq [\mathbf{c}_{n1}\ \mathbf{c}_{n2}\ \cdots\ \mathbf{c}_{nM}], && \mathbf{S}_n \triangleq [\mathbf{s}_{n1}\ \mathbf{s}_{n2}\ \cdots\ \mathbf{s}_{nM}],\\
&\mathbf{N}_n \triangleq [\mathbf{n}_{n1}\ \mathbf{n}_{n2}\ \cdots\ \mathbf{n}_{nM}], && \boldsymbol{\Psi}_n \triangleq [\boldsymbol{\psi}_{n1}\ \boldsymbol{\psi}_{n2}\ \cdots\ \boldsymbol{\psi}_{nM}]\\
&\mathbf{Y}_n \triangleq [\mathbf{y}_{n1}\ \mathbf{y}_{n2}\ \cdots\ \mathbf{y}_{nM}], && \mathbf{J}_n \triangleq [\mathbf{j}_{1n}\ \mathbf{j}_{2n}\ \cdots\ \mathbf{j}_{\mathcal{U}n}]^{\text{T}}\\
&\mathbf{j}_{un} \triangleq [j_{un1}\ j_{un2}\ \cdots\ j_{unM}]^{\text{T}}. &&
\end{aligned} \tag{4.7}$$

In this chapter, the slow-time processing gain is included in the transmit beamformer and not visible in the transmitted symbols. Therefore, $D_t \times M$ DL transmit symbol matrix $\mathbf{X}_n$ and $\mathcal{U} \times M$ UL transmit symbol matrix $\mathbf{J}_n$ are normalized accordingly. The average power per stream per subcarrier is selected to be unity, therefore

$$\text{Tr}\{\mathbb{E}\left\{\mathbf{X}_n \mathbf{X}_n^{\text{H}}\right\}\} = D_t \tag{4.8}$$

and

$$\text{Tr}\{\mathbb{E}\left\{\mathbf{J}_n \mathbf{J}_n^{\text{H}}\right\}\} = \mathcal{U}. \tag{4.9}$$

To simplify the notation, four $M \times M$ diagonal matrices are defined next.

$$\mathbf{D}_k^{\mathcal{C}} \triangleq \text{diag}\{[1\ e^{j2\pi\rho_k^{\mathcal{C}}}\ \cdots\ e^{j2\pi(M-1)\rho_k^{\mathcal{C}}}]\}, \boldsymbol{\Lambda}_k^{\mathcal{C}} \triangleq \text{diag}\{\boldsymbol{\alpha}_k\} \tag{4.10}$$

are the matrices that represent the mean Doppler shift and the Doppler spread of the k^{th} scatterer. $\boldsymbol{\Lambda}_k^{\mathcal{C}}$ includes the amplitude information of the k^{th} scatterer as $\boldsymbol{\alpha}_k$ is the reflected complex gain vector as described before.

$$\mathbf{D}_u^{\mathcal{S}} \triangleq \text{diag}\{[1\ e^{j2\pi\rho_u^{\mathcal{S}}}\ \cdots\ e^{j2\pi(M-1)\rho_u^{\mathcal{S}}}]\}, \boldsymbol{\Lambda}_u^{\mathcal{S}} \triangleq \text{diag}\{\boldsymbol{\beta}_u\} \tag{4.11}$$

are the matrices that represent the mean Doppler shift and the Doppler spread of the u^{th} communication user, which have the same forms as $\mathbf{D}_k^{\mathcal{C}}$ and $\mathbf{\Lambda}_k^{\mathcal{C}}$.

Using (4.6), (4.7) and (4.10), $D_r \times M$ received symbol matrix $\mathbf{Y}_n$ is written and its elements can be defined as below[6]:

$$\mathbf{Y}_n = \mathbf{T}_n + \mathbf{\Psi}_n = \mathbf{T}_n + \underbrace{\sum_{k=1}^{\mathcal{K}} \mathbf{C}_{kn}}_{\mathbf{C}_n} + \underbrace{\sum_{u=1}^{\mathcal{U}} \mathbf{S}_{un}}_{\mathbf{S}_n} + \mathbf{N}_n \,, \tag{4.12}$$

where

$$\begin{aligned} \mathbf{T}_n &\triangleq \mathbf{H}_{0n}\mathbf{X}_n\mathbf{D}_0^{\mathcal{C}}\mathbf{\Lambda}_0^{\mathcal{C}}, \\ \mathbf{C}_{kn} &\triangleq \mathbf{H}_{kn}\mathbf{X}_n\mathbf{D}_k^{\mathcal{C}}\mathbf{\Lambda}_k^{\mathcal{C}}, \\ \mathbf{S}_{un} &\triangleq \mathbf{g}_{un}\mathbf{j}_{un}^{\mathrm{T}}\mathbf{D}_u^{\mathcal{S}}\mathbf{\Lambda}_u^{\mathcal{S}}. \end{aligned} \tag{4.13}$$

It should be noted that (4.12) can be written because the MIMO channel matrix $\mathbf{H}_{kn}$ defined in (4.1) and SoI channel vector $\mathbf{g}_{un}$ are assumed to stay the same for the duration of M symbols. The formation of the received symbol matrix $\mathbf{Y}_n$ from its components is visually shown in Figure 4.1.

4.2.2 Analog Beamformers

In this chapter, transmit and receive analog beamformers, $\mathbf{W}_t$ and $\mathbf{W}_r$, are adjusted separately. $\mathbf{W}_t(\mathbf{W}_r)$ is an $N_t \times D_t(N_r \times D_r)$ matrix, which is formed to cover the angular sector where DL (UL) users are located, and the UL and DL users may or may not be inside the same sector in a real-life application. Therefore, different scenarios in which the sectors fully overlap or do not overlap are investigated in the simulations section. Figure 4.1 shows how the Tx and Rx sectors, DL and UL users, UITs, and the IT can be located in an example scenario of partially overlapping Tx-Rx sectors.

[6] Eqs. (4.12) and (4.13) state that radial velocities of scatterers affect the model only through phase shifts across OFDM symbols. Other Doppler effects such as time scaling and ICI are ignored; time scaling is typically negligible, and ICI is avoided by assuming large Δf or small velocities, as reflected in (4.6) where $\mathbf{y}_{nm}$ depends only on $\mathbf{x}_{nm}$. Nonetheless, even under these assumptions, the unavoidable mismatch between $\mathbf{D}_k^{\mathcal{C}}$ and $\mathbf{D}_0^{\mathcal{C}}$, upon which the Doppler processing will be constructed, degrades the interference suppression capabilities and sensing performance, as will be discussed in Section 4.3.2.

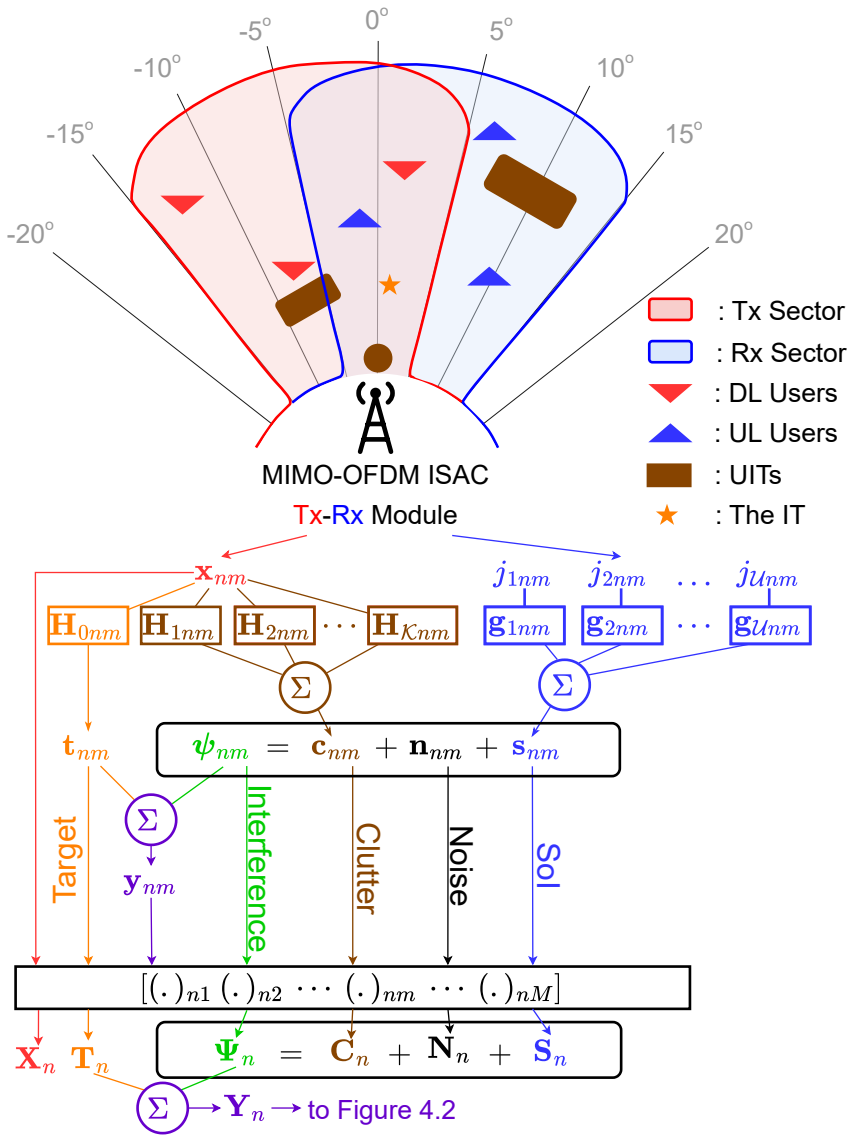


Figure 4.1: Visualization of Tx-Rx sectors, DL and UL users, UITs and the IT in an example scenario of partially overlapping Tx-Rx sectors (top), and diagram of transmitted and received data matrices (bottom).

To reduce the power fluctuations inside the angular sectors, the columns of $\mathbf{W}_t(\mathbf{W}_r)$ are selected to be the eigenvectors of the intended angular sector corresponding to $D_t(D_r)$ largest eigenvalues. The transmit power constraint is adjusted so that the transmit analog beamforming matrix satisfy $\mathrm{Tr}\{\mathbf{W}_t\mathbf{W}_t^{\mathrm{H}}\} = M$. This means that the system's slow-time processing gain is included through transmit beamforming, and the total transmit power is constrained. In the receiver part, however, to preserve the

second-order stationarity of the noise after receive beamforming, $\mathbf{W}_r$ is scaled so that $\mathbf{W}_r^{\mathrm{H}}\mathbf{W}_r = \mathbf{I}_{D_r}$ is satisfied.

4.3 Proposed Signal Processing Methods and Detector Structure

In this chapter, an IT is to be detected under the disruptive effects of UITs and UL users, by implementing knowledge-aided or adaptive detection strategies. In the given system model, detection will be conducted in range, angle and Doppler domains. To have a maximum-SINR filter for all domains, a $D_rNM \times D_rNM$ matrix must be known using the tracker or learned from the environment and its inverse must be taken in the filter implementation. Practically, this dimension is so large that neither effectively learning the matrix is possible before the channel decorrelates, nor is there enough processing power to implement this matrix inversion in real-time. Therefore, this article pursues a sub-optimal processing that separates range, angle and Doppler domains.

Due to possible beam-squint effects, MIMO processing should be done separately for each subcarrier, forcing angle processing to come before range processing. However, $D_rM \times D_rM$ matrix processing for each of the N subcarriers is still hard to work with. Besides, eliminating the Tx symbols at the first stage is crucial for OFDM radars, as the residual symbols would deteriorate the performance for the subsequent processing, as will be shown. For these reasons, a Doppler-Aware Code Bank is proposed as the first stage of the processing, as in [60, 65]. With DACB, M symbols of transmitted data are combined separately for each Doppler CUT, and their dimension is reduced to $D_t < M$. It should be noted that for classical phased-array systems with $D_t = 1$, this processing would be equivalent to slow-time match filtering, namely coherent combination of M slow-time samples into one scalar for each of the D_r receive streams. Mathematical details of the case in which $D_t = 1$ will be provided later in Section 4.3.2. In the MIMO case, the processing combines the slow-time samples into D_t dimensional vectors for each of the D_r receive streams, allowing transmit beamforming on the receiver side to utilize full MIMO gain of D_rD_t [60], while easing the computations on the subsequent processing.

After applying DACB, a novel Sequential Angle-Range Processing is proposed to combine data from $D_r D_t$ different streams and N different subcarriers into a single decision metric for the CUT. As described before, jointly and optimally combining $D_r D_t N$ amount of data is computationally burdensome, therefore MIMO processing is done separately for each subcarrier, and then the results for the subcarriers are combined. This sub-optimal method results in an SINR loss in some specific cases, therefore a two-variant detector scheme is proposed to overcome this challenge. The details of this detector scheme are explained in Section 4.3.3.

The output of the SARP stage is the decision metric for each CUT. This metric is then compared with the threshold and a decision is made on whether there is no detection (H_0 hypothesis) or detection (H_1 hypothesis). A block diagram showing the frame, symbol and subcarrier structures, the proposed signal processing methods starting from the observations $\mathbf{Y}_n$ up to the detector decisions, including the two-variant detector scheme, is given in Figure 4.2.

In the following part of this section, the proposed processing method will be investigated in more detail. First, the possible negative effects of channel Doppler will be explained and the assumptions for this work will be made. Next, the DACB will be explained and its interpretation will be provided. In the following part, why the proposed two-variant detector scheme is needed and how to apply it will be explained. Finally, the theoretical derivation of the SARP will be provided. Different detector structures shown in Figure 4.2 will be explained in Section 4.4.

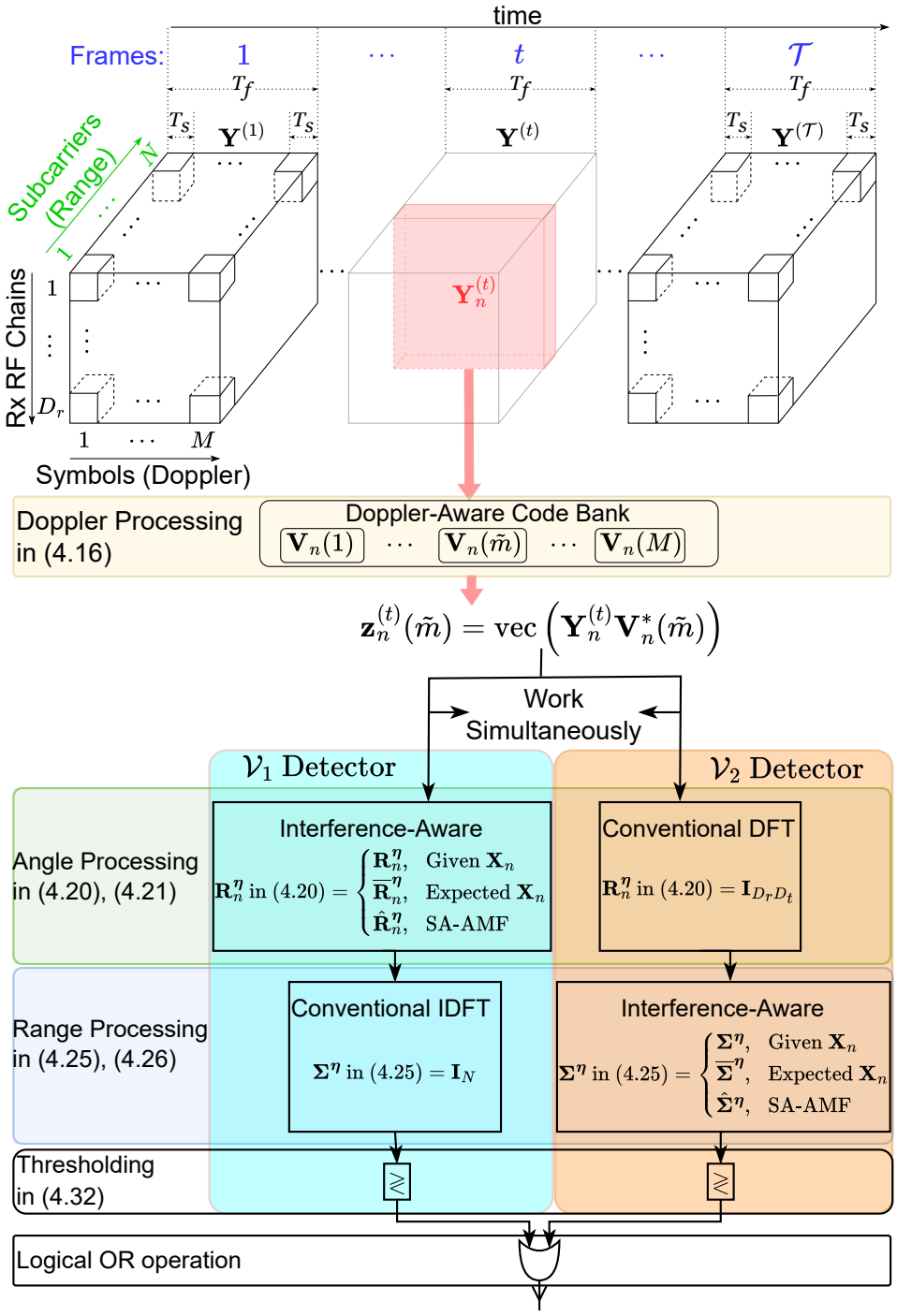


Figure 4.2: Block diagram of proposed frame, symbol and subcarrier structures and signal processing, including the two-variant detector scheme.

4.3.1 Negative Effects of Channel Doppler

The radial velocities of the targets cause three different effects on the received echo signals. The first effect is about the time scale of the signals. If the target is moving closer to the radar, the echo signal shrinks in time, and if the target moves away from the radar, the echo signal expands in time. This effect is significantly small for low-velocity targets, therefore it is usually ignored in the literature, as well as in this thesis.

The second effect is about the frequency of the echo signal. The echo signals from the targets moving closer to the radar have a slight increase in their frequency, and vice versa. This effect can be significant in some systems, especially those with multicarrier waveforms if the target velocities are high. For example, in OFDM radar systems, if the subcarrier frequency gap is comparable with the maximum Doppler frequency, echoes of one subcarrier can be received in the next one, causing the well-known problem of ICI. In the literature, there are lots of works focusing on ICI problem, some of them even exploit ICI to gain some advantages. [73, 124, 125] are some examples of such studies. However, the focus of this thesis is not on the ICI effect of moving targets with high velocity.

The third effect of moving targets in the echo signals is the phase difference between the consecutive pulses. This effect is the basis for almost all Doppler processing algorithms for pulsed Doppler radars. Depending on the total observation time on target, even small velocities can result in a detectable phase difference among pulses, making it possible to distinguish between different targets with different velocities. In conventional radars, this phase rotation is usually detected by DFT operation. If a target is at the center of a DFT bin, it can be detected with the corresponding Doppler filter, and it can be suppressed with other Doppler filters looking at other DFT bins. If a target is not at the center but on a fractional bin, then the target's detection probability would be the largest for the Doppler bin nearest to it. On the contrary, in OFDM-based MIMO ISAC systems, a target in a fractional Doppler bin can show itself in a completely irrelevant Doppler bin, because its Doppler response would be affected by the transmitted symbol sequence, if the symbols are not eliminated perfectly. This would cause both the target and the clutter to be spread over the whole Doppler spectrum.

Moreover, the residual signal-dependent interference spreads the clutter in angle and range domains too, making the interference suppression even harder.

The problem of symbol-dependent shift in Doppler phase is challenged in this thesis, distinguishing this work from most of the other works mentioned in the literature review part. In [125], the writers mention this problem and they propose a signal processing method to tackle the problem. They first combine the received signal samples in receive antenna domain (by angular DFT operation) and then apply element-wise division by the transmit symbols to get rid of them. In this thesis, on the other hand, the samples are first combined in Doppler domain (by slow-time DFT operation) but it is done in a way that the MIMO angular channel in both transmit and receive antenna domains is directly estimated. Therefore, it is managed to apply classical joint MIMO processing (and get the whole SINR improvement factor of both transmit and receive beamforming operations) in ISAC systems, which is not achieved in other works in the literature as far as it is observed.

4.3.2 Doppler-Aware Code Bank (DACB)

In this thesis, the signal processing includes two stages, namely the channel estimation and parameter extraction, as explained in Chapter 2. When (4.12) and (4.13) are investigated, it is seen that to reach the channel $\mathbf{H}_{0n}$ of the IT for detection, the transmitted symbols and Doppler effects must be removed from the received signal. For SISO channels, where $\mathbf{H}_{0n}$ is a scalar for each subcarrier and OFDM symbol, the suppression of $\mathbf{X}_n$ can be done via Hadamard division, as in [80, 118], and as explained in Chapter 3 of this thesis. However in MIMO channels, as seen in (4.13), Hadamard division cannot give a good estimate of $\mathbf{H}_{0n}$. In this chapter, the channel is estimated using LS approach, as in [65], but the Doppler processing is also conducted during the channel estimation process. In this sense, Doppler parameter extraction step is embedded into the channel estimation in this chapter, due to the intrinsic properties of the proposed signal model in matrix form.

For the preprocessing, and for the rest of the chapter, it is assumed that the CUT is at $\tilde{n}^{\text{th}}$ range bin, $\tilde{m}^{\text{th}}$ Doppler bin and $\tilde{\theta}^{\text{th}}$ angle bin. In general, $\tilde{n}, \tilde{m}$ and $\tilde{\theta}$ can be fractional bins. Parentheses notation, e.g. $(\tilde{m})$, will be explicitly used when it is

needed to clarify the dependence of a variable to any of the CUT parameters, like $\tilde{m}$ in this example. The $M \times D_t$ preprocessing matrix for $\tilde{m}^{\text{th}}$ Doppler bin is defined as:

$$\mathbf{V}_n(\tilde{m}) \triangleq \mathbf{D}_{\tilde{m}}^{T}(\mathbf{X}_n^{\#})^{*} = \mathbf{D}_{\tilde{m}}^{\mathrm{T}}\mathbf{X}_n^{\mathrm{T}}(\mathbf{X}_n^{*}\mathbf{X}_n^{\mathrm{T}})^{-1} \tag{4.14}$$

where $\mathbf{X}_n^{\#} = \mathbf{X}_n^{\mathrm{H}}(\mathbf{X}_n\mathbf{X}_n^{\mathrm{H}})^{-1}$ is pseudo-inverse of $\mathbf{X}_n$ and

$$\mathbf{D}_{\tilde{m}} = \mathrm{diag}\{1 \; e^{j2\pi\tilde{m}/M} \; e^{j2\pi 2\tilde{m}/M} \; \cdots \; e^{j2\pi(M-1)\tilde{m}/M}\} \tag{4.15}$$

is the Doppler preprocessing matrix for $\tilde{m}^{\text{th}}$ Doppler bin.

After the preprocessing operation, the $D_r \times D_t$ MIMO channel estimate at n^{th} subcarrier for the CUT becomes:

$$\begin{aligned}
&\widehat{\mathbf{H}}_n(\tilde{m}) \triangleq \mathbf{Z}_n(\tilde{m}) \triangleq \mathbf{Y}_n\mathbf{D}_{\tilde{m}}^{H}\mathbf{X}_n^{\#} = \mathbf{Y}_n\mathbf{V}_n^{*} \\
&= \mathbf{T}_n\mathbf{V}_n^{*} + \mathbf{C}_n\mathbf{V}_n^{*} + \mathbf{S}_n\mathbf{V}_n^{*} + \mathbf{N}_n\mathbf{V}_n^{*} = \mathbf{T}_n\mathbf{V}_n^{*} + \mathbf{\Psi}_n\mathbf{V}_n^{*} \\
&= \mathbf{H}_{0n}\mathbf{X}_n\mathbf{D}_0^{\mathcal{C}}\mathbf{\Lambda}_0^{\mathcal{C}}\mathbf{D}_{\tilde{m}}\mathbf{X}_n^{\#} + \sum_{k=1}^{\mathcal{K}}\mathbf{H}_{kn}\mathbf{X}_n\mathbf{D}_k^{\mathcal{C}}\mathbf{\Lambda}_k^{\mathcal{C}}\mathbf{D}_{\tilde{m}}\mathbf{X}_n^{\#} \\
&+ \sum_{u=1}^{\mathcal{U}}\mathbf{g}_{un}\mathbf{j}_{un}^{\mathrm{T}}\mathbf{D}_u^{\mathcal{S}}\mathbf{\Lambda}_u^{\mathcal{S}}\mathbf{D}_{\tilde{m}}\mathbf{X}_n^{\#} + \mathbf{N}_n\mathbf{D}_{\tilde{m}}\mathbf{X}_n^{\#}
\end{aligned} \tag{4.16}$$

Here are some remarks about the preprocessing, DACB:

- The dimension of the processed data in each subcarrier is reduced from $D_r \times M$ to $D_r \times D_t$ with this preprocessing, meaning that M OFDM symbols are coherently combined but there are still D_t dimensions to achieve subsequent MIMO processing, explained in Section 4.3.4.

- The Doppler processing and the elimination of Tx symbols are coupled. More specifically, $M \geq D_t$ must be satisfied to effectively find $\mathbf{X}_n^{\#}$ to eliminate the Tx symbols, but when M symbols are processed together, Doppler effects changes the slow-time codes of Tx symbols. This is a unique property of OFDM-based MIMO ISAC systems.

- If the Doppler processing for the CUT matches the Doppler of the IT ($\mathbf{D}_{\tilde{m}} = (\mathbf{D}_0^{\mathcal{C}})^{*}$), and there is no Doppler spread of the target ($\mathbf{\Lambda}_0^{\mathcal{C}} = \mathbf{I}_M$), then $\mathbf{T}_n\mathbf{V}_n^{*} = \mathbf{H}_{0n}$, which means that the channel of the IT at the CUT to be used in hypothesis testing is extracted.

- However, it is almost always the case that there are other scatterers in the environment which have different Doppler shifts and Doppler spreads, meaning that there will be a Doppler mismatch between the preprocessing and some of the scatterers in the environment ($\mathbf{D}_{\tilde{m}} \neq (\mathbf{D}_k^{\mathcal{C}})^*$ and/or $\mathbf{\Lambda}_k^{\mathcal{C}} \neq \mathbf{I}_M$ for some ks). Therefore, the second term in (4.16) cannot be simplified to $\mathbf{H}_{kn}$.

- If $D_t = 1$, namely the system is not MIMO but a classical phased-array system, then $\mathbf{X}_n \mathbf{D}_k^{\mathcal{C}} \mathbf{\Lambda}_k^{\mathcal{C}} \mathbf{D}_{\tilde{m}} \mathbf{X}_n^{\#}$ in (4.16) would be a scalar and the Doppler mismatch effect would not change the matrix structure of the clutter channel $\mathbf{H}_{kn}$ (UIT channels). However in MIMO systems, $\mathbf{H}_{kn}$ is multiplied from right with a matrix dependent on $\mathbf{X}_n$. This means that both angle and range information of the clutter are disturbed due to the Doppler mismatch in the preprocessing stage.

- As will be shown in (4.31), Doppler mismatch results in a Hadamard product-based disturbance in the range response of the scatterers. If this effect is taken into consideration, it acts as a diversity in Doppler domain and results in an increased output SINR (due to clutter suppression in Doppler domain). If this effect is overseen, it makes the clutter spread over the whole range spectrum, disables the range processing to suppress the clutter and results in a reduced output SINR.

- Doppler mismatch also affects the angular response of the scatterers, which can be seen when (4.23) is investigated, but the details are not written in this thesis for the sake of neatness. The angular responses of the scatterers are linearly transformed due to the Doppler mismatch, which is also dependent on $\mathbf{X}_n$. Similar to the range processing part, detectors that take this effect into consideration achieve greater clutter suppression with MIMO filters.

4.3.3 Two-Variant Detector Scheme

As explained before, DACB is followed by sequential MIMO and range processing. In practice, using max-SINR filters for both MIMO and range processings separately rather than using a joint max-SINR filter can cause a performance degradation. This

is because the MIMO filter at the first stage tries to suppress the clutter without considering that there will be another filter which can also suppress the clutter. If the IT is angularly close to the clutter, it would also be suppressed to a level under the noise level, and range processing cannot do anything to increase the SINR. In other words, first stage can lose the useful information that second stage can exploit in order to maximize its own output SINR. Using jointly-optimal range-angle filter can solve this problem easily, but this is not realizable in real-time as explained before. Therefore, another suboptimal detector scheme is proposed in this chapter in order to get rid of this specific problematic case.

In the proposed detection scheme, two different detectors are utilized simultaneously and their detection results are combined (with or operation). The first set of detectors, identified with $\mathcal{V}_1$, use an interference-aware processing in MIMO domain and conventional IDFT processing in range domain. The other set of detectors, identified with $\mathcal{V}_2$, use conventional DFT processing in MIMO domain and an interference-aware processing in range domain. This way, in both angle and range domains, the max-SINR filters can use all useful information about the interference, not affecting each other. The working principle of this detector scheme is shown in Figure 4.2. In the following parts of this subsection, the need for using two-variants detector scheme will be deeply investigated and the two variants will be separately clarified. Details of the interference-aware processing will be given in Section 4.3.4.

4.3.3.1 The Need for Two-Variant Detector Scheme

In this part of the section, the suboptimality of the sequential angle-range processing will be clarified. It is assumed that clutter (UITs in this thesis) statistics in range and angle domains are stationary during the CPI. On the other hand, it is also assumed that covariance information about the range and angle of the UITs is either given to the receiver side (from a tracker), or can be adaptively estimated. Then, under these circumstances, the complete $D_r D_t N \times D_r D_t N$ range-angle covariance information could have been used to get the SINR-maximizing filters. This method is depicted as the "optimal" method because it maximizes the SINR at the filter output. However, there are two major concerns in this type of processing. Firstly, the

$D_r D_t N \times D_r D_t N$ covariance would depend on the transmitted symbols $\mathbf{X}_n$, and therefore would change for each OFDM symbol. Since the filters need to get the inverse of this matrix, the computational cost would be overwhelmingly high. Secondly, let's assume that an average or adaptive filter would be used in order to overcome the computational problems. In this case, since the number of elements to be estimated is still large (on the order of $D_r^2 D_t^2 N^2$), a large number of symbols would be required in a CPI. This would bring an additional computational cost, along with the fact that stationary clutter parameters assumption would be unrealistic. Because of these two reasons, it is proposed to process angle and range information sequentially. By doing this, $D_r D_t \times D_r D_t$ matrix inverses are taken N times and $N \times N$ matrix inverse is taken only once per frame, in the most complicated detector proposed. The ease of computation comes with the cost that the processing is now suboptimal.

The suboptimality of the SARP will be demonstrated in this paragraph. Consider that the target of interest (IT in this thesis) is located at 1 degrees and 50 meters from the radar transceiver. On top of this target, there is a powerful clutter source (a UIT) at 0 degrees and 5 meters from the radar. Assume that the range resolution of the radar is much smaller than these distances, e.g., 1 meters. For such a system, if both angle and range information are optimally used in the detector, the target should be easily detected because the range of the clutter is far away from the range of the target. However, if the angle processing is done without considering the range information, the processor would try to put a null at the direction of the clutter, which is around 0 degrees, but the target echo would also be nullified in the process because its angle is close to the clutter's angle. This problem is visualized in Figure 4.3.

In Figure 4.3, a toy example is visualized. There is only one point scatterer as UIT, and it is located at 0 degrees and 10^{th} range bin, while the CUT range is at 0^{th} range bin, and CUT angle changes between -3 and 3 degrees. It is also assumed that Doppler processing is perfectly done. Other parameters are the same as the remaining parts of this chapter, namely $N = 32, D_r = D_t = 10, N_r = N_t = 64$. The blue line in Figure 4.3 represents the SINR improvement factor when the max-SINR angle filter is followed by the max-SINR range filter. It can be seen that if the IT (CUT) is located near the UIT, the SINR drops significantly, even if the ranges of the IT and the UIT are widely separated. It should be noted that when the IT is exactly

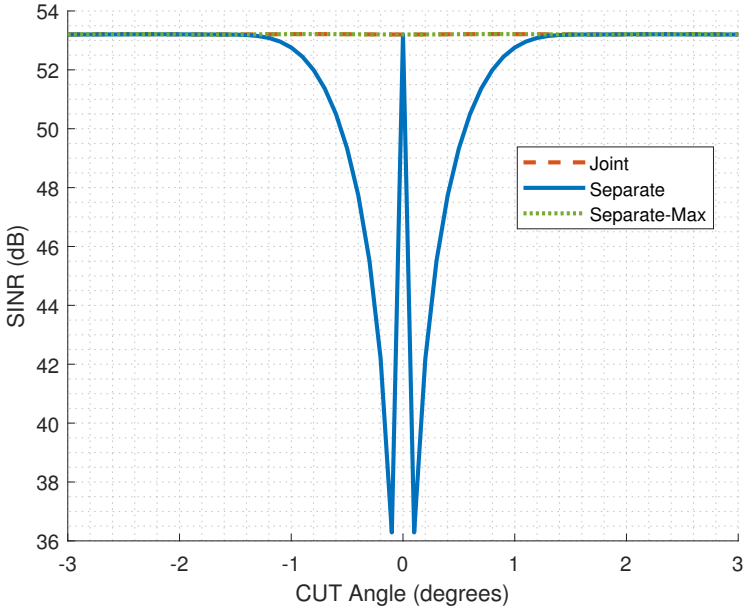


Figure 4.3: SINR vs CUT angle graphs for a fully-overlapping toy-example scenario, CUT Range bin: 0, UIT Range bin: 10, UIT Angle: 0 degrees.

on top of the UIT, the max-SINR angle filter does not eliminate the target itself, and the max-SINR range filter works properly to eliminate the clutter. However, this exact match is unlikely to happen in real life, meaning that the suboptimality of this method could result in serious SINR degradation in some scenarios. The red dashed line in Figure 4.3 represents the joint max-SINR filter. It can be seen that it does not have the SINR drop issue, as expected, but it requires a long computation time compared to other methods. Lastly, the green dotted line in Figure 4.3 represents the solution proposed in this chapter to overcome the SINR drop problem without significantly increasing the computational burden. In this method, two different SINR values are found and the maximum of them is selected. One value is found after applying max-SINR angle filter and conventional IDFT range filter, and the other value is found after applying conventional DFT angle filter and max-SINR range filter. It can be seen that the method of selecting the higher SINR value can reach the optimum max-SINR performance in some toy-example cases, with significantly easier computations.

In order to overcome this SINR drop issue, similar to the toy-example case, the two-variant detector scheme is proposed in this chapter. This scheme suggests that two different detectors work simultaneously, and their detection outputs are combined

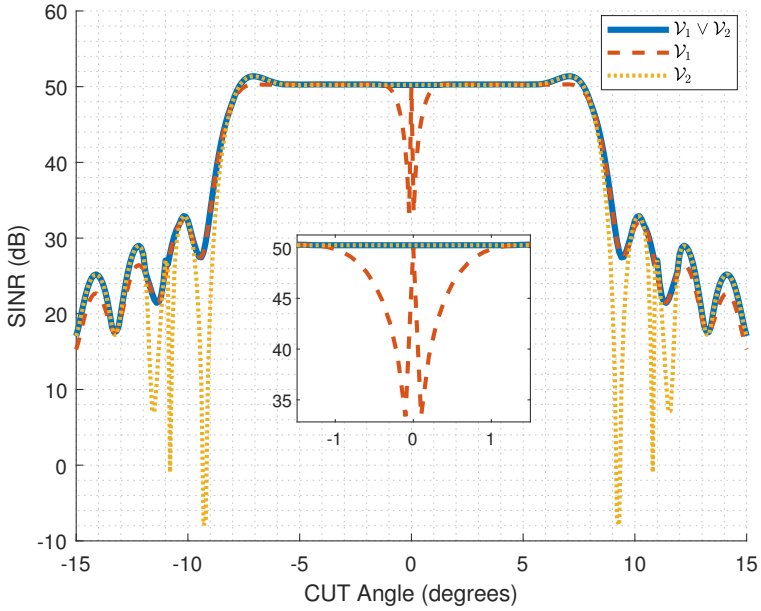


Figure 4.4: SINR vs CUT angle graphs for fully-overlapping scenarios, CUT Range bin: 0, CUT Doppler bin: 0 (0 m/s), UIT Range bin: 10, UIT Doppler bin: 0 (0 m/s), UIT Angle: 0 degrees.

with a logical OR operator. In other words, if any of the detectors detect the target, the final decision would be a detection; if both detectors reject a detection, the final decision would be no detection (this kind of detection would result in a slight increase in the false-alarm probability, and this increase is taken into account in the simulation results section of this chapter). These two detectors are called $\mathcal{V}_1$ and $\mathcal{V}_2$ in this chapter. $\mathcal{V}_1$ detectors use max-SINR angle filters and conventional IDFT range filters. $\mathcal{V}_2$ detectors use conventional DFT angle filters and max-SINR range filters. This would suggest that $\mathcal{V}_1$ detectors are better in eliminating clutter in angle dimension, while $\mathcal{V}_2$ detectors are better in eliminating clutter in range dimension. By combining these two detectors, the clutter can be suppressed if it is separated from the IT in at least one dimension. The individual performances of the $\mathcal{V}_1$ and $\mathcal{V}_2$ detectors are provided in Figure 4.4.

It can be seen in Figure 4.4 that $\mathcal{V}_1$ detector loses performance when the IT angle is around the UIT angle because of the reasons explained before. However, $\mathcal{V}_2$ detector successfully eliminates the clutter around that region because the IT and the UIT are far away from each other in range domain. On the other hand, there are also some regions that $\mathcal{V}_1$ outperforms $\mathcal{V}_2$. The logical OR combination of these two detectors

is drawn in blue line in Figure 4.4, which represents the maximum of these two SINR graphs. It can be seen that each detector compensates for the other's failures. In the rest of this chapter, only the combined detectors are given in the simulation results, because the figures would be significantly crowded if both $\mathcal{V}_1$ and $\mathcal{V}_2$ of all detectors were included in the figures. Besides this, $\mathcal{V}_1$ and $\mathcal{V}_2$ detectors are never intended to work separately, therefore their separate performances are of little importance and omitted in the simulation results.

4.3.3.2 $\mathcal{V}_1$ Detectors

The first set of detectors, which is called as $\mathcal{V}_1$ detectors, uses conventional IDFT for range processing. In other words, they select the range covariance matrix as identity matrix when calculating the range processing filter $\mathbf{u}$ in (4.25), in Section 4.3.4. For MIMO processing part, three different filter implementations are investigated in this chapter, as shown in Figure 4.2. It should be noted that if the beam-squint effect is neglected, the order of MIMO and range processings of $\mathcal{V}_1$ detectors can be changed. In other words, without the beam-squint effects, conventional IDFT in range domain can be applied directly to $\{\mathbf{Z}_n\}$ and MIMO processing can be applied to each subcarrier afterward, without any change in the resultant detection metrics.

4.3.3.3 $\mathcal{V}_2$ Detectors

The second set of detectors in the two-variant detector scheme, $\mathcal{V}_2$ detectors, use conventional DFT for MIMO processing. Namely, they select the angle covariance matrix as identity matrix in (4.20), in Section 4.3.4. For range processing part, three different filter implementations are investigated in this chapter, as shown in Figure 4.2.

It should be noted that the two-variant detector scheme does not suggest only one of these detectors is selected and utilized. Instead, both detectors are working simultaneously and their decisions are combined. In general, $\mathcal{V}_1$ detectors are better at suppressing clutter in angle domain, and $\mathcal{V}_2$ detectors are better at suppressing clutter in range domain. When utilized together, they compensate for each other's weaknesses and suppress clutter effectively in both domains.

4.3.4 Interference-Aware Sequential Angle-Range Processing

In the first signal processing stage, channel estimation is done via LS method and Doppler parameter of the CUT is used simultaneously. As the next step of processing, angle and range information of the CUT should be used to extract the whole useful information from the channel. To this end, spatial processing is applied for each subcarrier to resolve any beam-squint effect before combining the symbols in range domain. As seen in Figure 4.2, three different filters are proposed for spatial processing for $\mathcal{V}_1$ detectors and three different filters are proposed for range processing for $\mathcal{V}_2$ detectors. These filters are common in the sense that they are all interference-aware, meaning that they use the prior covariance information of the UITs, possibly coming from the tracker or obtained from the training data adaptively, with the aim of increasing output SINR. What differentiates the proposed filters from each other is the covariance matrices they use. The conventional DFT and IDFT filters do not depend on any information about UITs; however, they can be written as a special case of the proposed filters when the covariances are selected to be identity matrices. Therefore, the filter structures explained in this section will be the basis for all detectors that are investigated in this chapter, only difference between them being the selection of covariance matrices.

The spatial filter at each subcarrier is derived as follows. At each subcarrier, the MIMO channel is a $D_r \times D_t$ matrix and to jointly use all elements of this matrix, vectorization is used. Define the vectorized forms of the matrices in (4.16) as:

$$\begin{aligned}
\boldsymbol{\phi}_n &\triangleq \mathrm{vec}\{\mathbf{T}_n \mathbf{V}_n^*\} \triangleq \overline{\mathbf{V}}_n^{\mathrm{H}} \mathrm{vec}\{\mathbf{T}_n\}, \\
\boldsymbol{\eta}_n &\triangleq \mathrm{vec}\{\boldsymbol{\Psi}_n \mathbf{V}_n^*\} \triangleq \overline{\mathbf{V}}_n^{\mathrm{H}} \mathrm{vec}\{\boldsymbol{\Psi}_n\}, \\
\mathbf{z}_n &\triangleq \mathrm{vec}\{\mathbf{Z}_n\} = \boldsymbol{\phi}_n + \boldsymbol{\eta}_n
\end{aligned} \tag{4.17}$$

where

$$\overline{\mathbf{V}}_n = \mathbf{V}_n \otimes \mathbf{I}_{D_r} \tag{4.18}$$

is $MD_r \times D_t D_r$ effective preprocessing matrix which is defined for notational simplicity in the rest of the chapter. Let's define the result of the processing at the n^{th} subcarrier as:

$$r_n = [\mathbf{r}]_{(n)}(\tilde{m}, \tilde{\theta}) = \boldsymbol{\omega}_n^{\mathrm{H}}(\tilde{m}, \tilde{\theta}) \, \mathrm{vec}\{\mathbf{Z}_n\} \triangleq \boldsymbol{\omega}_n^{\mathrm{H}} \mathbf{z}_n(\tilde{m}) \tag{4.19}$$

where $\boldsymbol{\omega}_n$ is the spatial filter applied to n^{th} subcarrier after the DACB and $\mathbf{r}$ is the $N \times 1$ result of the processing whose n^{th} element is r_n. $\boldsymbol{\omega}_n$ can be formulated as:

$$\boldsymbol{\omega}_n = \frac{(\mathbf{R}_n^{\boldsymbol{\eta}})^{-1}(\tilde{m})\mathbf{p}_n(\tilde{\theta})}{\mathbf{p}_n^{\mathrm{H}}(\tilde{\theta})(\mathbf{R}_n^{\boldsymbol{\eta}})^{-1}(\tilde{m})\mathbf{p}_n(\tilde{\theta})} \tag{4.20}$$

where $\mathbf{p}_n(\tilde{\theta})$ is the $D_tD_r \times 1$ spatial steering vector towards $\tilde{\theta}$ and $\mathbf{R}_n^{\boldsymbol{\eta}}(\tilde{m})$ is the $D_tD_r \times D_tD_r$ spatial covariance matrix of the preprocessed received frame under H_0. It should be noted that $\boldsymbol{\omega}_n$ is the minimum variance distortionless response (MVDR) filter [129], meaning that it minimizes the total average power at the output while making the output unity when $\mathbf{z}_n$ happens to be equal to $\mathbf{p}_n$. Assuming that the IT is at angle $\tilde{\theta}$, the spatial steering vector towards the IT is:

$$\begin{aligned}\mathbf{p}_n(\tilde{\theta}) &= \mathrm{vec}\{\mathbf{W}_r^{\mathrm{H}}\mathbf{a}_n(\tilde{\theta})(\mathbf{b}_n(\tilde{\theta}))^{\mathrm{T}}\mathbf{W}_t^{*}\} \\ &= (\mathbf{W}_t^{\mathrm{H}}\mathbf{b}_n(\tilde{\theta})) \otimes (\mathbf{W}_r^{\mathrm{H}}\mathbf{a}_n(\tilde{\theta})),\end{aligned} \tag{4.21}$$

which is the spatial response coming from a hypothetical point target at angle $\tilde{\theta}$ in vectorized form. The spatial covariance matrix of $\mathbf{z}_n$ under H_0, namely when there is no IT contamination, can be defined as:

$$\begin{aligned}&\mathbf{R}_n^{\boldsymbol{\eta}}(\tilde{m}) \triangleq \mathbb{E}\{\mathbf{z}_n(\tilde{m})\mathbf{z}_n^{\mathrm{H}}(\tilde{m})|H_0\} \triangleq \mathbb{E}\{\boldsymbol{\eta}_n(\tilde{m})\boldsymbol{\eta}_n^{\mathrm{H}}(\tilde{m})\} \\ &= \overline{\mathbf{V}}_n^{\mathrm{H}}\mathbb{E}\left\{\mathrm{vec}\{\boldsymbol{\Psi}_n\}\,\mathrm{vec}\{\boldsymbol{\Psi}_n\}^{\mathrm{H}}\right\}\overline{\mathbf{V}}_n \triangleq \overline{\mathbf{V}}_n^{\mathrm{H}}\mathbf{R}_n^{\boldsymbol{\psi}}\overline{\mathbf{V}}_n\end{aligned} \tag{4.22}$$

where $\mathbf{R}_n^{\boldsymbol{\psi}}$ is the $MD_r \times MD_r$ spatial covariance matrix of the interference before the DACB. It should be noted that both $\mathbf{R}_n^{\boldsymbol{\psi}}$ and $\mathbf{R}_n^{\boldsymbol{\eta}}$ are dependent on $\mathbf{X}_n$. Therefore, $\boldsymbol{\omega}_n$ must be calculated for each Tx symbol sequence $\mathbf{X}_n$, which can be computationally burdensome. To ease the calculations, $\boldsymbol{\omega}_n$ can be computed with the expectation of the $\mathbf{R}_n^{\boldsymbol{\eta}}$ over $\mathbf{X}_n$, with a performance loss. When the transmitted symbols $\mathbf{X}_n$ are given, $\mathbf{R}_n^{\boldsymbol{\psi}}$ can be written as in (4.23). The derivation of (4.23) and the expectation of $\mathbf{R}_n^{\boldsymbol{\eta}}$ over $\mathbf{X}_n$ are provided in the Appendix A. When (4.22) and (4.23) are investigated, it can be seen that the range information of the scatterers, which is the scalar phase component in the channel $\mathbf{H}_{kn}$ defined in (4.1), is canceled out in $\mathbf{R}_n^{\boldsymbol{\eta}}$. This means that the proposed MIMO processing has no information about the range profile of the interference.

$$\begin{aligned}\mathbf{R}_n^{\boldsymbol{\psi}} = &\sum_{k=1}^{\mathcal{K}}(\mathbf{I}_M \otimes \mathbf{H}_{kn})(\mathbf{I}_M \circledcirc (\mathbf{X}_n\mathbf{D}_k^{\mathcal{C}}))\mathbf{R}_k^{\boldsymbol{\alpha}}(\mathbf{I}_M \circledcirc (\mathbf{X}_n\mathbf{D}_k^{\mathcal{C}}))^{\mathrm{H}}(\mathbf{I}_M \otimes \mathbf{H}_{kn})^{\mathrm{H}} \\ &+ \sum_{u=1}^{\mathcal{U}}\frac{\gamma_u^{\mathcal{S}}}{M}(\mathbf{I}_M \otimes \mathbf{g}_{un}\mathbf{g}_{un}^{\mathrm{H}}) + \sigma_n^2\mathbf{I}_{MD_r}\end{aligned} \tag{4.23}$$

As the last step of processing, an $N \times 1$ temporal filter $\mathbf{u}$ is applied on $\mathbf{r}$ to get the decision metric ξ as:

$$\xi(\tilde{n}, \tilde{m}, \tilde{\theta}) = \left|\mathbf{u}^{\mathrm{H}}\mathbf{r}\right|^2. \tag{4.24}$$

The temporal filter $\mathbf{u}$ can be written as:

$$\mathbf{u}(\tilde{n}, \tilde{m}, \tilde{\theta}) = \frac{\boldsymbol{\Sigma}^{\boldsymbol{\eta}^{-1}}(\tilde{m}, \tilde{\theta})\mathbf{q}(\tilde{n})}{\sqrt{\mathbf{q}^{\mathrm{H}}(\tilde{n})\boldsymbol{\Sigma}^{\boldsymbol{\eta}^{-1}}(\tilde{m}, \tilde{\theta})\mathbf{q}(\tilde{n})}} \tag{4.25}$$

where $\mathbf{q}(\tilde{n})$ is the $N \times 1$ range steering vector towards $\tilde{n}$ and $\boldsymbol{\Sigma}^{\boldsymbol{\eta}}(\tilde{m}, \tilde{\theta})$ is defined as the $N \times N$ range covariance matrix of the preprocessed and spatial filtered received frame, again without the IT contamination. It should be noted that the normalization in $\mathbf{u}$ makes sure that $\mathbb{E}\{\xi|H_0\} = 1$ if $\boldsymbol{\Sigma}^{\boldsymbol{\eta}} = \mathbb{E}\{\mathbf{r}\mathbf{r}^{\mathrm{H}}|H_0\}$ is indeed satisfied. This means that the expected output of the filter, the detection metric, is not dependent on interference characteristics under H_0 hypothesis, namely the detector exhibits CFAR property.

Assuming that the IT is at a range corresponding to $\tilde{n}^{\text{th}}$ subcarrier (range bin), n^{th} element of the temporal steering vector towards the IT is:

$$[\mathbf{q}(\tilde{n})]_n = e^{-j(2\pi/N)\tilde{n}n}\boldsymbol{\omega}_n^{\mathrm{H}}\mathbf{p}_n = e^{-j(2\pi/N)\tilde{n}n}, \tag{4.26}$$

which is the temporal response coming from a hypothetical point target at $\tilde{n}^{\text{th}}$ range cell. The range covariance matrix of $\mathbf{r}$ under H_0 can be defined as:

$$\boldsymbol{\Sigma}^{\boldsymbol{\eta}}(\tilde{m}, \tilde{\theta}) \triangleq \mathbb{E}\{\mathbf{r}(\tilde{m}, \tilde{\theta})\mathbf{r}^{\mathrm{H}}(\tilde{m}, \tilde{\theta})|H_0\} \tag{4.27}$$

When all transmitted symbols $\mathbf{X}_1, \mathbf{X}_2, \cdots, \mathbf{X}_N$ are given, $(n_1, n_2)^{\text{th}}$ element of $\boldsymbol{\Sigma}^{\boldsymbol{\eta}}$ can be written as:

$$\begin{aligned}
[\boldsymbol{\Sigma}^{\boldsymbol{\eta}}]_{(n_1,n_2)} &= \mathbb{E}\left\{\boldsymbol{\omega}_{n_1}^{\mathrm{H}}\mathbf{z}_{n_1}\mathbf{z}_{n_2}^{\mathrm{H}}\boldsymbol{\omega}_{n_2}|H_0, \mathbf{X}_{n_1}, \mathbf{X}_{n_2}\right\} \\
&= \boldsymbol{\omega}_{n_1}^{\mathrm{H}}\mathbb{E}\left\{\boldsymbol{\eta}_{n_1}\boldsymbol{\eta}_{n_2}^{\mathrm{H}}|\mathbf{X}_{n_1}, \mathbf{X}_{n_2}\right\}\boldsymbol{\omega}_{n_2} \\
&\triangleq \boldsymbol{\omega}_{n_1}^{\mathrm{H}}\mathbf{R}_{n_1n_2}^{\boldsymbol{\eta}}\boldsymbol{\omega}_{n_2}
\end{aligned} \tag{4.28}$$

where $\mathbf{R}_{n_1n_2}^{\boldsymbol{\eta}}$ is the $D_tD_r \times D_tD_r$ spatial cross-correlation matrix of the preprocessed interference terms between $n_1{}^{\text{st}}$ and $n_2{}^{\text{nd}}$ subcarriers, which can also be written as:

$$\begin{aligned}
\mathbf{R}_{n_1n_2}^{\boldsymbol{\eta}} &= \overline{\mathbf{V}}_{n_1}^{\mathrm{H}}\mathbb{E}\left\{\mathrm{vec}\{\boldsymbol{\Psi}_{n_1}\}\,\mathrm{vec}\{\boldsymbol{\Psi}_{n_2}\}^{\mathrm{H}}\right\}\overline{\mathbf{V}}_{n_2} \\
&= \overline{\mathbf{V}}_{n_1}^{\mathrm{H}}\mathbf{R}_{n_1n_2}^{\boldsymbol{\psi}}\overline{\mathbf{V}}_{n_2}
\end{aligned} \tag{4.29}$$

where $\mathbf{R}^{\boldsymbol{\psi}}_{n_1 n_2}$ is the $D_t D_r \times D_t D_r$ spatial cross-correlation matrix of the raw interference terms between $n_1{}^{\text{st}}$ and $n_2{}^{\text{nd}}$ subcarriers, whose closed form expression is given in (4.30). The derivation of (4.30) and the expectation of $\mathbf{R}^{\boldsymbol{\eta}}_{n_1 n_2}$ over $\mathbf{X}_{n_1}$ and $\mathbf{X}_{n_2}$ are given in the Appendix A. It should be noted that both $\mathbf{R}^{\boldsymbol{\psi}}_{n_1 n_2}$ and $\mathbf{R}^{\boldsymbol{\eta}}_{n_1 n_2}$ are also dependent on $\mathbf{X}_n$. Therefore, $\mathbf{u}$ must be calculated for each Tx symbol sequence $\mathbf{X}_n$ to get the range filter with maximum output SINR. To ease the calculations, $\mathbf{u}$ can be computed with the expectation of the $\boldsymbol{\Sigma}^{\boldsymbol{\eta}}$ over $\mathbf{X}_n$, with a performance loss.

$$\mathbf{R}^{\boldsymbol{\psi}}_{n_1 n_2} = \begin{cases} \mathbf{R}^{\boldsymbol{\psi}}_{n_1}, & \text{if } n_1 = n_2 \\ \sum_{k=1}^{\mathcal{K}} \left(\mathbf{I}_M \otimes \mathbf{H}_{kn_1}\right) \left(\mathbf{I}_M \circledcirc (\mathbf{X}_{n_1} \mathbf{D}^{\mathcal{C}}_k)\right) \mathbf{R}^{\boldsymbol{\alpha}}_k & \text{if } n_1 \neq n_2 \\ \quad \times \left(\mathbf{I}_M \circledcirc (\mathbf{X}_{n_2} \mathbf{D}^{\mathcal{C}}_k)\right)^{\text{H}} \left(\mathbf{I}_M \otimes \mathbf{H}_{kn_2}\right)^{\text{H}}, & \end{cases} \tag{4.30}$$

When (4.1), (4.29) and (4.30) are investigated, it can be seen that the range information of the scatterers are carried in the off-diagonal elements of the $\boldsymbol{\Sigma}^{\boldsymbol{\eta}}$ matrix. More explicitly, the contribution from the k^{th} scatterer to the $(n_1, n_2)^{\text{th}}$ element of $\boldsymbol{\Sigma}^{\boldsymbol{\eta}}$ is $e^{-j2\pi\tau_k \Delta f (n_1 - n_2)}$ times another scalar which does not depend on the range of the corresponding scatterer. If $\mathbf{q}^{\mathcal{C}}_k$ is defined to be the range response of the k^{th} scatterer where $\left[\mathbf{q}^{\mathcal{C}}_k\right]_n \triangleq e^{-j2\pi\tau_k \Delta f n}$ for $n = 0, 1, \cdots, N-1$, then

$$\boldsymbol{\Sigma}^{\boldsymbol{\eta}} = \sum_{k=1}^{\mathcal{K}} \mathbf{q}^{\mathcal{C}}_k (\mathbf{q}^{\mathcal{C}}_k)^{\text{H}} \odot \mathbf{A}_k(\tilde{m}, \tilde{\theta}, \mathbf{X}_n) \tag{4.31}$$

where $\mathbf{A}_k$, which depends on $\tilde{m}, \tilde{\theta}, \mathbf{X}_n$ for all subcarriers, as well as the angle and Doppler properties of k^{th} scatterer but not the range of it, can be found easily but not written here for the sake of neatness. It should be noted that if there were only a single scatterer with no Doppler spread and the Doppler processing perfectly matched the Doppler of the scatterer, $\mathbf{A}_k$ would become an all-ones matrix and $\boldsymbol{\Sigma}^{\boldsymbol{\eta}}$ would become a rank-1 matrix which includes the range information of the scatterer. However, in a more realistic scenario, even a slight Doppler spread or a Doppler mismatch between the DACB and any of the scatterers results in an increase in the rank of $\mathbf{A}_k$ and $\boldsymbol{\Sigma}^{\boldsymbol{\eta}}$. In other words, the Doppler mismatch causes the range response of the scatterers, which would be impulsive otherwise, to spread over the whole range spectrum. In addition to this, this spread depends on the transmitted symbols $\mathbf{X}_n$. As a consequence, if

$\boldsymbol{\Sigma}^{\boldsymbol{\eta}}$ matrix information is not used at the receiver side, the range information of the scatterers cannot be learned and the output SINR is reduced when there is Doppler mismatch. On the other hand, if the $\boldsymbol{\Sigma}^{\boldsymbol{\eta}}$ matrix is exploited at the receiver side, which requires tracker information and a relatively high computation power, the effects of the Doppler mismatch can be resolved and due to the increased rank of $\boldsymbol{\Sigma}^{\boldsymbol{\eta}}$, output SINR can be increased even more with respect to the case with no Doppler mismatch.

After the decision metric ξ is determined, it is compared to the pre-determined CFAR threshold γ_{th} to make the decision:

$$\xi(\tilde{n}, \tilde{m}, \tilde{\theta}) \underset{H_0}{\overset{H_1}{\gtrless}} \gamma_{th}, \tag{4.32}$$

where γ_{th} can be adaptively found using previous uncontaminated frames of data. A similar threshold map calculation is explained in detail in [118] and in Chapter 3 of this thesis for OFDM-based SISO ISAC systems. In this chapter, Tx symbols cannot be completely eliminated as explained before, therefore instantaneous thresholds depend on Tx symbols. However, the system can calculate average thresholds over Tx symbols and use them in the long term as the clutter is assumed to be stationary for multiple frames.

As a metric to compare the processing methods fairly, the output SINR is defined as:

$$\mathrm{SINR} = \frac{\mathbf{u}^{\mathrm{H}} \boldsymbol{\Sigma}^{\boldsymbol{\phi}} \mathbf{u}}{\mathbf{u}^{\mathrm{H}} \boldsymbol{\Sigma}^{\boldsymbol{\eta}} \mathbf{u}}, \tag{4.33}$$

where the range covariance matrix of the IT after MIMO processing is:

$$\boldsymbol{\Sigma}^{\boldsymbol{\phi}}(\tilde{m}, \tilde{\theta}) \triangleq \mathbb{E}\{\mathbf{r}\mathbf{r}^{\mathrm{H}} | H_1\} - \mathbb{E}\{\mathbf{r}\mathbf{r}^{\mathrm{H}} | H_0\}. \tag{4.34}$$

It should be noted that in this section, the filters in (4.20) and (4.25) are written for the benchmark interference-aware detector. In the later sections, filter calculations will remain the same but the covariances used in them will change depending on the filter type. In the next section, different implementations of filters used in this chapter will be investigated.

4.4 Alternative Filter Implementations in the Proposed Detector Structure

In this section, alternative filter implementations used in this chapter will be investigated. In the first subsection, seven different filters investigated in this chapter will be explained. In the next subsection, the interpretation of these filters with respect to the beam-squint effect will be provided.

4.4.1 Alternative Filter Implementations

There are seven different filter implementations investigated in this chapter. The first three filters correspond to three different $\mathcal{V}_1$ detectors. As can be seen in Figure 4.2, only the angular covariance matrix in the MIMO filters is different in these three detectors. The next three filters correspond to three different $\mathcal{V}_2$ detectors. As it can be seen in Figure 4.2, only the range covariance matrix in the temporal filters is different in these three detectors. The final filter corresponds to the benchmark 3D Periodogram detector, which uses conventional DFT and IDFT for MIMO and range processing, respectively. This detector is not shown in Figure 4.2, but it can be seen as a special case of either $\mathcal{V}_1$ or $\mathcal{V}_2$ detector, when the corresponding covariance matrix is selected as identity matrix.

4.4.1.1 KA-SARP Given $\mathbf{X}_n$, $\mathcal{V}_1$ Detector

This detector utilizes the proposed MIMO filter structure in (4.20) using the true knowledge of interference angular covariance matrix $\mathbf{R}_n^{\boldsymbol{\eta}}$, which can be supplied to the detector as target maps from trackers. The MIMO filter $\boldsymbol{\omega}_n$ is constructed for each subcarrier and each Tx symbol $\mathbf{X}_n$, which requires $D_r D_t \times D_r D_t$ matrix inversions N times per frame. In each subcarrier, the angular filter depends on the transmitted symbols. Therefore, this detector is denoted as "Given $\mathbf{X}_n$". This detector is the only one in this chapter that uses different MIMO filters for each subcarrier due to changing Tx symbols $\mathbf{X}_n$. This unique property results in an improved angular interference suppression with a high computational cost. This detector must be used only if the angular information of UITs is available and there is not a constraint on

the computational power.

4.4.1.2 KA-SARP with Expected $\mathbf{X}_n$, $\mathcal{V}_1$ Detector

As mentioned previously, the true covariances $\mathbf{R}, \boldsymbol{\Sigma}$ and thus the max-SINR filters $\boldsymbol{\omega}, \mathbf{u}$ depend on the symbol sequence $\mathbf{X}_n$ at each subcarrier. In order to ease the calculation of the filters, expected filters over symbols $\mathbf{X}_n$ at each subcarrier can be found. The calculations of the expectations are given in the Appendix A. The expectations of $\mathbf{R}_n^{\eta}$ and $\boldsymbol{\Sigma}^{\eta}$ over $\mathbf{X}_n$ are denoted as $\overline{\mathbf{R}}_n^{\eta}$ and $\overline{\boldsymbol{\Sigma}}^{\eta}$, respectively. Since the expectations are taken over $\mathbf{X}_n$ symbols, this detector is denoted as "Expected $\mathbf{X}_n$". Expected $\mathbf{X}_n$, $\mathcal{V}_1$ detector forms the max-SINR MIMO filter $\boldsymbol{\omega}_n$ in (4.20) by using $\overline{\mathbf{R}}_n^{\eta}$ instead of $\mathbf{R}_n^{\eta}$. The angular correlation time is assumed to be much larger than the OFDM frame duration. Therefore, the filters in Expected $\mathbf{X}_n$, $\mathcal{V}_1$ detector can be calculated only once in several frames. This detector can be used when the angular information of UITs is available but there is only a limited computational power.

4.4.1.3 Fully Adaptive AMF-like SARP with SA, $\mathcal{V}_1$ Detector

The previous detectors are knowledge-aided, meaning that their performances significantly depend on the true knowledge of the interference covariance matrices. Alternatively, a fully adaptive filter learning the interference covariance using only $\mathcal{T}$ frames of data via sample averaging (SA) method is proposed. This detector can be considered the application of the well-known AMF detector in MIMO scenarios where clutter consists of multiple and extended scatterers and beam-squint effects are visible. This is why this kind of detector is denoted as "SA-AMF".

In (4.20), instead of $\mathbf{R}_n^{\eta}$, SA-AMF, $\mathcal{V}_1$ detector uses the estimated interference angle covariance matrix $\hat{\mathbf{R}}_n^{\eta}$ which was learnt via SA method. Similar to Given $\mathbf{X}_n$, $\mathcal{V}_1$ detector, the $\boldsymbol{\omega}_n$ filters must be constructed N times per frame. However, if the beam-squint and Doppler mismatch are ignored, $\mathbf{R}_n^{\eta}$ can be assumed to be the same for all subcarriers. Therefore, it might be sufficient to use all subcarriers to learn a single covariance matrix $\hat{\mathbf{R}}^{\eta}$ and use it to construct a single MIMO filter $\boldsymbol{\omega}$. On the other hand, if the beam-squint is effective, the angular channel of interference would

depend on the subcarrier frequency, and a subband approach could be used to ease the calculations.

The working principle of SA-AMF detectors with a subband approach is explained in more detail in Figure 4.5. As seen in Figure 4.5, SA-AMF detectors divide the spectrum into subbands to mitigate the effects of beam-squint. There are $N/N' = \mathcal{N}$ ISAC subcarriers in each of the N' subbands, where $\mathcal{N}$ can be selected so that the beam-squint effect is negligible inside the subbands [122]. $\mathcal{T}$ frames of observation are assumed to be taken before the IT is present. The SA-AMF, $\mathcal{V}_1$ detector uses these $\mathcal{T}$ frames and $\bar{\mathcal{N}} \triangleq \bar{N}/N'$ subcarriers (not only ISAC subcarriers) to estimate the angular interference covariance matrix $\hat{\mathbf{R}}_{n'}^{\boldsymbol{\eta}}$ of $(n')^{\text{th}}$ subband via SA. Then, the same $\boldsymbol{\omega}_{n'}$ is used for all $\mathcal{T}$ frames and $\mathcal{N}$ ISAC subcarriers in each subband. As the result of the angular processing, there are $\mathcal{T}$ vectors to be processed in range domain, t^{th} of them being denoted as $\mathbf{r}^{(t)}$. $\mathbf{D}^{\boldsymbol{\eta}}$ in Figure 4.5 represents a diagonal load matrix, which guarantees that the matrix inversion converges. In this chapter, $\mathbf{D}^{\boldsymbol{\eta}}$ is proportional to expected noise angle covariance matrix, which is $\mathbf{D}^{\boldsymbol{\eta}} = \gamma_{\text{load}}\sigma_n^2 \operatorname{diag}\{\mathbf{I}_{D_t} \otimes (\mathbf{W}_r^{\text{H}}\mathbf{W}_r)\}$, where γ_{load} is the diagonal loading factor.

SA-AMF, $\mathcal{V}_1$ detector can be used when the angular information of UITs is not available at hand, but to be estimated. This detector is also compatible with subband processing, therefore it can learn the angular information of UITs in the scenarios with severe beam-squint effects.

4.4.1.4 KA-SARP Given $\mathbf{X}_n$, $\mathcal{V}_2$ Detector

In this detector, the range filter $\mathbf{u}$ in (4.25) is constructed using the true knowledge of interference range covariance matrix $\boldsymbol{\Sigma}^{\boldsymbol{\eta}}$, provided by the tracker. As shown in (4.28), this range filter is dependent on Tx symbols $\mathbf{X}_n$, but only one matrix inversion of size $N \times N$ is required per frame. Therefore, this detector is computationally less burdensome than Given $\mathbf{X}_n$, $\mathcal{V}_1$ detector. This detector must be used only if both angular and range information of UITs are available and there is not a constraint on the computational power.

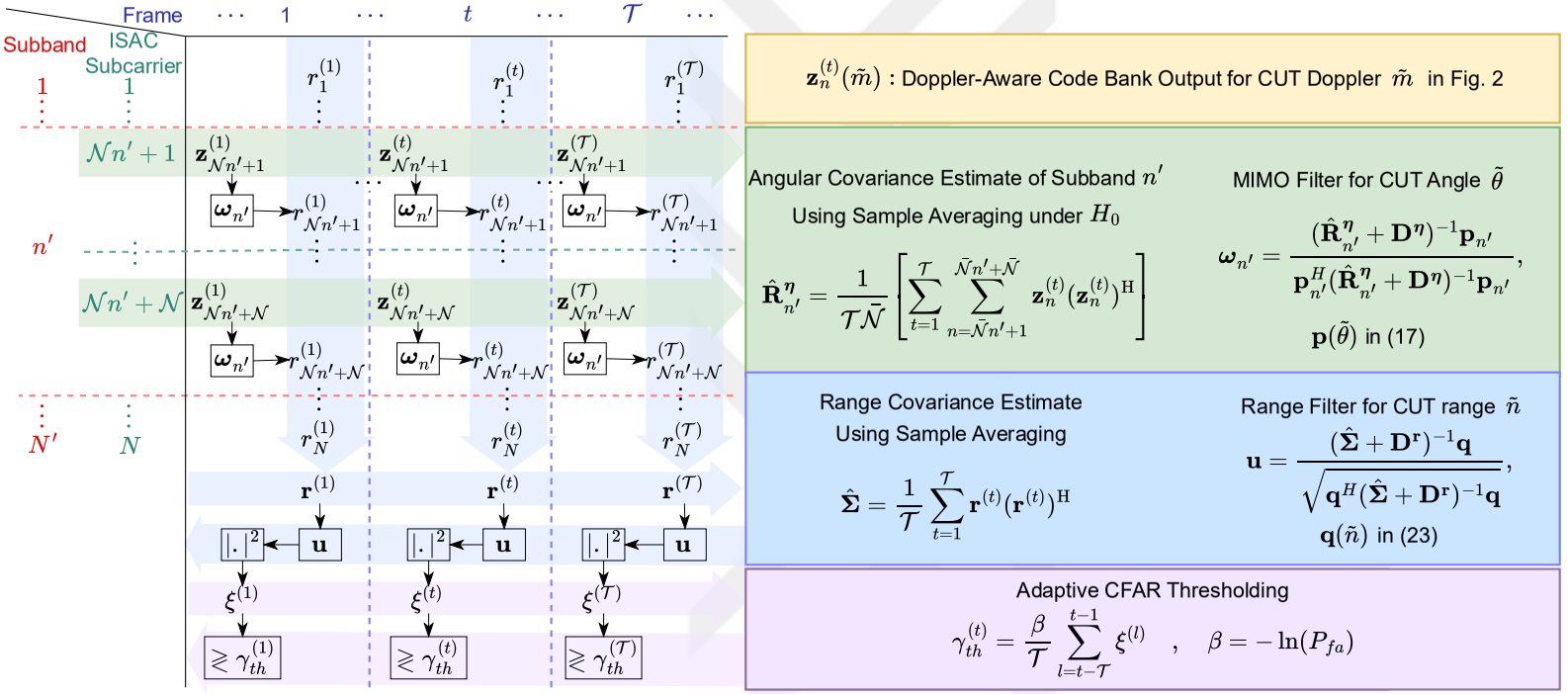


Figure 4.5: Working principal and frame structure of the Fully-Adaptive (FA) Sample-Averaging detector, focusing on subband approach.

Table 4.1: Alternative Filter Types for the Proposed Detector Structure

Name of Processing Method	MIMO Filter $\boldsymbol{\omega}_n$	Range Filter $\mathbf{u}$	Knowledge Required	Computational Complexity per CUT
Given $\mathbf{X}_n$, $\mathcal{V}_1$	$\boldsymbol{\omega}_n(\mathbf{R}_n^{\boldsymbol{\eta}})$	$\mathbf{u}(\mathbf{I}_N)$	$\mathbf{X}_n, \mathbf{D}_k^{\mathcal{C}}, \theta_k, \mathbf{R}_k^{\boldsymbol{\alpha}}$	$\mathcal{O}(\mathcal{K}NM^3D_t^2D_r\mathcal{T})$
Given $\mathbf{X}_n$, $\mathcal{V}_2$	$\boldsymbol{\omega}_n(\mathbf{I}_{D_rD_t})$	$\mathbf{u}(\boldsymbol{\Sigma}^{\boldsymbol{\eta}})$	$\mathbf{X}_n, \mathbf{D}_k^{\mathcal{C}}, \theta_k, \tau_k, \mathbf{R}_k^{\boldsymbol{\alpha}}$	$\mathcal{O}(\mathcal{K}N^2M^3D_t^4D_r^3\mathcal{T})$
Expected, $\mathcal{V}_1$	$\boldsymbol{\omega}_n(\overline{\mathbf{R}}_n^{\boldsymbol{\eta}})$	$\mathbf{u}(\mathbf{I}_N)$	$\mathbf{D}_k^{\mathcal{C}}, \theta_k, \mathbf{R}_k^{\boldsymbol{\alpha}}$	$\mathcal{O}(N'D_t^2D_r^2)$
Expected, $\mathcal{V}_2$	$\boldsymbol{\omega}_n(\mathbf{I}_{D_rD_t})$	$\mathbf{u}(\overline{\boldsymbol{\Sigma}}^{\boldsymbol{\eta}})$	$\mathbf{D}_k^{\mathcal{C}}, \theta_k, \tau_k, \mathbf{R}_k^{\boldsymbol{\alpha}}$	$\mathcal{O}(N^2)$
SA-AMF, $\mathcal{V}_1$	$\boldsymbol{\omega}_n(\hat{\mathbf{R}}_n^{\boldsymbol{\eta}})$	$\mathbf{u}(\mathbf{I}_N)$	—	$\mathcal{O}(\bar{N}D_t^2D_r^2\mathcal{T})$
SA-AMF, $\mathcal{V}_2$	$\boldsymbol{\omega}_n(\mathbf{I}_{D_rD_t})$	$\mathbf{u}(\hat{\boldsymbol{\Sigma}}^{\boldsymbol{\eta}})$	—	$\mathcal{O}(N^2\mathcal{T}+N^3)$
3D Perio	$\boldsymbol{\omega}_n(\mathbf{I}_{D_rD_t})$	$\mathbf{u}(\mathbf{I}_N)$	—	$\mathcal{O}(N'D_tD_r)$

4.4.1.5 KA-SARP with Expected $\mathbf{X}_n$, $\mathcal{V}_2$ Detector

This detector forms the max-SINR range filter $\mathbf{u}$ in (4.25) by using $\overline{\boldsymbol{\Sigma}^{\boldsymbol{\eta}}}$ instead of $\boldsymbol{\Sigma}^{\boldsymbol{\eta}}$. Similar to Expected $\mathbf{X}_n$, $\mathcal{V}_1$ detector, the filters can be calculated only once in several frames because the range response of the scatterers is assumed to stay correlated for several OFDM frame durations. This detector can be used when both angular and range information of UITs are available but there is only a limited computational power.

4.4.1.6 Fully Adaptive AMF-like SARP with SA, $\mathcal{V}_2$ Detector

In (4.25), instead of $\boldsymbol{\Sigma}^{\boldsymbol{\eta}}$, SA-AMF, $\mathcal{V}_2$ detector uses the estimated interference range covariance matrix $\hat{\boldsymbol{\Sigma}}^{\boldsymbol{\eta}}$ which was learnt via SA method. As shown in Figure 4.5, $\hat{\boldsymbol{\Sigma}}^{\boldsymbol{\eta}}$ is learned in each frame, and then the average of these matrices is used to create the range filter $\mathbf{u}$ to be used in all $\mathcal{T}$ frames. $\mathbf{D}^{\mathbf{r}}$ in Figure 4.5 represents a diagonal load matrix, which guarantees that the matrix inversion converges. In this chapter, $\mathbf{D}^{\mathbf{r}}$ is proportional to the expected noise range covariance matrix, whose $(n,n)^{\text{th}}$ element is $[\mathbf{D}^{\mathbf{r}}]_{(n,n)} = \gamma_{\text{load}}\sigma_n^2||\mathbf{W}_t^{\text{H}}\mathbf{b}_n(\tilde{\theta})||^2||\mathbf{W}_r\mathbf{W}_r^{\text{H}}\mathbf{a}_n(\tilde{\theta})||^2$, where γ_{load} is the diagonal loading factor.

As explained in (4.31), Doppler mismatch results in $\boldsymbol{\Sigma}^{\boldsymbol{\eta}}$ being dependent on $\mathbf{X}_n$. This dependence can be described as element-wise multiplication with a random matrix $\mathbf{A}_k$, which is zero-mean when the expectation is taken over $\mathbf{X}_n$. To estimate the deterministic part in $\boldsymbol{\Sigma}^{\boldsymbol{\eta}}$, which is $\mathbf{q}_k^{\mathcal{C}}(\mathbf{q}_k^{\mathcal{C}})^{\text{H}}$ in (4.31), the same $\mathbf{X}_n$ matrix must be repeated for multiple frames to prevent the range information from being nullified. Therefore, $\mathbf{X}_n$ symbols are repeated frame-to-frame in this chapter, which has an adverse effect on the communication rate. However, it should be noted that the repetition occurs only in N ISAC subcarriers among all $\bar{N}$ subcarriers; and after the training period is finished, the range filters of SA-AMF, $\mathcal{V}_2$ detector can be fixed and the communication rate can be recovered. [7] SA-AMF, $\mathcal{V}_2$ detector can be used when the range information of UITs is not available at hand, but to be estimated with a slight decrease in the communication rate.

[7] The training of SA-AMF filters is done under H_0 hypothesis in this thesis. However, it can also be done under H_1 hypothesis without losing SINR by using an increased number of training symbols.

It should be noted that as the training goes to infinity, SA-AMF, $\mathcal{V}_1$ detector approaches Expected $\mathbf{X}_n$, $\mathcal{V}_1$ detector, and SA-AMF, $\mathcal{V}_2$ detector approaches Given $\mathbf{X}_n$, $\mathcal{V}_2$ detector. This is because in SA-AMF, $\mathcal{V}_1$, different $\mathbf{X}_n$ sequences are used in training, effectively averaging the MIMO filters over $\mathbf{X}_n$. On the other hand, in SA-AMF, $\mathcal{V}_2$, the same $\mathbf{X}_n$ is repeated so that the range covariance is learned as if $\mathbf{X}_n$ is given.

4.4.1.7 3D Periodogram Detector

3D Periodogram, which is a nonparametric method commonly used in the literature, as in [67, 81], is also utilized in this chapter as a benchmark detector. This detector uses no knowledge of interference and performs conventional DFT or IDFT in range, angle and Doppler domains. This detector is used if the computational power is severely limited.

The calculation of filters for different processing methods, along with the required knowledge and computational complexities of them, are summarized in Table 4.1. For the computational complexities, the most complex operation that is done for each frame is considered for each method. Given $\mathbf{X}_n$ methods must calculate the true covariances for each frame. Therefore, they are by far the most complex methods.

4.4.2 The Effects of Beam-Squint on Different Filter Types

When f_c/W ratio of the system is significantly low, beam-squint effects become non-negligible. A discussion on how large the bandwidth of the system can be while keeping the beam-squint effect small is provided in [122], and is not in the scope of this thesis. The beam-squint directly affects the receive and transmit steering vectors, $\mathbf{a}_n$ and $\mathbf{b}_n$, making them dependent on the subcarrier index n. Consequently, the angular covariance matrix, $\mathbf{R}_n^{\boldsymbol{\eta}}$ in (4.22) and (4.23), and the angular steering vector towards the IT, $\mathbf{p}_n$ in (4.21), are directly affected by beam-squint. The steering vectors $\mathbf{p}_n$ can be easily calculated once for each subcarrier, therefore it does not bring additional computational complexity to the system. However, $\mathbf{R}_n^{\boldsymbol{\eta}}$ depends on the transmitted symbols $\mathbf{X}_n$ and should be calculated for each transmitted OFDM symbol. On the other hand, to calculate the angular filter $\boldsymbol{\omega}_n$, the inverse of the $\mathbf{R}_n^{\boldsymbol{\eta}}$ matrix must be

taken for each OFDM symbol, requiring a large computational power. Therefore, this chapter proposes different filter types that ease the $\mathbf{R}_n^{\eta}$ calculations, effectively having different behaviors against beam-squint. In this section, these behaviors will be briefly discussed for three different implementations of $\mathcal{V}_1$ detector, as they are the only ones which use $\mathbf{R}_n^{\eta}$ information.

4.4.2.1 KA-SARP Given $\mathbf{X}_n$, $\mathcal{V}_1$ detector

As explained in Section 4.4.1.1, this filter type calculates the covariance matrix $\mathbf{R}_n^{\eta}$ for every subcarrier. Therefore, it can mitigate the effects of beam-squint inherently, using a high computational power. On the other hand, the covariance matrix can be calculated for only N' number of subbands to ease the calculations. As the f_c/W ratio decreases, the number of subbands required to keep the performance loss at minimum increases. If this filter is used with fewer subbands than required, it can suffer from performance losses due to beam-squint because it selectively suppresses the clutter in angular domain. Therefore, this filter must be used with enough number of subbands to get the optimal interference suppression in angular domain.

4.4.2.2 Expected $\mathbf{X}_n$, $\mathcal{V}_1$ detector

As explained in Section 4.4.1.2, this filter type calculates only one covariance matrix for the sake of ease of calculations. Therefore, its performance would be negatively affected by the beam-squint. The subband approach can also be used with this filter to mitigate the beam-squint effects; the expected covariance matrices can be calculated for each of the N' subbands, taking the expectations over the corresponding $\mathcal{N}$ subcarriers in the subbands.

4.4.2.3 Fully Adaptive AMF-like SARP with SA, $\mathcal{V}_1$ detector

As explained in Section 4.4.1.3, this filter type estimates the covariance matrices for each of the N' subbands, training over the corresponding $\bar{\mathcal{N}}$ subcarriers in the subbands. Namely, since $\bar{N}$ subcarriers are used for communication purposes, the train-

ing of SA-AMF, $\mathcal{V}_1$ detector can be done using all $\bar{N}$ subcarriers to increase the estimation accuracy. This filter suffers from beam-squint if N' is selected smaller than needed, but increasing N' might result in reduction in estimation accuracy of $\mathbf{R}_{n'}^{\boldsymbol{\eta}}$, indicating a trade-off.

4.5 Numerical Evaluations

In this section, the proposed and benchmark detectors are numerically evaluated. First, the simulation parameters are provided and their effects on output SINR are discussed. Then, two beamforming schemes investigated in this thesis are explained. Finally, the simulation results are given for the cases when beam-squint effect is small and severe.

4.5.1 Simulation Parameters

The simulation parameters are provided in Table 4.2. In Table 4.2, (BS) represents the cases where beam-squint effect is severe, which is satisfied by increasing the actual number of subcarriers, $\bar{N}$, 16 times while keeping the number of subcarriers for radar signal processing, N, the same. Therefore, effectively, Δf is increased and range resolution is decreased 16 times in the BS simulations. There are $\mathcal{K} = 10$ UIT scatterers and $\mathcal{U} = 2$ UL users. The first UIT is assumed to be a single scatterer at 0 degrees with $r_1 = 0$ m, $v_1 = 0$ m/s, $\sigma_k^{\mathcal{C}} = 0$ Hz and $\gamma_k^{\mathcal{C}} = 30$ dB, depicting a strong self-interference. The other UIT scatterers are in a cluster, which depicts an object of finite and nonzero length and width. The center range is 18.11 m (10^{th} range bin) and the center angle is -12 degrees for this object. The length and width of the object are half of the range and angle resolutions of the system, respectively. It is considered that the scattering points are on the edge centers and corners of the object in both range and angle dimensions, as well as the center of it, resulting in 9 scattering points. The velocity, Doppler spread and total reflected power from the object are 20 m/s (0.63^{th} Doppler bin), 200 Hz and 20 dB, respectively. The UL users are either at 7.5 and 17.5 degrees or at -3 and 3 degrees depending on the scenario, and the average received powers from them are 10 dB each. The UL users are assumed to

have no velocity or Doppler spread, and they are not considered as separate scattering objects for the sake of simplicity. To ease the understanding of the graphs, red dashed and blue dash-dotted vertical lines are drawn wherever the UITs and SoIs are located, respectively.

It should be noted that the output SINR metric corresponds to the SINR improvement factor (IF) in the simulations because the IT power is selected to be unity. Each parameter has different effects on the SINR IF. For example, by increasing the number of antenna elements, the SINR IF, the angular resolution and angular interference suppression capabilities can be improved, with a higher computational cost. Increasing M while keeping T_s the same would improve the SINR IF and Doppler resolution, but the channel correlation time would be a limitation on M. Increasing N would result in different types of effects. As explained in Chapter 2, this thesis focuses on a communication system that uses $\bar{N}$ subcarriers, while N of them are utilized for sensing purposes in ISAC. It is assumed that the N subcarriers are selected to cover the whole bandwidth W with uniform spacing. A staggered or clustered selection of subcarriers might reduce the angular shifts between subcarriers due to beam-squint, but would degrade the range resolution. Nonetheless, the beam-squint effects can be mitigated by utilizing subband approaches, as will be shown in Section 4.5.3.2. Within this configuration, increasing N while keeping $\bar{N}$ the same would result in an increase in SINR IF and the maximum unambiguous range, and additional interference suppression in range domain. Increasing N while keeping Δf the same would result in an improvement in range resolution due to the increase in total bandwidth.

4.5.2 Beamforming Scenarios

Two different beamforming schemes are simulated in this chapter. In the first scenario, both Tx and Rx beams are formed to cover the angle interval of $(-7.5, 7.5)$ degrees, which is called as *fully overlapping (FO) scheme*. In the second scenario, Tx beamformer covers the angle interval of $(-20, -5)$ degrees and Rx beamformer covers the angle interval of $(5, 20)$ degrees, which is called as *no overlapping (NO) scheme*.

Table 4.2: Simulation Parameters

Parameter	Meaning	Value
$\bar{N}$	total # of subcarriers	1024
N	# of ISAC subcarriers	32
M	# of OFDM symbols	16
$\mathcal{T}$	# of frames	16
N'	# of subbands	1
N' (BS)	# of subbands for BS case	8, 1
$\mathcal{N}$	# of ISAC subcar. per subband	32
$\mathcal{N}(BS)$	# of ISAC subcar. per subband for BS case	4, 32
N_t, N_r	# of Tx, Rx antennas	64
D_t, D_r	# of Tx, Rx RF chains	10
T_s	OFDM symbol duration	12.38 μs
T_f	frame duration	198 μs
$\Delta f = W/N$	subcarrier spacing	2.59 MHz
W	bandwidth	82.75 MHz
Δf (BS)	subcarrier spacing for BS case	41.37 MHz
W (BS)	bandwidth for BS case	1.32 GHz
f_c	center frequency	24 GHz
λ_c	center wavelength	12.5 mm
c_0	speed of light in vacuum	2.998×10^8 m/s
$\gamma_0^{\mathcal{C}}/\sigma_n^2$	target power	1 (0 dB)
$\gamma_k^{\mathcal{C}}/\sigma_n^2$	clutter power	30, 20 dB
$\gamma_u^{\mathcal{S}}/\sigma_n^2$	SoI power	10 dB
γ_{load}	diagonal loading factor	3
NMN_rN_t/D_t	maximum processing gain	53.22 dB

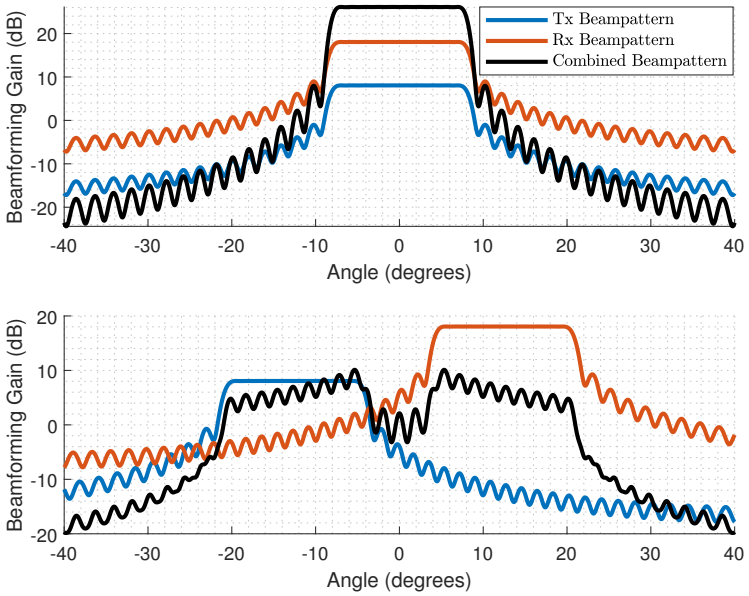


Figure 4.6: Tx, Rx and combined antenna gain patterns for fully overlapping (top) and no overlapping (bottom) schemes.

The Tx and Rx beamforming gain patterns, and their multiplication depicting the total beamforming gain pattern, are provided in Figure 4.6. Tx and Rx beamforming gain pattern values at the n^{th} subcarrier for angle θ is equal to $\text{Tr}\{\mathbf{a}_n(\theta)^{\text{H}}\mathbf{W}_t\mathbf{W}_t^{\text{H}}\mathbf{a}_n(\theta)/M\}$ and $\text{Tr}\{\mathbf{b}_n(\theta)^{\text{H}}\mathbf{W}_r\mathbf{W}_r^{\text{H}}\mathbf{b}_n(\theta)\}$, respectively. It should be noted that the gain is N_t/D_t inside the flat Tx sector because a total Tx power constraint is assumed. On the other hand, the whole N_r beamforming gain is achieved on the receiver side. It should be noted that for a classical phased array system, D_t would be equal to 1 so that the maximum Tx processing gain would be N_t but the beam would be narrowed.

4.5.3 Simulation Results

In this section, output SINR values for five different detectors will be given for different values of CUT angle, range and Doppler bins. In addition, P_d vs input SNR curves for two different CUT locations are also provided for these detectors. The first detector uses 'Given $\mathbf{X}_n$' processing for both $\mathcal{V}_1$ and $\mathcal{V}_2$, and it is labeled as '$\mathcal{V}_1$&$\mathcal{V}_2$ Given $\mathbf{X}_n$' in the legends. Since this detector uses $\mathbf{X}_n$ data for both variants, its SINR is expected to be the upper limit for all other detectors. The second detector uses 'Ex-

pected $\mathbf{X}_n$' processing for both $\mathcal{V}_1$ and $\mathcal{V}_2$, and it is labeled as '$\mathcal{V}_1\&\mathcal{V}_2$ Expected $\mathbf{X}_n$' in the legends. Since this detector does not use $\mathbf{X}_n$ data for any variants, it is expected to suffer from the Doppler mismatch effect mentioned before, but its filters must be calculated only once per several frames. The third detector uses 'Expected $\mathbf{X}_n$' processing for $\mathcal{V}_1$ but 'Given $\mathbf{X}_n$'processing for $\mathcal{V}_2$, and it is labeled as '$\mathcal{V}_1$ Expected $\mathbf{X}_n\&\mathcal{V}_2$ Given $\mathbf{X}_n$' in the legends. This detector does require $\mathbf{X}_n$ data for range processing but uses expected filters for angle processing. Since the Doppler mismatch effect is more severe in range rather than angle processing, this detector is expected to overcome this difficulty while its complexity is reduced with respect to the '$\mathcal{V}_1\&\mathcal{V}_2$ Given $\mathbf{X}_n$' detector. The fourth detector uses 'SA-AMF' processing for both $\mathcal{V}_1$ and $\mathcal{V}_2$, and it is labeled as '$\mathcal{V}_1\&\mathcal{V}_2$ SA-AMF' in the legends. This detector adaptively learns both angle and range covariance matrices. Since its learning inherently includes the effects of $\mathbf{X}_n$, this detector is expected to overcome the Doppler mismatch problem, and its MIMO filters can be calculated only once after the training period of several frames. The last detector uses 'conventional DFT,' or '3D Periodogram' processing for both $\mathcal{V}_1$ and $\mathcal{V}_2$, and it is labeled as '3-D Perio' in the legends. This detector does not use any information about the interference or $\mathbf{X}_n$ and is expected to perform the worst among others in general. For DFT and IDFT processings in angle and range domains, windowing is applied conventionally [115]. Therefore in this thesis, Chebyshev windows are used with sidelobe suppression values of 50 dB and 100 dB, respectively. Since all detectors use conventional DFT or IDFT processing at one of their variants, they suffer from a windowing loss of around 3.2 dB. The detectors other than 3-D Perio can bypass windowing without losing sidelobe performances, but the windows are kept for all detectors in the simulations for the sake of fairness.

4.5.3.1 Beam-squint effect is small

SINR vs CUT angle graphs for two different scenarios are provided in Figure 4.7.

The top graph in Figure 4.7 represents a FO case where both a UIT and two SoIs are inside the overlapping Tx-Rx sectors. It is seen that all detectors except 3-D Perio perform similarly when the CUT angle is away from UITs or SoIs. However, when CUT is on top of the UIT in both angle and range, $\mathcal{V}_1\&\mathcal{V}_2$ Expected $\mathbf{X}_n$ and 3-D Perio

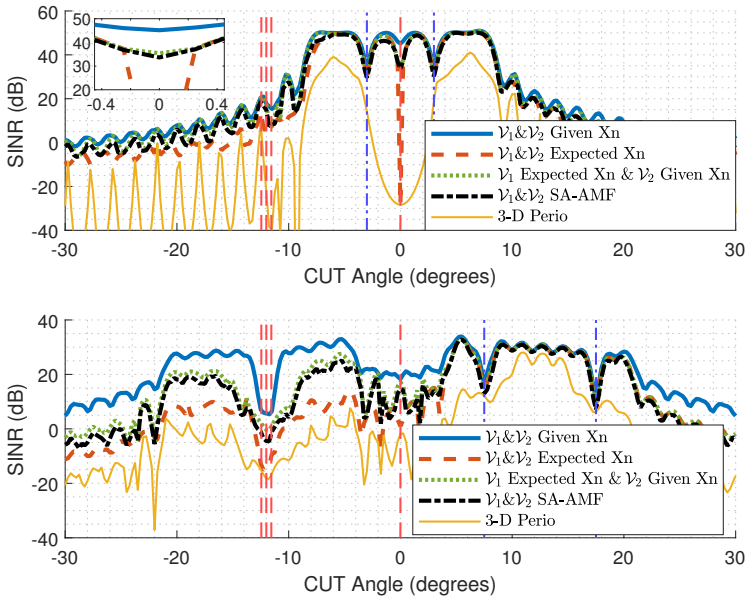


Figure 4.7: SINR vs CUT angle graphs for fully-overlapping (top) and non-overlapping (bottom) scenarios, CUT Range bin: 0 (top) and 10 (bottom), CUT Doppler bin: 0.32 (10 m/s).

detectors fail to suppress the interference while other detectors can. This region is where the only difference between the IT and the UIT is in Doppler domain. However, as explained before, $\mathbf{X}_n$ knowledge is required to suppress the interference using the Doppler diversity. Therefore, the detectors that know (or learn) $\mathbf{X}_n$ information can suppress the UITs while other detectors which do not use $\mathbf{X}_n$ information fail to reach a high SINR improvement factor.

An important aspect of the clutter suppression here is that all detectors use the same Doppler preprocessing. However, the Doppler mismatch shows itself in both angle and range covariance matrices, and the clutter can be suppressed in Doppler domain with MIMO and range processing. The only difference between $\mathcal{V}_1\&\mathcal{V}_2$ Expected $\mathbf{X}_n$ and $\mathcal{V}_1$ Expected $\mathbf{X}_n\&\mathcal{V}_2$ Given $\mathbf{X}_n$ detectors is the range processing part, but the SINR difference is more than 60 dB between them at CUT angle 0 degree. Similarly, the only difference between $\mathcal{V}_1$ Expected $\mathbf{X}_n\&\mathcal{V}_2$ Given $\mathbf{X}_n$ and $\mathcal{V}_1\&\mathcal{V}_2$ Given $\mathbf{X}_n$ detectors is the MIMO processing part, and the SINR difference is around 10 dB between them at CUT angle 0 degree. This shows that Doppler mismatch effect is effective in both range and angle domains, but it is more severe in the range rather than the angle processing in this specific simulation scenario.

The bottom graph in Figure 4.7 represents a NO case, where Tx and Rx sectors are separated. It can be seen that the importance of good MIMO processing is more visible when the sectors are separated. When the CUT angle is near (but not on top of) the UIT, $\mathcal{V}_1\&\mathcal{V}_2$ Given $\mathbf{X}_n$ detector can outperform the closest detector by around 7 dB. The effects of Doppler mismatch on both range and angle processings are still visible in this case.

An important aspect that can be deduced from the bottom graph in Figure 4.7 is that the difference between the detectors where Tx beams are illuminating is significantly larger than the difference where Rx beams are illuminating. This phenomenon is expected due to the intrinsic nature of transmit beamforming operation in MIMO systems. As seen in (4.16), after the DACB, the angular channels of the UITs are multiplied with an $\mathbf{X}_n$-dependent matrix from right. This matrix is nonzero when at least one UIT has a mismatched Doppler with the CUT or has a nonzero Doppler spread. As a result, the null-space of the angular channel matrix of the UITs, which is related to the transmit beamforming operation, changes depending on the Tx symbols. If a detector knows the $\mathbf{X}_n$-dependent exact null-space of this matrix, it can find a direction in D_t dimensional space towards which the UITs can be mitigated but the IT is not affected, effectively increasing the SINR by using the mismatch (separation) between the velocities of UITs and the IT. On the other hand, the detectors that do not know (or use) the $\mathbf{X}_n$ information cannot correctly determine the optimal direction to suppress the UITs, losing the ability to apply transmit beamforming. It should be noted that in classical phase-array systems, the transmit beamforming ability is already nullified because $D_t = 1$. Therefore, it can be deduced that interference suppression capabilities of MIMO systems is superior to the classical phased-array ones even though there is no difference in maximum SINR gain that they can achieve.

SINR vs CUT range bin graphs for FO and NO scenarios are provided in Figure 4.8 and Figure 4.9, respectively.

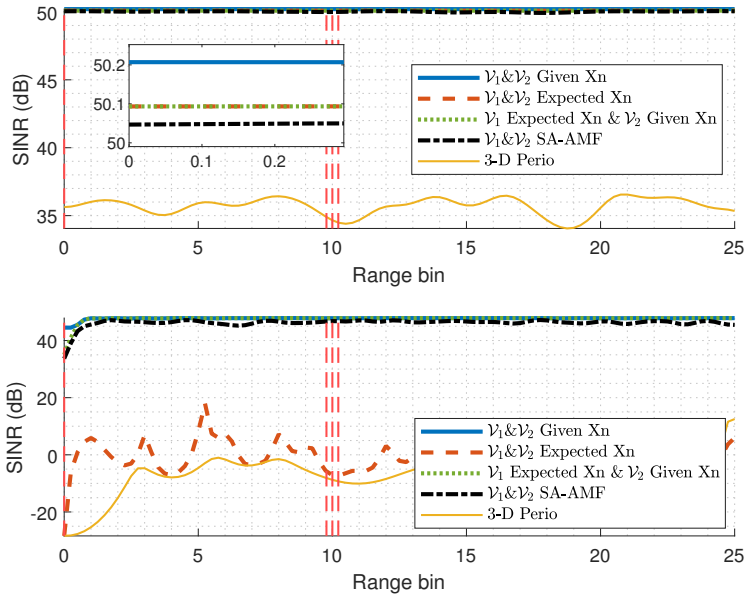


Figure 4.8: SINR vs CUT range bin graphs for FO scenario, CUT Angle: 5 degrees (top) and 0 degrees (bottom), CUT Doppler bin: 0.32 (10 m/s).

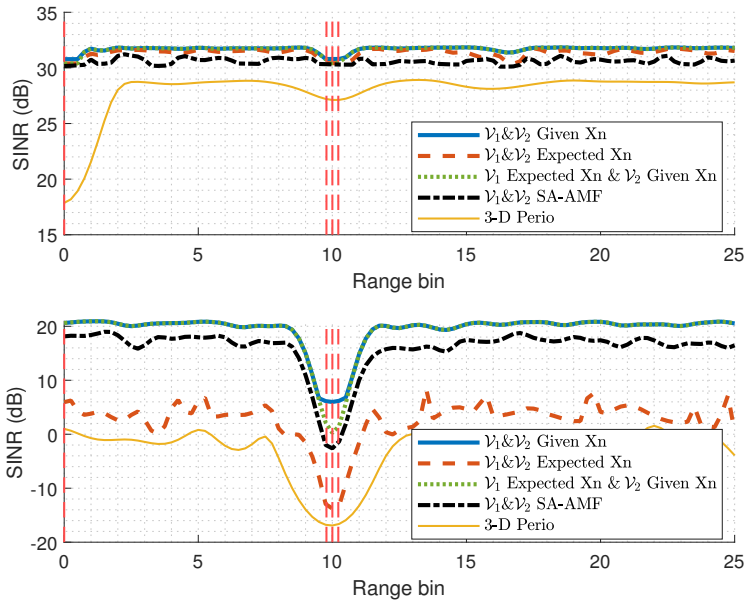


Figure 4.9: SINR vs CUT range bin graphs for NO scenario, CUT Angle: 12 degrees (top) and -12.5 degrees (bottom), CUT Doppler bin: 0.32 (10 m/s).

Similar to the case in Figure 4.7, when the CUT angle is away from the interference, all detectors except 3-D Perio perform similarly, and when the CUT is on top of the interference, using $\mathbf{X}_n$ knowledge is important. In Figure 4.9, it is seen that $\mathcal{V}_1\&\mathcal{V}_2$ Given $\mathbf{X}_n$ and $\mathcal{V}_1$ Expected $\mathbf{X}_n\&\mathcal{V}_2$ Given $\mathbf{X}_n$ detectors perform the same for most CUT ranges, only except on top of the UIT range. This shows that $\mathcal{V}_1$ variant performs better than $\mathcal{V}_2$ variant only when the CUT range is so close to UIT range. This is expected because $\mathcal{V}_1$ uses max-SINR MIMO processing and $\mathcal{V}_2$ uses max-SINR range processing. Figure 4.9 shows that this 2-variant detector scheme benefits the scenarios where the interference can only be suppressed in one dimension.

To evaluate the effects of the number of ISAC subcarriers N on range processing performance, SINR vs CUT range bin graphs in a NO scenario for different N values are provided in Figure 4.10.

In Figure 4.10, N value is changed while $\bar{N}$ is kept the same, meaning that the total bandwidth and range resolution remained constant. It can be seen that both $\mathcal{V}_1\&\mathcal{V}_2$ Given $\mathbf{X}_n$ and $\mathcal{V}_1\&\mathcal{V}_2$ SA-AMF detectors can suppress the interference in range domain when the IT and the UITs are separated enough. The SINR difference between the two methods is due to the limited training data of SA-AMF detector ($\mathcal{T} = 16$ frames). The SINR differences between consecutive N selections are roughly 3 dB, as expected. On the other hand, as the dimensions of $\mathbf{\Sigma}^{\eta}$ increases, interference suppression capabilities in range domain also increase, resulting in a smoother SINR response. It should be noted that when $N = 8$, the maximum unambiguous range is decreased so much that the range response is seen as folded in Figure 4.10. It can also be seen that $N = 32$ selection is a useful compromise between interference suppression capabilities and computational complexity.

SINR vs CUT Doppler bin graphs for two different CUT angles for a FO scenario are provided in Figure 4.11.

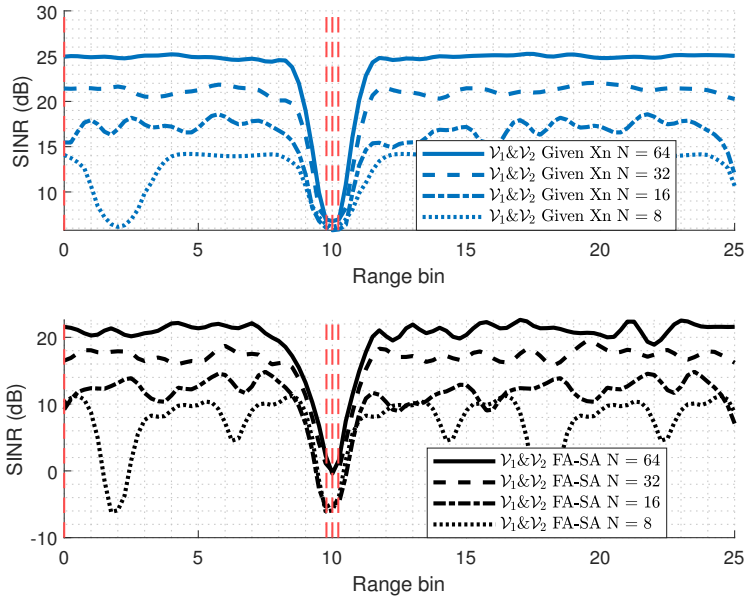


Figure 4.10: SINR vs CUT range bin graphs for $\mathcal{V}_1\&\mathcal{V}_2$ Given $\mathbf{X}_n$ (top) and $\mathcal{V}_1\&\mathcal{V}_2$ SA-AMF (bottom) detectors in a NO scenario, CUT Angle: -12.5 degrees, CUT Doppler bin: 0.32 (10 m/s).

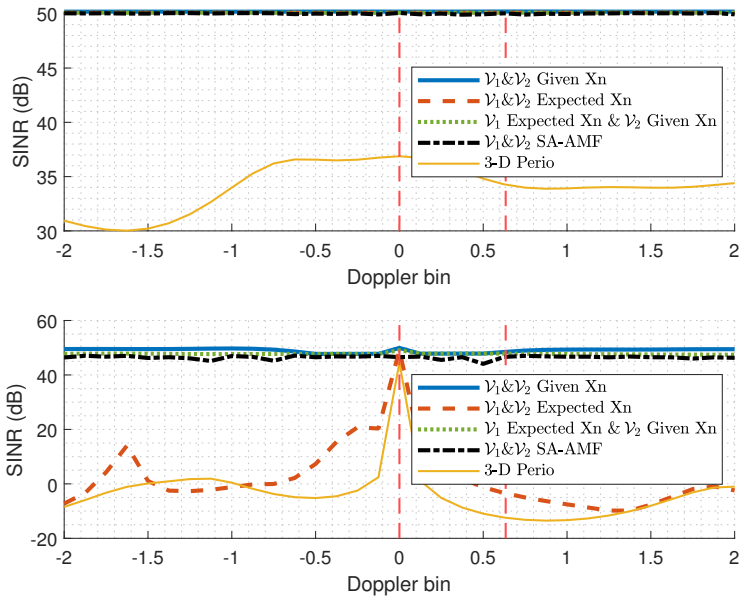


Figure 4.11: SINR vs CUT Doppler bin graphs for FO scenario, CUT Angle: 5 degree (top) and 0 degree (bottom), CUT Range bin: 10.

In the top graph of Figure 4.11, all detectors except 3-D Perio perform similarly as in the other graphs before. In the bottom graph of Figure 4.11, it is seen that when the suppression in angle domain is impossible, the suppression in the range domain depends on the CUT Doppler. When the CUT Doppler is the same as the UIT Doppler, range processing can successfully suppress the clutter for all detectors. However, when there is Doppler mismatch, the detectors that do not use $\mathbf{X}_n$ information fail to suppress the UIT even if it is separated in range domain. This clearly shows that Doppler mismatch can harm range processing if $\mathbf{X}_n$ information is not exploited.

SINR vs CUT Doppler bin graphs for the scenarios in which CUT angle and range bins are on top of UITs are provided in Figure 4.12.

When the CUT is on top of any UIT in both angle and range domains, the UIT can be suppressed only in Doppler domain. Therefore, the detectors using $\mathbf{X}_n$ information outperform the others when the CUT Doppler is separated from the UIT Doppler. It can also be seen that Doppler spread of the UIT is also important and determines how much separation in Doppler is needed to create diversity and suppress the UIT.

P_d vs input SNR curves for two different CUT locations are provided in Figure 4.13. In this figure, input SNR means the SNR value per subcarrier per antenna per symbol. For each detector, the CFAR threshold is determined by the formula

$$\gamma_{th} = -\ln(P_{fa}) * \beta, \tag{4.35}$$

where β is the detection metric at the detector input when H_0 hypothesis is true. Theoretically, this metric is equal to the denominator of the SINR expression in (4.33) for each detector. Since the covariance matrix and the filters in the expression depend on $\mathbf{X}_n$, the theoretic threshold also depends on $\mathbf{X}_n$. However, for successful detectors, interference is suppressed so that the $\mathbf{X}_n$ dependence of the thresholds is weak. On the other hand, adaptive CFAR thresholding using multiple training frames with different $\mathbf{X}_n$ data can also be used to average out the effects of $\mathbf{X}_n$ on the thresholds. A similar adaptive thresholding method is explained in [118]. In Figure 4.13, average thresholds are found for $P_{fa} = 10^{-3}$ and 300 Monte-Carlo trials are conducted to find P_d values. It can be seen in Figure 4.13 that P_d vs input SNR curves give similar results to SINR curves, as expected.

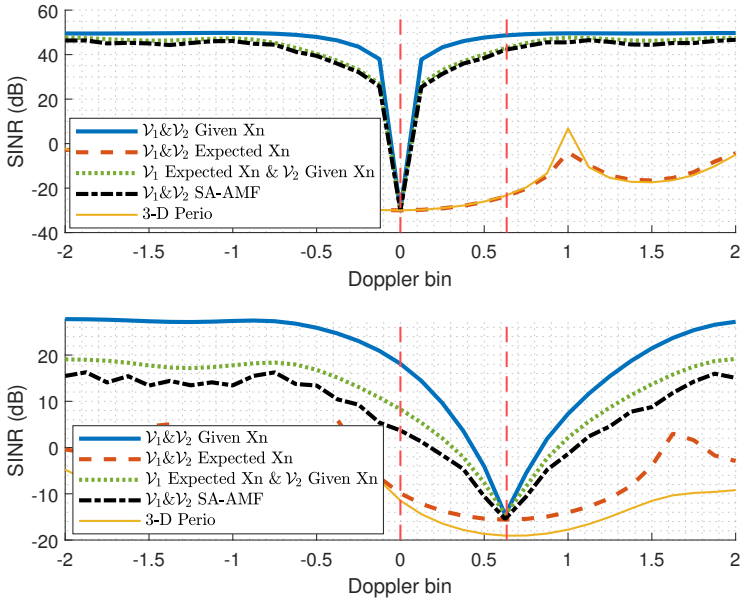


Figure 4.12: SINR vs CUT Doppler bin graphs for FO (top) and NO (bottom) scenarios, CUT Angle: 0 degrees (top) and -12 degrees (bottom), CUT Range bin: 0 (top) and 10 (bottom).

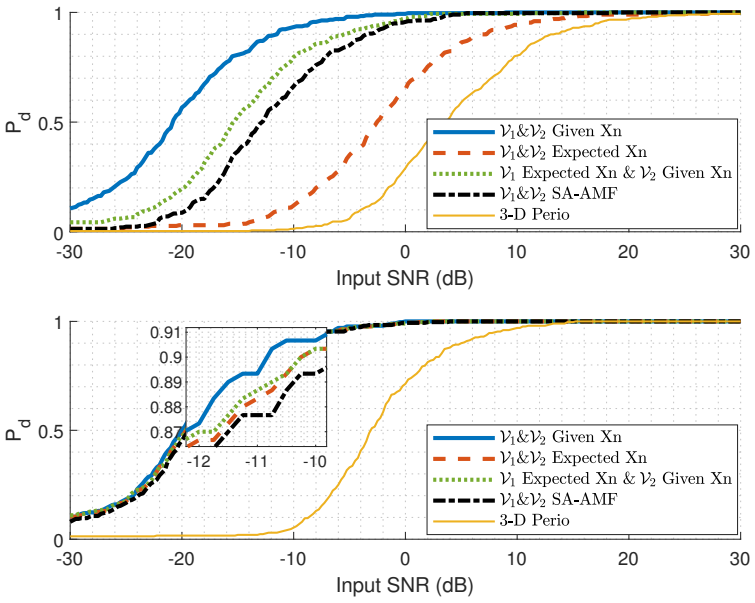


Figure 4.13: P_d vs input SNR curves for NO scenarios, $P_{fa} = 10^{-3}$, number of Monte-Carlo trials: 300, CUT Range bin: 10, CUT Doppler bin: 0.32 (10 m/s), CUT Angle: -6 degree (top) and 16 degrees (bottom).

To make sure that 300 Monte-Carlo simulations are enough, simulations have been conducted to investigate the cumulative density functions (CDF) of output SINR values for different detector implementations. The CDF results are given in Figure 4.14. It can be seen that CDF graphs with 50, 100, 300, 500 and 1000 Monte-Carlo simulations are almost exactly the same, while 10 and 30 simulations resemble some differences, meaning that they do not have enough Monte-Carlo trials to represent the actual random behavior. Therefore, it can be deduced that 300 Monte-Carlo simulations are enough for the simulations to represent the correct random behavior of output SINR values. On the other hand, these graphs indicate another important aspect of the detectors. As it can be seen, the CDF corresponding to the proposed $\mathcal{V}_1\&\mathcal{V}_2$ Given $\mathbf{X}_n$ detector is significantly sharp, while the CDF corresponding to 3-D periodogram is the widest of all detectors. This means that even if transmitted symbols $\mathbf{X}_n$ is changing randomly, the proposed $\mathcal{V}_1\&\mathcal{V}_2$ Given $\mathbf{X}_n$ detector can eliminate the effects of $\mathbf{X}_n$ so that its output SINR does not show significant randomness. On the other hand, the output SINR of 3-D periodogram method shows a large variance due to the randomness of $\mathbf{X}_n$, showing that it cannot eliminate $\mathbf{X}_n$ successfully. This was indeed a key point this thesis points out.

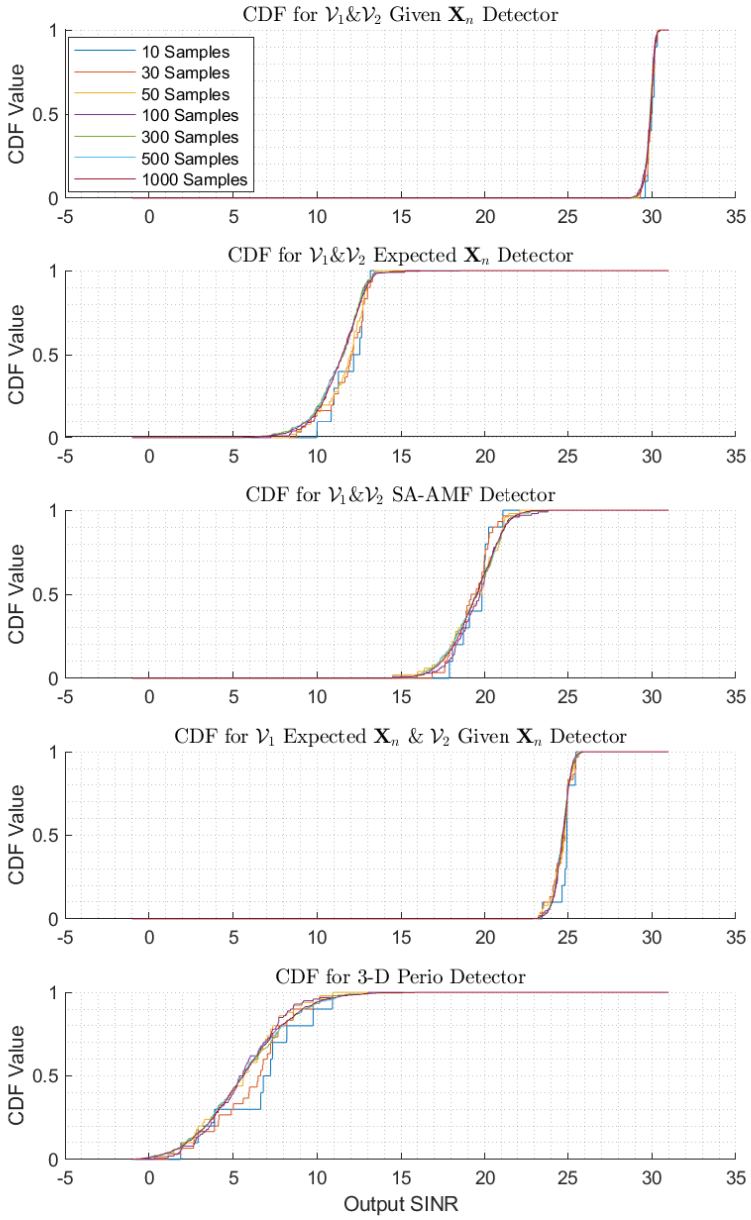


Figure 4.14: CDF values vs output SINR for different detector implementations with different numbers of Monte-Carlo trials.

4.5.3.2 Beam-squint effect is severe

The beam-squint effect when f_c/W ratio is relatively small is investigated in Figure 4.15. In the top graph of Figure 4.15, the detectors do not care about the beam-squint effect and use only a single subband, applying the same angular processing for all subcarriers. It can be seen that the performance of the detectors decreases due to the misinformation on MIMO processing caused by the beam-squint effect. On the other hand, $\mathcal{V}_1\&\mathcal{V}_2$ Given $\mathbf{X}_n$ detector tries to put a sharp null on a wrong angle and therefore its SINR cannot be interpreted as an upper limit to other detectors anymore. Besides this, SA-AMF detector learns the angle information from all subcarriers, which all have different angle information due to the beam-squint effect, and therefore tries to nullify a wider set of angles than it should be.

When the bottom graph of Figure 4.15 is investigated, it can be seen that subband approach can be used to mitigate the negative effects of beam-squint. When $N' = 8$, the MIMO processing filters consider different amounts of suppression for 8 different angles, therefore the UIT can be suppressed better for both detectors. The performance increase in $\mathcal{V}_1\&\mathcal{V}_2$ Given $\mathbf{X}_n$ detector is around 10 dB for some angles, showing that subband approach is a valid method to mitigate the negative effects of beam-squint and make full use of the UIT covariance information while keeping the computational complexity lower than the case when $N' = 32$.

It can be inferred from Figure 4.15 that beam-squint effect can be detrimental if it is not taken into account and the same filter is used for all subcarriers. However, it is not necessary to always use different filters for all subcarriers, a subband approach can be enough depending on the severity of beam-squint effect. It can also be seen in Figure 4.15 that the proposed KA-SARP filters outperform others by suppressing the interference even if it spreads angularly due to the beam-squint effect.

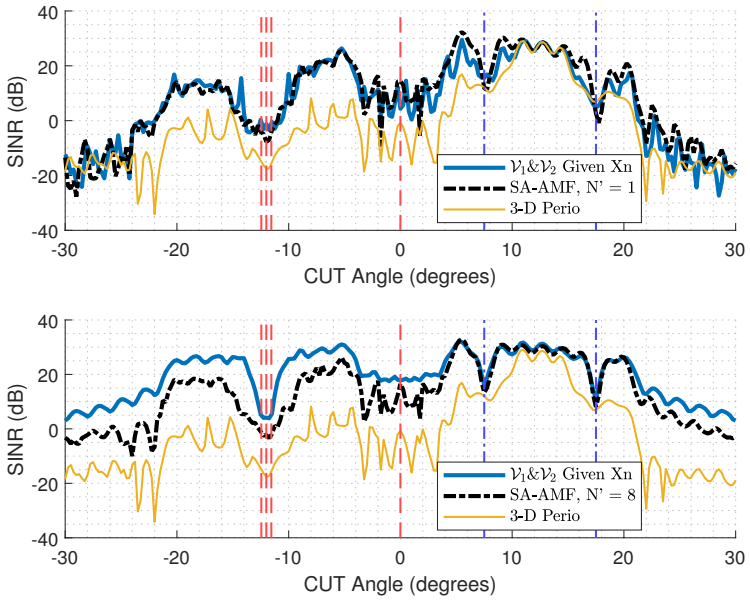


Figure 4.15: SINR vs CUT angle graphs for NO scenarios when beam-squint effect is severe, CUT Range bin: 10, CUT Doppler bin: 0.32 (10 m/s). $f_c/W = 18.1274$. Number of subbands: 1 (top) and 8 (bottom).

4.6 Conclusion

In this chapter, a radar detector structure for an OFDM-based MIMO ISAC system is proposed under the disruptive effects of Doppler mismatch, beam-squint, UL users and multiple scatterers in fractional Doppler-angle-range bins. The introduction of the DACB and coupling between Doppler mismatch and Tx symbols was crucial in understanding the nature of the OFDM-based MIMO ISAC systems. The sub-optimal SARP method proved effective in maximizing the output SINR, with the help of a novel two-variant detector scheme. On the other hand, the possible beam-squint effect dictated that MIMO processing should be done before range processing in SARP. The proposed subband approach effectively addressed the negative effects of beam-squint. Simulation results confirmed the superior performance of the proposed detectors compared to conventional methods, highlighting their potential in enhancing MIMO ISAC system performance.

In the next chapter, the system model and detector structure proposed in this chapter will be extended to multistatic case in which multiple transmitters and receivers that

have MIMO capabilities are spread across an area and a coherent signal processing is done using the combined information of all antenna arrays.

CHAPTER 5

KNOWLEDGE-AIDED AND ADAPTIVE GLRT DETECTORS FOR MULTISTATIC MIMO-OFDM ISAC SYSTEMS

In the previous chapter, the integration of MIMO architectures into ISAC systems was investigated in detail. Among MIMO-ISAC architectures, multistatic systems supported by Distributed MIMO (D-MIMO) frameworks offer significant potential due to their spatial diversity and compatibility with modern wireless infrastructure. This chapter focuses on the development and evaluation of signal processing techniques for D-MIMO ISAC systems operating in multistatic configurations. First, a mathematical model for OFDM-based multistatic MIMO channels including multiple scatterer clutter model and disruptive effects of range and Doppler mismatches. Then, a knowledge-aided GLRT detector is proposed to improve the detection performance of weak targets near strong interferences. To reduce the computational complexity, a novel approximate GLRT detector is also presented. Furthermore, two fully-adaptive detectors are developed to eliminate the dependency on prior knowledge. Performance evaluations demonstrate that the proposed detectors significantly outperform the conventional 3D Periodogram method, especially in scenarios with strong interference. Additionally, the benefits of multistatic architectures in resolving range and Doppler ambiguities are explicitly demonstrated, underscoring their potential for future ISAC deployments.

The upcoming section introduces the assumptions of the proposed multistatic scenario, surveys additional related work, and addresses the main phenomena observed under the new model.

5.1 Introduction and Literature Review

As explained in the previous chapters, ISAC systems have been one of the most popular research areas in recent years because of the ever-increasing need for spectrum efficiency, as they enable the use of the same devices, time or frequency spectrum for both purposes. On the other hand, MIMO architecture constitutes a good basis for ISAC systems because it provides high angular resolution and interference suppression capabilities, as well as it is compatible with the already-existing MIMO communication systems. Similar to classical radar systems, MIMO ISAC systems can be investigated under two categories with respect to the antenna positions for sensing operations, namely monostatic and multistatic systems. Each system has its own benefits and challenges, a general understanding of these systems are well-documented in the classical radar literature [115]. The focus of this chapter will be multistatic ISAC systems. By their nature, D-MIMO systems are suitable for applying a multistatic ISAC operation, therefore the ISAC system will be denoted as D-MIMO ISAC or multistatic ISAC throughout the chapter, interchangeably.

The basic assumption of the multistatic ISAC system is that the complex channels between each of the Tx-Rx pairs are uncorrelated from each other. This assumption is investigated in detail in the literature [108], and it is shown that when the Tx and Rx are separated enough, Tx-Rx pairs are further enough from the targets, and the targets are large enough, this assumption is valid. In this chapter, Tx and Rx locations are chosen to be far away from each other and from the targets, and the targets are chosen to be large objects with multiple scattering centers, so that the uncorrelation assumption is valid.

In this chapter, general notation rules indicated in Section 1.4 will be followed with some slight additions. In this chapter, the parenthesized superscripts denote the transmitter or receiver indices. In light of this general description, $a^{(i,j)}$ denotes the a parameter of $(i,j)^{\text{th}}$ receiver-transmitter pair; $a_t^{(j)}$ denotes the a parameter of $(j)^{\text{th}}$ transmitter; and $a_r^{(i)}$ denotes the a parameter of $(i)^{\text{th}}$ receiver. As a consequence, to distinguish between the transmitter index and the imaginary unit, $\jmath$ will be used to indicate $\sqrt{-1}$ in this chapter.

The rest of this chapter is organized as follows. The detailed system model of OFDM-based D-MIMO ISAC operation will be constructed in Section 5.2. According to the constructed system model, the proposed signal processing algorithms are developed in Section 5.3. Different detector implementations of the proposed signal processing algorithms are indicated in Section 5.4. Properties of simulation environments and the numerical evaluations are provided in Section 5.5. Finally, some concluding remarks are included in Section 5.6.

5.2 System Model

In this section, the mathematical model used in this chapter will be explained in detail.

5.2.1 Mapping to Physical Coordinates

In this chapter, like in the other parts of the thesis, the focus is on a 2D scenario for the sake of simplicity. The extension of this work to 3D scenarios with elevation domain is trivial and not in the scope of this thesis. Like in the classical radar signal processing and previous chapters, there are CUTs on the 2D plane of interest, and each CUT is tested separately for the decision of target detection or not. However, instead of using range-angle-Doppler cells like in monostatic radar scenarios, this chapter prefers to use position and velocity cells on a well-defined Cartesian coordinate system. Specifically, a cell is defined with a 4 dimensional (4D) vector $[\mathbf{p}, \dot{\mathbf{p}}]^{\mathrm{T}} \triangleq [x, y, \dot{x}, \dot{y}]^{\mathrm{T}}$ where x, y are positions and $\dot{x}, \dot{y}$ are the velocities of the cell *w.r.t.* x and y coordinates, respectively. The Euclidean distance between two points in the space, $\mathbf{p}_1 = [x_1, y_1]^{\mathrm{T}}$ and $\mathbf{p}_2 = [x_2, y_2]^{\mathrm{T}}$, is denoted with a custom function d as:

$$\begin{aligned} d(\mathbf{p}_1, \mathbf{p}_2) &= d(x_1, y_1, x_2, y_2) \\ &= ||\mathbf{p}_2 - \mathbf{p}_1|| = \sqrt{(x_2 - x_1)^2 + (y_2 - y_1)^2}. \end{aligned} \tag{5.1}$$

The above definition of cells is beneficial especially when the number of Tx-Rx pairs are large because range, angle or Doppler cells change depending on the Tx-Rx pair in multistatic scenarios. By defining the cells as above, it is guaranteed to perform

target detection for a pre-determined number of points in a 4D space, no matter how many Tx-Rx pairs are included in the system.

5.2.2 Basic Assumptions

In this chapter, it is assumed that there are $\mathcal{J}$ Tx antenna arrays and $\mathcal{I}$ Rx antenna arrays in the system. For the sake of simplicity, each Tx (Rx) antenna array is assumed to have the same number of antenna elements, N_t (N_r), and the antenna elements are positioned to form uniform linear arrays. With this configuration, the total number of Tx and Rx antenna elements become $\mathcal{J}N_t$ and $\mathcal{I}N_r$, respectively.

Like in the previous chapters, it is assumed that the ISAC system has been working for a while and the detection of 'newcomers' in the sector of interest is the main focus. In other words, UITs are considered to be detected before and being tracked by the tracker and the IT is considered to be recently-spawned and needs to be detected. Following the model in Chapter 3 and Chapter 4, the UITs are approximated as collections of several point scattering centers. There can be multiple UITs in the section of interest, each having a specific number of scatterers, which depends on the size of the corresponding UIT. A total of $\mathcal{K}$ UIT scatterers exist in the scenario and in the rest of this chapter, k is the index used for counting the UIT scatterers. The k^{th} scatterer is assumed to be at the position $\mathbf{p}_k \triangleq [x_k, y_k]^{\mathrm{T}}$ with the velocity $\dot{\mathbf{p}}_k \triangleq [\dot{x}_k, \dot{y}_k]^{\mathrm{T}}$. The corresponding round-trip time and radial velocity of each scatterer depends on the Tx-Rx pair under consideration.

The position of u^{th} antenna in the i^{th} Rx array is denoted as $\mathbf{p}_r^{(i_u)} \triangleq [x_r^{(i_u)}, y_r^{(i_u)}]^{\mathrm{T}}$. Similarly, the position of v^{th} antenna in the j^{th} Tx array is denoted as $\mathbf{p}_t^{(j_v)} \triangleq [x_t^{(j_v)}, y_t^{(j_v)}]^{\mathrm{T}}$. The center positions of i^{th} Rx array and j^{th} Tx array are specifically denoted as $\mathbf{p}_r^{(i_c)} \triangleq [x_r^{(i_c)}, y_r^{(i_c)}]^{\mathrm{T}}$ and $\mathbf{p}_t^{(i_c)} \triangleq [x_t^{(j_c)}, y_t^{(j_c)}]^{\mathrm{T}}$, respectively. Following this notation, the time it takes for the waveforms to travel from the v^{th} antenna of the j^{th} Tx array to the k^{th} scatterer point becomes $\tau_{t,k}^{(j_v)} \triangleq d(\mathbf{p}_t^{(j_v)}, \mathbf{p}_k)/c_0$ where c_0 is the speed of light in free space. Similarly, it takes $\tau_{r,k}^{(i_u)} \triangleq d(\mathbf{p}_k, \mathbf{p}_r^{(i_u)})/c_0$ seconds for the waveforms to travel from the k^{th} scatterer to the u^{th} antenna of the i^{th} Rx array. Then, total trip time

of the waveform on the propagation path becomes:

$$\tau_k^{(i_u,j_v)} \triangleq \tau_{t,k}^{(j_v)} + \tau_{r,k}^{(i_u)} \tag{5.2}$$

The rates of increase of the distances (velocities in radial direction) between k^{th} scatterer and v^{th} antenna of the j^{th} Tx array and u^{th} antenna of the i^{th} Rx array are denoted as $\dot{p}_{t,k}^{(j_v)}$ and $\dot{p}_{r,k}^{(i_u)}$, respectively, and they can be written as:

$$\dot{p}_{t,k}^{(j_v)} = \frac{(\mathbf{p}_k - \mathbf{p}_t^{(j_v)})^{\mathrm{T}}\dot{\mathbf{p}}_k}{d(\mathbf{p}_k, \mathbf{p}_t^{(j_v)})} \, , \; \dot{p}_{r,k}^{(i_u)} = \frac{(\mathbf{p}_k - \mathbf{p}_r^{(i_u)})^{\mathrm{T}}\dot{\mathbf{p}}_k}{d(\mathbf{p}_k, \mathbf{p}_r^{(i_u)})} \tag{5.3}$$

Then, the rate of change of the total propagation path, $\dot{p}_k^{(i_u,j_v)}$, is the sum of the radial velocities and it can be written as:

$$\dot{p}_k^{(i_u,j_v)} \triangleq \dot{p}_{t,k}^{(j_v)} + \dot{p}_{r,k}^{(i_u)}. \tag{5.4}$$

It should be noted that neither the position nor the velocity of any UIT scatterer has to be in the center of a position or velocity CUT. In other words, the UIT scatterer parameters are independent of how the CUTs are defined, as in reality. On the other hand, it is assumed that only one IT is present at the current frame and that IT is assumed to be a point-target. In other words, multiple target detection problem is not in the scope of this chapter; if multiple ITs appear in the current frame, each of them are detected separately while the others are being considered as UITs. The IT is a hypothetical target at the CUT, meaning that it is assumed that the IT exists in the center of the CUT in H_1 hypothesis, and it is assumed that no target exists at the CUT in H_0 hypothesis. The detectors try to make a comparison test to choose one of these two hypotheses, as usual in detection theory and in this thesis.

Following the notations described in Chapter 2, in this chapter, M OFDM symbols with symbol duration T are transmitted and received and coherently processed in a CPI. Considering the cyclic prefix duration T_{cp}, the PRI becomes $T_s = T + T_{\text{cp}}$ and total observation time becomes MT_s. There are $\bar{N}$ subcarriers with subcarrier spacing $\Delta\bar{f} = 1/T_s$, making the effective bandwidth $W = \bar{N}\Delta\bar{f}$. Among these subcarriers, N of them are used for ISAC purposes. These N ISAC subcarriers are selected to cover the whole bandwidth with uniform spacing, making the effective subcarrier spacing $\bar{N}/N$ times larger. In other words, the bandwidth of the system is still $W = N\Delta f = \bar{N}\Delta\bar{f}$. The center frequency and corresponding wavelength

of the system is f_c and λ_c, and each of the subcarrier frequencies and corresponding wavelengths are f_n and λ_n for $n = 1, 2, \cdots, N$, respectively.

Finally, it is assumed that beam-squint effects are neglected in this thesis. In other words, the beams formed from the antenna arrays to a specific position are assumed to be the same for all subcarriers. Even if the bandwidth of the system were comparable to the center frequency, a subband approach can be utilized so that in a subset of all subcarriers, the effective bandwidth and consequently the negative effects of beam-squint is small, as shown in Chapter 4. In this chapter, the beam-squint effect is assumed to be negligible in the selected band of N subcarriers, and the signal processing and detection procedures will be proposed accordingly. The case where different subbands are processed differently can be found in Chapter 4 of this thesis and not in the scope of this chapter.

5.2.3 Beamforming and Distributed MIMO Channels

In the ISAC system of this chapter, all antenna arrays use hybrid beamformers. Specifically, Tx and Rx arrays have D_t and D_r RF chains, the Tx and Rx analog beamformers are $N_t \times D_t$ and $N_r \times D_r$ matrices, and they are denoted as $\mathbf{W}_t^{(j)}, j = 1, 2, \cdots, \mathcal{J}$ and $\mathbf{W}_r^{(i)}, i = 1, 2, \cdots, \mathcal{I}$, respectively.

Using previous definitions, the receive and transmit steering vectors can be written as:

$$\begin{aligned} \mathbf{a}_k^{(i)} &\triangleq \left[e^{-\jmath 2\pi f_c(\tau_{r,k}^{(i_1)} - \tau_{r,k}^{(i_c)})} \cdots e^{-\jmath 2\pi f_c(\tau_{r,k}^{(i_{N_r})} - \tau_{r,k}^{(i_c)})} \right]^{\mathrm{T}}, \\ \mathbf{b}_k^{(j)} &\triangleq \left[e^{-\jmath 2\pi f_c(\tau_{t,k}^{(j_1)} - \tau_{t,k}^{(j_c)})} \cdots e^{-\jmath 2\pi f_c(\tau_{t,k}^{(j_{N_t})} - \tau_{t,k}^{(j_c)})} \right]^{\mathrm{T}}. \end{aligned} \tag{5.5}$$

In (5.5), $\mathbf{a}_k^{(i)}$ is the $N_r \times 1$ receive steering vector of i^{th} Rx array and $\mathbf{b}_k^{(j)}$ is the $N_t \times 1$ transmit steering vector of j^{th} Tx array towards k^{th} scatterer. As the positions of scatterers are assumed to be the same through a CPI and beam-squint is neglected, $\mathbf{a}_k^{(i)}$ and $\mathbf{b}_k^{(j)}$ do not depend on OFDM symbol index m or subcarrier index n. The normalizations in (5.5) are done with respect to the center of the arrays for the sake of notational simplicity. In fact, the deterministic complex phase regarding the propagation delay of the signal originated from j^{th} Tx array, echoed from k^{th} scatterer and

reached i^{th} Rx array can be written in terms of these normalization constants as:

$$\rho_{kn}^{(i,j)} \triangleq e^{-\jmath 2\pi f_n(\tau_{r,k}^{(i_c)}+\tau_{t,k}^{(j_c)})} = e^{-\jmath 2\pi f_n \tau_k^{(i_c,j_c)}}. \tag{5.6}$$

Using these variables, the $D_r \times D_t$ frequency-domain channel matrix of the k^{th} scatterer between i^{th} Rx array and j^{th} Tx array, for n^{th} subcarrier and m^{th} OFDM symbol is:

$$\mathbf{H}_{knm}^{(i,j)} = \alpha_{km}^{(i,j)} \rho_{kn}^{(i,j)} \mathbf{H}_k^{(i,j)} \tag{5.7}$$

where

$$\mathbf{H}_k^{(i,j)} = \sqrt{\gamma_k^{(i,j)}} \left[(\mathbf{W}_r^{(i)})^{\text{H}} \mathbf{a}_k^{(i)} (\mathbf{b}_k^{(j)})^{\text{T}} (\mathbf{W}_t^{(j)})^* \right] \tag{5.8}$$

is the $D_r \times D_t$ effective MIMO channel, including the amplitude and the position information of the scatterer after dimensions are reduced via beamformers, which is assumed to be stationary along M symbols and N subcarriers.

$\gamma_k^{(i,j)}$ is a real scalar which represents the average power of the echoes from the k^{th} scatterer. $\gamma_k^{(i,j)}$ has neither m nor n index because the average power of the echo signals is assumed to be the same for different symbols and subcarriers.

The random variable $\alpha_{km}^{(i,j)}$ is the random complex phase in the m^{th} OFDM symbol and depicts the mean Doppler shift and Doppler spread information of the scatterer. This variable can be written as:

$$\alpha_{km}^{(i,j)} \triangleq \tilde{\alpha}_{km}^{(i,j)} \bar{\alpha}_{km}^{(i,j)} \triangleq \tilde{\alpha}_{km}^{(i,j)} \exp\left\{ \jmath 2\pi \frac{\dot{p}_k^{(i_c,j_c)}}{\lambda_c} mT \right\}, \tag{5.9}$$

where the exponential term, $\bar{\alpha}_{km}^{(i,j)}$, is the deterministic mean Doppler shift[1]. The other term, $\tilde{\alpha}_{km}^{(i,j)}$, is a realization of a stationary random process along m index, with a given PSD. Let's define

$$\begin{aligned} \tilde{\boldsymbol{\alpha}}_k^{(i,j)} &\triangleq [\tilde{\alpha}_{k1}^{(i,j)} \ \tilde{\alpha}_{k2}^{(i,j)} \ \cdots \ \tilde{\alpha}_{kM}^{(i,j)}]^{\text{T}}, \\ \mathbf{R}_k^{\tilde{\boldsymbol{\alpha}}^{(i,j)}} &\triangleq \mathbb{E}\left\{ \tilde{\boldsymbol{\alpha}}_k^{(i,j)} (\tilde{\boldsymbol{\alpha}}_k^{(i,j)})^{\text{H}} \right\}, \end{aligned} \tag{5.10}$$

where all of the diagonal elements of $\mathbf{R}_k^{\tilde{\boldsymbol{\alpha}}^{(i,j)}}$ are assumed to be equal to 1 because the average power of the returns from the scatterer is handled in $\gamma_k^{(i,j)}$. The off-

[1] The mean Doppler shift of a scatterer is actually dependent on the antenna indices u and v, but this kind of angle-Doppler coupling is ignored and the Doppler shifts are written with respect to the antenna centers in (5.9).

diagonal elements of $\mathbf{R}_k^{\tilde{\boldsymbol{\alpha}}^{(i,j)}}$ determines the slow-time correlation properties of the k^{th} scatterer[2].

For later use, $M \times 1$ vector and $M \times M$ diagonal matrix of random phases related to Doppler shifts are defined as:

$$\boldsymbol{\alpha}_k^{(i,j)} \triangleq [\alpha_{k1}^{(i,j)}\ \alpha_{k2}^{(i,j)}\ \cdots\ \alpha_{kM}^{(i,j)}]^{\mathrm{T}}, \quad \mathbf{D}_{\alpha_k}^{(i,j)} \triangleq \mathrm{diag}\{\boldsymbol{\alpha}_k^{(i,j)}\}, \tag{5.11}$$

and the $N \times 1$ vector and $N \times N$ diagonal matrix of deterministic phases related to propagation delay are defined as:

$$\boldsymbol{\rho}_k^{(i,j)} \triangleq [\rho_{k1}^{(i,j)}\ \rho_{k2}^{(i,j)}\ \cdots\ \rho_{kN}^{(i,j)}]^{\mathrm{T}}, \quad \mathbf{D}_{\rho_k}^{(i,j)} \triangleq \mathrm{diag}\{\boldsymbol{\rho}_k^{(i,j)}\}. \tag{5.12}$$

5.2.4 Cell Under Test and Hypothesis Testing

In this subsection, the notational details about the CUT of this chapter will be clarified. As explained before, the cells in this chapter are defined with 4D vectors like $[x, y, \dot{x}, \dot{y}]^{\mathrm{T}}$. Among these cells, the CUT is denoted with star $(\star)$ symbol. Namely, the position of the CUT is $\mathbf{p}_\star \triangleq [x_\star, y_\star]^{\mathrm{T}}$ and the velocity of the CUT is $\dot{\mathbf{p}}_\star \triangleq [\dot{x}_\star, \dot{y}_\star]^{\mathrm{T}}$. Similarly, any parameter which is defined for k^{th} scatterer will represent a hypothetical target at the CUT when k index is replaced by $\star$. For example, $\alpha_{\star m}^{(i,j)}$ is the random variable depicting the mean Doppler shift and Doppler spread related to the CUT, or $\tau_\star^{(i_u,j_v)}$ is the total trip time of the signals from Tx antenna j_v to CUT and from CUT to Rx antenna i_u. It should be noted that even if there is not a target at the CUT in reality, the signal processing can, and usually is, done as if a hypothetical IT exists at the CUT.

Using the notational definitions above, under the assumption that there is no target at the CUT (H_0 hypothesis), the received signal vector at i^{th} receiver at n^{th} subcarrier

[2] The random variable $\tilde{\alpha}_{km}^{(i,j)}$ is chosen to be a realization of a zero-mean complex Gaussian process, whose PSD function is Gaussian shaped with a standard variaton of $\sigma_k^{(i,j)}$ and mean of zero. Such processes can be easily shown to have their autocorrelation matrix entries as $[\mathbf{R}_k^{\tilde{\boldsymbol{\alpha}}^{(i,j)}}]_{(m,n)} = \exp(-2\pi^2(\sigma_k^{(i,j)})^2(m-n)^2T^2)$.

and m^{th} symbol is denoted as $\boldsymbol{\psi}_{nm}^{(i)}$ and it can be written as[3]:

$$\boldsymbol{\psi}_{nm}^{(i)} = \sum_{k=1}^{\mathcal{K}} \sum_{j=1}^{\mathcal{J}} \mathbf{H}_{knm}^{(i,j)} \mathbf{x}_{nm}^{(j)} + \mathbf{n}_{nm}^{(i)}. \tag{5.13}$$

where $\mathbf{x}_{nm}^{(j)}$ is the $D_t \times 1$ vector of frequency domain Tx streams to DL users associated with j^{th} transmitter and $\mathbf{n}_{nm}^{(i)}$ is the $D_r \times 1$ vector of noise samples at the receiver side after classical OFDM receiver signal processing steps including serial-to-parallel conversion, CP removal, FFT and receive beamforming operations. If there is a target at the CUT (H_1 hypothesis), then the echoes from that target can be written as:

$$\mathbf{y}_{nm\star}^{(i)} = \sum_{j=1}^{\mathcal{J}} \mathbf{H}_{\star nm}^{(i,j)} \mathbf{x}_{nm}^{(j)} \tag{5.14}$$

Then, the received signal vector can be written in general as:

$$\mathbf{y}_{nm}^{(i)} = \begin{cases} \boldsymbol{\psi}_{nm}^{(i)}, & \text{under } H_0 \\ \boldsymbol{\psi}_{nm}^{(i)} + \mathbf{y}_{nm\star}^{(i)}, & \text{under } H_1 \end{cases}. \tag{5.15}$$

5.3 Signal Model and Radar Signal Processing

In this section, the proposed radar signal processing steps will be explained in detail. Before explaining the steps of proposed signal processing method, the matrix notation used in this section will be provided. Following the two-stage signal processing explained in Chapter 2, the channel estimation takes place at the first place. In the channel estimation stage for each CUT, the transmitted symbols will be eliminated from the received signal while range and Doppler processings are done at the same time. This means that in this chapter, extraction of both range and Doppler parameters are embedded in the channel estimation stage. As a result, the parameter extraction stage focuses only on the MIMO processing in this chapter. To this end, the target and interference MIMO channel covariances before and after the channel estimation are theoretically derived. At the end of this section, the SINR-maximizing

[3] If there is a line-of-sight (LOS) path between the $(i,j)^{\text{th}}$ Rx-Tx pair, then an additional interference term must be added to $\boldsymbol{\psi}_{nm}^{(i)}$, which is: $\sqrt{\gamma_0^{(i,j)}} \left[(\mathbf{W}_r^{(i)})^{\text{H}} \mathbf{a}_0^{(i)} (\mathbf{b}_0^{(j)})^{\text{T}} (\mathbf{W}_t^{(j)})^* \right] \rho_{0n}^{(i,j)}$, where $\gamma_0^{(i,j)}$ is the power of the LOS path, $\rho_{0n}^{(i,j)} = e^{-\jmath 2\pi f_n d(\mathbf{p_t^{(j_c)}}, \mathbf{p_r^{(i_c)}})/c_0}$ is the phase shift due to the propagation in LOS path, and $\mathbf{a}_0^{(i)}$ and $\mathbf{b}_0^{(j)}$ are the steering vectors between the $(i,j)^{\text{th}}$ Rx-Tx pair.

MIMO processing is proposed using the derived covariances and the resultant SINR improvement factor is theoretically calculated.

5.3.1 Signal Model in Matrix Notation

As described previously, in this section, the beam-squint effects are ignored for the selected subband of N subcarriers. Therefore, the MIMO channel is equal to $\mathbf{H}_k^{(i,j)}$ for all n (subcarriers). However, for the sake of clarity for the following theoretical derivations, for each subcarrier, the received signal matrix $\mathbf{Y}_n^{(i)}$, received interference matrix $\mathbf{\Psi}_n^{(i)}$, received target echo matrix $\mathbf{Y}_{n\star}^{(i)}$, transmit signal matrix $\mathbf{X}_n^{(j)}$ and noise matrix $\mathbf{N}_n^{(i)}$ are defined by concatenating subsequent OFDM symbols side-by-side as:

$$\begin{aligned}
\mathbf{Y}_n^{(i)} &\triangleq \left[\mathbf{y}_{n1}^{(i)}\, \mathbf{y}_{n2}^{(i)} \cdots \mathbf{y}_{nM}^{(i)}\right], & \mathbf{\Psi}_n^{(i)} &\triangleq \left[\boldsymbol{\psi}_{n1}^{(i)}\, \boldsymbol{\psi}_{n2}^{(i)} \cdots \boldsymbol{\psi}_{nM}^{(i)}\right] \\
\mathbf{Y}_{n\star}^{(i)} &\triangleq \left[\mathbf{y}_{n1\star}^{(i)}\, \mathbf{y}_{n2\star}^{(i)} \cdots \mathbf{y}_{nM\star}^{(i)}\right], & \mathbf{X}_n^{(j)} &\triangleq \left[\mathbf{x}_{n1}^{(j)}\, \mathbf{x}_{n2}^{(j)} \cdots \mathbf{x}_{nM}^{(j)}\right] \\
\mathbf{N}_n^{(i)} &\triangleq \left[\mathbf{n}_{n1}^{(i)}\, \mathbf{n}_{n2}^{(i)} \cdots \mathbf{n}_{nM}^{(i)}\right].
\end{aligned} \tag{5.16}$$

Following the matrix definitions in (5.16), $D_r \times MN$ received signal matrix at i^{th} Rx antenna array $\mathbf{Y}^{(i)}$, received interference matrix $\mathbf{\Psi}^{(i)}$, received target echo matrix $\mathbf{Y}_\star^{(i)}$, $D_t \times MN$ transmit signal matrix from j^{th} Tx antenna array $\mathbf{X}^{(j)}$ and $D_r \times MN$ noise matrix at i^{th} Rx antenna array $\mathbf{N}^{(i)}$ can be defined as:

$$\begin{aligned}
\mathbf{Y}^{(i)} &\triangleq \left[\mathbf{Y}_1^{(i)}\, \mathbf{Y}_2^{(i)} \cdots \mathbf{Y}_N^{(i)}\right], & \mathbf{\Psi}^{(i)} &\triangleq \left[\mathbf{\Psi}_1^{(i)}\, \mathbf{\Psi}_2^{(i)} \cdots \mathbf{\Psi}_N^{(i)}\right] \\
\mathbf{Y}_\star^{(i)} &\triangleq \left[\mathbf{y}_{1\star}^{(i)}\, \mathbf{y}_{2\star}^{(i)} \cdots \mathbf{y}_{N\star}^{(i)}\right], & \mathbf{X}^{(j)} &\triangleq \left[\mathbf{X}_1^{(j)}\, \mathbf{X}_2^{(j)} \cdots \mathbf{X}_N^{(j)}\right] \\
\mathbf{N}^{(i)} &\triangleq \left[\mathbf{N}_1^{(i)}\, \mathbf{N}_2^{(i)} \cdots \mathbf{N}_N^{(i)}\right].
\end{aligned} \tag{5.17}$$

Then, using (5.7), (5.13), (5.15) and (5.17), $\mathbf{Y}^{(i)}$ can be written as:

$$\mathbf{Y}^{(i)} = \begin{cases} \mathbf{\Psi}^{(i)}, & \text{under } H_0 \\ \mathbf{\Psi}^{(i)} + \mathbf{Y}_\star^{(i)}, & \text{under } H_1 \end{cases} \tag{5.18}$$

where

$$\boldsymbol{\Psi}^{(i)} = \sum_{k=1}^{\mathcal{K}} \sum_{j=1}^{\mathcal{J}} \mathbf{H}_k^{(i,j)} \mathbf{X}^{(j)} \mathbf{D}_{\rho\alpha_k}^{(i,j)} + \mathbf{N}^{(i)}, \tag{5.19}$$

$$\mathbf{Y}_\star^{(i)} = \sum_{j=1}^{\mathcal{J}} \mathbf{H}_\star^{(i,j)} \mathbf{X}^{(j)} \mathbf{D}_{\rho\alpha_\star}^{(i,j)}, \tag{5.20}$$

$$\mathbf{D}_{\rho\alpha_k}^{(i,j)} \triangleq \mathbf{D}_{\rho_k}^{(i,j)} \otimes \mathbf{D}_{\alpha_k}^{(i,j)} = \mathrm{diag}\{\boldsymbol{\rho}_k^{(i,j)} \otimes \boldsymbol{\alpha}_k^{(i,j)}\}, \tag{5.21}$$

and

$$\mathbf{D}_{\rho\alpha_\star}^{(i,j)} \triangleq \mathbf{D}_{\rho_\star}^{(i,j)} \otimes \mathbf{D}_{\alpha_\star}^{(i,j)} = \mathrm{diag}\{\boldsymbol{\rho}_\star^{(i,j)} \otimes \boldsymbol{\alpha}_\star^{(i,j)}\}. \tag{5.22}$$

$\mathbf{D}_{\rho\alpha_k}^{(i,j)}$ and $\mathbf{D}_{\rho\alpha_\star}^{(i,j)}$ are an $MN \times MN$ diagonal matrices corresponding to phase shifts due to both propagation delay and Doppler shift. The summation over Tx antenna arrays in (5.19) can be rewritten using block matrices as in (5.23) for subsequent joint LS processing:

$$\boldsymbol{\Psi}^{(i)} = \sum_{k=1}^{\mathcal{K}} \left[\mathbf{H}_k^{(i,1)} \,\vdots\, \cdots \,\vdots\, \mathbf{H}_k^{(i,\mathcal{J})}\right] \mathbf{X} \begin{bmatrix} \mathbf{D}_{\rho\alpha_k}^{(i,1)} \\ \hdashline \vdots \\ \hdashline \mathbf{D}_{\rho\alpha_k}^{(i,\mathcal{J})} \end{bmatrix} + \mathbf{N}^{(i)}, \tag{5.23}$$

where

$$\mathbf{X} \triangleq \mathrm{bdiag}\{(\mathbf{X}^{(j)})_{j=1}^{\mathcal{J}}\}. \tag{5.24}$$

Similarly, (5.20) can be written using block matrices as in (5.25) for subsequent processing.

$$\mathbf{Y}_\star^{(i)} = \left[\mathbf{H}_\star^{(i,1)} \,\vdots\, \cdots \,\vdots\, \mathbf{H}_\star^{(i,\mathcal{J})}\right] \mathbf{X} \begin{bmatrix} \mathbf{D}_{\rho\alpha_\star}^{(i,1)} \\ \hdashline \vdots \\ \hdashline \mathbf{D}_{\rho\alpha_\star}^{(i,\mathcal{J})} \end{bmatrix}. \tag{5.25}$$

The multiple scatterer ISAC channel, transmitted and received signals and vector and matrix notations are visualized in Figure 5.1.

5.3.2 Processing along OFDM symbols and subcarriers

The focus of the signal processing for target parameter extraction will be on the MIMO processing in this chapter. Therefore, the aim of the first stage of processing is to estimate the MIMO channel for all Tx-Rx pairs, assuming that there is a

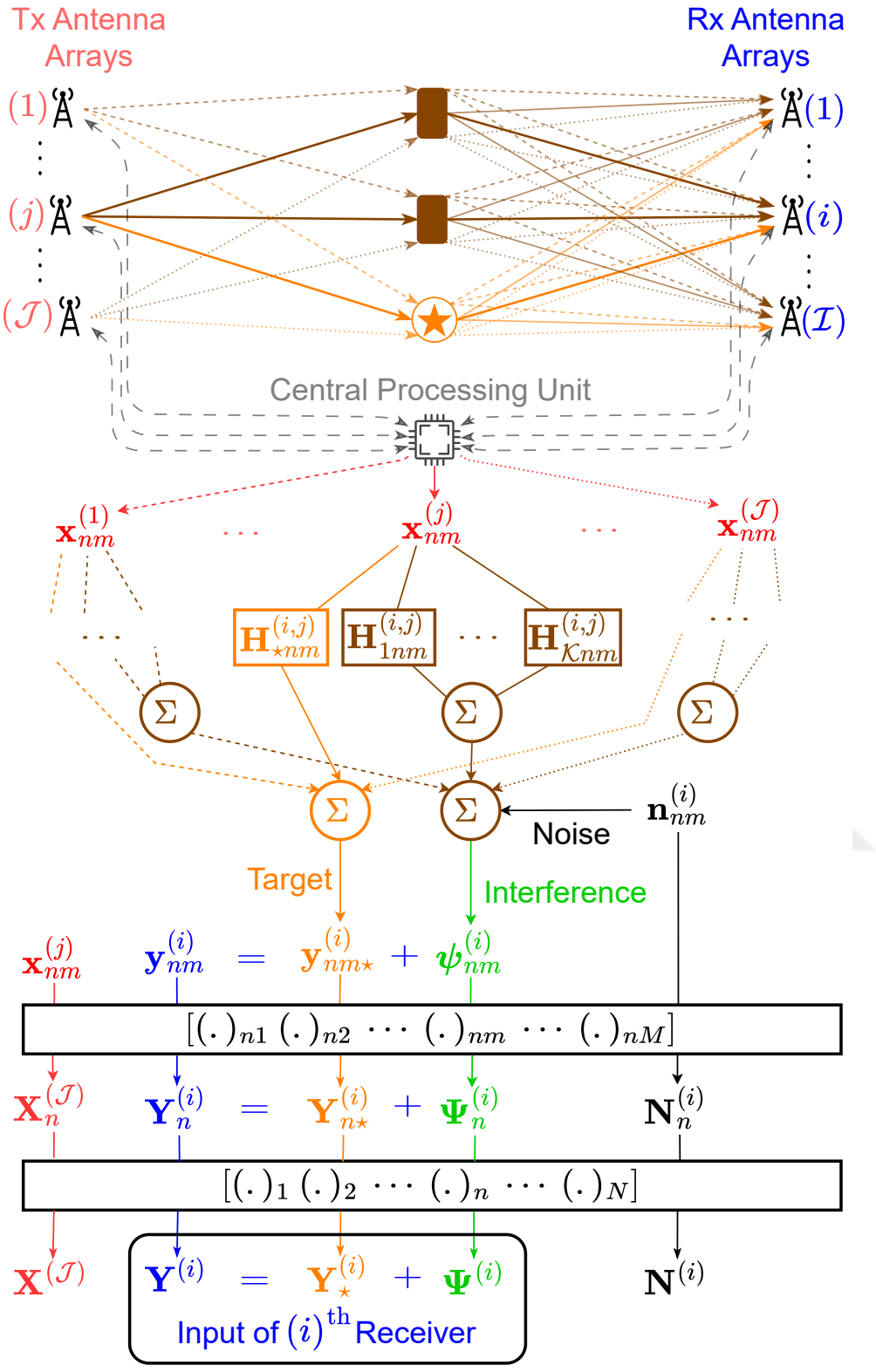


Figure 5.1: Visualization of the UITs and the IT in an example scenario (top) and diagram of transmitted and received data matrices (bottom).

target at the CUT. When (5.25) is investigated, it can be seen that the transmitted signal matrix $\mathbf{X}$ and range and Doppler phase shift matrices $\mathbf{D}_{\rho_\star}^{(i,j)}$ and $\mathbf{D}_{\alpha_\star}^{(i,j)}$ can be used to estimate the MIMO channel matrices $\mathbf{H}_\star^{(i,j)}$. As a centralized processing is assumed, $\mathbf{X}$ is known at the receiver side. On the other hand, for a hypothetical target at the CUT with position $\mathbf{p}_\star$ and velocity $\dot{\mathbf{p}}_\star$, $\mathbf{D}_{\rho_\star}^{(i,j)} = \mathrm{diag}\left\{\left[\rho_{\star 1}^{(i,j)}\ \rho_{\star 2}^{(i,j)}\cdots\ \rho_{\star N}^{(i,j)}\right]\right\}$ and $\mathbf{D}_{\bar{\alpha}_\star}^{(i,j)} = \mathrm{diag}\left\{\left[\bar{\alpha}_{\star 1}^{(i,j)}\ \bar{\alpha}_{\star 2}^{(i,j)}\cdots\ \bar{\alpha}_{\star M}^{(i,j)}\right]\right\}$ can be created for each $(i,j)^{\text{th}}$ Tx-Rx pair because all Tx and Rx locations are also assumed to be known. It should be noted that the IT is assumed to have no Doppler spread and its RCS is assumed to be stable inside a frame (Swerling-1 type target), therefore $\tilde{\alpha}_{\star m}^{(i,j)}$ is a realization of a Gaussian random process which is fully correlated among m axis. Therefore, m index can be removed from it and $\tilde{\alpha}_{\star m}^{(i,j)} = \tilde{\alpha}_\star^{(i,j)}$ can be written for the IT at the CUT. As a consequence, the random part of $\alpha_{\star m}^{(i,j)}$, namely $\tilde{\alpha}_\star^{(i,j)}$, cannot be known or created at the receiver side, because it is a random phase due to the physical structure of waves and scatterers, and must also be estimated alongside the MIMO channel.

In this chapter and in the previous chapters of this thesis, LS method is used to estimate $\tilde{\alpha}_\star^{(i,j)}\mathbf{H}_\star^{(i,j)}$ as it benefits from having a large number of observation samples. As seen in (5.25), there are MN observation samples per Tx-Rx pair for this estimation, which can be larger than a thousand in some practical scenarios, different from the case in Chapter 4. Therefore, a joint LS-type channel estimation is proposed in this chapter. As will be shown later, this processing can be written as a modified version of conventional DFT/IDFT type processings along OFDM symbols and subcarriers.

For further processings, let's define $\mathcal{J}MN \times MN$ block matrices:

$$\mathbf{D}_{\rho\alpha_k}^{(i)} \triangleq \begin{bmatrix} \mathbf{D}_{\rho\alpha_k}^{(i,1)} \\ \vdots \\ \mathbf{D}_{\rho\alpha_k}^{(i,\mathcal{J})} \end{bmatrix}, \mathbf{D}_{\rho\alpha_\star}^{(i)} \triangleq \begin{bmatrix} \mathbf{D}_{\rho\alpha_\star}^{(i,1)} \\ \vdots \\ \mathbf{D}_{\rho\alpha_\star}^{(i,\mathcal{J})} \end{bmatrix}, \mathbf{D}_{\rho\bar{\alpha}_\star}^{(i)} \triangleq \begin{bmatrix} \mathbf{D}_{\rho\bar{\alpha}_\star}^{(i,1)} \\ \vdots \\ \mathbf{D}_{\rho\bar{\alpha}_\star}^{(i,\mathcal{J})} \end{bmatrix}. \tag{5.26}$$

Then, the joint channel estimate and individual channel estimates are defined as:

$$\begin{aligned} \hat{\mathbf{H}}^{(i)} &\triangleq \left[\hat{\mathbf{H}}^{(i,1)} \,\vdots\, \cdots \,\vdots\, \hat{\mathbf{H}}^{(i,\mathcal{J})}\right] = \mathbf{Y}^{(i)}\left(\mathbf{X}\mathbf{D}_{\rho\bar{\alpha}_\star}^{(i)}\right)^{\#} \\ &= \mathbf{Y}^{(i)}\mathbf{D}_{\rho\bar{\alpha}_\star}^{(i)\mathrm{H}}\mathbf{X}^{\mathrm{H}}\left(\mathbf{X}\mathbf{D}_{\rho\bar{\alpha}_\star}^{(i)}\mathbf{D}_{\rho\bar{\alpha}_\star}^{(i)\mathrm{H}}\mathbf{X}^{\mathrm{H}}\right)^{-1} \\ &\triangleq \mathbf{Y}^{(i)}\mathbf{D}_{\rho\bar{\alpha}_\star}^{(i)\mathrm{H}}\mathbf{X}^{\mathrm{H}}\mathbf{B} \end{aligned} \tag{5.27}$$

where $\mathbf{B} \triangleq (\mathbf{X}\mathbf{X}^{\mathrm{H}})^{-1}$ is a $\mathcal{J}D_t \times \mathcal{J}D_t$ matrix defined for notational neatness in the

following derivations. In fact, considering that transmitted symbols are independent and identically distributed, $\mathbf{B}$ approaches to $\mathbf{I}_{\mathcal{J}D_t}$ as MN gets larger and larger. This means that the inverse operation in the processing can be eliminated without a significant performance loss if $MN >> \mathcal{J}D_t$. This kind of approximate processings will be investigated in later sections. On the other hand, $\mathbf{B}$ can be considered as a block matrix which consists of $\mathcal{J}^2$ blocks of $D_t \times D_t$ matrices. The $(j_1, j_2)^{\text{th}}$ block of $\mathbf{B}$ is denoted as:

$$[\mathbf{B}]_{[j_1,j_2]} \triangleq \mathbf{B}_{j_1}^{(j_2)}. \tag{5.28}$$

Then, using (5.22), (5.24), (5.26) and (5.28), (5.27) can be rewritten as:

$$\begin{aligned}\hat{\mathbf{H}}^{(i,j)} &= \mathbf{Y}^{(i)} \sum_{j'=1}^{\mathcal{J}} \mathbf{D}_{\rho\bar{\alpha}_\star}^{(i,j')\text{H}} \mathbf{X}^{(j)\text{H}} \mathbf{B}_{j'}^{(j)} \\ &= \sum_{j'=1}^{\mathcal{J}} \sum_{n=1}^{N} \sum_{m=1}^{M} \rho_{\star n}^{(i,j')*} \bar{\alpha}_{\star m}^{(i,j')*} \left[\mathbf{y}_{nm}^{(i)} \mathbf{x}_{nm}^{(j)\text{H}}\right] \mathbf{B}_{j'}^{(j)}.\end{aligned} \tag{5.29}$$

It should be noted that the processing in (5.29) is indeed a DFT along OFDM symbols and an IDFT along subcarriers, focused on a specific Doppler-range bin corresponding to the CUT. If $\mathbf{B}_{j'}^{(j)}$ is ignored for a moment, the matrix that is subject to DFT/IDFT processings is $\left[\mathbf{y}_{nm}^{(i)} \mathbf{x}_{nm}^{(i)\text{H}}\right]$, which is the estimate of the $D_r \times D_t$ MIMO channel between i^{th} receiver and j^{th} transmitter, at n^{th} subcarrier and m^{th} OFDM symbol. It can be seen that the channel estimate uses information from all $D_r D_t$ Tx-Rx streams, fully utilizing the MIMO processing for each Tx-Rx pair. However, the joint LS processing knows that the received observations include the signals from not only the corresponding transmitter but all other $\mathcal{J} - 1$ transmitters; and these extra signals can also be used to improve the channel estimate because their effects cannot be completely eliminated due to the finite number of OFDM symbols. Then, $\mathbf{B}_{j'}^{(j)}$ is indeed a weighting matrix for the effects of $(j')^{\text{th}}$ Tx to the MIMO channel estimate between any receiver and j^{th} transmitter. An important observation is that if $D_t = 1$, meaning that if the system is not a MIMO system but a classical phased-array system, the channel would be a vector and the weight would be a scalar. However, when the system has MIMO capability with $D_t > 1$, the weighting is done with a matrix multiplication and thus changes the matrix structure of weighted channels differently for each transmitter. Another important observation is that if the previously mentioned $\mathbf{B} \approx \mathbf{I}_{\mathcal{J}D_t}$ approximation is assumed to be correct, then $\mathbf{B}_{j'}^{(j)} = \delta[j - j']\mathbf{I}_{D_t}$ is sat-

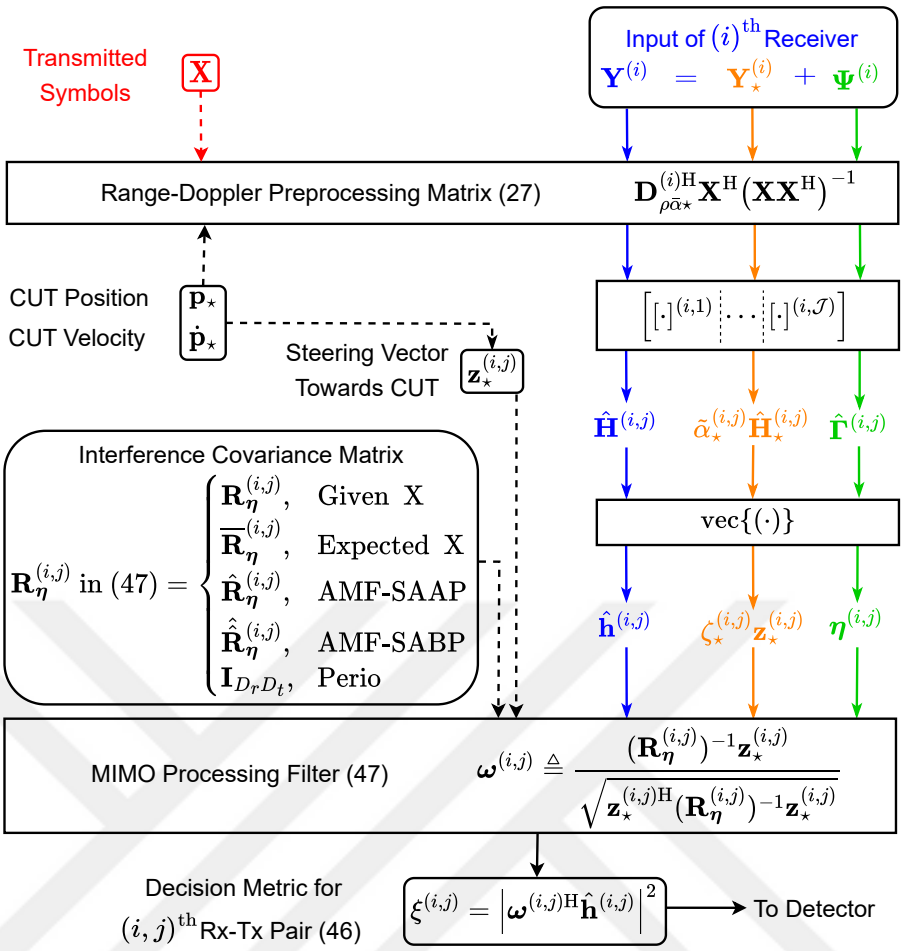


Figure 5.2: Block diagram of proposed signal processing for $(i,j)^{\text{th}}$ Rx-Tx pair.

isfied. This means that as MN gets larger and larger than $\mathcal{J}D_t$, the effects of other transmitters' signals on the channel estimate between any Tx-Rx pair becomes less and less significant as the different channels become decoupled. If this is the case, the summation over j' in (5.29) drops, leaving only the DFT/IDFT of the channel estimate as the result of the joint LS processing.

The range-Doppler preprocessing for MIMO channel estimation described in this subsection, and the MIMO processing for target parameter extraction which will be explained in the following subsection is visualized with a block diagram in Figure 5.2.

5.3.3 MIMO Processing and Detection

In the previous subsection, the observations $\mathbf{Y}^{(i)}$ are processed to get the estimates of MIMO channel matrices $\hat{\mathbf{H}}^{(i,j)}$. In this section, the MIMO channel estimates are used in a covariance-type processing to suppress interference in MIMO domain and detect the possible target in the CUT. To achieve this, the interference and target covariances should be distinguished from each other. Therefore, using (5.18) and (5.29), the following definitions can be made:

$$\hat{\mathbf{H}}^{(i,j)} \triangleq \begin{cases} \mathbf{\Gamma}^{(i,j)}, & \text{under } H_0 \\ \tilde{\alpha}_{\star}^{(i,j)}\mathbf{H}_{\star}^{(i,j)} + \mathbf{\Gamma}^{(i,j)}, & \text{under } H_1 \end{cases} \tag{5.30}$$

where

$$\mathbf{\Gamma}^{(i,j)} \triangleq \mathbf{\Psi}^{(i)} \sum_{j'=1}^{\mathcal{J}} \mathbf{D}_{\rho\tilde{\alpha}_{\star}}^{(i,j')\mathrm{H}} \mathbf{X}^{(j')\mathrm{H}} \mathbf{B}_{j'}^{(j)} \tag{5.31}$$

is the processed interference matrix between $(i,j)^{\text{th}}$ Rx-Tx pair. It can be easily shown that if there is only the hypothetical IT and no interference in the CUT, namely if $\mathbf{Y}^{(i)} = \mathbf{Y}_{\star}^{(i)}$, then the output of the processing would be $\tilde{\alpha}_{\star}^{(i,j)}\mathbf{H}_{\star}^{(i,j)}$, as the channel estimator is designed to estimate this matrix.

For the sake of notational clarity in later derivations, (5.31) can be rewritten using (5.16) as:

$$\begin{aligned} \mathbf{\Gamma}^{(i,j)} &= \sum_{j'=1}^{\mathcal{J}} \sum_{n=1}^{N} \rho_{\star n}^{(i,j')*} \mathbf{\Psi}_n^{(i)} \mathbf{D}_{\tilde{\alpha}_{\star}}^{(i,j')\mathrm{H}} \mathbf{X}_n^{(j')\mathrm{H}} \mathbf{B}_{j'}^{(j)} \\ &\triangleq \sum_{j'=1}^{\mathcal{J}} \sum_{n=1}^{N} \rho_{\star n}^{(i,j')*} \mathbf{\Psi}_n^{(i)} \mathbf{V}_{nj'}^{(i,j)*} \end{aligned} \tag{5.32}$$

where

$$\mathbf{V}_{nj'}^{(i,j)} \triangleq \left(\mathbf{D}_{\tilde{\alpha}_{\star}}^{(i,j')\mathrm{H}} \mathbf{X}_n^{(j')\mathrm{H}} \mathbf{B}_{j'}^{(j)} \right)^* \tag{5.33}$$

is the processing matrix explained in the previous subsection, and defined here explicitly for the sake of clarity. To find the covariance of the interference, let's define the vectorized form of the interference matrix:

$$\boldsymbol{\eta}^{(i,j)} \triangleq \mathrm{vec}\{\mathbf{\Gamma}^{(i,j)}\} = \sum_{j'=1}^{\mathcal{J}} \sum_{n=1}^{N} \rho_{\star n}^{(i,j')*} \, \mathrm{vec}\{\mathbf{\Psi}_n^{(i)} \mathbf{V}_{nj'}^{(i,j)*}\}. \tag{5.34}$$

Then, the covariance matrix of the processed interference is defined as:

$$\begin{aligned}\mathbf{R}_{\eta}^{(i,j)} &\triangleq \mathbb{E}\left\{\boldsymbol{\eta}^{(i,j)}\boldsymbol{\eta}^{(i,j)\mathrm{H}}\right\} \\ &= \sum_{j_1,j_2}\sum_{n_1,n_2} \rho_{\star n_1}^{(i,j_1)*}\rho_{\star n_2}^{(i,j_2)}\overline{\mathbf{V}}_{n_1 j_1}^{(i,j)\mathrm{H}}\mathbf{R}_{\psi n_1 n_2}^{(i)}\overline{\mathbf{V}}_{n_2 j_2}^{(i,j)}\end{aligned} \tag{5.35}$$

where

$$\overline{\mathbf{V}}_{nj'}^{(i,j)} \triangleq \mathbf{V}_{nj'}^{(i,j)} \otimes \mathbf{I}_{D_r}, \tag{5.36}$$

$$\mathbf{R}_{\psi n_1 n_2}^{(i)} \triangleq \mathbb{E}\left\{\boldsymbol{\psi}_{n_1}\boldsymbol{\psi}_{n_2}^{\mathrm{H}}\right\}, \tag{5.37}$$

$$\boldsymbol{\psi}_n \triangleq \mathrm{vec}\{\boldsymbol{\Psi}_n\}, \tag{5.38}$$

and the double summations directly follow the summations in (5.34), namely j_1 and j_2 are going from 1 to $\mathcal{J}$ and n_1 and n_2 are going from 1 to N. $\mathbf{R}_{\psi n_1 n_2}^{(i)}$ is the cross-covariance matrix of the raw (before processing) interferences observed in i^{th} receiver between different subcarriers, and it can be written as in (5.39) and (5.40). The derivation of this cross-covariance can be found in Appendix B and is skipped in this chapter.

$$\mathbf{R}_{\boldsymbol{\psi} n}^{(i)} = \left(\begin{aligned}\sum_{j=1}^{\mathcal{J}}\sum_{k=1}^{\mathcal{K}} &(\mathbf{I}_M \otimes \mathbf{H}_k^{(i,j)})(\mathbf{I}_M \circledcirc (\mathbf{X}_n^{(j)}\mathbf{D}_{\bar{\alpha}_k}^{(i,j)}))\mathbf{R}_k^{\tilde{\boldsymbol{\alpha}}(i,j)} \\ &\times (\mathbf{I}_M \circledcirc (\mathbf{X}_n^{(j)}\mathbf{D}_{\bar{\alpha}_k}^{(i,j)}))^{\mathrm{H}}(\mathbf{I}_M \otimes \mathbf{H}_k^{(i,j)})^{\mathrm{H}}\end{aligned}\right) + \sigma_n^2\mathbf{I}_{MD_r} \tag{5.39}$$

$$\mathbf{R}_{\boldsymbol{\psi} n_1 n_2}^{(i)} = \begin{cases}\mathbf{R}_{\boldsymbol{\psi} n_1}^{(i)}, & \text{if } n_1 = n_2 \\ \begin{aligned}\sum_{j=1}^{\mathcal{J}}\sum_{k=1}^{\mathcal{K}} &(\mathbf{I}_M \otimes \rho_{k n_1}^{(i,j)}\mathbf{H}_k^{(i,j)})(\mathbf{I}_M \circledcirc (\mathbf{X}_{n_1}^{(j)}\mathbf{D}_{\bar{\alpha}_k}^{(i,j)}))\mathbf{R}_k^{\tilde{\boldsymbol{\alpha}}(i,j)} \\ &\times (\mathbf{I}_M \circledcirc (\mathbf{X}_{n_2}^{(j)}\mathbf{D}_{\bar{\alpha}_k}^{(i,j)}))^{\mathrm{H}}(\mathbf{I}_M \otimes \rho_{k n_2}^{(i,j)}\mathbf{H}_k^{(i,j)})^{\mathrm{H}},\end{aligned} & \text{if } n_1 \neq n_2\end{cases} \tag{5.40}$$

It should be noted that $\mathbf{R}_{\psi n_1 n_2}^{(i)}$ depends only on the interference channel and the transmitted signals, but not on the processing. On the other hand, $\mathbf{R}_{\eta}^{(i,j)}$ depends on the processing method via $\mathbf{V}_{nj'}^{(i,j)}$. Therefore, even if the first stage of processing changes, $\mathbf{R}_{\psi n_1 n_2}^{(i)}$ would remain the same and $\mathbf{R}_{\eta}^{(i,j)}$ would be updated by updating only $\mathbf{V}_{nj'}^{(i,j)}$.

It should also be noted that $\mathbf{R}_{\eta}^{(i,j)}$ found in (5.35) is the true interference covariance and can only be created if all parameters of the interference, locations of Tx-Rx antennas, and Tx symbols are known. In the following sections, detectors that use

true $\mathbf{R}_{\eta}^{(i,j)}$ will be investigated as a benchmark, but detectors that use approximate or adaptively estimated covariance matrices will also be proposed to be used in scenarios where information about the interference parameters do not exist or computational power is limited.

Finally, it is worth noting that $\boldsymbol{\eta}^{(i,j)}$ includes zero-mean random variables $\tilde{\alpha}_{km}^{(i,j)}$ for each of the $\mathcal{K}$ scatterers, and these random variables are assumed to be independent for different (i,j) pairs and different scatterers [108] when the summations over j's and k's in (5.39) and (5.40) are written. In other words, the realizations of the channel of any scatterer between j_1^{th} Tx and i_1^{th} Rx are uncorrelated from the realizations of the channel of the same scatterer between j_2^{th} Tx and i_2^{th} Rx, unless $i_1 = i_2$ and $j_1 = j_2$. This assumption is intuitive because if these two realizations are correlated, two Tx(Rx) antennas could be considered as one Tx(Rx) antenna with a wide aperture, making the system bistatic, instead of multistatic. Assuming a multistatic system then validates the independence of the interference between different Tx-Rx pairs.

After the vectorization operation, the hypothesis test in (5.30) becomes:

$$\hat{\mathbf{h}}^{(i,j)} \triangleq \text{vec}\{\hat{\mathbf{H}}^{(i,j)}\} = \begin{cases} \boldsymbol{\eta}^{(i,j)}, & \text{under } H_0 \\ \zeta_{\star}^{(i,j)}\mathbf{z}_{\star}^{(i,j)} + \boldsymbol{\eta}^{(i,j)}, & \text{under } H_1 \end{cases} \tag{5.41}$$

where

$$\mathbf{z}_{\star}^{(i,j)} \triangleq (\mathbf{W}_t^{(j)\text{H}}\mathbf{b}_{\star}^{(j)}) \otimes (\mathbf{W}_r^{(i)\text{H}}\mathbf{a}_{\star}^{(i)}) \tag{5.42}$$

is the vectorized form of the desired MIMO channel of the hypothetical target and

$$\zeta_{\star}^{(i,j)} \triangleq \tilde{\alpha}_{\star}^{(i,j)}\gamma_{\star}^{(i,j)} \tag{5.43}$$

is the unknown scalar multiple of the MIMO channel that is to be estimated for detection purposes.

The independence of the interference in (5.41) among different Tx-Rx pairs eases the calculation of the joint GLRT. The joint likelihood function of all $\mathcal{I}\mathcal{J}$ observations is nothing but the multiplication of individual likelihood functions of the observations $\hat{\mathbf{h}}^{(i,j)}$. Therefore, individual GLRT statistics can be computed and summed to reach the joint GLRT statistic. If $\zeta_{\star}^{(i,j)}$ is considered as an unknown non-random parameter, the ML estimation of $\zeta_{\star}^{(i,j)}$ must be found as the first step of writing the GLRT statistic.

The ML estimator of $\zeta_{\star}^{(i,j)}$ can be found by generalized least-squares (GLS) solution of (5.41) as:

$$\hat{\zeta}_{\star}^{(i,j)} = \frac{\mathbf{z}_{\star}^{(i,j)\mathrm{H}}(\mathbf{R}_{\boldsymbol{\eta}}^{(i,j)})^{-1}\hat{\mathbf{h}}^{(i,j)}}{\mathbf{z}_{\star}^{(i,j)\mathrm{H}}(\mathbf{R}_{\boldsymbol{\eta}}^{(i,j)})^{-1}\mathbf{z}_{\star}^{(i,j)}}. \tag{5.44}$$

It is worth noting that this estimator is unbiased, and thus its estimation error variance is equal to the mean-square error (MSE) which is also equal to:

$$\mathrm{Var}\{\hat{\zeta}_{\star}^{(i,j)}\} = \frac{1}{\mathbf{z}_{\star}^{(i,j)\mathrm{H}}(\mathbf{R}_{\boldsymbol{\eta}}^{(i,j)})^{-1}\mathbf{z}_{\star}^{(i,j)}}. \tag{5.45}$$

Replacing $\zeta_{\star}^{(i,j)}$ by its ML estimate in the log likelihood ratio, the GLRT statistic for an individual Tx-Rx pair becomes:

$$\xi^{(i,j)} \triangleq \frac{\left|\mathbf{z}_{\star}^{(i,j)\mathrm{H}}(\mathbf{R}_{\boldsymbol{\eta}}^{(i,j)})^{-1}\hat{\mathbf{h}}^{(i,j)}\right|^2}{\mathbf{z}_{\star}^{(i,j)\mathrm{H}}(\mathbf{R}_{\boldsymbol{\eta}}^{(i,j)})^{-1}\mathbf{z}_{\star}^{(i,j)}} = \left|\boldsymbol{\omega}^{(i,j)\mathrm{H}}\hat{\mathbf{h}}^{(i,j)}\right|^2 \tag{5.46}$$

where

$$\boldsymbol{\omega}^{(i,j)} \triangleq \frac{(\mathbf{R}_{\boldsymbol{\eta}}^{(i,j)})^{-1}\mathbf{z}_{\star}^{(i,j)}}{\sqrt{\mathbf{z}_{\star}^{(i,j)\mathrm{H}}(\mathbf{R}_{\boldsymbol{\eta}}^{(i,j)})^{-1}\mathbf{z}_{\star}^{(i,j)}}} \tag{5.47}$$

is the effective $D_r D_t \times 1$ MIMO filter applied to the processed observations $\hat{\mathbf{h}}^{(i,j)}$. Finally, the joint GLRT statistic becomes:

$$\xi \triangleq \sum_{i=1}^{\mathcal{I}}\sum_{j=1}^{\mathcal{J}}\xi^{(i,j)} = \sum_{i=1}^{\mathcal{I}}\sum_{j=1}^{\mathcal{J}}\frac{\left|\mathbf{z}_{\star}^{(i,j)\mathrm{H}}(\mathbf{R}_{\boldsymbol{\eta}}^{(i,j)})^{-1}\hat{\mathbf{h}}^{(i,j)}\right|^2}{\mathbf{z}_{\star}^{(i,j)\mathrm{H}}(\mathbf{R}_{\boldsymbol{\eta}}^{(i,j)})^{-1}\mathbf{z}_{\star}^{(i,j)}} \tag{5.48}$$

It should be noted that the final statistic can also be written using (5.44) and (5.45) as:

$$\xi \triangleq \sum_{i=1}^{\mathcal{I}}\sum_{j=1}^{\mathcal{J}}\frac{|\hat{\zeta}_{\star}^{(i,j)}|^2}{\mathrm{Var}\{\hat{\zeta}_{\star}^{(i,j)}\}}. \tag{5.49}$$

This means that the joint GLRT detector finds the individual complex gain estimates for each of the $(i,j)^{\text{th}}$ Tx-Rx pairs. Then, instead of directly summing them, it weights each of the gain with the inverse of the estimator variance. If the echoes between a Tx-Rx pair has lower estimator variance, meaning that CUT has more information under the inverse space of the interference between that Tx-Rx pair, then the gain estimates of that Tx-Rx pair is weighted more. On the contrary, if the CUT is contaminated with the interference from the eyes of a Tx-Rx pair, the gain estimates of that Tx-Rx pair is weighted less. This detector intuitively takes advantage of using multistatic configuration.

As a final comment on the detector, the individual test statistic in (5.46) is independent of the interference statistics under H_0 hypothesis. In other words, $\mathbb{E}\left\{\xi^{(i,j)}|H_0\right\} = 1$. Therefore, this GLRT detector is implicitly a CFAR detector.

5.4 Processing Alternatives

In the previous section, a range-Doppler-angle signal processing method and the detection scheme are proposed for the case where the interference covariance matrix is known to each Rx unit. This “genie aided" case is an upper bound to the detection performance but it also requires a significant amount of computation power because of the signal-dependent pseudo-inverse operation. In this section, different processing alternatives that trades off some detection performance to ease the calculations and reduce the knowledge requirements with respect to the genie aided method are proposed. First, a summary of the genie aided method is provided for the sake of clarity. Next, another MIMO filter is proposed which uses the expectation of ICM to reduce the number of matrix inverse operations. Thirdly, two fully-adaptive detectors that estimate the ICM in a way that resembles the infamous AMF are proposed, which use no prior information about the interference. Finally, the multistatic extension of the 3D Periodogram method into MIMO ISAC systems is investigated.

5.4.1 Knowledge-Aided Processing Given X

This processing method is what is explained in the previous section. It assumes that all transmitted symbols and Tx locations are known at each receiver. The ICM is found as in (5.35) to (5.40), and the MIMO filter is found as in (5.47). Therefore, the MIMO filter depends on $\mathbf{X}$ and the ICM inverse is taken every time $\mathbf{X}$ changes.

5.4.2 Knowledge-Aided Processing with Expectation over X

This processing method is an alternative to the previous one, which reduces the computational requirements in exchange for detection performance. Let’s define

$$\overline{\mathbf{R}}_{\boldsymbol{\eta}}^{(i,j)} \triangleq \mathbb{E}\left\{\mathbf{R}_{\boldsymbol{\eta}}^{(i,j)}\right\} \tag{5.50}$$

where the expectation is taken over $\mathbf{X}$. Then, the MIMO filters for this processing can be defined as

$$\overline{\boldsymbol{\omega}}^{(i,j)} \triangleq \frac{(\overline{\mathbf{R}}_{\boldsymbol{\eta}}^{(i,j)})^{-1}\mathbf{z}_{\star}^{(i,j)}}{\sqrt{\mathbf{z}_{\star}^{(i,j)\mathrm{H}}(\overline{\mathbf{R}}_{\boldsymbol{\eta}}^{(i,j)})^{-1}\mathbf{z}_{\star}^{(i,j)}}} \tag{5.51}$$

and the GLRT statistic becomes

$$\overline{\xi}^{(i,j)} \triangleq \left|\overline{\boldsymbol{\omega}}^{(i,j)\mathrm{H}}\hat{\mathbf{h}}^{(i,j)}\right|^2. \tag{5.52}$$

Since the expectation is taken over transmitted symbols, the MIMO filter does not depend on $\mathbf{X}$ and the ICM inverse is taken only when the angular channel is aged, which occurs once per several frames.

The first step in the calculation of $\overline{\mathbf{R}}_{\boldsymbol{\eta}}^{(i,j)}$ is making the previously mentioned approximations of $\mathbf{B} \approx \mathbf{I}_{\mathcal{J}D_t}$ and $\mathbf{B}_{j'}^{(j)} = \delta[j-j']\mathbf{I}_{D_t}$, which are satisfied when $MN >> \mathcal{J}D_t$. Then, due to the Kronecker delta operation, (5.33) becomes $\mathbf{V}_n^{(i,j)} = \left(\mathbf{D}_{\bar{\alpha}_\star}^{(i,j)\mathrm{H}}\mathbf{X}_n^{(j)\mathrm{H}}\right)^*$, bypassing the inverse operation that must be performed for each Tx symbol matrix $\mathbf{X}$. In addition, the summations over j' are dropped in (5.31), (5.32), (5.34) and (5.35); and (5.36) becomes $\overline{\mathbf{V}}_n^{(i,j)} = \mathbf{V}_n^{(i,j)} \otimes \mathbf{I}_{D_r}$ with the approximations. The expected ICM can then be written as

$$\overline{\mathbf{R}}_{\boldsymbol{\eta}}^{(i,j)} = \sum_{n_1,n_2} \rho_{\star n_1}^{(i,j)*}\rho_{\star n_2}^{(i,j)}\overline{\mathbf{V}}_{n_1}^{(i,j)\mathrm{H}}\overline{\mathbf{R}}_{\boldsymbol{\psi} n_1 n_2}^{(i)}\overline{\mathbf{V}}_{n_2}^{(i,j)} \tag{5.53}$$

where $\overline{\mathbf{R}}_{\boldsymbol{\psi} n_1 n_2}^{(i)}$ is the expectation of $\mathbf{R}_{\boldsymbol{\psi} n_1 n_2}^{(i)}$ defined in (5.39) and (5.40) over transmitted symbols $\mathbf{X}$. The calculation of this expectation can be found in Appendix B and skipped in this chapter.

5.4.3 AMF-like Processing with Sample Averaging After Preprocessing (AMF-SAAP)

This processing method does not assume any knowledge about the ICM but estimates it using the processed observations from the neighbor cells of the CUT. If multiple frames of data are processed together, the ICM estimates are found for each frame and averaged over the frames. The estimate of the ICM $\mathbf{R}_{\eta}^{(i,j)}$ is denoted as $\hat{\mathbf{R}}_{\boldsymbol{\eta}}^{(i,j)}$. Figure 5.3 shows how cell-averaging is utilized to find the ICM estimate at the CUT.

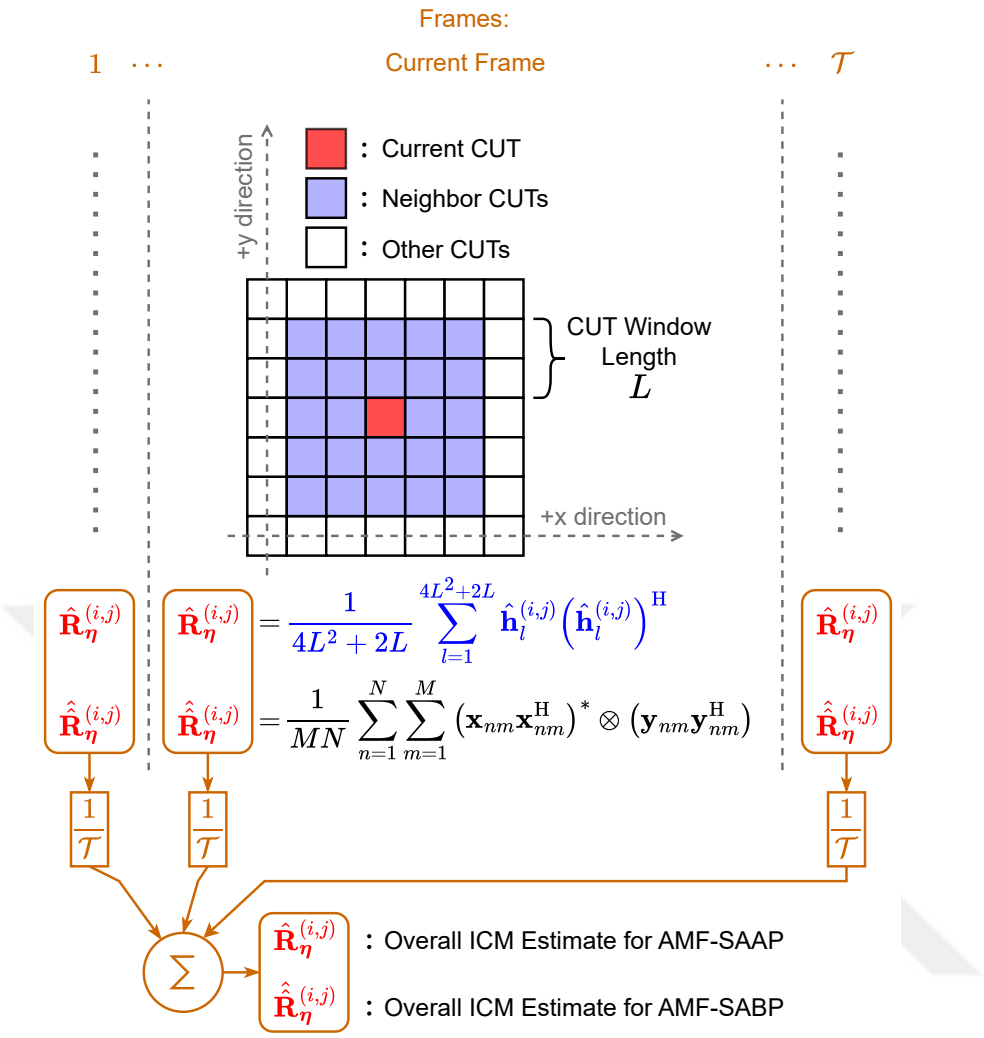


Figure 5.3: Block diagram of ICM estimation processes for AMF-like detectors.

The MIMO filters for this processing can be defined as:

$$\hat{\boldsymbol{\omega}}^{(i,j)} \triangleq \frac{(\hat{\mathbf{R}}_{\boldsymbol{\eta}}^{(i,j)} + \hat{\mathbf{D}}^{(i,j)})^{-1}\mathbf{z}_{\star}^{(i,j)}}{\sqrt{\mathbf{z}_{\star}^{(i,j)\mathrm{H}}(\hat{\mathbf{R}}_{\boldsymbol{\eta}}^{(i,j)} + \hat{\mathbf{D}}^{(i,j)})^{-1}\mathbf{z}_{\star}^{(i,j)}}} \tag{5.54}$$

and the GLRT statistic becomes

$$\hat{\xi}^{(i,j)} \triangleq \left|\hat{\boldsymbol{\omega}}^{(i,j)\mathrm{H}}\hat{\mathbf{h}}^{(i,j)}\right|^2, \tag{5.55}$$

where $\hat{\mathbf{D}}^{(i,j)}$ is the diagonal load matrix added to the ICM estimate in order to improve interference cancellation.

5.4.4 AMF-like Processing with Sample Averaging Before Preprocessing (AMF-SABP)

This processing method estimates the ICM like the previous method, but uses the raw observations instead of the preprocessed ones. In (5.29), it is shown that the channel estimate after the Doppler-range preprocessing is the DFT/IDFT of a raw channel estimate $\mathbf{y}_{nm}^{(i)}\mathbf{x}_{nm}^{(j)\mathrm{H}}$, with a correction matrix $\mathbf{B}_{j'}^{(j)}$. Using the raw channel estimates, this processing method estimates the ICM as:

$$\begin{aligned}\hat{\hat{\mathbf{R}}}_{\boldsymbol{\eta}}^{(i,j)} &\triangleq \frac{1}{MN}\sum_{n=1}^{N}\sum_{m=1}^{M}\mathrm{vec}\{\mathbf{y}_{nm}^{(i)}\mathbf{x}_{nm}^{(j)\mathrm{H}}\}\,\mathrm{vec}\{\mathbf{y}_{nm}^{(i)}\mathbf{x}_{nm}^{(j)\mathrm{H}}\}^{\mathrm{H}} \\ &= \frac{1}{MN}\sum_{n=1}^{N}\sum_{m=1}^{M}\left(\mathbf{x}_{nm}\mathbf{x}_{nm}^{\mathrm{H}}\right)^{*}\otimes\left(\mathbf{y}_{nm}\mathbf{y}_{nm}^{\mathrm{H}}\right). \end{aligned} \tag{5.56}$$

Then, the MIMO filters for this processing are:

$$\hat{\boldsymbol{\omega}}^{(i,j)} \triangleq \frac{(\hat{\hat{\mathbf{R}}}_{\boldsymbol{\eta}}^{(i,j)}+\hat{\hat{\mathbf{D}}}^{(i,j)})^{-1}\mathbf{z}_{\star}^{(i,j)}}{\sqrt{\mathbf{z}_{\star}^{(i,j)\mathrm{H}}(\hat{\hat{\mathbf{R}}}_{\boldsymbol{\eta}}^{(i,j)}+\hat{\hat{\mathbf{D}}}^{(i,j)})^{-1}\mathbf{z}_{\star}^{(i,j)}}} \tag{5.57}$$

and the GLRT statistic becomes

$$\hat{\hat{\xi}}^{(i,j)} \triangleq \left|\hat{\boldsymbol{\omega}}^{(i,j)\mathrm{H}}\hat{\mathbf{h}}^{(i,j)}\right|^{2}, \tag{5.58}$$

where $\hat{\hat{\mathbf{D}}}^{(i,j)}$ is the diagonal load matrix added to the ICM estimate in order to improve interference cancellation. Similar to the previous method, if multiple frames of data are processed together, the ICM estimates are found for each frame and averaged over the frames. The estimation of ICM with this processing is also provided in Figure 5.3.

5.4.5 3D Periodogram Processing

The previous processing methods use the ICM information, either provided by the tracker or learned adaptively, to suppress the interference. On the contrary, nonparametric methods can also be used to make the processing independent of the ICM information. 3D Periodogram method is one of the most commonly used processings in the literature. This method suggests combining the symbols received in all subcarriers, symbols and antennas with basic FFT or IFFT operations.

Similar to the previous detectors, Doppler and range processings are done as in (5.29) to combine energy from subcarriers and symbols while compensating for the transmitted symbols and estimating the MIMO channel. However, no prior ICM information is assumed in 3D Periodogram method, meaning that ICM is selected to be identity matrix. This trivial ICM in this method is denoted as $\dot{\mathbf{R}}_{\boldsymbol{\eta}}^{(i,j)}$ and it can be written as:

$$\dot{\mathbf{R}}_{\boldsymbol{\eta}}^{(i,j)} = \mathbf{I}_{D_r D_t}. \tag{5.59}$$

In conventional DFT-based methods, windows are used to suppress the interference sidelobes [115]. To apply windows in the spatial domain, this method modifies the steering vector towards the CUT defined in (5.42). The new steering vector becomes:

$$\dot{\mathbf{z}}_{\star}^{(i,j)} \triangleq (\mathbf{W}_t^{(j)\mathrm{H}} \mathbf{b}_{\star}^{(j)} \mathbf{D}_{w_t}) \otimes (\mathbf{W}_r^{(i)\mathrm{H}} \mathbf{a}_{\star}^{(i)} \mathbf{D}_{w_r}) \tag{5.60}$$

where $\mathbf{D}_{w_t}$ and $\mathbf{D}_{w_r}$ are $N_t \times N_t$ and $N_r \times N_r$ diagonal window matrices for transmit and receive beamformers, respectively, whose diagonal elements constitute Chebyshev windows with 75 dB sidelobe suppression. Then, the MIMO filters for this processing can be defined as

$$\dot{\boldsymbol{\omega}}^{(i,j)} \triangleq \frac{\dot{\mathbf{z}}_{\star}^{(i,j)}}{\sqrt{\dot{\mathbf{z}}_{\star}^{(i,j)\mathrm{H}} \dot{\mathbf{z}}_{\star}^{(i,j)}}} \tag{5.61}$$

and the GLRT statistic becomes

$$\dot{\xi}^{(i,j)} \triangleq \left| \dot{\boldsymbol{\omega}}^{(i,j)\mathrm{H}} \hat{\mathbf{h}}^{(i,j)} \right|^2. \tag{5.62}$$

5.5 Numerical Evaluations

In this section, numerical evaluations of the proposed detectors will be provided.

5.5.1 Beamformers

In this chapter, each transmitter and receiver has its own analog beamformer, which are denoted as $\mathbf{W}_t^{(j)}$ and $\mathbf{W}_r^{(i)}$. $\mathbf{W}_t^{(j)}(\mathbf{W}_r^{(i)})$ is formed to cover the angular sector where DL (UL) users of j^{th} transmitter (i^{th} receiver) are located. In general, a large

coverage can be obtained by utilizing large number of antennas, as in cell-free systems. The focus of this chapter is the case in which the transmit and receive sectors overlap for a limited region contaminated by several UITs.

To reduce the power fluctuations inside the angular sectors, the columns of $\mathbf{W}_t(\mathbf{W}_r)$ are selected to be the eigenvectors of the intended angular sector corresponding to $D_t(D_r)$ largest eigenvalues. The transmit power constraint is adjusted to limit the total transmit power, so that $\mathrm{tr}\{\mathbf{W}_t\mathbf{W}_t^{\mathrm{H}}\} = MN$ is satisfied. This means that the system's fast-and-slow-time processing gains are included through transmit beamforming, and the total transmit power is constrained. In the receiver part, however, to preserve the second-order stationarity of the noise after receive beamforming, $\mathbf{W}_r$ is scaled so that $\mathrm{tr}\{\mathbf{W}_r^{\mathrm{H}}\mathbf{W}_r\} = D_r$ is satisfied.

5.5.2 Performance Metrics

In this chapter, two different performance metrics will be used to compare different detectors, which will be explained in the following parts.

5.5.2.1 Bistatic Processing Gain / SINR Improvement Factor

In multistatic ISAC systems, each Tx-Rx pair is subject to a different channel as explained in the previous sections. Consequently, each Tx-Rx pair experiences a different SINR for given system and channel configurations. However, it is impractical to present SINR results for all Tx-Rx pairs separately or to define a unified SINR metric. Therefore, this chapter provides processing gain curves of different detectors and compare them for a representative Tx–Rx pair. The insights and conclusions drawn from this pair are also valid for the other pairs, as similar trends have been observed across the system. It should be noted that these curves represent the *output SINR*, the power ratio between the signal term and the interference and noise terms in the resulting GLRT metrics of the detectors ($\xi^{(i)}$), for a given *input SINR*, the same ratio at the input of the receivers ($\mathbf{Y}^{(i)}$). Therefore, neither the propagation loss from any Tx to any Rx through any scatterer nor the actual transmit power of any Tx is visible in this performance metric, because this metric measures the ratio between the output

and input SINR, namely the signal processing gain, of the representative Rx.

In the simulations for processing gain metric, the UIT power scalings are defined so that the input signal-to-clutter power ratio (SCR) at the representative receiver, $\gamma_\star/\gamma_k$, is always the same wherever the CUT is located. Specifically, the average power of the received echoes from the first (second) UIT is always 30 (20) dB larger than the average power of the received echoes from the IT, wherever the IT is.

5.5.2.2 Multistatic Probability of Detection (P_d)

Since this chapter is focused on sensing performances of multistatic ISAC systems, probability of detecting a target at the CUT (P_d) for a given probability of false alarm (P_{fa}) is an important metric to compare different detectors. To acquire the P_d curves, Monte-Carlo simulations have been conducted to get the final decision metrics of all detectors (ξ in (5.48)) both under H_0 and H_1 hypotheses. Unlike the processing gain metric, to get the joint GLRT metrics and calculate the overall P_d, the propagation loss must be taken into account because a target that is closer to a Tx-Rx pair is inherently more likely to be detected by that pair instead of the other pairs. To include the effects of propagation loss without delving into the actual transmit powers of the transmitters and the noise levels of the receivers, a *reference input SINR* (γ_{ref}) value is defined and the gains of all channels (γ_k) are calculated according to this reference.

The reference input SINR is defined to be the input SINR at the 1^{st} Rx when the signal is transmitted from the 1^{st} Tx (constituting $(1,1)^{\text{th}}$ Tx-Rx pair) and scattered from a scatterer located at position $\mathbf{p}_{\text{ref}} = [0,0]^{\text{T}}\, m$ with $1\, m^2$ RCS. Then, the average received power at $(i,j)^{\text{th}}$ Rx-Tx pair from any scattering target located at $\mathbf{p} = [x,y]^{\text{T}}$ with $\gamma_{\text{RCS}}\ m^2$ RCS becomes:

$$\gamma^{(i,j)} = \gamma_{\text{RCS}}\gamma_{\text{ref}} \times \Delta\gamma^{(i,j)} \tag{5.63}$$

where

$$\Delta\gamma^{(i,j)} = \frac{d(\mathbf{p}_{\text{ref}}, \mathbf{p}_r^{(i_c)})^2 d(\mathbf{p}_{\text{ref}}, \mathbf{p}_t^{(j_c)})^2}{d(\mathbf{p}, \mathbf{p}_r^{(i_c)})^2 d(\mathbf{p}, \mathbf{p}_t^{(j_c)})^2}. \tag{5.64}$$

Similarly, the power of the LOS path between $(i,j)^{\text{th}}$ Rx-Tx pair in (5.13) becomes:

$$\gamma_0^{(i,j)} = \gamma_{\text{ref}} \times \frac{d(\mathbf{p}_{\text{ref}}, \mathbf{p}_r^{(i_c)})^2 d(\mathbf{p}_{\text{ref}}, \mathbf{p}_t^{(j_c)})^2}{d(\mathbf{p}_t^{(j_c)}, \mathbf{p}_r^{(i_c)})^2}, \tag{5.65}$$

as the propagation LOS path is only one-way from the Tx to the Rx.

In the simulations for the (P_d) metric, the UIT power scalings are defined so that the input SCR value, $\gamma_\star/\gamma_k$, represents the ratio of radar cross-sections of the target and the UITs. Specifically, the average power of the received echoes from the first (second) UIT is $30\,(20)$ dB larger than the average power of the received echoes from the IT, if the IT is located exactly on top of the UIT. If a UIT is closer to one of the Tx-Rx pairs, its average received power will be even larger even if its RCS is $\gamma_k/\gamma_\star$ times larger than the IT.

5.5.3 Simulation Environment and Model Parameters

The locations of Tx and Rx antennas and UITs, illuminated Tx and Rx sectors, LOS paths, and CUT locations used in the simulations are provided in Figure 5.4. As seen in Figure 5.4, $\mathcal{I} = \mathcal{J} = 2$ Rx and Tx antennas are used in multistatic MIMO ISAC simulations. The antenna arrays are numbered as shown in the figure. The direct LOS paths from transmitters to receivers are also drawn in the figure. The areas and the lines under test are the CUT locations that are scanned in the bistatic processing gain simulations.

The system parameters used for the simulations in this chapter are provided in Table 5.1. The OFDM communication-related parameters such as carrier frequency, sub-carrier spacing and number of active resource blocks are selected in accordance with the 5G New-Radio technical specifications.

5.5.4 Numerical Results

In this section, the results of numerical evaluations are provided. In these results, 6 different detector configurations are included with different legend names. 'Given X' detector uses the 'Knowledge-Aided Processing Given $\mathbf{X}$' signal processing method, and it constitutes the upper limit for the performances under consideration. 'Expected X' detector uses the 'Knowledge-Aided Processing with Expectation over $\mathbf{X}$' signal processing method, and it is a faster alternative for 'Given X' detector, trading

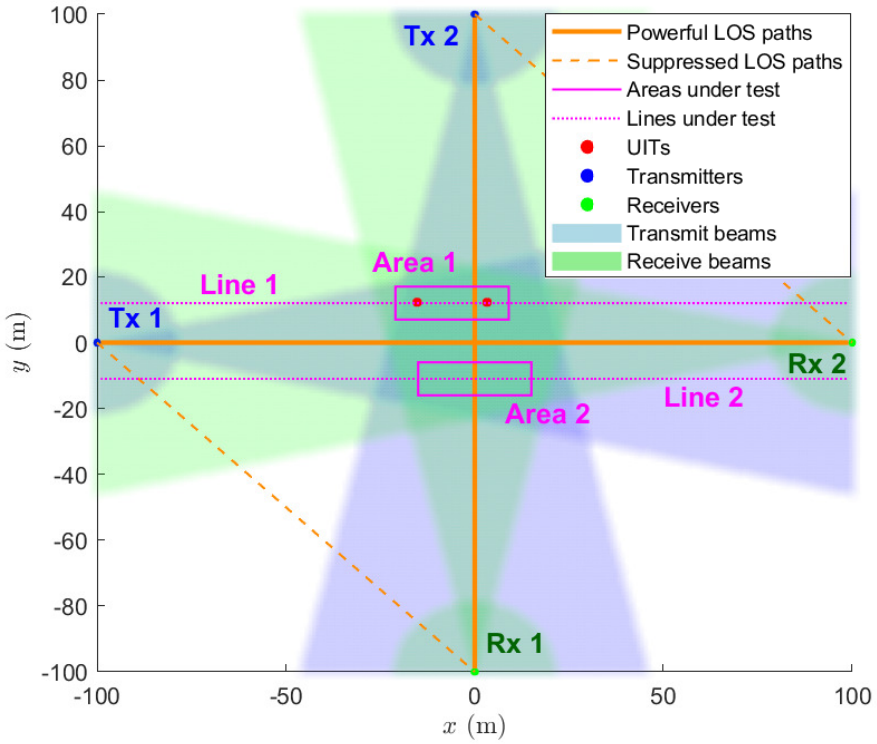


Figure 5.4: Locations of Tx and Rx antennas and UITs, illuminated Tx and Rx sectors, LOS paths, and CUT locations used in the simulations.

off performance. 'AMF-SAAP' and 'AMF-SABP' detectors use the signal processing methods that match their names, and they are two fully-adaptive alternatives for the previous knowledge-aided detectors. 'Perio (Windowed)' and 'Perio (No Window)' detectors use '3D Periodogram' signal processing method with and without the Chebyshev windows in their MIMO filters, and they are the benchmark detectors which are commonly used in the literature due to their significantly low computational requirements.

In the simulations, there are two UITs in the sector of interest, both of which including 4 scatterers placed on the corners of a square with side length of 50 cm. The center positions of the UIT #1 and UIT #2 are $[-15, 12]^{\mathrm{T}}$ m and $[3, 12]^{\mathrm{T}}$ m, respectively. UIT #1 is a stationary object, its velocity is $[0, 0]^{\mathrm{T}}$ m/s and Doppler spread is 0 Hz. UIT #2 is a moving object, its velocity is $[10, 10]^{\mathrm{T}}$ m/s and Doppler spread is 200 Hz. In bistatic SINR improvement factor simulations, the SCR for the UIT #1 (UIT #2) is -30 dB (-20 dB). In multistatic $\mathrm{P_d}$ simulations, the RCS of the UIT #1 (UIT #2) is

Table 5.1: Simulation Parameters

M	# of OFDM symbols per frame	16
T_s	OFDM symbol duration	8.33 μs
T_f	frame duration (CPI)	133.33 μs
V_{res}	Velocity resolution ($\lambda_c/(2MT_s)$)	40,16 m/s
$\mathcal{T}$	# of frames	32
$\mathcal{J}$	# of transmitters	2
$\mathcal{I}$	# of receivers	2
N_t, N_r	# of Tx, Rx antennas	64
D_t, D_r	# of Tx, Rx RF chains	12
$\bar{N}$	total # of subcarriers	1368
N	# of ISAC subcarriers	72
$\Delta\bar{f} = W/\bar{N}$	subcarrier spacing	120 kHz
$\Delta f = W/N$	ISAC subcarrier spacing	2.28 MHz
W	bandwidth	164.16 MHz
f_c	center frequency	28 GHz
λ_c	center wavelength	10.71 mm
c_0	speed of light in vacuum	2.998×10^8 m/s
$\gamma_{\text{ref}}/\sigma_n^2$	reference power	1 (0 dB)
$\gamma_\star/\sigma_n^2$	signal to noise power ratio (SNR)	0 dB
$\gamma_\star/\gamma_k$	signal to clutter power ratio (SCR)	–30, –20 dB
L	CUT window length	2
NMN_rN_t/D_t	maximum processing gain	55.95 dB

-30 dB (-20 dB) larger than the RCS of the target.

As explained in Section 5.5.2 the simulations are done for two different performance metrics, therefore the results will be discussed under two categories.

5.5.4.1 Bistatic Processing Gain / SINR Improvement Factor

The bistatic SINR improvement factor versus CUT position and velocity graphs for Given X and Expected X are provided in Figure 5.5. In the top subfigures, the CUT velocity is selected to be 5 m/s ($\sim 0.125^{\text{th}}$ Doppler bin) in both x and y coordinates, therefore, none of the UITs can be effectively suppressed through Doppler processing. It can be seen that Given X detector suffers from a performance loss only when the CUT is significantly close to the UITs, and provides the maximum SINR improvement that can be reached when the CUT is slightly separated from the UITs. Expected X detector can also reach similar performances at some CUT locations, but it suffers from a performance loss in a line passing through the UITs and the receiver. This line shows that the interference suppression through transmit beamforming is not successful in Expected X detector, which does not use the actual transmitted symbols $\mathbf{X}$ but takes expectation over them. This result can be investigated using (5.8) and (5.19), in which it can be seen that the transmit symbols $\mathbf{X}$ multiplies the transmit steering vector and effectively distorts the channel for each UIT scatterer. Since there are different UIT scatterers with different positions and velocities and the CUT is matched to only a single position and velocity, the preprocessing in Section 5.3.2 cannot eliminate the effects of $\mathbf{X}$ completely. Given X detector uses the knowledge of $\mathbf{X}$ in each frame to eliminate the remaining effects of the ISAC symbols in the MIMO processing. However, other detectors proposed in this chapter ignore the residual effects of $\mathbf{X}$ after preprocessing, resulting in a less effective transmit beamforming.

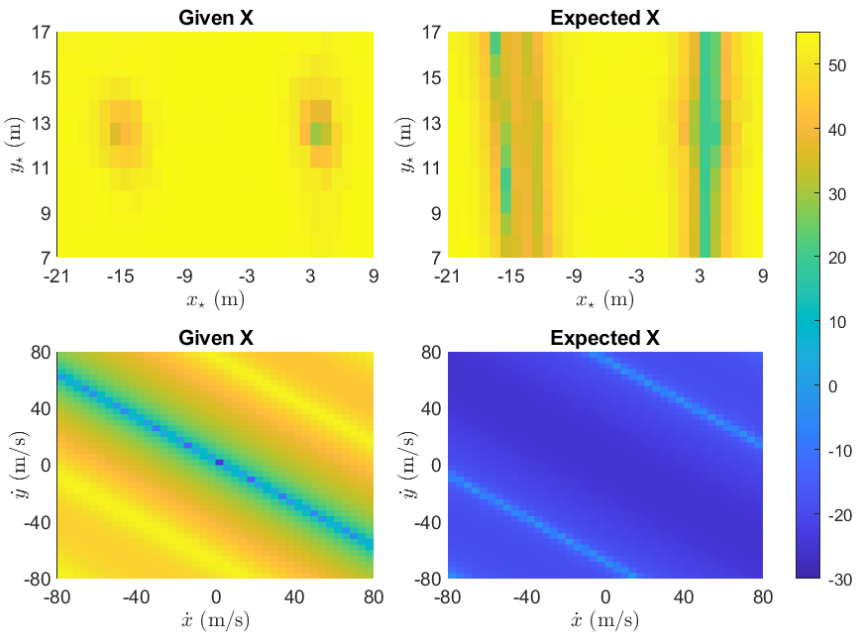


Figure 5.5: SINR improvement factor maps for Given X (left) and Expected X (right) detectors. In top figures, the coordinates represent $\mathbf{p}_\star$ and $\dot{\mathbf{p}}_\star = [5, 5]^{\mathrm{T}}$ m/s. In bottom figures, the coordinates represent $\dot{\mathbf{p}}$ and $\mathbf{p}_\star = [-15, 12]^{\mathrm{T}}$ m.

In the bottom subfigures of Figure 5.5, the CUT position is selected to be on top of the UIT #1, preventing it from being suppressed by positional (range and MIMO) processings. It can be seen that Given X detector can suppress the interference when the CUT is separated from the UITs even only in Doppler dimension, but Expected X detector fails in this regard. It should be noted that the range-Doppler preprocessing in Section 5.3.2 is the same for all detectors. This fact also shows that the mismatch between the CUT position/velocity and the interference positions/velocities results in a distortion at the output of the preprocessing, which depends on $\mathbf{X}$. Given X detector uses the information about the Doppler of the scatterers in this $\mathbf{X}$-dependent residual interference to suppress it through MIMO processing. The line on which the UIT cannot be suppressed by the Given X detector is the CUT velocities that result in the same Doppler shift with the UIT #1, namely the *Doppler ghosts*, for this specific Rx-Tx pair. In multistatic scenarios, as the locations of Rx and Tx antennas change the orientation of the line would change and a diversity can be achieved. It should be noted that *range ghosts*, which is an inherent problem in classical multistatic radars that results in ambiguities on the isorange ellipse of each target, is severely suppressed

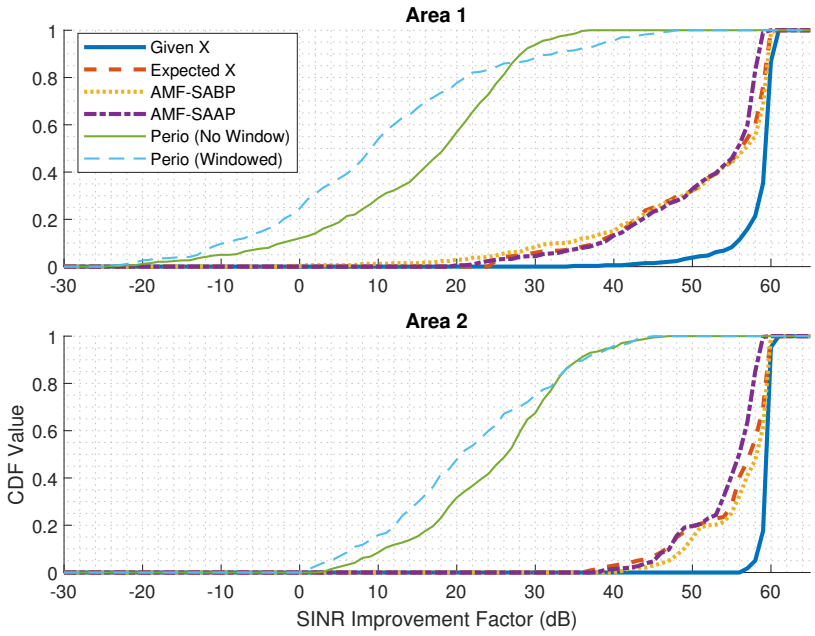


Figure 5.6: SINR improvement factor CDFs for the CUTs in Area 1 (top) and Area 2(bottom).

in this chapter because antenna arrays with MIMO capabilities are used instead of isotropic antennas.

In Figure 5.6, the cumulative distribution functions (CDFs) of the SINR values of different detectors are shown. In this figure, the SINR values are considered to be random parameters depending on $\mathbf{p}_\star$, and the CDF samples are the SINR values at different CUTs in Area 1 (top) and Area 2 (bottom). This figure highlights the best and worst performances of the detectors when the CUT position is changed, when $\dot{\mathbf{p}}_\star = [5, 5]^{\mathrm{T}}$ m/s. It can be seen that Given X detector outperforms the others, as expected, and Perio detectors are the worst ones as they cannot effectively suppress the interference. Both AMF-like detectors perform well as their SINR values are close to their theoretical limit, which is the Expected X detector. Applying windows in MIMO processing increases the number of interference-contaminated CUTs in the mainlobe but also increases the number of interference-free CUTs in the sidelobes, as expected. On the other hand, the most significant increase in SINR values between Area 1 and Area 2 is seen in the 3D Periodogram methods, as they cannot effectively eliminate the strong interference when it is near the CUT, but they can achieve higher performances when the CUTs are separated from the interferences.

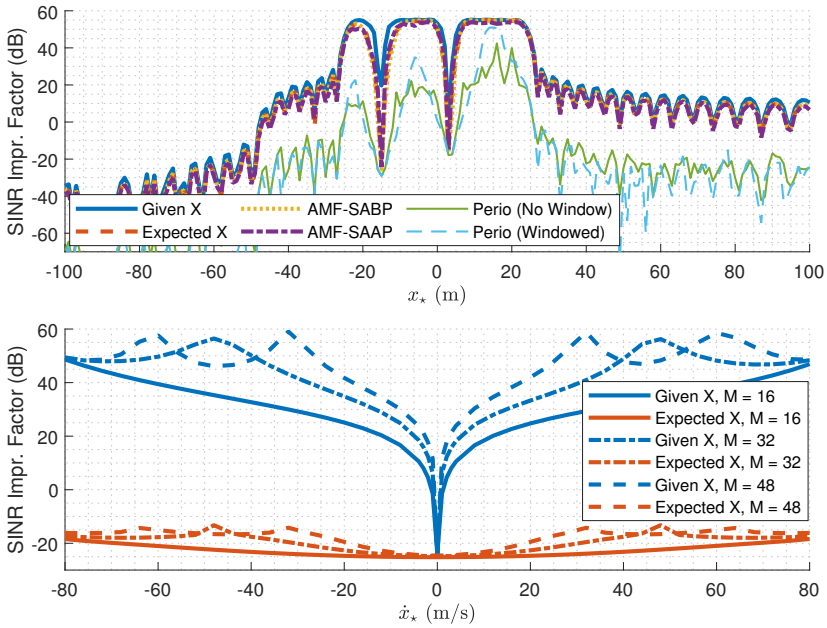


Figure 5.7: SINR improvement factor vs $x_\star$ as CUT moves along Line 1 when $\dot{\mathbf{p}}_\star = [5, 5]^{\mathrm{T}}$ m/s (top) and SINR improvement factor vs $\dot{x}_\star$ for different M values, $\mathbf{p}_\star = [-15, 12]^{\mathrm{T}}$ m, $\dot{y}_\star = 0$ m/s (bottom).

In Figure 5.7, two different subgraphs are plotted. In top side, SINR improvement factors are drawn with respect to changing $x_\star$ as the CUTs move along Line 1 when $\dot{\mathbf{p}}_\star = [5, 5]^{\mathrm{T}}$ m/s. In this figure, the effects of illuminated sectors and the UITs on the SINR can be clearly seen. It should be noted that even if the windowed 3D Periodogram method can achieve optimal performance for CUTs that are far away from the UITs and illuminated by both Tx and Rx, such CUTs are significantly less in number than UIT-contaminated CUTs. This result indicates the importance of ICM-aware signal-processing methods in suppressing the interference and increasing the detection performance.

In the bottom subgraph of Figure 5.7, SINR improvement factors of Given X and Expected X detectors are drawn with respect to changing $\dot{x}_\star$, when $\dot{y}_\star = 5$ m/s and $\mathbf{p}_\star = [-12, 5]^{\mathrm{T}}$, for different M values. In this figure, it can be seen that as M increases, the Doppler resolution gets smaller and the UITs can be suppressed better for both detectors, meaning that the range-Doppler preprocessing can also help interference suppression with increased bandwidth or CPI duration. However, the difference between Given X and Expected X detectors indicates that most of the interference suppression is done via symbol-dependent MIMO processing.

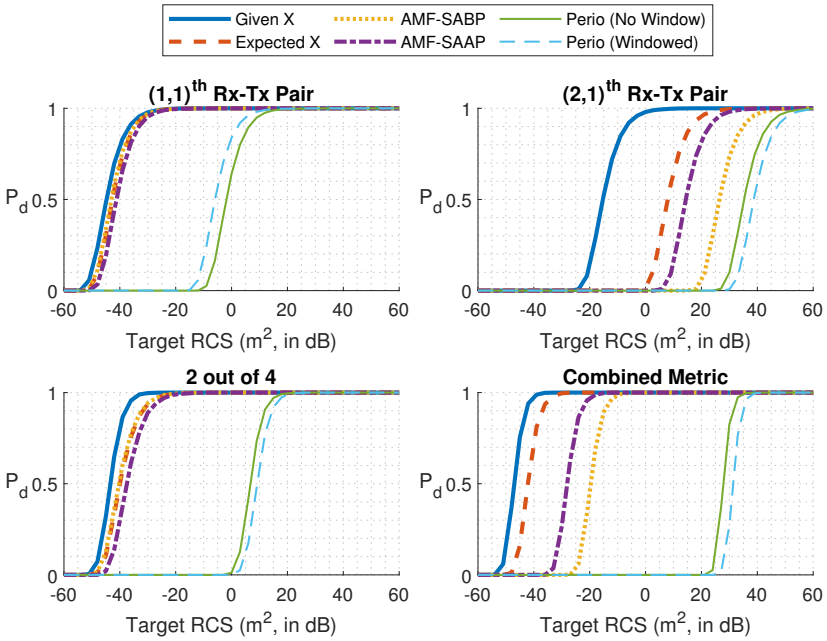


Figure 5.8: Probability of detection vs IT RCS graphs for different thresholding schemes, $\mathbf{p}_\star = [-5, 12]^{\mathrm{T}}$ m, $\dot{\mathbf{p}}_\star = [5, 5]^{\mathrm{T}}$ m/s, $\mathrm{P_{fa}} = 10^{-3}$.

5.5.4.2 Multistatic Probability of Detection ($\mathrm{P_d}$)

In Figure 5.8, $\mathrm{P_d}$ versus IT RCS curves are drawn for a CUT position selected in Area 1, which is located in between the two UITs. In the top subfigures, each Rx-Tx pair makes detection individually with their own metrics and thresholds, and the results for $(1, 1)^{\mathrm{th}}$ and $(2, 1)^{\mathrm{th}}$ Rx-Tx pairs are provided. In the bottom left figure, a combined detection scheme is employed, where a detection is declared if at least 2 out of 4 Rx-Tx pairs report a detection. In the bottom right figure, the metrics for all Rx-Tx pairs are combined as in (5.48) to get a single threshold and detection for the overall system. It can be seen that some Rx-Tx pairs have advantages over the others for the specific geometry chosen in this simulations. Specifically between Rx 2 and Tx 1, all detectors suffer from serious performance loss. However, noncoherently combining the different Rx-Tx pairs as in the bottom figures helps compensating the performance losses of bistatic pairs suffering from strong interferences. This shows that successful implementation of multistatic ISAC systems can create a spatial diversity and help eliminate the interference to achieve higher probabilities of detecting weaker targets.

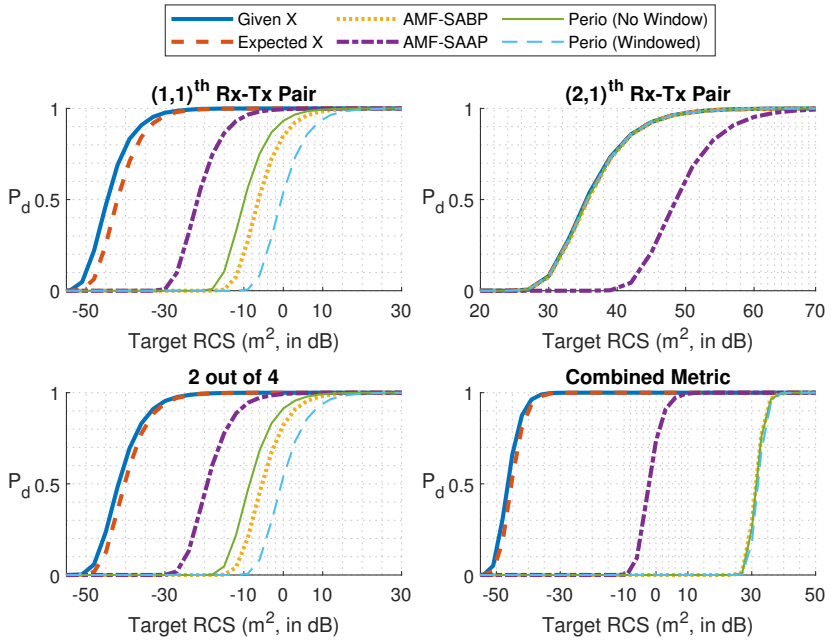


Figure 5.9: Probability of detection vs IT RCS graphs for different thresholding schemes, $\mathbf{p}_\star = [0, 0]^{\mathrm{T}}$ m, $\dot{\mathbf{p}}_\star = [5, 5]^{\mathrm{T}}$ m/s, $\mathrm{P_{fa}} = 10^{-3}$.

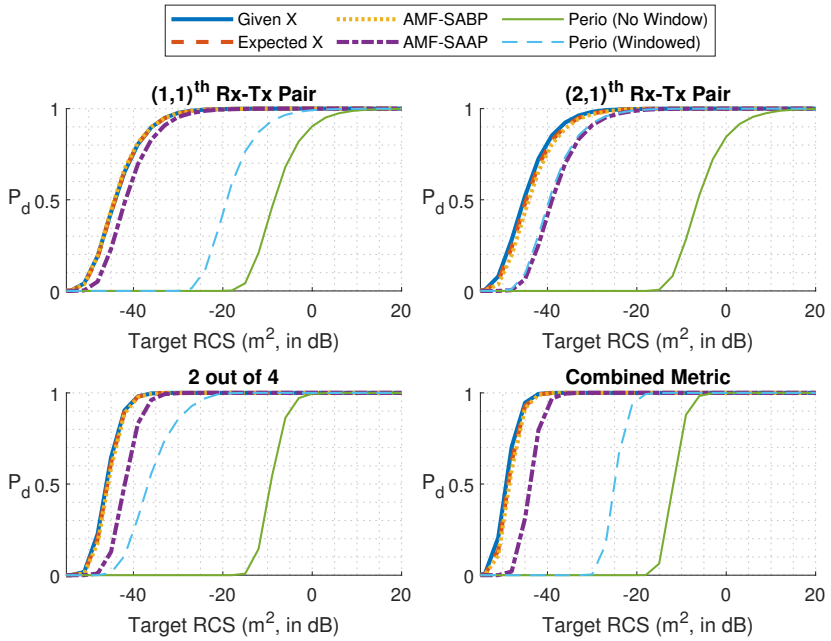


Figure 5.10: Probability of detection vs IT RCS graphs for different thresholding schemes, $\mathbf{p}_\star = [15, -11]^{\mathrm{T}}$ m, $\dot{\mathbf{p}}_\star = [5, 5]^{\mathrm{T}}$ m/s, $\mathrm{P_{fa}} = 10^{-3}$.

In Figure 5.9, P_d versus IT RCS curves are drawn for a CUT position selected at the intersection point of two powerful LOS paths in the scenario. In the top right subfigure of this figure, the negative effect of LOS path can be clearly seen. However, from the bottom subfigures it can be deduced that using multistatic configuration can increase the probability of finding a suitable Rx-Tx pair to detect the targets even if some of the Rx-Tx pairs suffers from extreme interference sources.

In Figure 5.10, P_d versus IT RCS curves are drawn for a CUT position in Area 2 which is far away from the interferences. It can be seen that when the CUT position is separated enough from the UITs or LOS paths, all detectors can achieve relatively good detection performances.

5.6 Conclusion

In this chapter, the system model constructed in the previous chapter for an OFDM-based monostatic MIMO ISAC system is extended to include D-MIMO architecture and multistatic sensing capability. The multiple scatterer UIT model that has been used throughout the entire thesis remained the same, but expressed in Cartesian coordinate system due to the requirements of multistatic geometry. The channel estimation step is conducted using a joint LS operation including range and Doppler information of CUTs for all Tx-Rx pairs. Then, the angle information is extracted via an ICM-aware max-SINR filter and the GLRT detector is proposed under the assumptions of this chapter. Different ICM-aware and adaptive detector implementations are investigated and compared to the benchmark 3D Periodogram detector in terms of bistatic SINR improvement factor and multistatic probability of detection metrics.

In the following chapter, concluding remarks for this thesis will be provided, including a summary of the problems investigated in the thesis, proposed solution methods to these problems, and some ideas to improve the work done in this thesis for the future researchers.

CHAPTER 6

CONCLUSION

This thesis is a comprehensive work on the fundamentals, challenges and advantages of communication-centric ISAC systems using OFDM waveform due to its existing and anticipated dominance in the communication standards. The phenomenon of integrating sensing capability into OFDM communication systems is investigated through a single-antenna monostatic ISAC system framework. The framework is then extended to incorporate a MIMO architecture, with the system models further enhanced to account for beam-squint effects. Finally, the multistatic extension of the MIMO ISAC system is done, using a completely different coordinate system than the previous approaches. For all of these frameworks, rigorous mathematical models are constructed to support the theoretical findings as well as to internalize the simulation results.

In this thesis, the focus is on scenarios in which a weak target is to be detected under strong interference sources, such as large objects acting as clutter, communication signals coming from UL users, beam-squint effect due to exceptionally high bandwidth, or LOS paths between transmitters and receivers. Under all these circumstances, the primary objective of the detectors is to estimate the channel between the transmitters and the receivers as the whole information of position or velocity of the targets lies in this channel. To this end, the main challenge for the channel estimation in ISAC systems is shown to be the randomly generated and ever-changing transmitted communication symbols. While a slight mismatch between the actual target and the matched filter of the detector results in a slight and well-determined straddle loss in classical radar systems, a similar mismatch causes a random and ever-changing symbol-dependent contamination of whole position and Doppler spectra in ISAC sys-

tems. This phenomenon is theoretically shown, thoroughly explained, and supported with evidences from simulation results throughout the entire thesis.

The proposed signal processing algorithms in this thesis consider the aforementioned challenge of ISAC systems as an opportunity to outperform the classical methods. As the transmitted symbols spread the mismatched echo signals to the entire position-Doppler spectra, an otherwise-strong and localized interference source can be suppressed using this mismatch. Especially in MIMO systems with multiple transmit streams, thanks to the diversity created by the mismatch, interference can always be suppressed in one domain if not in the other. Specifically, it is demonstrated multiple times in this thesis that MIMO processing can suppress the interference not only in angular domain but also in range-Doppler domains even in cases where the actual range-Doppler filters are inherently incapable of achieving such suppression.

Based on the opportunity to strongly mitigate the interference, multiple detectors are proposed in this thesis. The main detectors proposed are all GLRT detectors that inherently show CFAR properties. However, they require significantly high computation powers than the classical methods. Therefore, several other detectors are also proposed in this thesis to help ease the computational burden while trading off detection performance. All of these proposed methods are compared with benchmark detectors in the literature and their powers and weaknesses are investigated in detail.

As the demand for bandwidth and integrated functionalities escalates, ISAC systems are expected to gain more attention in both academia and industry. The frameworks developed in this thesis may serve as valuable building blocks for future research and practical implementations in this emerging field. In line with this growing interest, several promising directions for future work can be considered. For instance, synchronization or localization errors in multistatic systems may be examined in detail to assess their impact on system performance, especially from the detection perspective. Similarly, well-known and commonly investigated phenomena such as phase noise or carrier frequency offset may be examined under the proposed MIMO-ISAC framework in future studies. Additionally, the use of alternative waveforms or designing custom waveforms for ISAC systems can be explored to better balance the sensing and communication trade-offs. Furthermore, a full-duplex extension of the

proposed multistatic framework can be achieved, especially addressing the challenge of self-interference cancellation. These examples represent only a subset of the many possible research directions, highlighting that ISAC will continue to be a fertile and dynamic area for scientific exploration in the years to come.

REFERENCES

[1] J. Navarro-Ortiz, P. Romero-Díaz, S. Sendra, P. Ameigeiras, J. Ramos-Munoz, and J. López-Soler, "A Survey on 5G Usage Scenarios and Traffic Models," *IEEE Communications Surveys & Tutorials*, vol. 22, pp. 905–929, 2020.

[2] A. Esswie and K. Pedersen, "Opportunistic Spatial Preemptive Scheduling for URLLC and eMBB Coexistence in Multi-User 5G Networks," *IEEE Access*, vol. 6, pp. 38451–38463, 2018.

[3] H. Yang, W.-D. Zhong, C. Chen, and A. Alphones, "Integration of Visible Light Communication and Positioning within 5G Networks for Internet of Things," *IEEE Network*, vol. 34, no. 5, pp. 134–140, 2020.

[4] F. Wei, W. Chen, Y. Wu, J. Li, and Y. Luo, "Toward 5G Wireless Interface Technology: Enabling Nonorthogonal Multiple Access in the Sparse Code Domain," *IEEE Vehicular Technology Magazine*, vol. 13, no. 4, pp. 18–27, 2018.

[5] A. Ashraf, T. S. Gunawan, M. Kartiwi, L. Olivia Nur, B. Setia Nugroho, and R. Pudji Astuti, "Advancements and Challenges in Scalable Modular Antenna Arrays for 5G Massive MIMO Networks," *IEEE Access*, vol. 12, pp. 57895–57916, 2024.

[6] L. Yu, J. Wu, A. Zhou, E. G. Larsson, and P. Fan, "Massively Distributed Antenna Systems With Nonideal Optical Fiber Fronthauls: A Promising Technology for 6G Wireless Communication Systems," *IEEE Vehicular Technology Magazine*, vol. 15, no. 4, pp. 43–51, 2020.

[7] R. Ali, I. Ashraf, A. K. Bashir, and Y. B. Zikria, "Reinforcement-Learning-Enabled Massive Internet of Things for 6G Wireless Communications," *IEEE Communications Standards Magazine*, vol. 5, no. 2, pp. 126–131, 2021.

[8] W. Jiang, Q. Zhou, J. He, M. A. Habibi, S. Melnyk, M. El-Absi, B. Han, M. D. Renzo, H. D. Schotten, F.-L. Luo, T. S. El-Bawab, M. Juntti, M. Debbah,

and V. C. M. Leung, "Terahertz Communications and Sensing for 6G and Beyond: A Comprehensive Review," *IEEE Communications Surveys & Tutorials*, vol. 26, no. 4, pp. 2326–2381, 2024.

[9] I. F. Akyildiz, C. Han, Z. Hu, S. Nie, and J. M. Jornet, "Terahertz Band Communication: An Old Problem Revisited and Research Directions for the Next Decade," *IEEE Transactions on Communications*, vol. 70, no. 6, pp. 4250–4285, 2022.

[10] B. Ning, Z. Tian, W. Mei, Z. Chen, C. Han, S. Li, J. Yuan, and R. Zhang, "Beamforming Technologies for Ultra-Massive MIMO in Terahertz Communications," *IEEE Open Journal of the Communications Society*, vol. 4, pp. 614–658, 2023.

[11] Z. Chen, X. Ma, B. Zhang, Y. Zhang, Z. Niu, N. Kuang, W. Chen, L. Li, and S. Li, "A Survey on Terahertz Communications," *China Communications*, vol. 16, no. 2, pp. 1–35, 2019.

[12] C. Jansen, R. Piesiewicz, D. Mittleman, T. Kurner, and M. Koch, "The Impact of Reflections From Stratified Building Materials on the Wave Propagation in Future Indoor Terahertz Communication Systems," *IEEE Transactions on Antennas and Propagation*, vol. 56, no. 5, pp. 1413–1419, 2008.

[13] H. Pennanen, T. Hänninen, O. Tervo, A. Tölli, and M. Latva-Aho, "6G: The Intelligent Network of Everything," *IEEE Access*, vol. 13, pp. 1319–1421, 2025.

[14] W. M. Othman, A. A. Ateya, M. E. Nasr, A. Muthanna, M. ElAffendi, A. Koucheryavy, and A. A. Hamdi, "Key Enabling Technologies for 6G: The Role of UAVs, Terahertz Communication, and Intelligent Reconfigurable Surfaces in Shaping the Future of Wireless Networks," *Journal of Sensor and Actuator Networks*, vol. 14, no. 2, p. 30, 2025.

[15] L. G. De Oliveira, B. Nuss, M. B. Alabd, A. Diewald, M. Pauli, and T. Zwick, "Joint Radar-Communication Systems: Modulation Schemes and System Design," *IEEE Trans. Microw. Theory Techn.*, vol. 70, pp. 1521–1551, 3 2022.

[16] F. Liu, Y. Cui, C. Masouros, J. Xu, T. X. Han, Y. C. Eldar, and S. Buzzi, "Integrated Sensing and Communications: Toward Dual-Functional Wireless

Networks for 6G and Beyond," *IEEE J. Sel. Areas Commun.*, vol. 40, pp. 1728–1767, 6 2022.

[17] J. A. Zhang, F. Liu, C. Masouros, R. W. Heath, Z. Feng, L. Zheng, and A. Petropulu, "An Overview of Signal Processing Techniques for Joint Communication and Radar Sensing," *IEEE J. Sel. Topics Signal Process.*, vol. 15, no. 6, pp. 1295–1315, 2021.

[18] C. B. Barneto, S. D. Liyanaarachchi, M. Heino, T. Riihonen, and M. Valkama, "Full Duplex Radio/Radar Technology: The Enabler for Advanced Joint Communication and Sensing," *IEEE Wirel. Commun.*, vol. 28, no. 1, pp. 82–88, 2021.

[19] N. González-Prelcic, M. Furkan Keskin, O. Kaltiokallio, M. Valkama, D. Dardari, X. Shen, Y. Shen, M. Bayraktar, and H. Wymeersch, "The Integrated Sensing and Communication Revolution for 6G: Vision, Techniques, and Applications," *Proceedings of the IEEE*, vol. 112, no. 7, pp. 676–723, 2024.

[20] E. S. Lohan, "Emerging Topics in Joint Radio-Based Positioning, Sensing, and Communications," *Sensors*, vol. 25, no. 3, p. 948, 2025.

[21] K. Meng, C. Masouros, A. P. Petropulu, and L. Hanzo, "Cooperative ISAC Networks: Opportunities and Challenges," *IEEE Wireless Communications*, vol. 32, no. 3, pp. 212–219, 2025.

[22] S. Singh and U. Samal, "Integrated Sensing and Communication in Next-Generation Wireless Networks: Insights and Trends," *International Journal of Communication Systems*, vol. 38, no. 5, p. e70014, 2025. e70014 dac.70014.

[23] T. Wild, V. Braun, and H. Viswanathan, "Joint Design of Communication and Sensing for beyond 5G and 6G Systems," *IEEE Access*, vol. 9, pp. 30845–30857, 2021.

[24] F. Liu, C. Masouros, A. P. Petropulu, H. Griffiths, and L. Hanzo, "Joint Radar and Communication Design: Applications, State-of-the-Art, and the Road Ahead," *IEEE Trans. Commun.*, vol. 68, pp. 3834–3862, 6 2020.

[25] B. Zhang, S. Ma, W. Liang, and L. Li, "ISAC-Assisted OTFS Communication in Vehicle Networks," in *2023 International Conference on Ubiquitous Communication (Ucom)*, pp. 7–11, 2023.

[26] R. S. Sam, A. Dey, and S. Ramanath, "Learning-Based Sensing Mode Selection for ISAC in Intelligent Transportation Systems," in *2025 17th International Conference on COMmunication Systems and NETworks (COMSNETS)*, pp. 174–178, 2025.

[27] G. Zhang, X. Cai, N. Franchi, and M. Lübke, "A Geometry-Based ISAC Channel Model for Vehicle-to-Vehicle Scenarios," in *2025 19th European Conference on Antennas and Propagation (EuCAP)*, pp. 1–5, 2025.

[28] M. R. Thadathil and N. Saeed, "Smart Traffic Intersections: Leveraging ISAC and Millimeter-Wave for Advanced Vehicle Platooning," in *2025 Global Information Infrastructure and Networking Symposium (GIIS)*, pp. 1–6, 2025.

[29] Q. Zhang, H. Sun, X. Gao, X. Wang, and Z. Feng, "Time-Division ISAC Enabled Connected Automated Vehicles Cooperation Algorithm Design and Performance Evaluation," *IEEE Journal on Selected Areas in Communications*, vol. 40, no. 7, pp. 2206–2218, 2022.

[30] W. Yang, X. Liu, and Z. Liu, "Joint Trajectory and Resource Allocation Optimization for Mobile Vehicles in UAV Assisted Secure ISAC System," in *2024 IEEE 24th International Conference on Communication Technology (ICCT)*, pp. 321–325, 2024.

[31] Q. Zhu, R. Liu, X. Lv, Q. Meng, and Y. Wang, "AoI-Optimal Trajectory Planning in UAV-Assisted ISAC Networks," in *2023 IEEE 23rd International Conference on Communication Technology (ICCT)*, pp. 428–433, 2023.

[32] Y. Liu, X. Liu, Z. Liu, Y. Yu, M. Jia, Z. Na, and T. S. Durrani, "Secure Rate Maximization for ISAC-UAV Assisted Communication Amidst Multiple Eavesdroppers," *IEEE Transactions on Vehicular Technology*, vol. 73, no. 10, pp. 15843–15847, 2024.

[33] Y. Wu, C. Liu, X. Hu, and M. Peng, "Sensing and Beamtracking Scheme De-

sign for UAV-Enabled ISAC Systems," in *2023 International Conference on Wireless Communications and Signal Processing (WCSP)*, pp. 146–151, 2023.

[34] Z. Xing, Z. Zhao, C. Du, M. Sha, and S. Zhou, "Sensing Assisted Full-Duplex Unmanned Aerial Vehicle for Maximum Coverage of Users," in *2024 IEEE International Conference on Signal, Information and Data Processing (ICSIDP)*, pp. 1–6, 2024.

[35] Q. Gao, R. Zhong, and Y. Liu, "Trajectory and Beamforming Optimization in UAV-enabled ISAC System," in *GLOBECOM 2024 - 2024 IEEE Global Communications Conference*, pp. 1527–1532, 2024.

[36] Zhong, Jincheng and Wu, Jilong and Li, Yaqi and Zhang, Chenyu and Zhu, Pengcheng, "Joint beamforming design and trajectory optimization for uav-enabled cell-free isac mimo systems," *IEEE Communications Letters*, pp. 1–1, 2025.

[37] F. Dong, F. Liu, Y. Cui, S. Lu, and Y. Li, "Sensing as a Service in 6G Perceptive Mobile Networks: Architecture, Advances, and the Road Ahead," *IEEE Network*, vol. 38, no. 2, pp. 87–96, 2024.

[38] A. Zhang, M. L. Rahman, X. Huang, Y. J. Guo, S. Chen, and R. W. Heath, "Perceptive Mobile Networks: Cellular Networks With Radio Vision via Joint Communication and Radar Sensing," *IEEE Vehicular Technology Magazine*, vol. 16, no. 2, pp. 20–30, 2021.

[39] M. L. Rahman, J. A. Zhang, X. Huang, Y. J. Guo, and R. W. Heath, "Framework for a Perceptive Mobile Network Using Joint Communication and Radar Sensing," *IEEE Transactions on Aerospace and Electronic Systems*, vol. 56, no. 3, pp. 1926–1941, 2020.

[40] L. Xie, S. Song, and K. B. Letaief, "Networked Sensing With AI-Empowered Interference Management: Exploiting Macro-Diversity and Array Gain in Perceptive Mobile Networks," *IEEE Journal on Selected Areas in Communications*, vol. 41, no. 12, pp. 3863–3877, 2023.

[41] W. Jiang, Z. Wei, S. Yang, Z. Feng, and P. Zhang, "Cooperation-Based Joint Active and Passive Sensing with Asynchronous Transceivers for Perceptive

Mobile Networks," *IEEE Trans. Wireless Commun.*, vol. 23, no. 10, pp. 15627–15641, 2024.

[42] X.-Y. Wang, S. Yang, J. Zhang, C. Masouros, and P. Zhang, "Clutter Suppression, Time-Frequency Synchronization, and Sensing Parameter Association in Asynchronous Perceptive Vehicular Networks," *IEEE J. Sel. Areas Commun.*, vol. 42, no. 10, pp. 2719–2736, 2024.

[43] X.-Y. Wang, S. Yang, H.-Y. Zhai, C. Masouros, and J. Andrew Zhang, "Windowing Optimization for Fingerprint-Spectrum-Based Passive Sensing in Perceptive Mobile Networks," *IEEE Transactions on Communications*, vol. 73, no. 2, pp. 1367–1382, 2025.

[44] W. Zhou, R. Zhang, G. Chen, and W. Wu, "Integrated Sensing and Communication Waveform Design: A Survey," *IEEE Open Journal of the Communications Society*, vol. 3, pp. 1930–1949, 2022.

[45] L. Zheng, M. Lops, Y. C. Eldar, and X. Wang, "Radar and Communication Coexistence: An Overview: A Review of Recent Methods," 9 2019.

[46] S. Chen, C. Chen, Z. Zeng, Y. Yang, and H. Haas, "Full-Duplex RO-ISAC System: Wavelength Division Duplexing and Hybrid Waveform Design," *IEEE Photonics Technology Letters*, vol. 37, no. 15, pp. 869–872, 2025.

[47] Z. Yu, H. Zhao, Q. Guo, and J. Ding, "Converting Interference to Gain: Enhancing Sensing Capabilities of ISAC Systems via Noncooperative Base Station Signals," *IEEE Signal Processing Letters*, vol. 32, pp. 1675–1679, 2025.

[48] Y. Awad, A. Celik, and A. Eltawil, "SSB-Based Multi-Target Detection and Joint Velocity, Angle, and Range Estimation in 5G-NR," *IEEE Communications Letters*, vol. 29, no. 6, pp. 1340–1344, 2025.

[49] M. Bednarz and T. P. Zielinski, "Remote Radio Frequency Sensing Based on 5G New Radio Positioning Reference Signals," *Sensors*, vol. 25, no. 2, p. 337, 2025.

[50] Z. Wang and V. W. Wong, "Cooperative ISAC for Localization and Velocity Estimation Using OFDM Waveforms in Cell-Free MIMO Systems," in *ICASSP*

2025 - 2025 IEEE International Conference on Acoustics, Speech and Signal Processing (ICASSP), pp. 1–5, 2025.

[51] N. González-Prelcic, D. Tagliaferri, M. F. Keskin, H. Wymeersch, and L. Song, "Six Integration Avenues for ISAC in 6G and Beyond," *IEEE Vehicular Technology Magazine*, vol. 20, no. 1, pp. 18–39, 2025.

[52] D. T. Bellini, D. Tagliaferri, M. Mizmizi, S. Tebaldini, and U. Spagnolini, "Multi-View Integrated Imaging and Communication," in *2025 IEEE 5th International Symposium on Joint Communications & Sensing (JC&S)*, pp. 1–6, 2025.

[53] G. Torcolacci, A. Guerra, H. Zhang, F. Guidi, Q. Yang, Y. C. Eldar, and D. Dardari, "Holographic Imaging With XL-MIMO and RIS: Illumination and Reflection Design," *IEEE Journal of Selected Topics in Signal Processing*, vol. 18, no. 4, pp. 587–602, 2024.

[54] F. Ayten, M. C. Ilter, A. Jain, E. S. Lohan, and M. Valkama, "Neural Network-Integrated Multistatic Sensing for Joint Angle Estimation in Cell-Free JCAS Systems," in *2025 IEEE 5th International Symposium on Joint Communications & Sensing (JC&S)*, pp. 1–6, 2025.

[55] K. R. R. Ranasinghe, H. Seok Rou, G. Thadeu Freitas de Abreu, T. Takahashi, and K. Ito, "Joint Channel, Data, and Radar Parameter Estimation for AFDM Systems in Doubly-Dispersive Channels," *IEEE Transactions on Wireless Communications*, vol. 24, no. 2, pp. 1602–1619, 2025.

[56] M. Bayraktar, N. González-Prelcic, H. Chen, and C. J. Zhang, "Near-Field Full-Duplex Integrated Sensing and Communication with Dynamic Metasurface Antennas," in *2024 58th Asilomar Conference on Signals, Systems, and Computers*, pp. 609–613, 2024.

[57] M. Bayraktar, N. González-Prelcic, H. Chen, and C. J. Zhang, "Truly Full-Duplex Integrated Sensing and Single-User Communication at mmWave," in *2024 IEEE 25th International Workshop on Signal Processing Advances in Wireless Communications (SPAWC)*, pp. 116–120, 2024.

[58] G. Chrysanidis, Y. Liu, and A. Argyriou, "A Replay Attack Against ISAC Based on OFDM," *IEEE Access*, vol. 12, pp. 20998–21003, 2024.

[59] A. Hassanien and S. A. Vorobyov, "Phased-MIMO Radar: A Tradeoff Between Phased-Array and MIMO Radars," *IEEE Transactions on Signal Processing*, vol. 58, no. 6, pp. 3137–3151, 2010.

[60] S. Fortunati, L. Sanguinetti, F. Gini, M. S. Greco, and B. Himed, "Massive MIMO Radar for Target Detection," *IEEE Trans. Signal Process.*, vol. 68, pp. 859–871, 2020.

[61] Q. He, Z. Wang, J. Hu, and R. S. Blum, "Performance Gains From Cooperative MIMO Radar and MIMO Communication Systems," *IEEE Signal Processing Letters*, vol. 26, no. 1, pp. 194–198, 2019.

[62] X. Liu, T. Huang, N. Shlezinger, Y. Liu, J. Zhou, and Y. C. Eldar, "Joint Transmit Beamforming for Multiuser MIMO Communications and MIMO Radar," *IEEE Transactions on Signal Processing*, vol. 68, pp. 3929–3944, 2020.

[63] L. Chen, Z. Wang, Y. Du, Y. Chen, and F. R. Yu, "Generalized Transceiver Beamforming for DFRC With MIMO Radar and MU-MIMO Communication," *IEEE Journal on Selected Areas in Communications*, vol. 40, no. 6, pp. 1795–1808, 2022.

[64] W. Zhai, X. Wang, X. Cao, M. S. Greco, and F. Gini, "Reinforcement Learning Based Dual-Functional Massive MIMO Systems for Multi-Target Detection and Communications," *IEEE Transactions on Signal Processing*, vol. 71, pp. 741–755, 2023.

[65] S. D. Liyanaarachchi, T. Riihonen, C. B. Barneto, and M. Valkama, "Joint MIMO Communications and Sensing With Hybrid Beamforming Architecture and OFDM Waveform Optimization," *IEEE Trans. Wireless Commun.*, vol. 23, no. 2, pp. 1565–1580, 2024.

[66] M. Temiz, E. Alsusa, and L. Danoon, "A Receiver Architecture for Dual-Functional Massive MIMO OFDM RadCom Systems," in *Proc. IEEE Int. Conf. Commun. Workshops*, pp. 1–6, IEEE, 2020.

[67] M. Temiz, E. Alsusa, and M. W. Baidas, "A Dual-Functional Massive MIMO OFDM Communication and Radar Transmitter Architecture," *IEEE Trans. Veh. Technol.*, vol. 69, no. 12, pp. 14974–14988, 2020.

[68] L. Pucci, E. Matricardi, E. Paolini, W. Xu, and A. Giorgetti, "Performance Analysis of Joint Sensing and Communication based on 5G New Radio," in *2021 IEEE GC Wkshps.*, pp. 1–6, IEEE, 2021.

[69] S. D. Liyanaarachchi, C. B. Barneto, T. Riihonen, M. Heino, and M. Valkama, "Range–Angle Processing for Target Detection in Joint MIMO-OFDM Communications and Sensing," in *Proc. IEEE SPAWC*, pp. 486–490, IEEE, 2021.

[70] Z. Wan, Z. Gao, S. Tan, and L. Fang, "Joint Channel Estimation and Radar Sensing for UAV Networks with mmWave Massive MIMO," in *Proc. Int. Wireless Commun. Mobile Comput. (IWCMC)*, pp. 44–49, 2022.

[71] Q. Yang, H. Wu, Q. Huang, J. Zhang, H. Chen, W. Li, X. Tao, and Q. Zhang, "Side-lobe Can Know More: Towards Simultaneous Communication and Sensing for mmWave," *Proc. ACM Interact. Mob. Wearable Ubiquitous Technol.*, vol. 6, jan 2023.

[72] S. Buzzi, C. D'Andrea, and M. Lops, "Using Massive MIMO Arrays for Joint Communication and Sensing," in *Proc. 53rd Asilomar Conf. Signals Syst. Comput.*, pp. 5–9, IEEE, 2019.

[73] M. F. Keskin, H. Wymeersch, and V. Koivunen, "MIMO-OFDM Joint Radar-Communications: Is ICI Friend or Foe?," *IEEE J. Sel. Topics Signal Process.*, vol. 15, no. 6, pp. 1393–1408, 2021.

[74] F. Wang and H. Li, "Power Allocation for Coexisting Multicarrier Radar and Communication Systems in Cluttered Environments," *IEEE Trans. Signal Process.*, vol. 69, pp. 1603–1613, 2021.

[75] M. A. Islam, G. C. Alexandropoulos, and B. Smida, "Integrated Sensing and Communication with Millimeter Wave Full Duplex Hybrid Beamforming," in *Proc. IEEE Int. Conf. Commun.*, pp. 4673–4678, 2022.

[76] X. Li, V. C. Andrei, U. J. Mönich, and H. Boche, "Optimal and Robust Waveform Design for MIMO-OFDM Channel Sensing: A Cramér-Rao Bound Perspective," in *Proc. IEEE Int. Conf. Commun.*, pp. 3516–3521, 2023.

[77] L. Chen, Z. Wang, Y. Du, Y. Chen, and F. R. Yu, "Generalized Transceiver Beamforming for DFRC With MIMO Radar and MU-MIMO Communication," *IEEE J. Sel. Areas Commun.*, vol. 40, no. 6, pp. 1795–1808, 2022.

[78] X. Yu, L. Tu, Q. Yang, M. Yu, Z. Xiao, and Y. Zhu, "Hybrid Beamforming in mmWave Massive MIMO for IoV With Dual-Functional Radar Communication," *IEEE Trans. Veh. Technol.*, vol. 72, no. 7, pp. 9017–9030, 2023.

[79] M. F. Keskin, M. M. Mojahedian, J. O. Lacruz, C. Marcus, O. Eriksson, A. Giorgetti, J. Widmer, and H. Wymeersch, "Fundamental Trade-Offs in Monostatic ISAC: A Holistic Investigation Towards 6G," 2024.

[80] C. B. Barneto, T. Riihonen, M. Turunen, L. Anttila, M. Fleischer, K. Stadius, J. Ryynänen, and M. Valkama, "Full-Duplex OFDM Radar with LTE and 5G NR Waveforms: Challenges, Solutions, and Measurements," *IEEE Trans. Microw. Theory Techn.*, vol. 67, no. 10, pp. 4042–4054, 2019.

[81] Z. Xiao, R. Liu, M. Li, Q. Liu, and A. L. Swindlehurst, "A Novel Joint Angle-Range-Velocity Estimation Method for MIMO-OFDM ISAC Systems," *IEEE Trans. Signal Process.*, vol. 72, pp. 3805–3818, 2024.

[82] W. Cho, K. Chang, W. Shin, Y. Kim, and Y.-J. Ko, "OFDM-Based In-Band Full-Duplex ISAC Systems," *IEEE Wireless Communications Letters*, vol. 14, no. 2, pp. 365–369, 2025.

[83] Y. Xiang, Y. Gao, X. Yang, S. Kang, and M. Shao, "An ESPRIT-Based Moving Target Sensing Method for MIMO-OFDM ISAC Systems," *IEEE Communications Letters*, vol. 27, no. 12, pp. 3205–3209, 2023.

[84] A. Bouziane, S. Eddine Zegrar, and H. Arslan, "A Novel OFDM-FMCW Waveform for Low-Complexity Joint Sensing and Communication," *IEEE Wireless Communications Letters*, vol. 14, no. 2, pp. 425–429, 2025.

[85] D. Brunner, L. Giroto de Oliveira, C. Muth, S. Mandelli, M. Henninger, A. Diewald, Y. Li, M. Basim Alabd, L. Schmalen, T. Zwick, and B. Nuss,

"Bistatic OFDM-Based ISAC With Over-the-Air Synchronization: System Concept and Performance Analysis," *IEEE Transactions on Microwave Theory and Techniques*, vol. 73, no. 5, pp. 3016–3029, 2025.

[86] P. Li, M. Li, R. Liu, Q. Liu, and A. Lee Swindlehurst, "MIMO-OFDM ISAC Waveform Design for Range-Doppler Sidelobe Suppression," *IEEE Transactions on Wireless Communications*, vol. 24, no. 2, pp. 1001–1015, 2025.

[87] K. M. Braun, *OFDM Radar Algorithms in Mobile Communication Networks*. PhD thesis, Karlsruhe, Karlsruher Institut für Technologie (KIT), Diss., 2014, 2014.

[88] S. D. Liyanaarachchi, T. Riihonen, C. B. Barneto, and M. Valkama, "Optimized Waveforms for 5G-6G Communication with Sensing: Theory, Simulations and Experiments," *IEEE Trans. Wireless Commun.*, vol. 20, pp. 8301–8315, 12 2021.

[89] N. M. Idrees, Z. Lu, M. Saqlain, H. Zhang, S. Wang, L. Zhang, and X. Yu, "A W-Band Communication and Sensing Convergence System Enabled by Single OFDM Waveform," *Micromachines*, vol. 13, no. 2, p. 312, 2022.

[90] C. B. Barneto, S. D. Liyanaarachchi, T. Riihonen, M. Heino, L. Anttila, and M. Valkama, "Beamforming and Waveform Optimization for OFDM-based Joint Communications and Sensing at mm-Waves," in *Proc. 54th Asilomar Conf. Signals Syst. Comput.*, pp. 895–899, 2020.

[91] Y. Lai, M. F. Keskin, H. Wymeersch, L. Venturino, W. Yi, and L. Kong, "Subspace-Based Detection in OFDM ISAC Systems Under Different Constellations," in *ICASSP 2024*, pp. 9126–9130, 2024.

[92] Y. Huang, S. Hu, S. Ma, Z. Liu, and M. Xiao, "Designing Low-PAPR Waveform for OFDM-Based RadCom Systems," *IEEE Trans. Wireless Commun.*, vol. 21, no. 9, pp. 6979–6993, 2022.

[93] B. Kong, Y. Wang, X. Deng, and D. Qin, "Joint Range-Doppler-Angle Estimation for OFDM-Based RadCom System via Tensor Decomposition," *Wirel. Commun. Mob. Comput.*, vol. 2018, pp. 1–12, 08 2018.

[94] C. R. Berger, B. Demissie, J. Heckenbach, P. Willett, and S. Zhou, "Signal Processing for Passive Radar Using OFDM Waveforms," *IEEE J. Sel. Topics Signal Process.*, vol. 4, pp. 226–238, 2 2010.

[95] J.-F. Gu, J. Moghaddasi, and K. Wu, "Delay and Doppler Shift Estimation for OFDM-Based Radar-Radio (RadCom) System," in *2015 IEEE International Wireless Symposium (IWS 2015)*, pp. 1–4, 2015.

[96] H. Guo, H. Wymeersch, B. Makki, H. Chen, Y. Wu, G. Durisi, M. F. Keskin, M. H. Moghaddam, C. Madapatha, H. Yu, *et al.*, "Integrated Communication, Localization, and Sensing in 6G D-MIMO Networks," *arXiv preprint arXiv:2403.19785*, 2024.

[97] M. Leinonen *et al.*, "Initial Radio Models and Analysis Towards Ultra-High Data Rate Links in 6G," *Hexa-X project Deliverable D2. 2*, 2021.

[98] H. Chen, M. F. Keskin, A. Sakhnini, N. Decarli, S. Pollin, D. Dardari, and H. Wymeersch, "6G Localization and Sensing in the Near Field: Features, Opportunities, and Challenges," *IEEE Wireless Communications*, vol. 31, no. 4, pp. 260–267, 2024.

[99] S. R. Doughty, *Development and Performance Evaluation of a Multistatic Radar System*. University of London, University College London (United Kingdom), 2008.

[100] T. Derham, S. Doughty, K. Woodbridge, and C. Baker, "Design and Evaluation of a Low-Cost Multistatic Netted Radar System," *IET Radar, Sonar & Navigation*, vol. 1, pp. 362–368, 2007.

[101] T. Johnsen and K. E. Olsen, "Bi-and Multistatic Radar," *Advanced Radar Signal and Data Processing*, pp. 4–1, 2006.

[102] M. Sadeghi, F. Behnia, R. Amiri, and A. Farina, "Target Localization Geometry Gain in Distributed MIMO Radar," *IEEE Transactions on Signal Processing*, vol. 69, pp. 1642–1652, 2021.

[103] D. Tagliaferri, M. Manzoni, M. Mizmizi, S. Tebaldini, A. V. Monti-Guarnieri, C. M. Prati, and U. Spagnolini, "Cooperative Coherent Multistatic Imaging

and Phase Synchronization in Networked Sensing," *IEEE Journal on Selected Areas in Communications*, 2024.

[104] M. Koivisto, M. Costa, J. Werner, K. Heiska, J. Talvitie, K. Leppänen, V. Koivunen, and M. Valkama, "Joint Device Positioning and Clock Synchronization in 5G Ultra-Dense Networks," *IEEE Transactions on Wireless Communications*, vol. 16, no. 5, pp. 2866–2881, 2017.

[105] Y. Liang, G. Wen, L. Zhu, D. Luo, Y. Kuai, and B. Li, "Target Detection Performance of Distributed MIMO Radar Systems under Non-ideal Conditions," *IEEE Transactions on Aerospace and Electronic Systems*, 2023.

[106] H. Li, F. Wang, C. Zeng, and M. A. Govoni, "Signal Detection in Distributed MIMO Radar with Non-Orthogonal Waveforms and Sync Errors," *IEEE Transactions on Signal Processing*, vol. 69, pp. 3671–3684, 2021.

[107] A. Sakhnini, S. De Bast, M. Guenach, A. Bourdoux, H. Sahli, and S. Pollin, "Near-Field Coherent Radar Sensing Using a Massive MIMO Communication Testbed," *IEEE Transactions on Wireless Communications*, vol. 21, no. 8, pp. 6256–6270, 2022.

[108] E. Fishler, A. Haimovich, R. Blum, L. Cimini, D. Chizhik, and R. Valenzuela, "Spatial Diversity in Radars—Models and Detection Performance," *IEEE Transactions on Signal Processing*, vol. 54, no. 3, pp. 823–838, 2006.

[109] S. K. Dehkordi, L. Pucci, P. Jung, A. Giorgetti, E. Paolini, and G. Caire, "Multi-static Parameter Estimation in the Near/Far Field Beam Space for Integrated Sensing and Communication Applications," *arXiv preprint arXiv:2309.14778*, 2023.

[110] P. Wang, H. Li, and B. Himed, "Moving Target Detection Using Distributed MIMO Radar in Clutter With Nonhomogeneous Power," *IEEE Transactions on Signal Processing*, vol. 59, no. 10, pp. 4809–4820, 2011.

[111] C. Zeng, F. Wang, H. Li, and M. A. Govoni, "Target Detection for Distributed MIMO Radar With Nonorthogonal Waveforms in Cluttered Environments," *IEEE Transactions on Aerospace and Electronic Systems*, vol. 59, no. 5, pp. 5448–5459, 2023.

[112] J. Lu, S. Zhou, X. Peng, and A. Wang, "Distributed Radar Multi-frame Detection with Local Censored Observations," *IEEE Transactions on Aerospace and Electronic Systems*, 2024.

[113] T. Bacchielli, L. Pucci, D. Dardari, and A. Giorgetti, "Bistatic Sensing at THz Frequencies via a Two-Stage Ultra-Wideband MIMO-OFDM System," *arXiv preprint arXiv:2405.17990*, 2024.

[114] F. Robey, D. Fuhrmann, E. Kelly, and R. Nitzberg, "A CFAR Adaptive Matched Filter Detector," *IEEE Trans. Aerosp. Electron. Syst.*, vol. 28, no. 1, pp. 208–216, 1992.

[115] M. I. Skolnik, *Radar Handbook*. McGraw-Hill, Inc., 1970.

[116] M. A. Richards, *Fundamentals of Radar Signal Processing*, vol. 1. McGraw-Hill, Inc., 2005.

[117] F. Robey, D. Fuhrmann, E. Kelly, and R. Nitzberg, "A CFAR Adaptive Matched Filter Detector," *IEEE Trans. Aerosp. Electron. Syst.*, vol. 28, no. 1, pp. 208–216, 1992.

[118] U. B. Sarac and G. M. Guvensen, "On the Effects of Range-Doppler Processing for Target Detection in OFDM-Based RadCom," *IEEE Commun. Lett.*, vol. 27, no. 7, pp. 1864–1868, 2023.

[119] K. B. Petersen and M. S. Pedersen, *The Matrix Cookbook*. Technical University of Denmark, 10 2012.

[120] U. B. Saraç and G. M. Güvensen, "A Subspace-Aware Kelly's Detector using Reduced Secondary Data with Fast and Slow Time Preprocessing," in *2019 IEEE Radar Conference (RadarConf)*, pp. 1–6, 2019.

[121] A. Kurt, M. B. Salman, U. B. Sarac, and G. M. Guvensen, "An Adaptive-Iterative Nonlinear Interference Cancellation in Time-Varying Full-Duplex Channels," *IEEE Trans. Veh. Technol.*, vol. 72, no. 2, pp. 1862–1878, 2023.

[122] H. Ozen and G. M. Guvensen, "Interference and Beam Squint Aware TTD-Aided Beamforming for Dual Wideband Massive MIMO," *IEEE Wireless Commun. Lett.*, vol. 13, no. 1, pp. 64–68, 2024.

[123] F. Gao, L. Xu, and S. Ma, "Integrated Sensing and Communications With Joint Beam-Squint and Beam-Split for mmWave/THz Massive MIMO," *IEEE Trans. Commun.*, vol. 71, no. 5, pp. 2963–2976, 2023.

[124] G. Hakobyan and B. Yang, "A Novel Intercarrier-Interference Free Signal Processing Scheme for OFDM Radar," *IEEE Trans. Veh. Technol.*, vol. 67, no. 6, pp. 5158–5167, 2018.

[125] H. Noh, H. Lee, and H. J. Yang, "ICI-Robust Transceiver Design for Integration of MIMO-OFDM Radar and MU-MIMO Communication," *IEEE Trans. Veh. Technol.*, vol. 72, no. 1, pp. 821–838, 2023.

[126] H. S. Rou, G. T. F. de Abreu, J. Choi, D. González G., M. Kountouris, Y. L. Guan, and O. Gonsa, "From Orthogonal Time–Frequency Space to Affine Frequency-Division Multiplexing: A comparative study of next-generation waveforms for integrated sensing and communications in doubly dispersive channels," *IEEE Signal Process. Mag.*, vol. 41, no. 5, pp. 71–86, 2024.

[127] L. Gaudio, G. Colavolpe, and G. Caire, "OTFS vs. OFDM in the Presence of Sparsity: A Fair Comparison," *IEEE Trans. Wireless Commun.*, vol. 21, no. 6, pp. 4410–4423, 2022.

[128] U. B. Sarac and G. M. Guvensen, "Knowledge-Aided and Adaptive Beam-Squint Aware MIMO-OFDM Radar Detectors for ISAC," *IEEE Transactions on Communications*, pp. 1–1, 2025.

[129] M. Murthi and B. Rao, "Minimum Variance Distortionless Response (MVDR) Modeling of Voiced Speech," in *Proc. Int. Conf. Acoustics Speech Signal Processing '97*, vol. 3, pp. 1687–1690 vol.3, 1997.

APPENDICES

A Calculation of autocorrelation matrices in Chapter 4

A.1 Transmitted symbols are given

When the transmitted symbols $\mathbf{X}_n$ are known, $\mathbf{R}_n^{\psi}(\tilde{m})$ in (4.23) can be written as:

$$\begin{aligned}\mathbf{R}_n^{\psi} &= \mathbb{E}\left\{\mathrm{vec}\{\mathbf{\Psi}_n\}\,\mathrm{vec}\{\mathbf{\Psi}_n\}^{\mathrm{H}}\right\} \\ &= \sum_{k=1}^{\mathcal{K}} \mathbb{E}\left\{\mathrm{vec}\{\mathbf{C}_{kn}\}\,\mathrm{vec}\{\mathbf{C}_{kn}\}^{\mathrm{H}}\right\} \\ &\quad + \sum_{u=1}^{\mathcal{U}} \mathbb{E}\left\{\mathrm{vec}\{\mathbf{S}_{un}\}\,\mathrm{vec}\{\mathbf{S}_{un}\}^{\mathrm{H}}\right\} \\ &\quad + \mathbb{E}\left\{\mathrm{vec}\{\mathbf{N}_n\}\,\mathrm{vec}\{\mathbf{N}_n\}^{\mathrm{H}}\right\}. \end{aligned} \tag{A.1}$$

We can calculate clutter, SoI and noise parts separately. Let's define:

$$\begin{aligned}\mathbf{R}_{kn}^{\mathbf{c}} &\triangleq \mathbb{E}\left\{\mathrm{vec}\{\mathbf{C}_{kn}\}\,\mathrm{vec}\{\mathbf{C}_{kn}\}^{\mathrm{H}}\right\}, \\ \mathbf{R}_{un}^{\mathbf{s}} &\triangleq \mathbb{E}\left\{\mathrm{vec}\{\mathbf{S}_{un}\}\,\mathrm{vec}\{\mathbf{S}_{un}\}^{\mathrm{H}}\right\}, \\ \mathbf{R}_{n}^{\mathbf{n}} &\triangleq \mathbb{E}\left\{\mathrm{vec}\{\mathbf{N}_{n}\}\,\mathrm{vec}\{\mathbf{N}_{n}\}^{\mathrm{H}}\right\}. \end{aligned} \tag{A.2}$$

Following the definition in (4.13),

$$\begin{aligned}\mathrm{vec}\{\mathbf{C}_{kn}\} &= \mathrm{vec}\{\mathbf{H}_{kn}\mathbf{X}_n\mathbf{D}_k^{\mathcal{C}}\mathbf{\Lambda}_k^{\mathcal{C}}\} \\ &= (\mathbf{I}_M \otimes \mathbf{H}_{kn})\,\mathrm{vec}\{\mathbf{X}_n\mathbf{D}_k^{\mathcal{C}}\mathbf{\Lambda}_k^{\mathcal{C}}\} \\ &= (\mathbf{I}_M \otimes \mathbf{H}_{kn})(\mathbf{I}_M \otimes (\mathbf{X}_n\mathbf{D}_k^{\mathcal{C}}))\,\mathrm{vec}\{\mathbf{\Lambda}_k^{\mathcal{C}}\} \\ &= \underbrace{(\mathbf{I}_M \otimes \mathbf{H}_{kn})}_{\mathbf{K}_{kn}^{\mathcal{C}}}\underbrace{(\mathbf{I}_M \circledcirc (\mathbf{X}_n\mathbf{D}_k^{\mathcal{C}}))}_{\mathbf{L}_{kn}^{\mathcal{C}}}\boldsymbol{\alpha}_k \end{aligned} \tag{A.3}$$

where in the last equality, column-wise Kronecker product (Khatri-Rao product) is used to separate the diagonal elements of $\mathbf{\Lambda}_k^{\mathcal{C}}$ as a column vector $\boldsymbol{\alpha}_k$. It should be noted that $\mathbf{K}_{kn}^{\mathcal{C}}$ represents the MIMO channel for k^{th} UIT and $\mathbf{L}_{kn}^{\mathcal{C}}$ represents the

temporal code of the k^{th} UIT. The MIMO channel is not dependent on the symbols $\mathbf{X}_n$, which is expected, so it is deterministic and it repeats itself through the Kronecker product operation because it is assumed to be the same for M symbol duration. The temporal code actually depends on the transmitted symbols $\mathbf{X}_n$ but since the symbols are assumed to be given, $\mathbf{L}_{kn}^{\mathcal{C}}$ also becomes deterministic. Then,

$$\begin{aligned}\mathbf{R}_{kn}^{\mathbf{c}} &= \mathbf{K}_{kn}^{\mathcal{C}}\mathbf{L}_{kn}^{\mathcal{C}}\mathbb{E}\left\{\boldsymbol{\alpha}_k\boldsymbol{\alpha}_k^{\mathrm{H}}\right\}(\mathbf{L}_{kn}^{\mathcal{C}})^{\mathrm{H}}(\mathbf{K}_{kn}^{\mathcal{C}})^{\mathrm{H}} \\ &= \mathbf{K}_{kn}^{\mathcal{C}}\mathbf{L}_{kn}^{\mathcal{C}}\mathbf{R}_k^{\boldsymbol{\alpha}}(\mathbf{L}_{kn}^{\mathcal{C}})^{\mathrm{H}}(\mathbf{K}_{kn}^{\mathcal{C}})^{\mathrm{H}}. \end{aligned} \tag{A.4}$$

Similarly,

$$\begin{aligned}\mathrm{vec}\{\mathbf{S}_{un}\} &= \mathrm{vec}\{\mathbf{g}_{un}\mathbf{j}_{un}^{\mathrm{T}}\mathbf{D}_u^{\mathcal{S}}\boldsymbol{\Lambda}_u^{\mathcal{S}}\} \\ &= (\mathbf{I}_M \otimes \mathbf{g}_{un})\,\mathrm{vec}\{\mathbf{j}_{un}^{\mathrm{T}}\mathbf{D}_u^{\mathcal{S}}\boldsymbol{\Lambda}_u^{\mathcal{S}}\} \\ &= (\mathbf{I}_M \otimes \mathbf{g}_{un})(\mathbf{I}_M \otimes (\mathbf{j}_{un}^{\mathrm{T}}\mathbf{D}_u^{\mathcal{S}}))\,\mathrm{vec}\{\boldsymbol{\Lambda}_u^{\mathcal{S}}\} \\ &= \underbrace{(\mathbf{I}_M \otimes \mathbf{g}_{un})}_{\mathbf{K}_{un}^{\mathcal{S}}}\underbrace{(\mathbf{I}_M \circledast (\mathbf{j}_{un}^{\mathrm{T}}\mathbf{D}_u^{\mathcal{S}}))}_{\mathbf{L}_{un}^{\mathcal{S}}}\boldsymbol{\beta}_u \end{aligned} \tag{A.5}$$

and

$$\begin{aligned}\mathbf{R}_{un}^{\mathbf{s}} &= \mathbf{K}_{un}^{\mathcal{S}}\mathbb{E}\left\{\mathbf{L}_{un}^{\mathcal{S}}\boldsymbol{\beta}_u\boldsymbol{\beta}_u^{\mathrm{H}}(\mathbf{L}_{un}^{\mathcal{S}})^{\mathrm{H}}\right\}(\mathbf{K}_{un}^{\mathcal{S}})^{\mathrm{H}} \\ &= \mathbf{K}_{un}^{\mathcal{S}}\mathbb{E}\left\{\mathbf{L}_{un}^{\mathcal{S}}\mathbf{R}_u^{\boldsymbol{\beta}}(\mathbf{L}_{un}^{\mathcal{S}})^{\mathrm{H}}\right\}(\mathbf{K}_{un}^{\mathcal{S}})^{\mathrm{H}}. \end{aligned} \tag{A.6}$$

The last expectation in (A.6) is over $\mathbf{j}_{un}$ because SoI signals are always assumed to be random, even if $\mathbf{X}_n$ are given. On the other hand, since $\mathbf{j}_{un}^{\mathrm{T}}\mathbf{D}_u^{\mathcal{S}}$ is a row vector, $\mathbf{L}_{un}^{\mathcal{S}} = \mathrm{diag}\{\mathbf{j}_{un}\}\mathbf{D}_u^{\mathcal{S}}$ and

$$\begin{aligned}\mathbf{R}_{un}^{\mathbf{s}} &= \mathbf{K}_{un}^{\mathcal{S}}\mathbb{E}\left\{\mathrm{diag}\{\mathbf{j}_{un}\}\mathbf{D}_u^{\mathcal{S}}\mathbf{R}_u^{\boldsymbol{\beta}}(\mathrm{diag}\{\mathbf{j}_{un}\}\mathbf{D}_u^{\mathcal{S}})^{\mathrm{H}}\right\}(\mathbf{K}_{un}^{\mathcal{S}})^{\mathrm{H}} \\ &= \mathbf{K}_{un}^{\mathcal{S}}\left(\mathbb{E}\left\{\mathbf{j}_{un}\mathbf{j}_{un}^{\mathrm{H}}\right\} \odot \mathbf{D}_u^{\mathcal{S}}\mathbf{R}_u^{\boldsymbol{\beta}}(\mathbf{D}_u^{\mathcal{S}})^{\mathrm{H}}\right)(\mathbf{K}_{un}^{\mathcal{S}})^{\mathrm{H}} \\ &= \mathbf{K}_{un}^{\mathcal{S}}\left(\frac{1}{M}\mathbf{I}_M \odot \mathbf{D}_u^{\mathcal{S}}\mathbf{R}_u^{\boldsymbol{\beta}}(\mathbf{D}_u^{\mathcal{S}})^{\mathrm{H}}\right)(\mathbf{K}_{un}^{\mathcal{S}})^{\mathrm{H}} \\ &= \frac{1}{M}\mathbf{K}_{un}^{\mathcal{S}}\,\mathrm{diag}\{\mathbf{R}_u^{\boldsymbol{\beta}}\}(\mathbf{K}_{un}^{\mathcal{S}})^{\mathrm{H}} \\ &= \frac{\gamma_u^{\mathcal{S}}}{M}(\mathbf{I}_M \otimes \mathbf{g}_{un})(\mathbf{I}_M \otimes \mathbf{g}_{un})^{\mathrm{H}} \\ &= \frac{\gamma_u^{\mathcal{S}}}{M}(\mathbf{I}_M \otimes \mathbf{g}_{un}\mathbf{g}_{un}^{\mathrm{H}}). \end{aligned} \tag{A.7}$$

The noise is assumed to be uncorrelated both spatially and temporally before the receive beamforming. After the beamforming, the noise covariance matrix becomes

$\mathbf{R}_n^{\mathbf{n}} = \sigma_n^2(\mathbf{I}_M \otimes (\mathbf{W}_r^{\mathrm{H}}\mathbf{W}_r))$. However, $\mathbf{W}_r$ is chosen such that $\mathbf{W}_r^{\mathrm{H}}\mathbf{W}_r = \mathbf{I}_{D_r}$ is satisfied, therefore $\mathbf{R}_n^{\mathbf{n}} = \sigma_n^2\mathbf{I}_{MD_r}$ after receive beamforming. Finally, $\mathbf{R}_n^{\boldsymbol{\psi}}$ in (A.1) becomes

$$\mathbf{R}_n^{\boldsymbol{\psi}} = \sum_{k=1}^{\mathcal{K}} \mathbf{R}_{kn}^{\mathbf{c}} + \sum_{u=1}^{\mathcal{U}} \mathbf{R}_{un}^{\mathbf{s}} + \mathbf{R}_n^{\mathbf{n}}, \tag{A.8}$$

which is consistent with (4.23).

When the transmitted symbols $\mathbf{X}_n$ are known, $\mathbf{R}_{n_1n_2}^{\boldsymbol{\psi}}(\tilde{m})$ in (5.38) can be written as:

$$\begin{aligned}
\mathbf{R}_{n_1n_2}^{\boldsymbol{\psi}} &= \mathbb{E}\left\{\mathrm{vec}\{\boldsymbol{\Psi}_{n_1}\}\,\mathrm{vec}\{\boldsymbol{\Psi}_{n_2}\}^{\mathrm{H}}\right\} \\
&= \sum_{k=1}^{\mathcal{K}} \mathbb{E}\left\{\mathrm{vec}\{\mathbf{C}_{kn_1}\}\,\mathrm{vec}\{\mathbf{C}_{kn_2}\}^{\mathrm{H}}\right\} \\
&\quad + \sum_{u=1}^{\mathcal{U}} \mathbb{E}\left\{\mathrm{vec}\{\mathbf{S}_{un_1}\}\,\mathrm{vec}\{\mathbf{S}_{un_2}\}^{\mathrm{H}}\right\} \\
&\quad + \mathbb{E}\left\{\mathrm{vec}\{\mathbf{N}_{n_1}\}\,\mathrm{vec}\{\mathbf{N}_{n_2}\}^{\mathrm{H}}\right\}.
\end{aligned} \tag{A.9}$$

We can again calculate clutter, SoI and noise parts separately. Let's define:

$$\begin{aligned}
\mathbf{R}_{kn_1n_2}^{\mathbf{c}} &\triangleq \mathbb{E}\left\{\mathrm{vec}\{\mathbf{C}_{kn_1}\}\,\mathrm{vec}\{\mathbf{C}_{kn_2}\}^{\mathrm{H}}\right\}, \\
\mathbf{R}_{un_1n_2}^{\mathbf{s}} &\triangleq \mathbb{E}\left\{\mathrm{vec}\{\mathbf{S}_{un_1}\}\,\mathrm{vec}\{\mathbf{S}_{un_2}\}^{\mathrm{H}}\right\}, \\
\mathbf{R}_{n_1n_2}^{\mathbf{n}} &\triangleq \mathbb{E}\left\{\mathrm{vec}\{\mathbf{N}_{n_1}\}\,\mathrm{vec}\{\mathbf{N}_{n_2}\}^{\mathrm{H}}\right\}.
\end{aligned} \tag{A.10}$$

Following the derivation in (A.3),

$$\mathbf{R}_{kn_1n_2}^{\mathbf{c}} = \mathbf{K}_{kn_1}^{\mathcal{C}}\mathbf{L}_{kn_1}^{\mathcal{C}}\mathbf{R}_k^{\boldsymbol{\alpha}}(\mathbf{L}_{kn_2}^{\mathcal{C}})^{\mathrm{H}}(\mathbf{K}_{kn_2}^{\mathcal{C}})^{\mathrm{H}}. \tag{A.11}$$

On the other hand, SoI symbols are assumed to be uncorrelated among both users and subcarriers, namely,

$$\mathbb{E}\left\{\mathbf{j}_{u_1n_1}\mathbf{j}_{u_2n_2}^{\mathrm{H}}\right\} = \frac{1}{M}\mathbf{I}_M\delta[u_1 - u_2]\delta[n_1 - n_2]. \tag{A.12}$$

Therefore, following the derivation in (A.7),

$$\begin{aligned}
\mathbf{R}_{un_1n_2}^{\mathbf{s}} &= \mathbf{K}_{un_1}^{\mathcal{S}}\left(\mathbb{E}\left\{\mathbf{j}_{un_1}\mathbf{j}_{un_2}^{\mathrm{H}}\right\} \odot \mathbf{D}_u^{\mathcal{S}}\mathbf{R}_u^{\boldsymbol{\beta}}(\mathbf{D}_u^{\mathcal{S}})^{\mathrm{H}}\right)(\mathbf{K}_{un_2}^{\mathcal{S}})^{\mathrm{H}} \\
&= \delta[n_1 - n_2]\frac{\gamma_u^{\mathcal{S}}}{M}(\mathbf{I}_M \otimes \mathbf{g}_{un_1}\mathbf{g}_{un_2}^{\mathrm{H}}).
\end{aligned} \tag{A.13}$$

The noise is again uncorrelated among spatial and temporal domains. As a result, $\mathbf{R}^{\mathbf{n}}_{n_1 n_2} = \delta[n_1 - n_2]\sigma_{n_1}\sigma_{n_2}\mathbf{I}_{MD_r}$. Finally, $\mathbf{R}^{\boldsymbol{\psi}}_{n_1 n_2}$ in (A.9) becomes

$$\mathbf{R}^{\boldsymbol{\psi}}_{n_1 n_2} = \sum_{k=1}^{\mathcal{K}} \mathbf{R}^{\mathbf{c}}_{k n_1 n_2} + \sum_{u=1}^{\mathcal{U}} \mathbf{R}^{\mathbf{s}}_{u n_1 n_2} + \mathbf{R}^{\mathbf{n}}_{n_1 n_2}, \tag{A.14}$$

which is consistent with (5.38).

A.2 Transmitted symbols are not given

It is computationally burdensome to calculate $\mathbf{R}^{\boldsymbol{\eta}}_n$ for each transmitted symbol sequence. To decrease the burden, $\mathbf{R}^{\boldsymbol{\eta}}_n$ can be calculated by taking another expectation over the transmitted symbols $\mathbf{X}_n$. This way, the autocorrelation estimate will be independent of the transmitted symbols, enabling the system to recalculate $\mathbf{R}^{\boldsymbol{\eta}}_n$ only when the UIT map is required to be updated. On the other hand, the new autocorrelation matrix will only be an approximation of the actual one. Let's define

$$\overline{\mathbf{R}}^{\boldsymbol{\eta}}_n \triangleq \mathbb{E}_{\mathbb{X}}\{\mathbf{R}^{\boldsymbol{\eta}}_n\}. \tag{A.15}$$

$\overline{\mathbf{R}}^{\boldsymbol{\eta}}_n$ is a $D_r D_t \times D_r D_t$ matrix. Let's consider it as a matrix consisting of $D_r \times D_r$ blocks, where these blocks are indexed by t_1 and t_2. The $(t_1, t_2)^{th}$ block of $\overline{\mathbf{R}}^{\boldsymbol{\eta}}_n$ can be defined as:

$$\mathbf{E}_{t_1 t_2} \triangleq [\overline{\mathbf{R}}^{\boldsymbol{\eta}}_n]_{[t_1, t_2]} \tag{A.16}$$

where the indices t_1 and t_2 goes from 1 to D_t. As it can be seen in (4.23), $\overline{\mathbf{R}}^{\boldsymbol{\eta}}_n$ consists of several covariance matrices from different scatterers and different SoIs, and so does $\mathbf{E}_{t_1 t_2}$. Since the returns from different scatterers and SoIs are assumed to be uncorrelated, the expectations can be separately calculated and added together. Then, the $(t_1, t_2)^{th}$ block of the covariance matrix corresponding to k^{th} scatterer can be written as:

$$\mathbf{E}^{\mathcal{C}}_{k t_1 t_2} = \sum_{m_1, m_2} \mathbb{E}\left\{ v_{t_1 m_1} \mathbf{H}_{kn} \mathbf{v}_{n m_1} [\mathbf{R}^{\boldsymbol{\alpha}}_k]_{(m_1, m_2)} \mathbf{v}^{\mathrm{H}}_{n m_2} (\mathbf{H}_{kn})^{\mathrm{H}} v^*_{t_2 m_2} \right\} \tag{A.17}$$

where

$$v_{t_1 m_1} = [\mathbf{V}^{\mathrm{H}}_n]_{(t_1, m_1)} = [(\mathbf{X}^*_n \mathbf{X}^{\mathrm{T}}_n)^{-1} \mathbf{X}^*_n \mathbf{D}^*_{\tilde{m}}]_{(t_1, m_1)} \tag{A.18}$$

and $\mathbf{v}_{n m_1}$ is the ${m_1}^{st}$ column of $\mathbf{X}_n \mathbf{D}^{\mathcal{C}}_k$. The indices m_1 and m_2 goes from 1 to M. The rows and columns of the $D_r \times D_r$ matrix $\mathbf{E}^{\mathcal{C}}_{k t_1 t_2}$ can be indexed by r_1 and r_2

so that the indices r_1 and r_2 goes from 1 to D_r. The matrix $\mathbf{v}_{nm_1}\mathbf{v}_{nm_2}^{\mathrm{H}}$ is a $D_t \times D_t$ matrix. Let its rows and columns be indexed by l_1 and l_2, respectively, so that the indices l_1 and l_2 go from 1 to D_t.

To further simplify the calculations, and assuming M is large enough, we can make an approximation as:

$$(\mathbf{X}_n^* \mathbf{X}_n^{\mathrm{T}}) \approx \mathbf{I}_{D_t}. \tag{A.19}$$

Then, $(r_1, r_2)^{th}$ element of $\mathbf{E}_{kt_1t_2}^{\mathcal{C}}$ can be calculated as:

$$\begin{aligned}[\mathbf{E}_{kt_1t_2}^{\mathcal{C}}]_{(r_1,r_2)} = &\sum_{m_1,m_2}\sum_{l_1,l_2}[\mathbf{R}_k^{\boldsymbol{\alpha}}]_{(m_1,m_2)} d_{m_1m_2}[\mathbf{H}_{kn}]_{(r_1,l_1)}[\mathbf{H}_{kn}]^*_{(r_2,l_2)} \\ &\times \underbrace{\mathbb{E}\left\{[\mathbf{X}_n^*]_{(t_1,m_1)}[\mathbf{X}_n]_{(t_2,m_2)}[\mathbf{X}_n]_{(l_1,m_1)}[\mathbf{X}_n^*]_{(l_2,m_2)}\right\}}_{\mu},\end{aligned} \tag{A.20}$$

where the scalar parameter $d_{m_1m_2}$ about the Doppler mismatches is defined as:

$$d_{m_1m_2} \triangleq [\mathbf{D}_{\tilde{m}}^* \mathbf{D}_k^{\mathcal{C}}]_{(m_1,m_1)}[\mathbf{D}_{\tilde{m}}(\mathbf{D}_k^{\mathcal{C}})^*]_{(m_2,m_2)}. \tag{A.21}$$

The expectation μ in (A.20) includes four random variables which are assumed to be zero-mean and iid. Therefore, μ is nonzero only for some elements in the summation. Let's call each element of $\mathbf{X}_n$ as $\tilde{x}$, a zero-mean complex random variable. Then, let's $\mathbb{E}\{|\tilde{x}|^2\} = 1/M$ and $\mathbb{E}\{|\tilde{x}|^4\} \triangleq \sigma_4$. Then, μ can be written as:

$$\mu = \begin{cases} 1/M^2, & m_1 = m_2, \quad t_1 = t_2, \quad l_1 = l_2, \quad t_1 \neq l_1 \\ 1/M^2, & m_1 = m_2, \quad t_1 = l_1, \quad t_2 = l_2, \quad t_1 \neq t_2 \\ 1/M^2, & m_1 \neq m_2, \quad t_1 = l_1, \quad t_2 = l_2, \quad t_1 = t_2 \\ 1/M^2, & m_1 \neq m_2, \quad t_1 = l_1, \quad t_2 = l_2, \quad t_1 \neq t_2 \\ \sigma_4, & m_1 = m_2, \quad t_1 = t_2, \quad l_1 = l_2, \quad t_1 = l_1 \\ 0, & \text{otherwise} \end{cases}. \tag{A.22}$$

For the SoI part inside $\overline{\mathbf{R}}_n^{\boldsymbol{\eta}}$, it is not necessary to begin investigation from the $(t_1, t_2)^{th}$ block because the calculations are easier. Following the (4.22) and (4.23), the expec-

tation of SoI part inside $\mathbf{R}_n^{\boldsymbol{\eta}}$ over $\mathbf{X}_n$ can be found as:

$$\begin{aligned}
&\mathbb{E}\left\{\overline{\mathbf{V}}_n^{\mathrm{H}}\left[\sum_{u=1}^{\mathcal{U}}\frac{\gamma_u^{\mathcal{S}}}{M}(\mathbf{I}_M\otimes\mathbf{g}_{un}\mathbf{g}_{un}^{\mathrm{H}})\right]\overline{\mathbf{V}}_n\right\}\\
&=\mathbb{E}\left\{\sum_{u=1}^{\mathcal{U}}\frac{\gamma_u^{\mathcal{S}}}{M}(\mathbf{V}_n^{\mathrm{H}}\otimes\mathbf{I}_{D_r})(\mathbf{I}_M\otimes\mathbf{g}_{un}\mathbf{g}_{un}^{\mathrm{H}})(\mathbf{V}_n\otimes\mathbf{I}_{D_r})\right\}\\
&=\mathbb{E}\left\{\sum_{u=1}^{\mathcal{U}}\frac{\gamma_u^{\mathcal{S}}}{M}(\mathbf{V}_n^{\mathrm{H}}\mathbf{V}_n)\otimes(\mathbf{g}_{un}\mathbf{g}_{un}^{\mathrm{H}})\right\}\\
&\approx\sum_{u=1}^{\mathcal{U}}\frac{\gamma_u^{\mathcal{S}}}{M}\mathbf{I}_{D_t}\otimes(\mathbf{g}_{un}\mathbf{g}_{un}^{\mathrm{H}}).
\end{aligned}\tag{A.23}$$

Then, the $(t_1,t_2)^{th}$ block of $\overline{\mathbf{R}}_n^{\boldsymbol{\eta}}$ corresponding to u^{th} user is seen to be written as:

$$\mathbf{E}_{ut_1t_2}^{\mathcal{S}}\approx\delta[t_1-t_2]\frac{\gamma_u^{\mathcal{S}}}{M}\mathbf{g}_{un}\mathbf{g}_{un}^{\mathrm{H}}\tag{A.24}$$

For the noise part, the calculations seem unnecessary. The $(t_1,t_2)^{th}$ block of $\overline{\mathbf{R}}_n^{\boldsymbol{\eta}}$ corresponding to noise is $\delta[t_1-t_2]\sigma_n^2\mathbf{I}_{D_r}$. Finally, the $(t_1,t_2)^{th}$ block of $\overline{\mathbf{R}}_n^{\boldsymbol{\eta}}$ is:

$$\mathbf{E}_{t_1t_2}=\sum_{k=1}^{\mathcal{K}}\mathbf{E}_{kt_1t_2}^{\mathcal{C}}+\sum_{u=1}^{\mathcal{U}}\mathbf{E}_{ut_1t_2}^{\mathcal{S}}+\delta[t_1-t_2]\sigma_n^2\mathbf{I}_{D_r}\tag{A.25}$$

for $t_1,t_2=1,2,\cdots,D_t$.

Similar to $\mathbf{R}_n^{\boldsymbol{\eta}}$, it is computationally burdensome to calculate $\mathbf{R}_{n_1n_2}^{\boldsymbol{\eta}}$ for each transmitted symbol sequence. Therefore, its expectation over $\mathbf{X}_{n_1}$ and $\mathbf{X}_{n_2}$ can be taken to reduce the computational complexity. In the following calculations, the symbols transmitted in different subcarriers are considered to be independent from each other, so that the double expectations can be separated. Let's define

$$\overline{\mathbf{R}}_{n_1n_2}^{\boldsymbol{\eta}}\triangleq\mathbb{E}_{\mathbb{X}n_1}\{\mathbb{E}_{\mathbb{X}n_2}\{\mathbf{R}_{n_1n_2}^{\boldsymbol{\eta}}\}\}.\tag{A.26}$$

Following the definition in (4.29),

$$\begin{aligned}
\overline{\mathbf{R}}_{n_1n_2}^{\boldsymbol{\eta}}&=\sum_{k=1}^{\mathcal{K}}\mathbb{E}\left\{\overline{\mathbf{V}}_{n_1}\mathbf{K}_{kn_1}^{\mathcal{C}}\mathbf{L}_{kn_1}^{\mathcal{C}}\mathbf{R}_k^{\boldsymbol{\alpha}}(\mathbf{L}_{kn_2}^{\mathcal{C}})^{\mathrm{H}}(\mathbf{K}_{kn_2}^{\mathcal{C}})^{\mathrm{H}}\overline{\mathbf{V}}_{n_2}^{\mathrm{H}}\right\}\\
&\qquad+\mathbb{E}\left\{\overline{\mathbf{V}}_{n_1}\right\}(\mathbf{R}_{un_1n_2}^{\mathbf{s}}+\mathbf{R}_{n_1n_2}^{\mathbf{n}})\mathbb{E}\left\{\overline{\mathbf{V}}_{n_2}^{\mathrm{H}}\right\}\\
&=\sum_{k=1}^{\mathcal{K}}\mathbb{E}\left\{\overline{\mathbf{V}}_{n_1}\mathbf{K}_{kn_1}^{\mathcal{C}}\mathbf{L}_{kn_1}^{\mathcal{C}}\mathbf{R}_k^{\boldsymbol{\alpha}}(\mathbf{L}_{kn_2}^{\mathcal{C}})^{\mathrm{H}}(\mathbf{K}_{kn_2}^{\mathcal{C}})^{\mathrm{H}}\overline{\mathbf{V}}_{n_2}^{\mathrm{H}}\right\}\\
&\qquad+\delta[n_1-n_2]\mathbb{E}\left\{\overline{\mathbf{V}}_{n_1}(\mathbf{R}_{un_1}^{\mathbf{s}}+\mathbf{R}_{n_1}^{\mathbf{n}})\overline{\mathbf{V}}_{n_1}^{\mathrm{H}}\right\}
\end{aligned}\tag{A.27}$$

because $\mathbf{R}^{\mathbf{s}}_{un_1n_2}$ in (A.13) includes $\delta[n_1 - n_2]$. Similar to (A.17), we can define a new matrix

$$\begin{aligned}\mathbf{F}^{\mathcal{C}}_{kn_1}(\tilde{m}) &\triangleq \mathbb{E}\{\overline{\mathbf{V}}^{\mathrm{H}}_{n_1}\mathbf{K}^{\mathcal{C}}_{kn_1}\mathbf{L}^{\mathcal{C}}_{kn_1}\} \\ &= \mathbb{E}\{(\mathbf{V}^{\mathrm{H}}_{n_1} \otimes \mathbf{H}_{kn_1})(\mathbf{I}_M \circledcirc (\mathbf{X}_{n_1}\mathbf{D}^{\mathcal{C}}_k))\} \\ &\approx \mathbb{E}\{(\mathbf{X}^*_{n_1}\mathbf{D}^*_{\tilde{m}} \otimes \mathbf{H}_{kn_1})(\mathbf{I}_M \circledcirc (\mathbf{X}_{n_1}\mathbf{D}^{\mathcal{C}}_k))\}, \end{aligned} \tag{A.28}$$

using the approximation in (A.19). $\mathbf{F}^{\mathcal{C}}_{kn_1}$ is a $D_rD_t \times M$ matrix. Let's consider it as a matrix consisting of $D_r \times 1$ blocks, where these blocks are indexed by t_1 and m_1. Then, $(t_1, m_1)^{th}$ block of $\mathbf{F}^{\mathcal{C}}_{kn_1}$ can be defined as:

$$\mathbf{f}^{\mathcal{C}}_{t_1m_1} \triangleq [\mathbf{F}^{\mathcal{C}}_{kn_1}]_{[t_1,m_1]} = \mathbb{E}\left\{v_{t_1m_1}\mathbf{H}_{kn_1}\mathbf{v}_{n_1m_1}\right\} \tag{A.29}$$

where $v_{t_1m_1}$ and $\mathbf{v}_{n_1m_1}$ are defined the same way as in (A.17). The r_1^{th} element of $D_r \times 1$ vector $\mathbf{f}^{\mathcal{C}}_{t_1m_1}$ can be written as:

$$\begin{aligned}[\mathbf{f}^{\mathcal{C}}_{t_1m_1}]_{(r_1)} &= \mathbb{E}\left\{\sum_{t_2=1}^{D_t} v_{t_1m_1}[\mathbf{H}_{kn_1}]_{(r_1,t_1)}[\mathbf{v}_{n_1m_1}]_{(t_2)}\right\} \\ &= \sum_{t_2=1}^{D_t}\mathbb{E}\left\{[\mathbf{X}^*_{n_1}\mathbf{D}^*_{\tilde{m}}]_{(t_1,m_1)}[\mathbf{H}_{kn_1}]_{(r_1,t_1)}[\mathbf{X}_{n_1}\mathbf{D}^{\mathcal{C}}_k]_{(t_2,m_1)}\right\} \\ &= \mathbb{E}\left\{|[\mathbf{X}^*_{n_1}]_{(t_1,m_1)}|^2\right\}[\mathbf{D}^*_{\tilde{m}}]_{(m_1,m_1)}[\mathbf{D}^{\mathcal{C}}_k]_{(m_1,m_1)}[\mathbf{H}_{kn_1}]_{(r_1,t_1)} \\ &= \frac{1}{M}[\mathbf{D}^*_{\tilde{m}}\mathbf{D}^{\mathcal{C}}_k]_{(m_1,m_1)}[\mathbf{H}_{kn_1}]_{(r_1,t_1)} \end{aligned} \tag{A.30}$$

where the third equality comes from the fact that transmitted symbols from different antennas are uncorrelated, namely $\mathbb{E}\left\{[\mathbf{X}^*_{n_1}]_{(t_1,m_1)}[\mathbf{X}_{n_1}]_{(t_2,m_1)}\right\} = 0$ for all $t_2 \neq t_1$. Then, the vector $\mathbf{f}^{\mathcal{C}}_{t_1m_1}$ becomes

$$\mathbf{f}^{\mathcal{C}}_{t_1m_1} = \frac{1}{M}[\mathbf{D}^*_{\tilde{m}}\mathbf{D}^{\mathcal{C}}_k]_{(m_1,m_1)}[\mathbf{H}_{kn_1}]_{[:,t_1]} \tag{A.31}$$

By some algebraic manipulations,

$$\mathbf{F}^{\mathcal{C}}_{kn_1} = \frac{1}{M}\,\mathrm{vec}\{\mathbf{H}_{kn_1}\}\mathbf{1}^{\mathrm{T}}\mathbf{D}^*_{\tilde{m}}\mathbf{D}^{\mathcal{C}}_k \tag{A.32}$$

where $\mathbf{1}$ is the all-ones vector of proper size. Then,

$$\overline{\mathbf{R}}^{\boldsymbol{\eta}}_{n_1n_2} \approx \begin{cases} \overline{\mathbf{R}}^{\boldsymbol{\eta}}_{n_1}, & \text{if } n_1 = n_2 \\ \sum_{k=1}^{\mathcal{K}} \mathbf{F}^{\mathcal{C}}_{kn_1}\mathbf{R}^{\boldsymbol{\alpha}}_k(\mathbf{F}^{\mathcal{C}}_{kn_2})^{\mathrm{H}}, & \text{if } n_1 \neq n_2 \end{cases} \tag{A.33}$$

B Calculation of autocorrelation matrices in Chapter 5

B.1 Transmitted symbols are given

The calculation of autocorrelation matrices in Chapter 5 is mostly similar to the ones in Chapter 4. However, the multistatic extension results in some slight changes in these calculations, which will be examined in this appendix section.

In Chapter 5, beam-squint effects are ignored so that the angular covariance matrices are the same in all subcarriers. Therefore, the calculation of $\mathbf{R}^{(i)}_{\psi n_1 n_2}$ is enough to describe all true covariance matrices in Chapter 5. Similar to the calculations in Appendix Section A, the clutter (UITs) and the noise parts in $\mathbf{R}^{(i)}_{\psi n_1 n_2}$ can be calculated separately.

Since the noise terms in different subcarriers are assumed to be independent like in Appendix Section A, the noise part in $\mathbf{R}^{(i)}_{\psi n_1 n_2}$ is visible only when $n_1 = n_2$, and it is equal to $\sigma_n^2 \mathbf{I}_{MD_r}$ because the noise is also assumed to be independent between different OFDM symbols and receive streams.

When (5.40) is investigated, it can be seen that the clutter part inside $\mathbf{R}^{(i)}_{\psi n_1 n_2}$ includes the summation over different transmit antennas. In this thesis, the multistatic assumption states that the reflected echo signals from an arbitrary scatterer due to each Rx-Tx pair is independent from each other, as explained in Section 5.1. Therefore, the covariance matrix at the i^{th} receiver can be written as a summation over all transmitters like:

$$\mathbf{R}^{(i)}_{\psi n_1 n_2} \triangleq \sum_{j=1}^{\mathcal{J}} \mathbf{R}^{(i,j)}_{\psi n_1 n_2} + \delta[n_1 - n_2]\sigma^2_{n_1} \mathbf{I}_{MD_r}, \tag{B.1}$$

where $\mathbf{R}^{(i,j)}_{\psi n_1 n_2}$ is the cross-covariance matrix between the $(i,j)^{\text{th}}$ Rx-Tx pair.

Similar to the definitions in (A.3), let's define:

$$\mathbf{K}^{(i,j)}_k \triangleq \mathbf{I}_M \otimes \mathbf{H}^{(i,j)}_k, \tag{B.2}$$

and

$$\mathbf{L}^{(i,j)}_{kn} \triangleq \mathbf{I}_M \circledcirc (\mathbf{X}^{(j)}_n \mathbf{D}^{(i,j)}_{\bar{\alpha}_k}). \tag{B.3}$$

Additionally, for the sake of neatness in this appendix section, define:

$$\mathbf{K}_{kn}^{(i,j)} \triangleq \mathbf{I}_M \otimes \rho_{kn}^{(i,j)} \mathbf{H}_k^{(i,j)}, \tag{B.4}$$

which is required because the channel definitions in Chapter 4 (in (4.1)) and Chapter 5 (in (5.8)) are slightly different.

Then, similar to (A.4), if $n_1 = n_2$, the covariance matrix of the raw interference becomes:

$$\mathbf{R}_{\boldsymbol{\psi} n}^{(i)} = \sum_{j=1}^{\mathcal{J}} \sum_{k=1}^{\mathcal{K}} \mathbf{K}_k^{(i,j)} \mathbf{L}_{kn}^{(i,j)} \mathbf{R}_k^{\tilde{\boldsymbol{\alpha}}^{(i,j)}} (\mathbf{L}_{kn}^{(i,j)})^{\mathrm{H}} (\mathbf{K}_k^{(i,j)})^{\mathrm{H}} + \sigma_n^2 \mathbf{I}_{MD_r}, \tag{B.5}$$

which is consistent with (5.39). On the other hand, if $n_1 \neq n_2$, similar to (A.11) and (A.14), the cross-covariance matrix of the raw interference between different subcarriers becomes:

$$\mathbf{R}_{\boldsymbol{\psi} n_1 n_2}^{(i)} = \sum_{j=1}^{\mathcal{J}} \sum_{k=1}^{\mathcal{K}} \mathbf{K}_{kn_1}^{(i,j)} \mathbf{L}_{kn_1}^{(i,j)} \mathbf{R}_k^{\tilde{\boldsymbol{\alpha}}^{(i,j)}} (\mathbf{L}_{kn_2}^{(i,j)})^{\mathrm{H}} (\mathbf{K}_{kn_2}^{(i,j)})^{\mathrm{H}}, \tag{B.6}$$

which is consistent with (5.40).

B.2 Transmitted symbols are not given

Similar to Appendix A.2, the expectation of covariance matrices over the transmitted symbols are required for the Expected $\mathbf{X}$ detectors. The derivations will follow Appendix A.2, where slight differences.

The expected covariance matrix is defined in (5.50) and rewritten here as:

$$\overline{\mathbf{R}}_{\boldsymbol{\eta}}^{(i,j)} \triangleq \mathbb{E}\left\{\mathbf{R}_{\boldsymbol{\eta}}^{(i,j)}\right\}. \tag{B.7}$$

As it can be seen in (5.35),

$$\overline{\mathbf{R}}_{\boldsymbol{\eta}}^{(i,j)} = \sum_{j_1,j_2} \sum_{n_1,n_2} \rho_{\star n_1}^{(i,j_1)*} \rho_{\star n_2}^{(i,j_2)} \mathbb{E}\left\{\overline{\mathbf{V}}_{n_1 j_1}^{(i,j)\mathrm{H}} \mathbf{R}_{\psi n_1 n_2}^{(i)} \overline{\mathbf{V}}_{n_2 j_2}^{(i,j)}\right\}. \tag{B.8}$$

It can be seen in (B.8) that the propagation delay terms are independent of $\mathbf{X}$ and are not included in the expectation. Let's define the remaining term which is an expectation over $\mathbf{X}$ as:

$$\mathbf{M}_{n_1 n_2 j_1 j_2}^{(i,j)} \triangleq \mathbb{E}\left\{\overline{\mathbf{V}}_{n_1 j_1}^{(i,j)\mathrm{H}} \mathbf{R}_{\psi n_1 n_2}^{(i)} \overline{\mathbf{V}}_{n_2 j_2}^{(i,j)}\right\}, \tag{B.9}$$

and using (5.40), it is seen that:

$$\mathbf{M}^{(i,j)}_{n_1n_2j_1j_2} = \mathbb{E}\left\{\overline{\mathbf{V}}^{(i,j)\mathrm{H}}_{n_1j_1}\left(\sum_{j'=1}^{\mathcal{J}}\mathbf{R}^{(i,j')}_{\psi n_1n_2} + \delta[n_1-n_2]\sigma^2_{n_1}\mathbf{I}_{MD_r}\right)\overline{\mathbf{V}}^{(i,j)}_{n_2j_2}\right\} \tag{B.10}$$

$\mathbf{M}^{(i,j)}_{n_1n_2j_1j_2}$ is a $D_rD_t \times D_rD_t$ matrix. Let's consider it as a matrix consisting of $D_r \times D_r$ blocks, where these blocks are indexed by t_1 and t_2. The $(t_1,t_2)^{th}$ block of $\mathbf{M}^{(i,j)}_{n_1n_2j_1j_2}$ can be defined as:

$$\mathbf{E}^{(i,j)}_{t_1t_2} \triangleq \left[\mathbf{M}^{(i,j)}_{n_1n_2j_1j_2}\right]_{[t_1,t_2]} \tag{B.11}$$

where the indices t_1 and t_2 goes from 1 to D_t.

$\mathbf{R}^{(i,j)}_{\psi n_1n_2}$ consists of several covariance matrices from different scatterers, and so does $\mathbf{E}^{(i,j)}_{t_1t_2}$. Since the returns coming from different scatterers are assumed to be uncorrelated, the expectations can be separately calculated and added together.

To keep the derivations similar to the ones in Appendix A, the elements of $\mathbf{M}^{(i,j)}_{n_1n_2j_1j_2}$ are found in two different cases, namely when $n_1 = n_2$ and when $n_1 \neq n_2$.

If $n_1 = n_2 = n$, then the $(t_1,t_2)^{\text{th}}$ block of the $\mathbf{M}^{(i,j)}_{n_1n_2j_1j_2}$ matrix corresponding to k^{th} scatterer can be written as:

$$\mathbf{E}^{(i,j)}_{kt_1t_2} = \sum_{j'=1}^{\mathcal{J}}\sum_{m_1,m_2}\mathbb{E}\left\{v^{(i,j)}_{j_1t_1m_1}\mathbf{H}_k\mathbf{v}^{(i,j')}_{nm_1}[\mathbf{R}^{\tilde{\boldsymbol{\alpha}}(i,j')}_k]_{(m_1,m_2)}\mathbf{v}^{(i,j')\mathrm{H}}_{nm_2}(\mathbf{H}_k)^{\mathrm{H}}v^{(i,j)*}_{j_2t_2m_2}\right\} \tag{B.12}$$

where $\mathbf{v}^{(i,j')}_{nm_1}$ is the $m_1{}^{\text{st}}$ column of $(\mathbf{X}^{(j')}_n\mathbf{D}^{(i,j')}_{\tilde{\alpha}_k})$ and

$$v^{(i,j)}_{j_1t_1m_1} = [\mathbf{V}^{(i,j)\mathrm{H}}_{nj_1}]_{(t_1,m_1)} = [\mathbf{B}^{(j)\mathrm{T}}_{j_1}\mathbf{X}^{(j_1)*}_n\mathbf{D}^{(i,j_1)*}_{\tilde{\alpha}_\star}]_{(t_1,m_1)}. \tag{B.13}$$

In the expectation calculations, assuming MN is large enough, $\mathbf{B} = (\mathbf{X}\mathbf{X}^{\mathrm{H}})^{-1} \approx \mathbf{I}_{\mathcal{J}D_t}$ approximation is assumed to be correct so that $\mathbf{B}^{(j)}_{j'} = \delta[j-j']\mathbf{I}_{D_t}$ is satisfied. Therefore, (B.13) becomes nonzero only when $j_1 = j$, which can be rewritten as:

$$v^{(i,j)}_{j_1t_1m_1} = v^{(i,j)}_{t_1m_1} = [\mathbf{V}^{(i,j)\mathrm{H}}_{n}]_{(t_1,m_1)} = [\mathbf{X}^{(j)*}_n\mathbf{D}^{(i,j)*}_{\tilde{\alpha}_\star}]_{(t_1,m_1)}, \tag{B.14}$$

relaxing the j_1 and j_2 dependence of $\mathbf{E}^{(i,j)}_{kt_1t_2}$.

The indices m_1 and m_2 goes from 1 to M. The rows and columns of the $D_r \times D_r$ matrix $\mathbf{E}^{(i,j)}_{kt_1t_2}$ can be indexed by r_1 and r_2 so that the indices r_1 and r_2 goes from 1 to

D_r. The matrix $\mathbf{v}_{nm_1}^{(i,j')}\mathbf{v}_{nm_2}^{(i,j')\mathrm{H}}$ is a $D_t \times D_t$ matrix. Let its rows and columns be indexed by l_1 and l_2, respectively, so that the indices l_1 and l_2 go from 1 to D_t.

Then, $(r_1, r_2)^{\text{th}}$ element of $\mathbf{E}_{kt_1t_2}^{(i,j)}$ can be calculated as:

$$[\mathbf{E}_{kt_1t_2}^{(i,j)}]_{(r_1,r_2)} = \sum_{j'=1}^{\mathcal{J}} \sum_{m_1,m_2} \sum_{l_1,l_2} [\mathbf{R}_k^{\tilde{\boldsymbol{\alpha}}(i,j')}]_{(m_1,m_2)} d_{m_1m_2}^{(i,j,j')} [\mathbf{H}_k]_{(r_1,l_1)} [\mathbf{H}_k]_{(r_2,l_2)}^* \times \underbrace{\mathbb{E}\left\{ [\mathbf{X}_n^{(j)*}]_{(t_1,m_1)} [\mathbf{X}_n^{(j)}]_{(t_2,m_2)} [\mathbf{X}_n^{(j')}]_{(l_1,m_1)} [\mathbf{X}_n^{(j')*}]_{(l_2,m_2)} \right\}}_{\mu}, \tag{B.15}$$

where the scalar parameter $d_{m_1m_2}^{(i,j,j')}$ about the Doppler mismatches is defined as:

$$d_{m_1m_2}^{(i,j,j')} \triangleq [\mathbf{D}_{\tilde{\alpha}_\star}^{(i,j)*} \mathbf{D}_{\tilde{\alpha}_k}^{(i,j')}]_{(m_1,m_1)} [\mathbf{D}_{\tilde{\alpha}_\star}^{(i,j)} (\mathbf{D}_{\tilde{\alpha}_k}^{(i,j')*})]_{(m_2,m_2)}. \tag{B.16}$$

The expectation μ in (B.15) includes four random variables which are assumed to be zero-mean and iid. Therefore, μ is nonzero only for some elements in the summation. Let's call each element of $\mathbf{X}_n^{(j)}$ as $\tilde{x}^{(j)}$, a zero-mean complex random variable. Then, let $\mathbb{E}\{|\tilde{x}^{(j)}|^2\} = \sigma_2$ and $\mathbb{E}\{|\tilde{x}^{(j)}|^4\} \triangleq \sigma_4$. Then, μ can be written as:

$$\mu = \begin{cases} (\sigma_2)^2, & m_1 = m_2, \quad t_1 = t_2, \quad l_1 = l_2, \quad t_1 \neq l_1, \quad j' = j \\ (\sigma_2)^2, & m_1 = m_2, \quad t_1 = l_1, \quad t_2 = l_2, \quad t_1 \neq t_2, \quad j' = j \\ (\sigma_2)^2, & m_1 \neq m_2, \quad t_1 = l_1, \quad t_2 = l_2, \quad t_1 = t_2, \quad j' = j \\ (\sigma_2)^2, & m_1 \neq m_2, \quad t_1 = l_1, \quad t_2 = l_2, \quad t_1 \neq t_2, \quad j' = j \\ \sigma_4, & m_1 = m_2, \quad t_1 = t_2, \quad l_1 = l_2, \quad t_1 = l_1, \quad j' = j \\ (\sigma_2)^2, & m_1 = m_2, \quad t_1 = t_2, \quad l_1 = l_2, \quad t_1 = l_1, \quad j' \neq j \\ (\sigma_2)^2, & m_1 = m_2, \quad t_1 = t_2, \quad l_1 = l_2, \quad t_1 \neq l_1, \quad j' \neq j \\ 0, & \text{otherwise} \end{cases}. \tag{B.17}$$

The $(t_1, t_2)^{\text{th}}$ block of $\mathbf{M}_{n_1n_2j_1j_2}^{(i,j)}$ when $n_1 = n_2 = n$ is then:

$$\mathbf{E}_{t_1t_2}^{(i,j)} = \sum_{k=1}^{\mathcal{K}} \mathbf{E}_{kt_1t_2}^{(i,j)} + \delta[t_1 - t_2]\sigma_n^2 \mathbf{I}_{D_r}. \tag{B.18}$$

When $n_1 \neq n_2$, using (B.6) and (B.9), the following expectation can be written:

$$\begin{aligned}
&\mathbf{M}^{(i,j)}_{n_1 n_2 j_1 j_2} \\
=&\mathbb{E}\left\{\overline{\mathbf{V}}^{(i,j)\mathrm{H}}_{n_1 j_1}\left(\sum_{j'=1}^{\mathcal{J}}\sum_{k=1}^{\mathcal{K}}\mathbf{K}^{(i,j')}_{kn_1}\mathbf{L}^{(i,j')}_{kn_1}\mathbf{R}^{\tilde{\boldsymbol{\alpha}}^{(i,j')}}_{k}(\mathbf{L}^{(i,j')}_{kn_2})^{\mathrm{H}}(\mathbf{K}^{(i,j')}_{kn_2})^{\mathrm{H}}\right)\overline{\mathbf{V}}^{(i,j)}_{n_2 j_2}\right\} \\
=&\mathbb{E}\left\{\sum_{j'=1}^{\mathcal{J}}\sum_{k=1}^{\mathcal{K}}\left(\overline{\mathbf{V}}^{(i,j)\mathrm{H}}_{n_1 j_1}\mathbf{K}^{(i,j')}_{kn_1}\mathbf{L}^{(i,j')}_{kn_1}\mathbf{R}^{\tilde{\boldsymbol{\alpha}}^{(i,j')}}_{k}(\mathbf{L}^{(i,j')}_{kn_2})^{\mathrm{H}}(\mathbf{K}^{(i,j')}_{kn_2})^{\mathrm{H}}\overline{\mathbf{V}}^{(i,j)}_{n_2 j_2}\right)\right\} \\
=&\sum_{j'=1}^{\mathcal{J}}\sum_{k=1}^{\mathcal{K}}\mathbb{E}\left\{\overline{\mathbf{V}}^{(i,j)\mathrm{H}}_{n_1 j_1}\mathbf{K}^{(i,j')}_{kn_1}\mathbf{L}^{(i,j')}_{kn_1}\right\}\mathbf{R}^{\tilde{\boldsymbol{\alpha}}^{(i,j')}}_{k}\mathbb{E}\left\{(\mathbf{L}^{(i,j')}_{kn_2})^{\mathrm{H}}(\mathbf{K}^{(i,j')}_{kn_2})^{\mathrm{H}}\overline{\mathbf{V}}^{(i,j)}_{n_2 j_2}\right\} \\
\triangleq&\sum_{j'=1}^{\mathcal{J}}\sum_{k=1}^{\mathcal{K}}\mathbf{F}^{(i,j,j')}_{kn_1 j_1}\mathbf{R}^{\tilde{\boldsymbol{\alpha}}^{(i,j')}}_{k}\mathbf{F}^{(i,j,j')}_{kn_2 j_2},
\end{aligned} \tag{B.19}$$

where

$$\begin{aligned}
\mathbf{F}^{(i,j,j')}_{kn_1 j_1} &= \mathbb{E}\left\{\overline{\mathbf{V}}^{(i,j)\mathrm{H}}_{n_1 j_1}\mathbf{K}^{(i,j')}_{kn_1}\mathbf{L}^{(i,j')}_{kn_1}\right\} \\
&= \mathbb{E}\left\{(\mathbf{V}^{(i,j)\mathrm{H}}_{n_1 j_1}\otimes\rho^{(i,j')}_{kn_1}\mathbf{H}^{(i,j')}_{k})(\mathbf{I}_M \circledcirc (\mathbf{X}^{(j')}_{n_1}\mathbf{D}^{(i,j')}_{\bar{\alpha}_k}))\right\} \\
&\approx \mathbb{E}\left\{(\mathbf{X}^{(j)*}_{n_1}\mathbf{D}^{(i,j)*}_{\bar{\alpha}_\star}\otimes\rho^{(i,j')}_{kn_1}\mathbf{H}^{(i,j')}_{k})(\mathbf{I}_M \circledcirc (\mathbf{X}^{(j')}_{n_1}\mathbf{D}^{(i,j')}_{\bar{\alpha}_k}))\right\}
\end{aligned} \tag{B.20}$$

is defined similar to (A.28), using the $\mathbf{B} \approx \mathbf{I}_{\mathcal{J}D_t}$ approximation. It should be noted that the first term includes $\mathbf{X}^{(j)*}_{n_1}$ and the second term includes $\mathbf{X}^{(j')}_{n_1}$ as the random variables over which the expectation is taken. Since the transmitted symbols from different Tx antennas are zero-mean and independent from each other, the expectation will be zero when $j \neq j'$. Therefore, (B.20) can be rewritten as:

$$\begin{aligned}
\mathbf{F}^{(i,j)}_{kn_1} &\triangleq \delta[j-j']\delta[j-j_1]\mathbf{F}^{(i,j,j')}_{kn_1 j_1} \\
&= \mathbb{E}\left\{(\mathbf{X}^{(j)*}_{n_1}\mathbf{D}^{(i,j)*}_{\bar{\alpha}_\star}\otimes\rho^{(i,j)}_{kn_1}\mathbf{H}^{(i,j)}_{k})(\mathbf{I}_M \circledcirc (\mathbf{X}^{(j)}_{n_1}\mathbf{D}^{(i,j)}_{\bar{\alpha}_k}))\right\},
\end{aligned} \tag{B.21}$$

which has the same form as in (A.28). Therefore, following the same steps from (A.28) to (A.32), $\mathbf{F}^{(i,j)}_{kn_1}$ can be written as:

$$\mathbf{F}^{(i,j)}_{kn_1} = \frac{\rho^{(i,j)}_{kn_1}}{MN}\,\mathrm{vec}\{\mathbf{H}^{(i,j)}_{k}\}\mathbf{1}^{\mathrm{T}}\mathbf{D}^{(i,j)*}_{\bar{\alpha}_\star}\mathbf{D}^{(i,j)}_{\bar{\alpha}_k}. \tag{B.22}$$

As a result, when $n_1 \neq n_2$,

$$\mathbf{M}^{(i,j)}_{n_1 n_2 j_1 j_2} = \sum_{k=1}^{\mathcal{K}}\mathbf{F}^{(i,j)}_{kn_1}\mathbf{R}^{\tilde{\boldsymbol{\alpha}}^{(i,j)}}_{k}\mathbf{F}^{(i,j)}_{kn_2}. \tag{B.23}$$

CURRICULUM VITAE

This CV belongs to Uğur Berkay Saraç, who is a PhD candidate in Electrical and Electronics Engineering at Middle East Technical University.

Education

2019 – 2025	**Ph.D. in Electrical and Electronics Engineering** Middle East Technical University, Ankara, Türkiye
2016 – 2019	**M.Sc. in Electrical and Electronics Engineering** Middle East Technical University, Ankara, Türkiye
2011 – 2016	**B.Sc. in Electrical and Electronics Engineering** Middle East Technical University, Ankara, Türkiye

Research Interests

Integrated Sensing and Communications, OFDM Radar, MIMO Radar, Interference Channel Models, Multistatic Radar Systems

Professional Experience

2019 –	**Research Assistant** Dept. of Electrical and Electronics Engineering Middle East Technical University, Ankara, Türkiye

Publications

2025 U. B. Sarac and G. M. Guvensen, "Knowledge-Aided and Adaptive Beam-Squint Aware MIMO-OFDM Radar Detectors for ISAC," *IEEE Transactions on Communications*, doi: 10.1109/TCOMM.2025.3568219.

2023 U. B. Sarac and G. M. Guvensen, "On the Effects of Range-Doppler Processing for Target Detection in OFDM-Based RadCom," *IEEE Communications Letters*, vol. 27, no. 7, pp. 1864-1868, July 2023, doi: 10.1109/LCOMM.2023.3279015.

2023 A. Kurt, M. B. Salman, U. B. Sarac and G. M. Guvensen, "An Adaptive-Iterative Nonlinear Interference Cancellation in Time-Varying Full-Duplex Channels," *IEEE Transactions on Vehicular Technology*, vol. 72, no. 2, pp. 1862-1878, Feb. 2023, doi: 10.1109/TVT.2022.3208766.